Nonlinear Models with Darcy-Forchheimer Relation

By

Farwa Haider

Department of Mathematics
Quaid-I-Azam University
Islamabad, Pakistan

2022

Nonlinear Models with Darcy-Forchheimer Relation

By

Farwa Haider

Supervised By

Prof. Dr. Tasawar Hayat

Department of Mathematics
Quaid-I-Azam University
Islamabad, Pakistan

2022

Nonlinear Models with Darcy-Forchheimer Relation

By

Farwa Haider

A DISSERTATION SUBMITTED IN THE PARTIAL FULFILLMENT OF THE REQUIREMENT FOR THE DEGREE OF

DOCTOR OF PHILOSOPHY

IN

MATHEMATICS

Supervised By

Prof. Dr. Tasawar Hayat

Department of Mathematics
Quaid-I-Azam University
Islamabad, Pakistan

2022

Author's Declaration

I **Farwa Haider** hereby state that my PhD thesis titled **Nonlinear Models with Darcy-Forchheimer Relation** is my own work and has not been submitted previously by me for taking any degree from the Quaid-I-Azam University Islamabad, Pakistan or anywhere else in the country/world.

At any time if my statement is found to be incorrect even after my graduate the university has the right to withdraw my PhD degree.

Name of Student: **Farwa Haider**

Date: **17-05-2022**

Plagiarism Undertaking

I solemnly declare that research work presented in the thesis titled **"Nonlinear Models with Darcy-Forchheimer Relation"** is solely my research work with no significant contribution from any other person. Small contribution/help wherever taken has been duly acknowledged and that complete thesis has been written by me.

I understand the zero tolerance policy of the HEC and **Quaid-I-Azam University** towards plagiarism. Therefore, I as an Author of the above titled thesis declare that no portion of my thesis has been plagiarized and any material used as reference is properly referred/cited.

I undertake that if I am found guilty of any formal plagiarism in the above titled thesis even afterward of PhD degree, the University reserves the rights to withdraw/revoke my PhD degree and that HEC and the University has the right to publish my name on the HEC/University Website on which names of students are placed who submitted plagiarized thesis.

Student/Author Signature: ______________

Name: **Farwa Haider**

Nonlinear Models with Darcy-Forchheimer Relation

By

Farwa Haider

CERTIFICATE

A THESIS SUBMITTED IN THE PARTIAL FULFILLMENT OF THE REQUIREMENTS FOR THE DEGREE OF THE

DOCTOR OF PHILOSOPHY IN MATHEMATICS

We accept this dissertation as conforming to the required standard

1. ____________
Prof. Dr. Tariq Shah
(Chairman)

2. ____________
Prof. Dr. Tasawar Hayat
(Supervisor)

3. ____________
Dr. Tariq Javed
Professor
Department of Mathematics & Statistics,
International Islamic University Islamabad,
Sector H-10 Islamabad
(External Examiner)

4. ____________
Dr. Meraj Mustafa Hashmi
Associate Professor
Department of Mathematics,
School of Natural Sciences (SNS),
National University of Sciences and Technology (NUST), Sector H-12
Islamabad
(External Examiner)

Department of Mathematics
Quaid-I-Azam University
Islamabad, Pakistan
2022

Certificate of Approval

This is to certify that the research work presented in this thesis entitled **Nonlinear Models with Darcy-Forchheimer Relation** was conducted by **Ms. Farwa Haider** under the kind supervision of **Prof. Dr. Tasawar Hayat**. No part of this thesis has been submitted anywhere else for any other degree. This thesis is submitted to the Department of Mathematics, Quaid-i-Azam University, Islamabad in partial fulfillment of the requirements for the degree of Doctor of Philosophy in field of Mathematics from Department of Mathematics, Quaid-i-Azam University Islamabad, Pakistan.

Student Name: **Farwa Haider** Signature: ____________

External committee:

a) **External Examiner 1:** Signature: ____________
Name: **Dr. Tariq Javed**
Designation: Professor
Office Address: Department of Mathematics & Statistics, International Islamic University, Sector H-10 Islamabad.

b) **External Examiner 2:** Signature: ____________
Name: **Dr. Meraj Mustafa Hashmi**
Designation: Associate Professor
Office Address: Department of Mathematics, School of Natural Sciences (SNS), National University of Sciences and Technology (NUST), Sector H-12 Islamabad.

c) **Internal Examiner:** Signature: ____________
Name: **Dr. Tasawar Hayat**
Designation: Professor
Office Address: Department of Mathematics, QAU Islamabad.

Supervisor Name: Signature: ____________
Prof. Dr. Tasawar Hayat

Name of Dean/HOD: Signature: ____________
Prof. Dr. Tariq Shah

DEDICATED TO MY

BELOVED PARENTS

ACKNOWLEDGEMENT

All praise for ***Almighty Allah****, the most Beneficent, the most merciful, the Lord of the whole world who has given me the courage and ability to complete this thesis. I am nothing without my Allah, but I can manage everything with His assistance. Also, I cannot forget the idea personality of the world for whom Allah has created the whole universe, who is forever a torch bearer of guidance for humanity, Hazrat Muhammad* ***(PBUH).***

I would like to express my gratitude to my worthy supervisor ***Prof. Dr. Tasawar Hayat (National Distinguished Professor)*** *for his valuable suggestions and comments that helped me to accomplish this highly important research. His knowledge, accessibility and availability have been a critical impetus in driving this research. It would never have been possible for me to take this work to completion without his incredible support and encouragement. I am ever indebted and obliged to him.*

My highest and special thanks go to my honorable teachers ***Prof. Dr. Muhammad Ayub, Prof. Dr. Malik Yousaf, Prof. Dr. Masood Khan, Prof. Dr. Sohail Nadeem, Dr. Babur Majid Mirza*** *and* ***Dr. Khalid Saifullah*** *for their valuable and constructive suggestions in all aspects.*

I want to convey my deepest thanks and sincere gratitude to my beloved and most caring father ***Manazar Hussain Faryad Shah****, my loving, adorable and caring mother* ***Samina Kausar,*** *my sister* ***Anaem Haider****, my brothers* ***Haseeb Ali Raza****,* ***Moieed Hassan Raza*** *and my brother-in-law* ***Syed Qulib Abbas*** *for their endless love, prayers, encouragement, cordial cooperation and continuous support. They selflessly encouraged me to explore new directions in my life and seek my own destiny. How can I forget to mention the naughtiest member of my family* ***Shaherbano Tirmazi (Niece)*** *who always disturbed me whenever I open up the laptop. This journey would have not been possible without my family, and I dedicated this milestone to them.*

I have been lucky enough to have good friends in my academic and social life and cannot forget their role in my education and university life. It is a matter of great delight and pleasure for me to mention my truly wonderful friends especially ***Aqeela Qaiser, Nisa Amir, Dr. Rehana Rahim, Samiya Bashir, Tayyaba Ayub, Asia Liaqat, Sana Shaheen, Fiza Shahid*** *and* ***Aqsa Saleem.*** *My profound thanks to all my lab fellows for their guidance and support throughout these years.*

*I would like to convey my heartiest gratitude to my respectable senior and co-advisor **Dr. Taseer Muhammad** for his kind support and guidance that helped me to complete this important work. This discussions with him helped me to sort out the technical details of my work. I am thankful to him for being so cooperative, kind, and helpful.*

*I would also like to thank the office staff of the Department of Mathematics that includes **Mr. Zahoor Jan, Mr. Sajid, Mr. Safdar, Mr. Bilal** and **Mr. Miskeen** for their constant help and right guidance.*

Farwa Haider

25-04-2022

Preface

Transport of fluid through porous space is quite important topic. Such importance is quite prevalent in various engineering process. Mathematical and analytical techniques to model flows in porous media vary from algebraic expressions to fluid models. Extensive studies have been undertaken for porous medium employing classical Darcy's expression. Darcy assumes a continuum approximation of both medium and fluid to study the fluid transport in porous media. Additional features are incorporated to increase its accuracy and validity for a wider range of porous media. Darcy-Forchheimer, Darcy-Brinkman and Darcy-Brinkman-Forchheimer are few examples which incorporate inertia and boundary features additionally. Modified Darcy's law is another continuum approach which is based on rheological properties of fluid. Rotating flows has significance in the field of meteorology and oceanography. It is because of the effects of Coriolis and centrifugal forces. Thus it is imperative to study the effect of rotating flows by continuously moving surfaces. In applications related to transport of blood, foam, emulsion or suspension the no slip boundary condition is not appropriate. In these situations, it is essential to use slip conditions which defines a relation between particles adjacent to surface to normal component of velocity at surface. Prescribed heat flux condition at the boundary is also utilized in this thesis.

Present thesis focuses on the characteristics of nonlinear models through Darcy-Forchheimer porous space. For more general view of engineering applications, the flows by different surfaces are also studied. This thesis is structured as follows:

Chapter one provides a detailed literature review and fundamental expressions.

Chapter two discussed the rotating flow of two-phase nanofluid through porous space. Velocity and thermal slip conditions are employed at the boundary.

Darcy-Brinkman expression is utilized to capture the effect of porous space. Inclined magnetic field is applied. Heat transfer aspects are studied in presence of viscous dissipation. Numerical solutions are computed through NDSolve technique. **The contents of this chapter are submitted in Numerical Methods for Partial Differential Equations.**

Darcy-Forchheimer flow of nanofluid subject to rotating frame is analyzed in Chapter three. Nanofluid consisting of carbon nanotubes is utilized. Exponential stretching sheet creates disturbance in flow. Prescribed heat flux condition is employed at the boundary. Behaviors of emerging variables on flow and physical quantities are physically interpreted. **The relevant observations are published in Physica Scripta 96 (2021) 025217.**

Chapter four aims to compute optimal series solutions for chemically reactive flow of carbon nanotubes through Darcy-Forchheimer porous space. Carbon nanotubes consisting of single and multiple layers of graphene are used in analysis. Heat generation/absorption and viscous dissipation are also accounted. Entropy generation in a system is modelled through second law of thermodynamics. Comparative results are obtained for single wall and multi wall carbon nanotubes. Optimal solutions are approximated through OHAM. **The data of this chapter is published in Physica Scripta 96 (2021) 095209.**

Chapter five presents the numerical investigation of carbon nanotubes through porous space. Carbon nanotubes namely single and multi walls are utilized in the analysis. Disturbance in flow is generated by the stretching sheet whose curvature is altered in a controllable manner. Flow in porous space is characterized by Darcy-Forchheimer relation. Graphical illustration for behavior of emerging variables on flow fields is provided. **Materials of this chapter are published in Journal of Central South University 26 (2019) 865-872.**

Chapter six elaborates the impact of prescribed heat flux condition in flow of water-based carbon nanotubes. Exponential curved stretching sheet creates disturbance in flow. Heat transfer aspect is analyzed in presence of heat generation/absorption. Porous space effect is characterized by Darcy-Forchheimer relation. NDSolve technique is employed for computation of numerical solutions. **The contents of this chapter are published in Physica A: Statistical Mechanics and its Applications 554 (2020) 124002.**

Features of hybrid nanofluid through Darcy-Forchheimer porous space is illustrated in Chapter seven. Molybdenum disulfide and Silicon dioxide are utilized in flow analysis. Comparative results are obtained for hybrid nanofluid and nanofluid. Porous space with variable characteristics is analyzed. Additional effects of nonlinear thermal radiation, heat generation/absorption and viscous and porous dissipation are considered. Entropy generated in a system is modelled by second law of thermodynamics. **Observations of this chapter are published in Entropy 23 (2021) 89.**

Chapter eight provides the comparative analysis for flow of carbon nanotubes due to a rotating disk. Boundary conditions for velocity and temperature are set so that slip effects are not ignored. Flow in porous space is described by Darcy-Forchheimer relation. Viscous dissipation is also considered. Optimum series solutions are computed by optimal homotopy analysis technique. **Data of this chapter is published in International Communications in Heat and Mass Transfer 116 (2020) 104641.**

Chapter nine develops the numerical solution for nanofluid flow filling porous space with variable characteristics. Mass transfer aspect is studied in presence of activation energy. Buongiorno model is utilized for nanoliquid transport phenomenon. Permeability and porosity of porous space are linear functions of space variable. Disturbance in flow is created by rotating disk. Variations of flow fields against emerging variables are interpreted through graphs. Numerical data of physical quantities is obtained and analyzed. **Material of this chapter is published in International Communications in Heat and Mass Transfer 119 (2020) 104904.**

Simultaneous features of thermal stratification and nonlinear thermal radiation in flow of hybrid nanofluid are interpreted in Chapter ten. Nanoparticles of two types namely Titanium dioxide and Aluminum oxide are accounted. Velocity slip conditions are employed at the boundary. Variable aspects of porosity and permeability are utilized through porous space effect. **Contents of this chapter are published in Alexandria Engineering Journal 60 (2021) 3047-3056.**

Chapter eleven aims to analyze the features of Carreau fluid through porous space with variable characteristics. Flow is created by a rotating disk. Flow properties are discussed subject to viscous dissipation. Rate of entropy generation is also calculated. Keeping in view the rheological characteristics of Carreau fluid, modified Darcy's law is utilized to capture the effect of porous space. Numerical solutions are computed. **Observations of this chapter are published in International Communications in Heat and Mass Transfer 120 (2021) 105073.**

Chapter twelve consists of the concluding remarks of present thesis.

Contents

1 Literature review and methodologies **5**

1.1 Introduction . . . 5

1.1.1 Nomenclature . . . 5

1.1.2 Subscript . . . 8

1.2 Literature review . . . 8

1.3 Basic conservation laws . . . 15

1.3.1 Mass conservation . . . 15

1.3.2 Momentum conservation . . . 15

1.3.3 Energy conservation . . . 16

1.3.4 Concentration equation . . . 17

1.4 Porous media models . . . 17

1.4.1 Darcy's law . . . 17

1.4.2 Darcy-Forchheimer law . . . 17

1.4.3 Modified Darcy's law . . . 18

1.5 Solution techniques . . . 18

1.5.1 Optimal homotopic analysis technique . . . 18

1.5.2 NDSolve technique . . . 19

2 Partial slip in rotating flow of nanomaterial through porous space **21**

2.1 Model development . . . 21

2.1.1 First order of truncation . . . 24

2.1.2 Second order of truncation . . . 24

2.2 Physical quantities . . . 26
2.3 Solution methodology . . . 26
2.4 Discussion . . . 27

3 Rotating flow of carbon nanotubes subject to prescribed heat flux condition 40
3.1 Model development . . . 40
3.1.1 First order of truncation . . . 43
3.1.2 Second order of truncation . . . 43
3.2 Physical quantities . . . 44
3.3 OHAM Solutions . . . 44
3.4 Solutions convergence . . . 45
3.5 Discussion . . . 47

4 Irreversibility analysis of carbon nanotubes subject to rotating frame 59
4.1 Model development . . . 59
4.1.1 First order of truncation . . . 63
4.1.2 Second order of truncation . . . 63
4.2 Entropy generation . . . 64
4.3 Physical quantities . . . 65
4.4 OHAM solutions . . . 65
4.5 Solutions convergence . . . 65
4.6 Discussion . . . 68

5 Flow of carbon nanotubes induced by curved stretching sheet 88
5.1 Model development . . . 88
5.2 Physical quantities . . . 91
5.3 Discussion . . . 92

6 Impact of heat flux condition in Darcy-Forchheimer nanofluid flow 100
6.1 Formulation . . . 100
6.2 Quantities of interest . . . 104
6.3 Discussion . . . 104

7 Outcome of entropy generation in hybrid nanomaterial 113

7.1 Model development 113

7.2 Entropy generation 117

7.3 Physical quantities 118

7.4 Discussion 118

8 Nanofluid flow by rotating disk with slip conditions 134

8.1 Model development 134

8.1.1 First order of truncation 137

8.1.2 Second order of truncation 137

8.2 Physical quantities 138

8.3 OHAM Solutions 138

8.4 Solutions convergence 139

8.5 Discussion 141

9 Unsteady flow of nanomaterial subject to variable characteristics 152

9.1 Model development 152

9.2 Physical quantities 155

9.3 Discussion 155

10 Flow of hybrid nanofluid saturating porous medium of variable characteristics 172

10.1 Model development 172

10.1.1 First order of truncation 175

10.1.2 Second order of truncation 176

10.2 Quantities of interest 176

10.3 Analysis 177

11 Entropy generation analysis of Carreau fluid with entire new concepts of modified Darcy's law and variable characteristics 190

11.1 Model development 191

11.1.1 First order of truncation 193

11.1.2 Second order of truncation 194
11.2 Entropy generation 196
11.3 Physical quantities 196
11.4 Solution methodology 196
11.5 Discussion 197

12 Conclusions **210**

Chapter 1

Literature review and methodologies

1.1 Introduction

This chapter provides the background related to porous space, nanofluid, non-Newtonian fluids, entropy generation and heat and mass transfer. Governing equations of fluid flow and heat and mass transfer are also included.

1.1.1 Nomenclature

u_w	surface stretching velocity
u_0, T_0	positive constant
(u, v, w)	velocity components
(s, r)	space coordinates
(x, y, z)	space coordinates
(r, ψ, z)	space coordinates
$\mu_j \, (j = hnf, nf, f)$	kinematic viscosity
$(c_p)_j \, (j = nf, f, CNT, \check{p})$	heat capacity
$\sigma_j \, (j = nf, f, \check{p})$	electrical conductivity
$\rho_j \, (j = hnf, nf, f, CNT, \check{p})$	density
$k_j \, (j = hnf, nf, f, CNT, \check{p})$	thermal conductivity
$\alpha_j \, (j = hnf, nf)$	thermal diffusivity
β	inclination angle

A	temperature exponent
ξ	nanoparticle volume fraction
ω	angular frequency
F	non-uniform inertia coefficient
K^*	permeability of porous space
C_b	drag coefficient
R	radius of curvature
L	reference length
p	pressure
ε	porosity
$K_\infty, \varepsilon_\infty$	constant porosity and permeability
d, d^*	variable porosity and permeability
b	measure of unsteadiness
μ_0	zero shear rate viscosity
$\mathring{\gamma}$	second-order invariant strain tensor
Γ, n	Carreau fluid parameters
Q	heat generation/absorption
ϵ	mean absorption coefficient
D_B	Brownian diffusion
D_T	thermophoresis
$\tilde{\sigma}$	Stefan Boltzmann coefficient
N_1, N_2	slip coefficients for velocity and temperature
$\tilde{A}, \tilde{B}$	dimensional constants
k_r	chemical reaction constant
m	constant exponent
E_a	activation energy
$\tilde{k}$	Boltzmann constant
k_c, k_s	rate constants for homogeneous-heterogeneous reactions
c_1, c_2	concentration of chemical species

$\breve{D}_{c_1}, \breve{D}_{c_2}$	diffusion coefficients of c_1 and c_2
B	concentration exponent
S'''_{gen}	entropy generation
T_m	mean temperature
$\breve{R}$	universal gas constant
$(f', g), \theta, \phi$	dimensionless ((velocities), temperature, concentration)
ζ	dimensionless variable
λ	local porosity parameter
Ω	local rotational parameter
M	magnetic parameter
F_r	inertia coefficient
S, δ	unsteadiness parameters
Pe	Peclet number
γ	parameter
K	curvature parameter
We	Weissenberg number
γ_1, γ_2	velocity and temperature slip parameter
C_f, C_g	skin friction coefficients
H	dimensionless pressure
N_b	Brownian motion parameter
N_t	thermophoresis parameter
S_t	thermal stratification parameter
Ec	Eckert number
$\Pr$	Prandtl number
Q^*	heat generation/absorption parameter
θ_w	temperature ratio parameter
Br	Brinkman number
Rd	radiation parameter
Nu	local Nusselt number

Re	local Reynolds number
Λ	reaction rate parameter
E	activation energy parameter
α_1	temperature difference parameter
Sc	Schmidt number
$\hat{K}$	strength of homogeneous reactions
$\hat{K}_s$	strength of heterogeneous reactions
Ψ	ratio of diffusion coefficients
Sh	local Sherwood number
N_g	entropy generation rate
L_1, L_2	diffusion parameters with respect to homogeneous and heterogeneous reactions
J_i^*	arbitrary constants
$\breve{k}$	integer
$\mathcal{N}$	non-linear operator
ε_m^t	total squared residual error

1.1.2 Subscript

w	condition at surface
∞	ambient condition
f	base fluid
nf	nanofluid
CNT	carbon nanotube
hnf	hybrid nanofluid
$\check{p}$	nanoparticle

1.2 Literature review

In engineering fluid mechanics, prediction of drag forces on surfaces of tubes, pipes, pumps, wings of aircraft and turbines is considered as an important task. These drag forces are generated due to fluid viscosity which causes shear stress on the surface. In 1904, Prandtl [1] revolutionized it by giving a concept of boundary layer theory which mainly focuses on how far from the surface viscosity dominates the flow field. Boundary layer theory is significantly utilized in literature to analyze the behavior of fluids over various surfaces such as stretching surfaces, circular cylinder and rotating disk. It is due to its applications in chemical, scientific and biological sciences. Blasius [2] employed boundary layer theory to flows over a plate and circular cylinder. Sakiadis [3] considered the flow over a continuos flat surface moving with uniform speed. Flows over a stretching sheet is initially analyzed by Crane [4]. Wang [5] extended the work of Crane for three-dimensional flows due to a stretching surface. He considered linear velocity distribution of stretching surface. However, it is not necessary for a stretching sheet to move with linear velocity. Several studies are conducted to study the flow for different types of stretching velocities and sheets such as unsteady, curved, power-law and exponential. Ali [6] analyzed the flow over a porous stretching sheet moving with power-law velocity. Magyari and Keller [7] illustrated the flow past an exponential stretching sheet. Flow past an exponential stretching in rotating frame is elaborated by Javed et al. [8] . Nadeem and Lee [9] discussed the flow of nanofluid by an exponential stretching surface. Mukhopadhay [10] examined the flow over such sheet with thermal radiation and MHD. Three-dimensional flow over an exponential stretching surface is provided by Liu et al. [11] . Rosali et al. [12] investigated flow by an exponentially porous stretching surface. Mustafa et al. [13] considered effects of thermal radiation over such surfaces. Flow of ferrofluid over an exponentially porous stretching surface is deliberated by Jusoh et al. [14] . Lund et al. [15] computed quadruple solutions for mixed convective flow of nanofluid by an exponential stretching surface. Flow of viscoelastic fluid over exponential stretching sheet with Cattaneo-Christov heat flux model is interpreted by Malik et al. [16]. Sajid et al. [17] illustrated the flow over a stretching sheet whose curvature is altered in a controllable manner. Such sheets are useful in making of stretch-forming machines with curving jaws. Rosca and Pop [18] provided unsteady flow by porous curved stretching sheet. Thermally radiative flow of nanofluid by curved stretching sheet is illustrated by Abbas et al. [19] . Okechi et al. [20] elaborated flow over exponential curved stretching sheet. Alblawi et al. [21] utilized Buongiorno's model for flow over exponentially curved sheet. Thermally radiative flow of Casson fluid over exponentially curved sheet is scrutinized by Kumar et al. [22] . Kempannagari et al. [23] interpreted flow of non-Newtonian fluid by exponentially curved sheet. Fluid flow near a rotating disk is encountered in industrial processes such as spin coating, centrifugal pumps, air cleaning machines and electrical power generating system. Von-Karman [24] was the first one who formulated such problems. He introduced similarity transformations to convert system of partial differential to system of ordinary differential equations of such problems. The work of Karman is the basis for several studies conducted in this direction (see refs. $[25-34]$).

Heat transfer plays crucial role in different systems such as domestic refrigerators, automobiles, electronic devices, buildings and heat exchangers. The optimum performance of these equipment depends on the rate heat is transferred. Low thermal conductivity of conventional fluids such as ethylene glycol, water and oil is a limitation in improving the performance. A suitable technique of heat transfer enhancement is required to optimize energy devices. Choi [35] introduced a technique by dispersion of small solid particles such as metals, carbide ceramics, carbon nanotubes and oxide ceramics in base material known as nanofluid. Since nanofluids have higher thermal conductivity when compared with conventional fluids. Thus these can remarkably enhance the heat transfer performance of engineering devices especially for cooling of electronic devices. Convective heat transfer of nanofluids can be modelled by using single phase or two-phase approach. The relative velocity between fluid and particles may not be zero in single phase approach. Slip in velocity is caused by seven mechanisms as suggested by Buongiorno [36]. Slip mechanism includes fluid drainage, inertia, magnus effect, thermophoresis, Brownian diffusion, diffusiophoresis and gravity. Several studies are conducted to study the characteristics of Bunogiorno's model in flow over different geometries. Few of them can be consulted via refs. $[37-42]$. Two-phase approach assumes no slip condition between fluid and nanometer sized particles. In two-phase approach, the governing equations with their specific heat, density, viscosity and thermal conductivity are modified differently through different models. Brinkman [43] provided a model for viscosity of nanofluid that takes into account the percentage of nanoparticles suspended in base fluid. Maxwell presented a theoretical model for thermal conductivity of nanomaterial which is based on spherical shaped particles. Hamilton and Crosser [44] provided the modified form of Maxwell's model. They observed the effect of nanoparticle shape on thermal efficiency of nanofluid. Xue [45] employed polarization theory to analyze the effect of interface interaction between bulk liquid and carbon nanotubes. Specific heat of a nanomaterial is modelled by Pak and Cho [46]. Later on, Eastman et al. [47] employed the concept of heat capacity and presented a model for it. Turkyilmazoglu [48] provided numerical simulation for nanofluid film flow and heat transfer. Entropy generation analysis of nanomaterial is elucidated by Hayat et al. [49]. Kumar et al. [50] illustrated chemically reactive flow of carbon nanotubes with entropy generation. Effects of Newtonian heating and chemical reaction in flow of nanofluid is explored by Aleem et al. [51]. Reddy and Sreedevi [52] studied the thermally radiative flow of nanofluid in a square chamber.

A new class of nanofluids is introduced with enhanced thermophysical characteristics namely hybrid nanofluid. In hybrid nanofluids, two dissimilar nanoparticles are suspended in base fluid. The appropriate composition of nanoparticles has to be chosen to enhance the positive compatible features of each other. Sundar et al. [53] discussed heat transfer enhancement in MWCNT-Fe_3O_4/water nanofluid. Viscosity of hybrid nanofluid using different nanoparticles is analyzed by Meybodi et al. [54] . They have considered Al_2O_3, TiO_2, SiO_2 and CuO nanoparticles. Mansour et al. [55] provided entropy generation analysis of Al_2O_3-Cu/water nanofluid with MHD. Influence of thermal deposition in flow of $C_3H_8O_2$ based MoS_2-SiO_2 nanofluid is seen by Shaiq et al. [56] . Manjunatha et al. [57] studied heat transfer characteristics of hybrid nanofluid with variable viscosity. Aladdin et al. [58] examined flow of Cu-Al_2O_3/water nanofluid over a permeable sheet. Stagnation point flow of hybrid nanomaterial is interpreted by Abbas et al. [59]. Mabood et al. [60] presented entropy generation analysis of water based Cu-Al_2O_3 with melting heat transfer.

Interest of researchers in analyzing the flow of fluids whose viscosity changes with the shear rate increases substantially in 20th century. Such fluids are referred as non-Newtonian fluids. Salt solutions, toothpaste, ketchup, paint, grease and blood are few examples of non-Newtonian fluids which are used extensively in everyday life. The characteristics of such fluids can not be described by a single fluid model. The rheological variables with differential system of higher order increases the complexity of non-Newtonian fluids. Thus, various fluid models are presented in literature to describe the non-Newtonian fluid depending on their rheological characteristics. Carreau [61, 62] fluid model is one of them which demonstrate power law as well as Newtonian behavior at high and low shear rates. Carreau fluid model has involvement in manufacturing processes such as aqueous, melts and polymer solutions. Vajravelu et al. [63] analyzed the flow of Carreau fluid in a non-uniform channel. Khan and Azam [64] studied unsteady flow of Carreau fluid over porous stretching sheet. Animasaun and Pop [65] provided numerical simulation for flow of Carreau fluid over paraboloid surface. Flow of Carreau fluid with heat generation/absorption is elaborated by Rehman et al. [66]. Mahanthesh et al. [67] illustrated the convective flow of dusty Casson and Carreau fluids. Nazir et al. [68] utilized Cattaneo-Christov heat flux model for flow of Carreau fluid. Temperature dependent diffusion coefficients is also considered. Irreversibility analysis of Carreau fluid with Ohmic heating is addressed by Khan et al. [69]. Elayarani et al. [70] considered gyrotactic microorganisms in flow of Carreau nanofluid.

Porous medium is a solid matrix consisting of interconnected voids distributed in such a way that it occupies measurable fraction of its volume. Wood, cork, bones, soil, aquifer, biological tissues and human lung are some examples of porous medium. Movement of fluid through porous medium is of utmost interest due to its implications in various scientific and technical fields such as atherosclerosis, gaseous diffusion in binary mixtures, artificial dialysis, geo-energy production, catalytic converters, gas turbines and electrochemical systems. The efficient utilization of such medium requires a careful study for modelling momentum and energy transport. In 1856, Darcy [71] suggested a model that relates pressure gradient in flow direction to fluid velocity through viscosity of fluid and permeability of space. Traditional Darcy's law is widely used for elaborating flows in porous media. However, validity of Darcy's law is restricted to incompressible, laminar, purely viscous, isothermal Newtonian flow. Several modifications such as Darcy-Forchheimer, Darcy-Brinkman and Darcy-Brinkman-Forchheimer models are suggested to overcome this limitation. The first non-Darcy model is presented by Forchheimer [72] by addition of square velocity term to account for inertial effects. Later on, Muskat [73] entitled this modification as Forchheimer term. Bakar et al. [74] analyzed stagnation-point flow through Darcy-Forchheimer porous space. Radiative flow of carbon nanotubes through Darcy-Forchheimer porous space is examined by Shah et al. [75]. Audu et al. [76] utilized finite element method for flow through porous space. Huda et al. [77] studied Cattaneo-Christov heat flux model through Darcy-Forchheimer porous space. Brinkman [78, 79] further modified the Darcy's model for viscous forces by the addition of Darcy resistance term which is known as Darcy-Brinkman expression. Nield [80] studied the importance of viscous dissipation in Darcy, Forchheimer and Brinkman models. Combined convective flow along a non-isothermal wedge through porous space is examined by Ibrahim and Hassanien [81]. Hadharami et al. [82] provided another model for viscous dissipation in porous media. Partial slip in flow through Darcy-Brinkman porous space is elaborated by Kausar et al. [83]. Darcy-Brinkman flow of couple-stress fluid is discussed by Yadav et al. [84]. By adjoining Darcy-Brinkman and Darcy-Forchheimer models, a generalized model entitled Darcy-Brinkman-Forchheimer [85] model is presented. Umavathi et al. [86] developed expressions for flow of nanofluid through Darcy-Brinkman-Forchheimer relation. Heat and mass transfer of two-phase nanofluid invoking Darcy-Brinkman-Forchheimer porous space is interpreted by Bhatti et al. [87] . Farooq et al. [88] developed flow of Casson fluid through Darcy-Brinkman-Forchheimer porous space. Above mentioned modifications are valid when the considered fluid is purely viscous in nature.

Since the flow phenomena through porous space becomes more complex when non-Newtonian fluid are involved. Thus Darcy's law is modified differently to describe more accurately such flows. Tan and Masuoka [89] employed modified Darcy's law for the flow of second grade fluid. Flow of generalized Burger's fluid through porous space with MHD is analyzed by Khan et al. [90]. Hayat et al. [91] provided exact expressions in flow of generalized Burger's fluid subject to rotating frame. Flow of micropolar fluid through porous space is examined by Khan et al. [92] . Flow is generated by a rotating disk. Tanveer et al. [93] studied flow of Carreau fluid in a curved channel through porous space. Haq et al. [94] utilized modified Darcy's law for flow of generalized second grade fluid through porous space.

In above discussed literature, the permeability and porosity of medium are considered constant. Schwartz and Smith [95] observed that porosity is not constant but varies from wall to interior which also affects permeability. Vafai [96] studied the flow and heat transfer in variable porous media. Experimental analysis of heat transfer in variable porous space is examined by Vafai et al. [97] . Chandrasekhra and Namoboudiri [98] illustrated the characteristics of variable porous space in flow over inclined surfaces. Combined convection in flow over a non-isothermal wedge through porous space is analyzed by Ibrahim and Hassanien [99] . Rees and Pop [100] discussed vertical free convective flow through variable characteristic porous space. Flow through variable permeability porous layers is developed by Hamdan and Kamel [101]. Saif et al. [102] explored the impact of inclined magnetic field in flow through porous space with variable characteristics.

Entropy is defined as a disorderliness is a system which explains the number of states a system can take in a conversion process. A system loses energy when converting from one state to another. Since degradation of energy reduces the thermal efficiency and increases entropy generated in a system. Thus, entropy minimization becomes a significant topic in thermo-fluid field. Main sources of entropy generation in a system are electrical conduction, heat and mass transfer, viscosity loses and chemical reaction. First and second law of thermodynamic are used to describe entropy generation in a system. However, second law of thermodynamics is more accurate because it relates heat associated with a system to entropy change in that system. The first attempt in this regard was by Bejan [103], who observed that entropy generation results in extreme decline of irreversibility in a system. Shojaeian and Kosar [104] investigated partial slip in Newtonian and non-Newtonian fluid with entropy generation. Thermally radiative flow of Carreau nanomaterial subject to entropy generation is interpreted by Bhatti et al. [105]. Kefayati and Tang [106] analyzed entropy generation analysis of Carreau nanofluid with double diffusive natural convection. Flow of hybrid nanofluids with entropy generation is studied by Huminic and Huminic [107]. Khan et al. [108] discussed flow of Carreau fluid with entropy generation. Yusuf et al. [109] explored the influence of thermal radiation in flow of hybrid nanofluid with entropy generation. Darcy-Forchheimer flow of fluid with entropy generation is examined by Muhammad et al. [110]. Sahoo and Nandkeolyar [111] considered entropy generation in flow of Casson nanofluid. Entropy generation analysis of magneto nanofluid is presented by Reddy and Sreedevi [112].

During the past few decades, researchers emphasized on the interaction of electrically conducting fluids and magnetic field. The exertion of magnetic field in a thermo-fluid system manipulates the suspended particles and rearranges their concentration. Such change in concentration of nanoparticles affects the heat transfer. Magnetic field can be applied in direction of flow as well as to the transverse direction of flow. However, it is observed that the magnetic field applied in transverse direction of flow acts directly on fluid and maybe more active in controlling the flow. In order to predict the transport of MHD fluid, both Maxwells and Navier-Stokes equations are mutually coupled through various laws. Important works on flow influenced by magnetic field are cited through [113 − 121]. From prevailing literature, it is analyzed that less attention has been given to the fluid flows caused by insertion of inclined magnetic field. Few significant studies on flow with inclined magnetic field can be seen through refs. [122 − 129].

Mass transfer is a natural phenomenon in which species of higher concentration region travels to region of lower concentration. Diffusion of nutrients in tissues, food processing, purification of blood in liver and kidneys, cooling towers and thermal insulation are some procedures which involves mass transfer. Mas transfer and chemical reactions have been given attention in the literature due to complex interactions between them. Initially Bestman [130] was the one who analyzed boundary layer flow in presence of chemical reaction. In chemical engineering, thermal oil recovery and nuclear reactor cooling, chemical reactions with finite Arrhenius activation energy are utilized. Activation energy is considered as an energy barrier between products and reactants of a reaction which has to be crossed to start a chemical reaction. Hsiao [131] utilized parameter control method for thermally radiative flow of Carreau nanofluid with activation energy. Second order slip in MHD flow with activation energy is discussed by Majeed et al. [132]. Hamid et al. [133] elaborated the unsteady flow of magneto-Williamson with activation energy. Few recent attempts in this direction can be studied via refs. [134 − 139].

1.3 Basic conservation laws

1.3.1 Mass conservation

Equation of continuity is mathematically expressed as

$$\frac{\partial \rho}{\partial t} + \boldsymbol{\nabla} . (\rho \mathbf{V}) = 0, \tag{1.1}$$

For an incompressible fluid Eq. (1.1) reduces to

$$\boldsymbol{\nabla} . \mathbf{V} = 0. \tag{1.2}$$

1.3.2 Momentum conservation

Law of conservation of linear momentum in differential form is

$$\rho \frac{d\mathbf{V}}{dt} = \operatorname{div} \breve{\boldsymbol{\tau}} + \rho \breve{\mathbf{b}}, \tag{1.3}$$

where $\breve{\boldsymbol{\tau}}$ represents the Cauchy stress tensor and $\breve{\mathbf{b}}$ the body force.

Viscous fluid

Cauchy stress tensor for an incompressible viscous fluid is

$$\breve{\boldsymbol{\tau}} = -p\mathbf{I} + \mu \mathbf{A}_1, \tag{1.4}$$

where

$$\mathbf{A}_1 = \mathbf{L} + \mathbf{L}^T. \tag{1.5}$$

Carreau fluid model

Cauchy stress tensor for Non-Newtonian fluids is

$$\breve{\boldsymbol{\tau}} = -p\mathbf{I} + \mathbf{S}, \tag{1.6}$$

where extra stress tensor for Carreau fluid is

$$\mathbf{S} = \mu\left(\mathring{\dot{\gamma}}\right)\mathbf{A}_1 = \left(\mu_\infty + (\mu_0 - \mu_\infty)\left(1 + (\Gamma\dot{\gamma})^2\right)^{\frac{n-1}{2}}\right)\mathbf{A}_1, \tag{1.7}$$

$$\dot{\gamma} = \sqrt{\frac{1}{2} tr \mathbf{A}_1^2}, \tag{1.8}$$

In above expressions, μ_0 depicts the zero shear rate viscosity, μ_∞ the infinite shear rate viscosity, $\mathbf{S}$ the extra stress tensor, n and Γ the Carreau fluid parameters and $\dot{\gamma}$ the second invariant rate of strain tensor. For $\mu_\infty = 0$, Eq. (1.7) reduces to

$$\mathbf{S} = \left(\mu_0\left(1 + (\Gamma\dot{\gamma})^2\right)^{\frac{n-1}{2}}\right)\mathbf{A}_1. \tag{1.9}$$

1.3.3 Energy conservation

Energy conservation law is based on first law of thermodynamics. Mathematically,

$$\rho c_p \frac{dT}{dt} = \breve{\boldsymbol{\tau}}.\mathbf{L} - \boldsymbol{\nabla}.\left(-K\boldsymbol{\nabla}T\right) + \tilde{Q}, \tag{1.10}$$

in which $\tilde{Q}$ is the source term for heat transport. It is used to represent heat generation/absorption, non-linear thermal radiation, viscous dissipation, thermophoresis, Brownian motion and porous media resistance throughout the thesis.

1.3.4 Concentration equation

Concentration equation is derived from Fick's first and second law. Mathematically

$$\frac{dC}{dt} = D\nabla^2 C, \tag{1.11}$$

Here C depicts the concentration of species and D for mass diffusivity.

1.4 Porous media models

The flow through porous medium is characterized by following models:

1.4.1 Darcy's law

Darcy's flow model states that flow rate at any point in reservoir is given by fluid permeability, viscosity and pressure gradient. Mathematically

$$\nabla p = -\frac{\mu}{K^*}\mathbf{V}. \tag{1.12}$$

1.4.2 Darcy-Forchheimer law

It is the modification of traditional Darcy's law to accounts for the pressure drop due to inertial losses at sufficiently high velocity. Mathematically one has

$$\nabla p = -\frac{\mu}{K^*}\mathbf{V} - F\mathbf{V}\left|\mathbf{V}\right|. \tag{1.13}$$

1.4.3 Modified Darcy's law

The rheological characteristics of non-Newtonian fluids varies with the strain rate. To account for such characteristics in porous space, we have

$$\nabla p = -\frac{\mu\left(\mathring{\gamma}\right)}{K^{*}}\mathbf{V}. \tag{1.14}$$

1.5 Solution techniques

1.5.1 Optimal homotopic analysis technique

Optimal homotopy analysis technique (OHAM) is an efficient tool for highly nonlinear differential equations. Here one or more auxiliary parameters are utilized for the convergence of approximate series solutions. These parameters can be determined by minimizing the certain function. OHAM is computationally efficient than other techniques. To understand it, we assume a non-linear differential equation

$$\mathcal{N}\left[\hat{g}\left(\zeta\right)\right] = 0, \tag{1.15}$$

where $\hat{g}\left(\zeta\right)$ is the unknown function, ζ the independent variable and $\mathcal{N}$ the non-linear operator.

Zeroth-order deformation problems

$$\left(1-q\right)\mathcal{L}\left[\hat{g}\left(\zeta;q\right) - \hat{g}_0\left(\zeta\right)\right] = q\hbar\mathcal{N}\left[\hat{g}\left(\zeta;q\right)\right], \tag{1.16}$$

in which $\hat{g}\left(\zeta;p\right)$ represents the unknown function of ζ and q, $\mathcal{L}$ the auxiliary linear operator, $\hat{g}_0\left(x\right)$ the initial approximation, $\hbar$ the nonzero auxiliary parameter and $q \in [0,1]$ the embedding parameter.

mth-order deformation problems

mth-order deformation can be calculated by

$$\mathcal{L}\left[\hat{g}_m\left(\zeta\right) - \chi_m\hat{g}_{m-1}\left(\zeta\right)\right] = \hbar\mathcal{R}_m\left(\zeta\right), \tag{1.17}$$

$$\mathcal{R}_m(\zeta) = \frac{1}{(m-1)!} \frac{\partial^m \mathcal{N}[\hat{g}(\zeta;q)]}{\partial q^m}\bigg|_{q=0}, \tag{1.18}$$

where

$$\chi_m = \begin{cases} 0, & m \leq 1 \\ 1, & m > 1 \end{cases}. \tag{1.19}$$

By choosing $q = 0$ and $q = 1$, we have

$$\hat{g}(\zeta;0) = \hat{g}_0(\zeta) \quad \text{and} \quad \hat{g}(\zeta;1) = \hat{g}(\zeta). \tag{1.20}$$

By using Taylor series expansion, the solution $\hat{g}(\zeta;q)$ is given as

$$\hat{g}(\zeta;q) = \hat{g}_0(\zeta) + \sum_{m=1}^{\infty} \hat{g}_m(\zeta) q^m, \; \hat{g}_m(\zeta) = \frac{1}{m!} \frac{\partial^m \hat{g}(\zeta;q)}{\partial q^m}\bigg|_{q=0}. \tag{1.21}$$

For $q = 1$ we have

$$\hat{g}(\zeta) = \hat{g}_0(\zeta) + \sum_{m=1}^{\infty} \hat{g}_m(\zeta). \tag{1.22}$$

Optimal convergence control parameters

Liao [140] computed the optimal data of auxiliary variable $\hbar$ by using the concept of minimization. He employed global optimization approach in which all the parameters are optimized simultaneously at last order for approximation. Optimal data of auxiliary variables is computed by Mathematica BVPh 2.0. The average squared residual error is given as

$$\varepsilon_m = \frac{1}{\breve{k}+1} \sum_{j=0}^{\breve{k}} \left[\mathcal{N}\left(\sum_{i=0}^{m} \hat{g}(\zeta) \right)_{\zeta = j\delta\zeta} \right]^2, \tag{1.23}$$

where ε_m depicts the total squared residual error.

1.5.2 NDSolve technique

NDSolve is a built-in function in mathematica which computes numerical approximations of solution to coupled differential equations. NDSolve provides an error-controlled solution of the differential equations. Error is controlled by reducing the step size until it finds solutions accurately. The default technique for boundary value problem is finite difference technique with

Richardson extrapolation.

Chapter 2

Partial slip in rotating flow of nanomaterial through porous space

This chapter elaborates the analysis of velocity and thermal slip conditions in nanomaterial flow. Whole system in rotating frame is taken. Darcy's relation models the porous space. An exponential stretching surface is used for disturbance of flow. Salient features of inclined magnetic field and dissipation are investigated. Adequate transformations are considered to dimensionless the problem. Resulting non-linear problem is solved numerically. Graphical description of involved variables is illustrated in detail. Skin friction coefficients and local Nusselt number are examined numerically.

2.1 Model development

Here rotating flow of nanomaterial through Darcy-Brinkman porous space is examined. An inclined magnetic field with angle β and strength B_0 is applied. Momentum and thermal slip conditions are employed. Viscous dissipation is taken. Stretching sheet at $z = 0$ is stretched with velocity $u_w = u_0 e^{\frac{x}{L}}$. Flow geometry is sketched in Fig. 2.1. Relevant equations for the problems are:

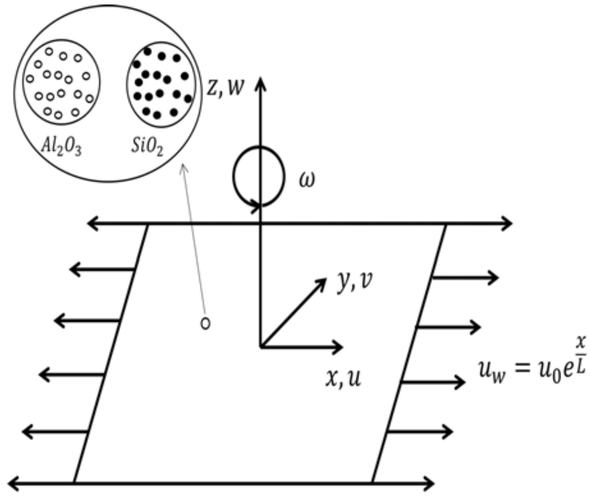

Fig. 2.1: Flow configuration.

$$\frac{\partial u}{\partial x}+\frac{\partial v}{\partial y}+\frac{\partial w}{\partial z}=0, \tag{2.1}$$

$$u\frac{\partial u}{\partial x}+v\frac{\partial u}{\partial y}+w\frac{\partial u}{\partial z}-2\omega v=\nu_{nf}\left(\frac{\partial^2 u}{\partial z^2}\right)-\frac{\nu_{nf}}{K^*}u-\frac{\sigma_{nf}B_0^2}{\rho_{nf}}\left(u\sin^2\beta-v\sin\beta\cos\beta\right), \tag{2.2}$$

$$u\frac{\partial v}{\partial x}+v\frac{\partial v}{\partial y}+w\frac{\partial v}{\partial z}+2\omega u=\nu_{nf}\left(\frac{\partial^2 v}{\partial z^2}\right)-\frac{\nu_{nf}}{K^*}v-\frac{\sigma_{nf}B_0^2}{\rho_{nf}}\left(v\cos^2\beta-u\sin\beta\cos\beta\right), \tag{2.3}$$

$$\begin{gathered}u\frac{\partial T}{\partial x}+v\frac{\partial T}{\partial y}+w\frac{\partial T}{\partial z}=\alpha_{nf}\left(\frac{\partial^2 T}{\partial z^2}\right)+\frac{\mu_{nf}}{(\rho c_p)_{nf}}\left(\left(\frac{\partial u}{\partial z}\right)^2+\left(\frac{\partial v}{\partial z}\right)^2\right)\\+\frac{\mu_{nf}}{(\rho c_p)_{nf}K^*}\left(u^2+v^2\right),\end{gathered} \tag{2.4}$$

$$u=u_w+N_1\frac{\partial u}{\partial z},\quad v=0,\quad w=0,\quad T=T_w=T_\infty+T_0e^{\frac{Ax}{2L}}+N_2\frac{\partial T}{\partial z}\quad \text{at}\quad z=0, \tag{2.5}$$

$$u\to 0,\quad v\to 0,\quad T\to T_\infty\quad \text{as}\quad z\to\infty. \tag{2.6}$$

Model for two-phase nanofluid satisfies [49] :

$$\left.\begin{array}{c}\mu_{nf}=\frac{\mu_f}{(1-\xi)^{2.5}},\ \nu_{nf}=\frac{\mu_{nf}}{\rho_{nf}},\ \rho_{nf}=\rho_f(1-\xi)+\rho_{\breve{p}}\xi,\\ \alpha_{nf}=\frac{k_{nf}}{(\rho c_p)_{nf}},\ (\rho c_p)_{nf}=(\rho c_p)_f(1-\xi)+(\rho c_p)_{\breve{p}}\xi,\\ \frac{\sigma_{nf}}{\sigma_f}=1+\frac{3\left(\frac{\sigma_{\breve{p}}}{\sigma_f}-1\right)}{\left(\frac{\sigma_{\breve{p}}}{\sigma_f}+2\right)-\left(\frac{\sigma_{\breve{p}}}{\sigma_f}-1\right)},\ \frac{k_{nf}}{k_f}=\frac{k_{\breve{p}}+2k_f-2\xi\left(k_f-k_{\breve{p}}\right)}{k_{\breve{p}}+2k_f+\xi\left(k_f-k_{\breve{p}}\right)}.\end{array}\right\} \tag{2.7}$$

Table 2.1: Thermophysical characteristics [54].

Physical properties	Base fluid	Nanoparticles	
	H_2O	Si O_2	Al_2O_3
$\rho\left(kg/m^3\right)$	997.1	2650	3970
$k\,(W/mK)$	0.613	1.5	40
$c_p\,(J/kgK)$	4179	730	765
$\sigma\,(\Omega.m)^{-1}$	0.05	10^{-21}	1×10^{-10}

Consider

$$\begin{gathered}u=u_0e^{\frac{x}{L}}\frac{\partial f(\eta,\zeta)}{\partial\zeta},\ v=u_0e^{\frac{x}{L}}g\left(\eta,\zeta\right),\ w=-\sqrt{\frac{\nu_fu_0}{2L}}e^{\frac{x}{2L}}\left(f+\zeta\frac{\partial f(\eta,\zeta)}{\partial\zeta}+2\eta\frac{\partial f}{\partial\eta}\right),\\ T=T_\infty+T_0e^{\frac{Ax}{2L}}\theta\left(\eta,\zeta\right),\ \zeta=z\left(\frac{u_0}{2\nu_fL}\right)^{1/2}e^{\frac{x}{2L}},\ \eta=e^{x/L}.\end{gathered}\tag{2.8}$$

Applying above transformations the incompressibility condition is trivially satisfied and remaining equations become

$$\begin{gathered}\frac{1}{(1-\xi)^{2.5}\left(1-\xi+\frac{\rho_{\breve{p}}}{\rho_f}\xi\right)}\left(\frac{\partial^3f}{\partial\zeta^3}-2\frac{\lambda}{\eta}\frac{\partial f}{\partial\zeta}\right)-2\left(\frac{\partial f}{\partial\zeta}\right)^2+f\frac{\partial^2f}{\partial\zeta^2}+4\frac{\Omega}{\eta}g-\\ \frac{2}{\eta}\frac{M}{\left(1-\xi+\frac{\rho_{\breve{p}}}{\rho_f}\xi\right)}\left(1+\frac{3\left(\frac{\sigma_{\breve{p}}}{\sigma_f}-1\right)}{\left(\frac{\sigma_{\breve{p}}}{\sigma_f}+2\right)-\left(\frac{\sigma_{\breve{p}}}{\sigma_f}-1\right)}\right)\left(\frac{\partial f}{\partial\zeta}\sin^2\beta-g\sin\beta\cos\beta\right)=2\eta\left(\frac{\partial f}{\partial\zeta}\frac{\partial^2f}{\partial\zeta\partial\eta}-\frac{\partial f}{\partial\eta}\frac{\partial^2f}{\partial\zeta^2}\right),\end{gathered}\tag{2.9}$$

$$\begin{gathered}\frac{1}{(1-\xi)^{2.5}\left(1-\xi+\frac{\rho_{\breve{p}}}{\rho_f}\xi\right)}\left(\frac{\partial^2g}{\partial\zeta^2}-2\frac{\lambda}{\eta}g\right)-2\frac{\partial f}{\partial\zeta}g+f\frac{\partial g}{\partial\zeta}-4\frac{\Omega}{\eta}\frac{\partial f}{\partial\zeta}-\\ \frac{2}{\eta}\frac{M}{\left(1-\xi+\frac{\rho_{\breve{p}}}{\rho_f}\xi\right)}\left(1+\frac{3\left(\frac{\sigma_{\breve{p}}}{\sigma_f}-1\right)}{\left(\frac{\sigma_{\breve{p}}}{\sigma_f}+2\right)-\left(\frac{\sigma_{\breve{p}}}{\sigma_f}-1\right)}\right)\left(g\cos^2\beta-\frac{\partial f}{\partial\zeta}\sin\beta\cos\beta\right)=2\eta\left(\frac{\partial f}{\partial\eta}\frac{\partial g}{\partial\zeta}-\frac{\partial f}{\partial\zeta}\frac{\partial g}{\partial\eta}\right),\end{gathered}\tag{2.10}$$

$$\begin{gathered}\frac{1}{\left(1-\xi+\frac{(\rho c_p)_{\breve{p}}}{(\rho c_p)_f}\xi\right)}\frac{k_{nf}}{k_f}\frac{\partial^2\theta}{\partial\zeta^2}+\frac{Ec\Pr\eta^{2-\frac{A}{2}}}{(1-\xi)^{2.5}\left(1-\xi+\frac{(\rho c_p)_{\breve{p}}}{(\rho c_p)_f}\xi\right)}\left(\left(\frac{\partial^2f}{\partial\zeta^2}\right)^2+\left(\frac{\partial g}{\partial\zeta}\right)^2\right)+\\ 2\frac{Ec\Pr\lambda\eta^{1-\frac{A}{2}}}{(1-\xi)^{2.5}\left(1-\xi+\frac{(\rho c_p)_{\breve{p}}}{(\rho c_p)_f}\xi\right)}\left(\left(\frac{\partial f}{\partial\zeta}\right)^2+g^2\right)+\Pr f\frac{\partial\theta}{\partial\zeta}-\Pr A\theta\frac{\partial f}{\partial\zeta}=2\eta\left(\frac{\partial\theta}{\partial\eta}\frac{\partial f}{\partial\zeta}-\frac{\partial\theta}{\partial\zeta}\frac{\partial f}{\partial\eta}\right),\end{gathered}\tag{2.11}$$

$$f\left(\eta,0\right)=-2\eta\frac{\partial f\left(\eta,0\right)}{\partial\eta},\ \frac{\partial f\left(\eta,0\right)}{\partial\zeta}=1+\gamma_1\sqrt{\eta}\frac{\partial^2f\left(\eta,0\right)}{\partial\zeta^2},\ g\left(\eta,0\right)=0,\ \theta\left(\eta,0\right)=1+\gamma_2\frac{\partial\theta\left(\eta,0\right)}{\partial\zeta},\tag{2.12}$$

$$\frac{\partial f(\eta,\infty)}{\partial \zeta} \to 0,\ g(\eta,\infty) \to 0,\ \theta(\eta,\infty) \to 0. \tag{2.13}$$

We have

$$\lambda = \frac{\nu_f L}{K^* u_0},\ \Omega = \frac{\omega L}{u_0},\ M = \frac{\sigma B_0^2 L}{\rho_f u_0},\ \gamma_1 = N_1\left(\frac{u_0}{2\nu_f L}\right)^{1/2},\ Ec = \frac{u_0^2}{T_0 (c_p)_f}, \\ \gamma_2 = N_2\left(\frac{u_0}{2\nu_f L}\right)^{1/2},\ \Pr = \frac{\nu_f}{\alpha_f}. \tag{2.14}$$

2.1.1 First order of truncation

In first order of truncation, the terms including $\frac{\partial(.)}{\partial\eta}$ are assumed to be very small and may be approximated by zero. Thus Eqs. (2.9) – (2.13) becomes

$$\frac{1}{(1-\xi)^{2.5}\left(1-\xi+\frac{\rho_{\breve{p}}}{\rho_f}\xi\right)}\left(f''' - 2\frac{\lambda}{\eta}f'\right) - 2f'^2 + ff'' + 4\frac{\Omega}{\eta}g - \\ \frac{2}{\eta}\frac{M}{\left(1-\xi+\frac{\rho_{\breve{p}}}{\rho_f}\xi\right)}\left(1+\frac{3\left(\frac{\sigma_{\breve{p}}}{\sigma_f}-1\right)}{\left(\frac{\sigma_{\breve{p}}}{\sigma_f}+2\right)-\left(\frac{\sigma_{\breve{p}}}{\sigma_f}-1\right)}\right)\left(f'\sin^2\beta - g\sin\beta\cos\beta\right) = 0, \tag{2.15}$$

$$\frac{1}{(1-\xi)^{2.5}\left(1-\xi+\frac{\rho_{\breve{p}}}{\rho_f}\xi\right)}\left(g'' - 2\frac{\lambda}{\eta}g\right) - 2f'g + fg' - 4\frac{\Omega}{\eta}f' - \\ \frac{2}{\eta}\frac{M}{\left(1-\xi+\frac{\rho_{\breve{p}}}{\rho_f}\xi\right)}\left(1+\frac{3\left(\frac{\sigma_{\breve{p}}}{\sigma_f}-1\right)}{\left(\frac{\sigma_{\breve{p}}}{\sigma_f}+2\right)-\left(\frac{\sigma_{\breve{p}}}{\sigma_f}-1\right)}\right)\left(g\cos^2\beta - f'\sin\beta\cos\beta\right) = 0, \tag{2.16}$$

$$\frac{1}{\left(1-\xi+\frac{(\rho c_p)_{\breve{p}}}{(\rho c_p)_f}\xi\right)}\frac{k_{nf}}{k_f}\theta'' + \frac{Ec\Pr\eta^{2-\frac{A}{2}}}{(1-\xi)^{2.5}\left(1-\xi+\frac{(\rho c_p)_{\breve{p}}}{(\rho c_p)_f}\xi\right)}\left(f''^2 + g'^2\right) + \\ 2\frac{Ec\Pr\lambda\eta^{1-\frac{A}{2}}}{(1-\xi)^{2.5}\left(1-\xi+\frac{(\rho c_p)_{\breve{p}}}{(\rho c_p)_f}\xi\right)}\left(f'^2 + g^2\right) + \Pr f\theta' - \Pr A\theta f' = 0, \tag{2.17}$$

$$f(\eta,0) = 0,\ f'(\eta,0) = 1 + \gamma_1\sqrt{\eta}f''(\eta,0),\ g(\eta,0) = 0,\ \theta(\eta,0) = 1 + \gamma_2\sqrt{\eta}\theta'(\eta,0), \tag{2.18}$$

$$f'(\eta,\infty) \to 0,\ g(\eta,\infty) \to 0,\ \theta(\eta,\infty) \to 0. \tag{2.19}$$

2.1.2 Second order of truncation

To approach non-similarity solutions of Eqs. (2.9) – (2.13), we introduce

$$f^* = \frac{\partial f}{\partial \eta},\ g^* = \frac{\partial g}{\partial \eta},\ \theta^* = \frac{\partial \theta}{\partial \eta} \text{ and } \frac{\partial f^*}{\partial \eta} = \frac{\partial g^*}{\partial \eta} = \frac{\partial \theta^*}{\partial \eta} = 0. \tag{2.20}$$

Taking partial derivatives of Eqs. (2.9) – (2.13) with respect to η, we have

$$\begin{aligned}&\frac{1}{(1-\xi)^{2.5}\left(1-\xi+\frac{\rho_{\breve{p}}}{\rho_f}\xi\right)}\left(f^{*\prime\prime\prime}-2\frac{\lambda}{\eta}f^{*\prime}+2\frac{\lambda}{\eta^2}f'\right)-4f'f^{*\prime}+ff^{*\prime\prime}+f^{*}f''-\\&\frac{2}{\eta}\frac{M}{\left(1-\xi+\frac{\rho_{\breve{p}}}{\rho_f}\xi\right)}\left(1+\frac{3\left(\frac{\sigma_{\breve{p}}}{\sigma_f}-1\right)}{\left(\frac{\sigma_{\breve{p}}}{\sigma_f}+2\right)-\left(\frac{\sigma_{\breve{p}}}{\sigma_f}-1\right)}\right)\left(f^{*\prime}\sin^2\beta-g^{*}\sin\beta\cos\beta\right)+\\&\frac{2}{\eta^2}\frac{M}{\left(1-\xi+\frac{\rho_{\breve{p}}}{\rho_f}\xi\right)}\left(1+\frac{3\left(\frac{\sigma_{\breve{p}}}{\sigma_f}-1\right)}{\left(\frac{\sigma_{\breve{p}}}{\sigma_f}+2\right)-\left(\frac{\sigma_{\breve{p}}}{\sigma_f}-1\right)}\right)\left(f'\sin^2\beta-g\sin\beta\cos\beta\right)+\\&4\frac{\Omega}{\eta}g^{*}-4\frac{\Omega}{\eta^2}g=2\left(f'f^{*\prime}-f^{*}f''\right)+2\eta\left(f^{*\prime 2}-f^{*}f^{*\prime\prime}\right),\end{aligned}\tag{2.21}$$

$$\begin{aligned}&\frac{1}{(1-\xi)^{2.5}\left(1-\xi+\frac{\rho_{\breve{p}}}{\rho_f}\xi\right)}\left(g^{*\prime\prime}-2\frac{\lambda}{\eta}g^{*}+2\frac{\lambda}{\eta^2}g\right)-2f'g^{*}-2gf^{*\prime}+f^{*}g'+fg^{*\prime\prime}-\\&\frac{2}{\eta}\frac{M}{\left(1-\xi+\frac{\rho_{\breve{p}}}{\rho_f}\xi\right)}\left(1+\frac{3\left(\frac{\sigma_{\breve{p}}}{\sigma_f}-1\right)}{\left(\frac{\sigma_{\breve{p}}}{\sigma_f}+2\right)-\left(\frac{\sigma_{\breve{p}}}{\sigma_f}-1\right)}\right)\left(g^{*}\cos^2\beta-f^{*\prime}\sin\beta\cos\beta\right)+\\&\frac{2}{\eta^2}\frac{M}{\left(1-\xi+\frac{\rho_{\breve{p}}}{\rho_f}\xi\right)}\left(1+\frac{3\left(\frac{\sigma_{\breve{p}}}{\sigma_f}-1\right)}{\left(\frac{\sigma_{\breve{p}}}{\sigma_f}+2\right)-\left(\frac{\sigma_{\breve{p}}}{\sigma_f}-1\right)}\right)\left(g\cos^2\beta-f'\sin\beta\cos\beta\right)+\\&4\frac{\Omega}{\eta^2}f'-4\frac{\Omega}{\eta}f^{*\prime}=2\left(f^{*}g'-g^{*}f'\right)+2\eta\left(f^{*}g^{*\prime}-f^{*\prime}g^{*}\right),\end{aligned}\tag{2.22}$$

$$\begin{aligned}&\frac{1}{\left(1-\xi+\frac{(\rho c_p)_{\breve{p}}}{(\rho c_p)_f}\xi\right)}\frac{k_{nf}}{k_f}\theta^{*\prime\prime}+\left(2-\frac{A}{2}\right)\frac{Ec\Pr\eta^{1-\frac{A}{2}}}{(1-\xi)^{2.5}\left(1-\xi+\frac{(\rho c_p)_{\breve{p}}}{(\rho c_p)_f}\xi\right)}\left(f''^2+g'^2\right)+\\&\frac{Ec\Pr\eta^{2-\frac{A}{2}}}{(1-\xi)^{2.5}\left(1-\xi+\frac{(\rho c_p)_{\breve{p}}}{(\rho c_p)_f}\xi\right)}\left(2f''f^{*\prime\prime}+2g'g^{*\prime}\right)+2\left(1-\frac{A}{2}\right)\frac{Ec\Pr\lambda\eta^{-\frac{A}{2}}}{(1-\xi)^{2.5}\left(1-\xi+\frac{(\rho c_p)_{\breve{p}}}{(\rho c_p)_f}\xi\right)}\left(f'^2+g^2\right)\\&2\frac{Ec\Pr\lambda\eta^{1-\frac{A}{2}}}{(1-\xi)^{2.5}\left(1-\xi+\frac{(\rho c_p)_{\breve{p}}}{(\rho c_p)_f}\xi\right)}\left(2f'f^{*\prime}+2gg^{*}\right)+\Pr f^{*}\theta'+\Pr f\theta^{*\prime}-\\&\Pr A\theta^{*}f'-\Pr A\theta f^{*\prime}=2\Pr\left(f^{*}\theta'-\theta^{*}f'\right)+2\eta\Pr\left(f^{*}\theta^{*\prime}-\theta^{*}f^{*\prime}\right),\end{aligned}\tag{2.23}$$

$$\begin{aligned}&f^{*}(\eta,0)=0,\ \ f^{*\prime}(\eta,0)=\frac{\gamma_1}{2\sqrt{\eta}}f''(\eta,0)+\gamma_1\sqrt{\eta}f^{*\prime\prime}(\eta,0),\ \ g^{*}(\eta,0)=0,\\&\theta^{*}(\eta,0)=\frac{\gamma_1}{2\sqrt{\eta}}\theta'(\eta,0)+\gamma_1\sqrt{\eta}\theta^{*\prime}(\eta,0),\end{aligned}\tag{2.24}$$

$$f^{*\prime}(\eta,\infty)\to 0,\ \ g^{*}(\eta,\infty)\to 0,\ \ \theta^{*}(\eta,\infty)\to 0,\tag{2.25}$$

where η is the constant prescribed variable at any streamwise location.

2.2 Physical quantities

We have skin friction coefficients and local Nusselt number in the forms

$$\left.\begin{aligned} \left(\frac{\mathrm{Re}}{2}\right)^{1/2} C_f &= \frac{1}{\sqrt{\eta}} \frac{1}{(1-\xi)^{2.5}} f''(\eta, 0), \\ \left(\frac{\mathrm{Re}}{2}\right)^{1/2} C_g &= \frac{1}{\sqrt{\eta}} \frac{1}{(1-\xi)^{2.5}} g'(\eta, 0), \\ \left(\frac{\mathrm{Re}}{2}\right)^{-1/2} Nu &= -\frac{k_{nf}}{k_f} \sqrt{\eta} \ln \eta \theta'(\eta, 0), \end{aligned}\right\} \tag{2.26}$$

in which $\mathrm{Re} = \frac{u_0 L}{\nu_f}$ indicates local Reynolds number.

2.3 Solution methodology

NDSolve technique of mathematica is employed to compute numerical approximations for solutions of nonlinear equations. NDSolve finds a numerical solution to the ordinary differential equations by adapting its step size so that the estimated error in the solution is just within the tolerances specified. Table 2.2 provides a comparison of present results with those in [8]. A good agreement with comparative study of [8] is found.

Table 2.2: Comparative values of $\left(\frac{\text{Re}}{2}\right)^{1/2} C_f$ and $\left(\frac{\text{Re}}{2}\right)^{1/2} C_g$ against Ω.

Ω	$-\left(\frac{\text{Re}}{2}\right)^{1/2} C_f$			$-\left(\frac{\text{Re}}{2}\right)^{1/2} C_g$		
	Keller-box [8]	Shooting [8]	NDSolve	Keller-box [8]	Shooting [8]	NDSolve
0.0	-1	-1	1.28437	0	0	0
0.2	1.34742	1.34742	1.33573	0.37015	0.37015	0.36791
0.5	1.51941	1.51941	1.50581	0.76251	0.76251	0.77428
1.0	1.80246	1.80246	1.79066	1.21796	1.21796	1.23433
2.0	2.28279	2.28279	2.27418	1.84850	1.84850	1.86418

2.4 Discussion

This section provides the graphical description of emerging variables such as (λ), (Ω), (M), (β), (γ_1), (Ec) and (A) on velocities and thermal field. Comparative analysis is done for SiO_2-water and Al_2O_3-water nanofluid. Fig. 2.2 displayed curves of $f'(\zeta)$ subject to (λ). $f'(\zeta)$ is decreasing function of higher (λ) for both SiO_2-water and Al_2O_3-water nanofluid. In fact presence of porous space disturbed fluid boundary layer which produces resistance in fluid flow causes reduction in velocity $f(\zeta)$. Fig. 2.3 depicts plots of $f'(\zeta)$ for higher estimation of (Ω). It is analyzed that (Ω) lowers $f'(\zeta)$ for both SiO_2-water and Al_2O_3-water nanofluids. Reduction in velocity field $f'(\zeta)$ is noted through higher (M) for both SiO_2-water and Al_2O_3-water nanofluids (see Fig. 2.4). Fig. 2.5 captured the influence of (ξ) on $f'(\zeta)$. It is seen that an enhancement in (ξ) give rise to higher $f'(\zeta)$ for both SiO_2-water and Al_2O_3-water nanofluids. Fig. 2.6 is sketched to inspect the behavior of (β) on $f'(\zeta)$. Here inclination angle (β) offers resistance to the fluid flow due to Lorentz force which lowers the velocity field. Velocity $f'(\zeta)$ is more for SiO_2-water nanofluid in comparison to Al_2O_3-water nanomaterial. Fig. 2.7 illustrates the impact of (γ_1) on $f'(\zeta)$. Clearly $f'(\zeta)$ decays for (γ_1) for both SiO_2-water and Al_2O_3-water nanofluid. Fig. 2.8 presents characteristics of (λ) on velocity $g(\zeta)$. Clearly $g(\zeta)$ reduces for higher (λ) for both SiO_2-water and Al_2O_3-water nanofluids. Fig. 2.9 declared attributes of (Ω) on $g(\zeta)$. An enhancement in (Ω) produces oscillation in fluid flow due to rotating frame which causes higher $g(\zeta)$ for both SiO_2-water and Al_2O_3-water nanofluids. From Fig. 2.10 it is noticed that higher (M) corresponds to lower $g(\zeta)$ for both SiO_2-water and Al_2O_3-water nanofluids.

Fig. 2.11 is sketched for impact of (ξ) on $g(\zeta)$. Higher velocity $g(\zeta)$ is observed through (ξ) for both SiO_2-water and Al_2O_3-water. Significant behavior of (β) on $g(\zeta)$ is declared in Fig. 2.12. An enhancement in $g(\zeta)$ is noticed through (β) for SiO_2-water and Al_2O_3-water. Fig. 2.13 highlighted outcomes of (γ_1) on velocity $g(\zeta)$. Clearly (γ_1) lowers the velocity $g(\zeta)$ for SiO_2-water and Al_2O_3-water. An increment in (λ) correspond to stronger thermal field $\theta(\zeta)$ for both SiO_2-water and Al_2O_3-water nanomaterials (see Fig. 2.14). Fig. 2.15 presents the role of (ξ) on $\theta(\zeta)$. Stronger $\theta(\zeta)$ and more related layer thickness is noted through (ξ) for both SiO_2-water and Al_2O_3-water. Physically, thermal conductivity of fluid increases due to insertion of nanoparticles which yield stronger $\theta(\zeta)$. Figs. 2.16 and 2.17 are drawn to deliberate influence of (A) and (Ec) on thermal field $\theta(\zeta)$. Opposite trend is observed through (A) and (Ec) for both SiO_2-water and Al_2O_3-water. Fig. 2.18 depicted the attributes of (γ_2) on thermal field $\theta(\zeta)$. It is noted that higher (γ_2) give rise to stronger $\theta(\zeta)$ for both SiO_2-water and Al_2O_3-water. Tables 2.3 and 2.4 are designed to analyze characteristics of skin friction coefficients for emerging variables. Skin friction coefficients enhances through (ξ) and (Ω) while reverse trend is noted for (γ_1). Similar results are noted for both SiO_2-water and Al_2O_3-water. Table 2.5 examined the features of local Nusselt number against (λ), (M), (ξ), (Ω), (β), (Ec) and (A). Local Nusselt number reduces against (λ), (M), (ξ), (Ω), (β) and (Ec) while (γ_2) possesses opposite trends for both SiO_2-water and Al_2O_3-water nanomaterials.

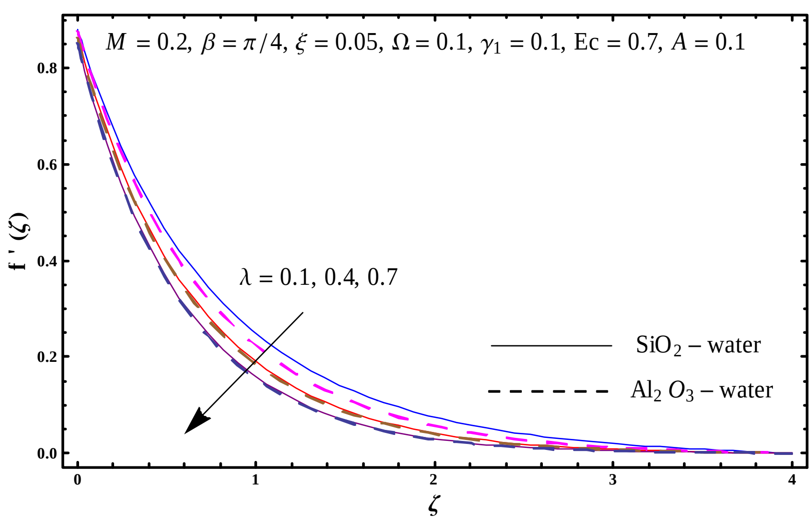

Fig. 2.2: Sketch of $f'(\zeta)$ against λ.

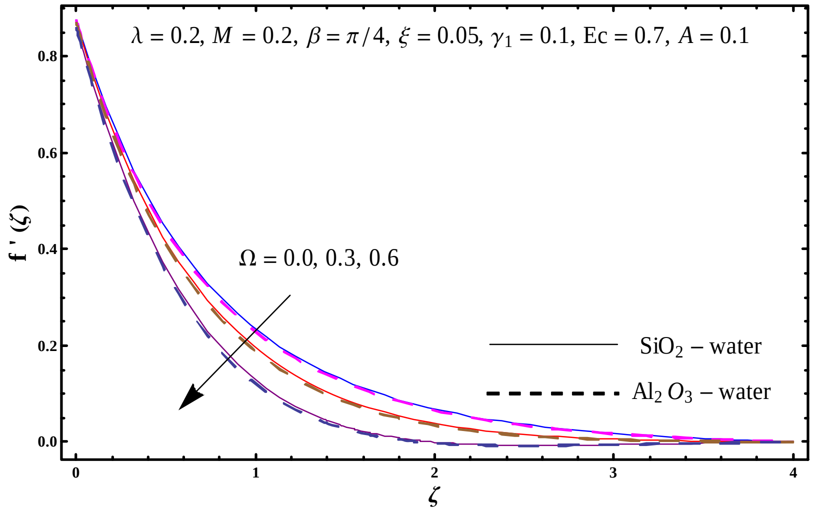

Fig. 2.3: Plot of $f'(\zeta)$ against Ω.

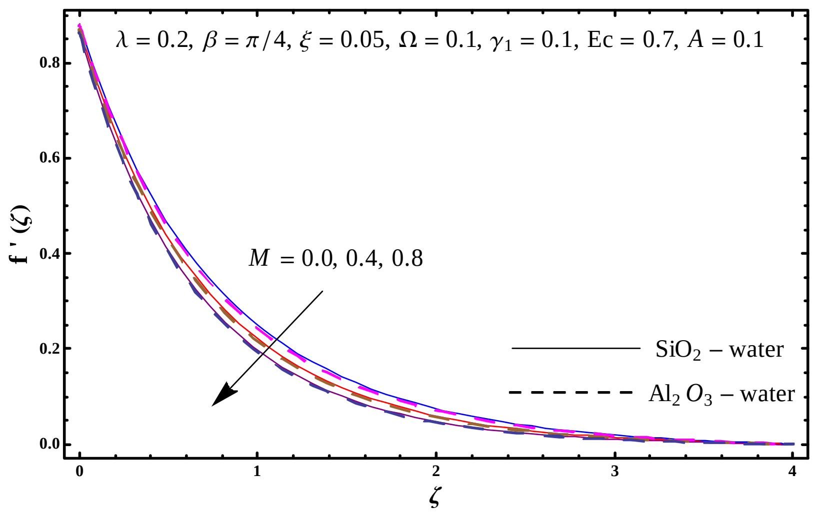

Fig. 2.4: Plot of $f'(\zeta)$ against M.

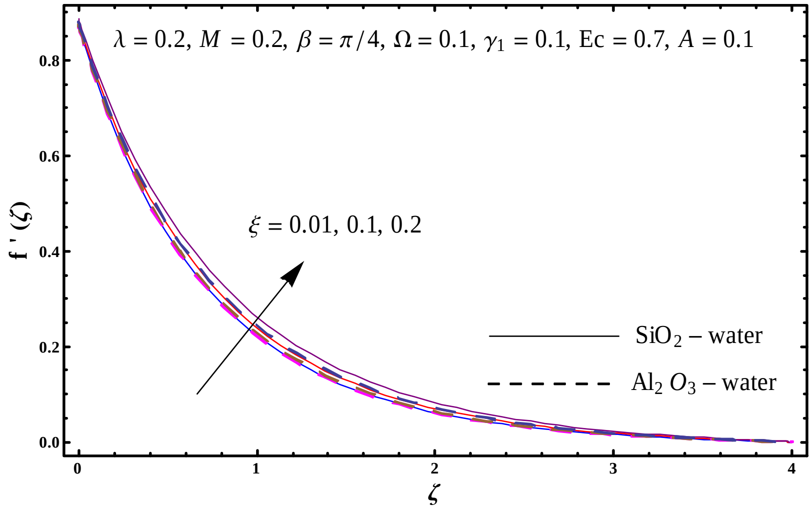

Fig. 2.5: Plot of $f'(\zeta)$ against ξ.

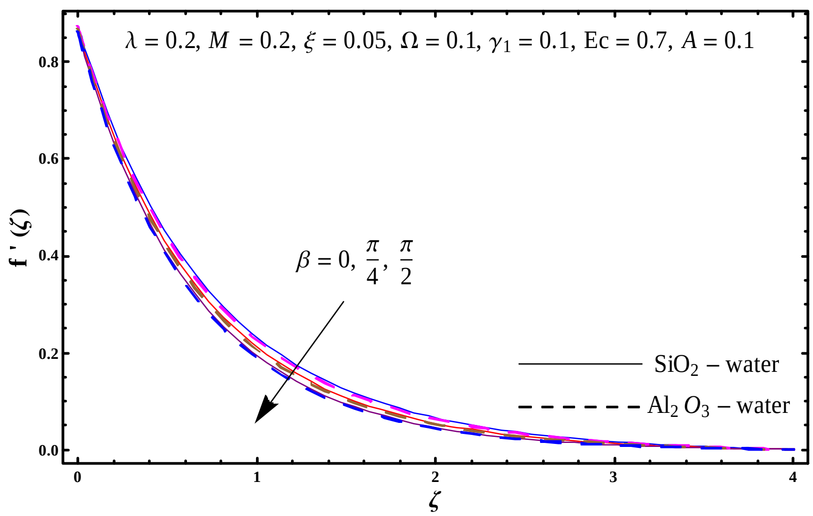

Fig. 2.6: Plot of $f'(\zeta)$ against β.

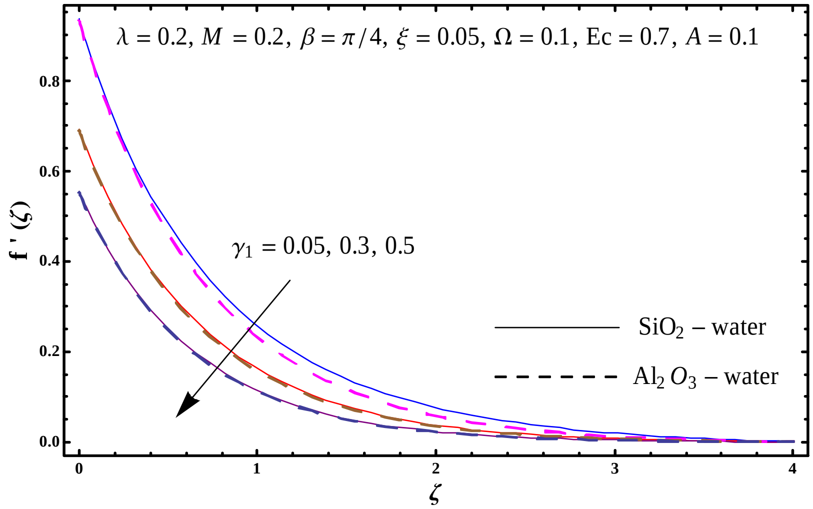

Fig. 2.7: Sketch of $f'(\zeta)$ against γ_1.

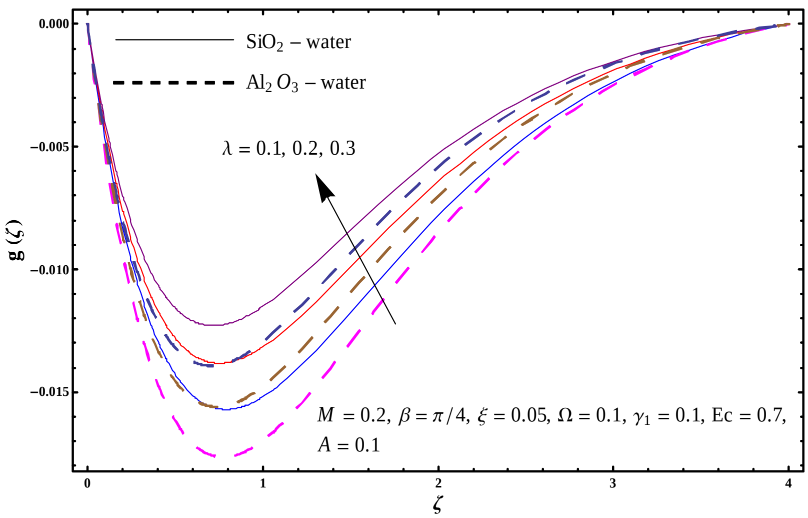

Fig. 2.8: Sketch of $g(\zeta)$ against λ.

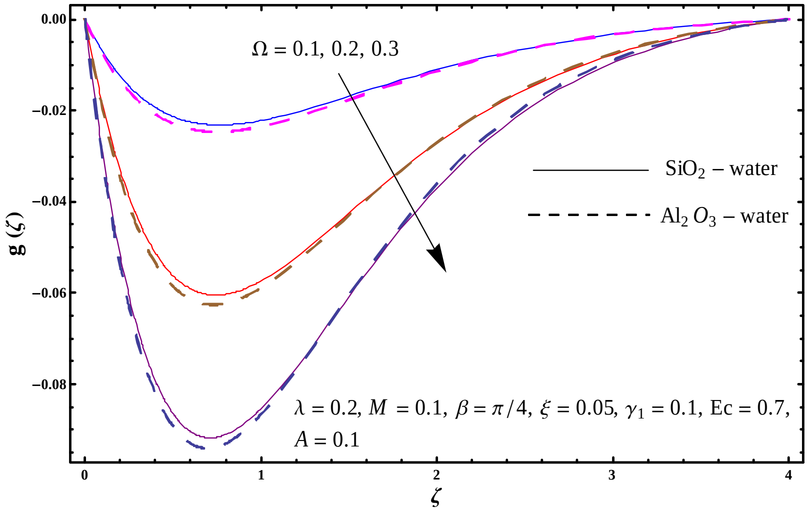

Fig. 2.9: Sketch of $g(\zeta)$ against Ω.

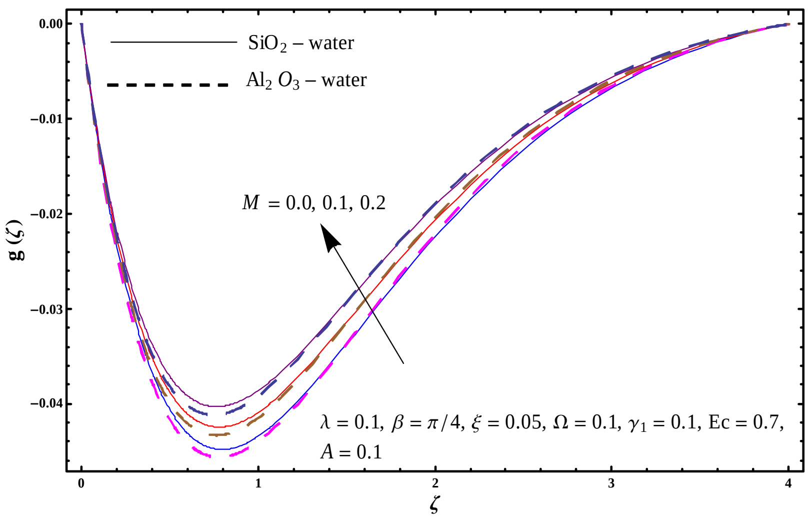

Fig. 2.10: Sketch of $g(\zeta)$ against M.

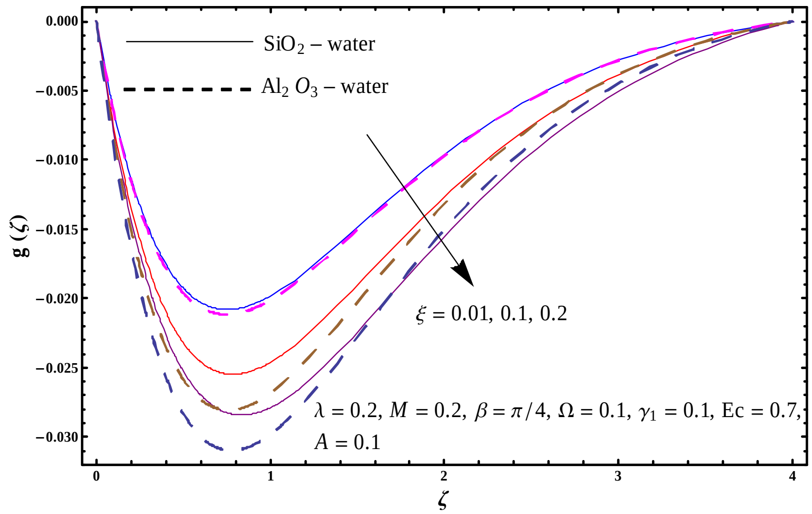

Fig. 2.11: Plot of $g(\zeta)$ against ξ.

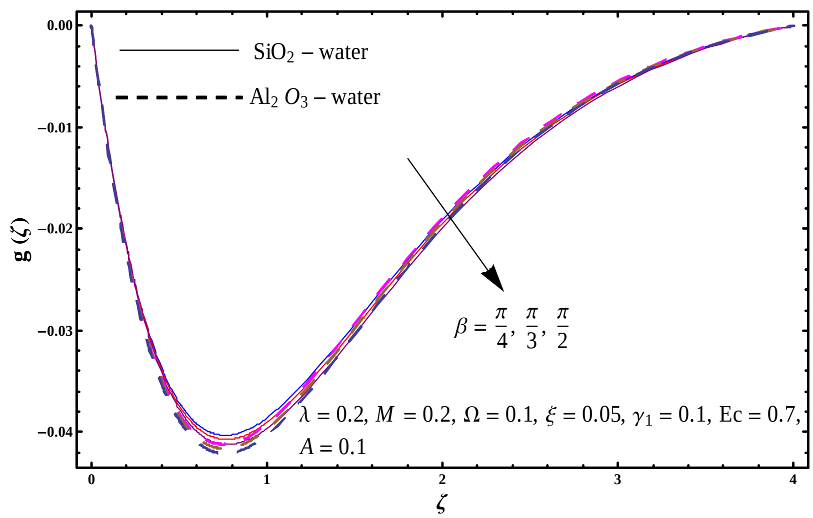

Fig. 2.12: Plot of $g(\zeta)$ against β.

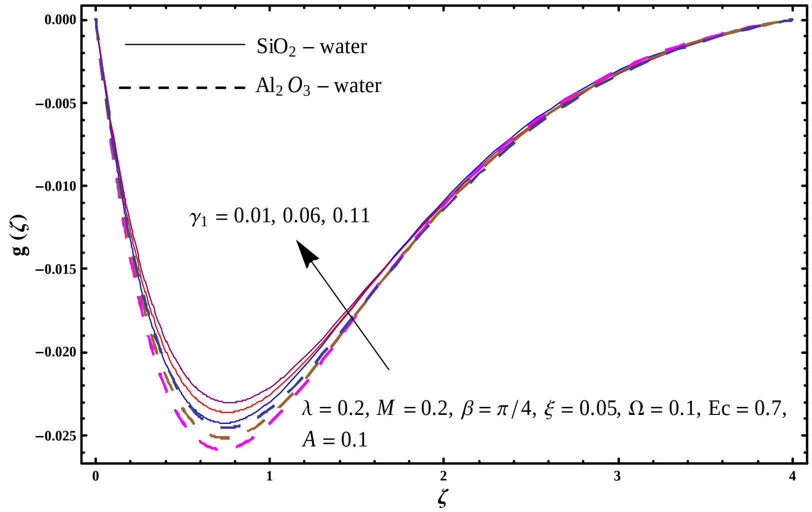

Fig. 2.13: Plot of $g(\zeta)$ against γ_1.

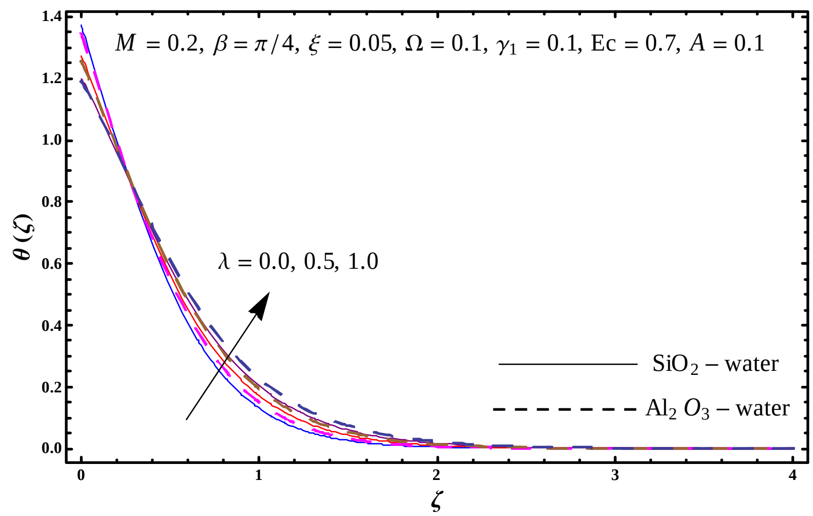

Fig. 2.14: Sketch of $\theta(\zeta)$ against λ.

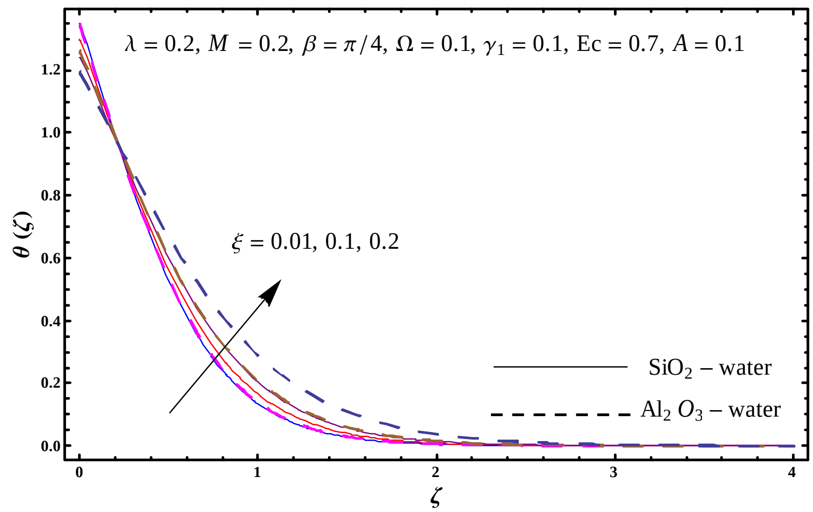

Fig. 2.15: Sketch of $\theta(\zeta)$ against ξ.

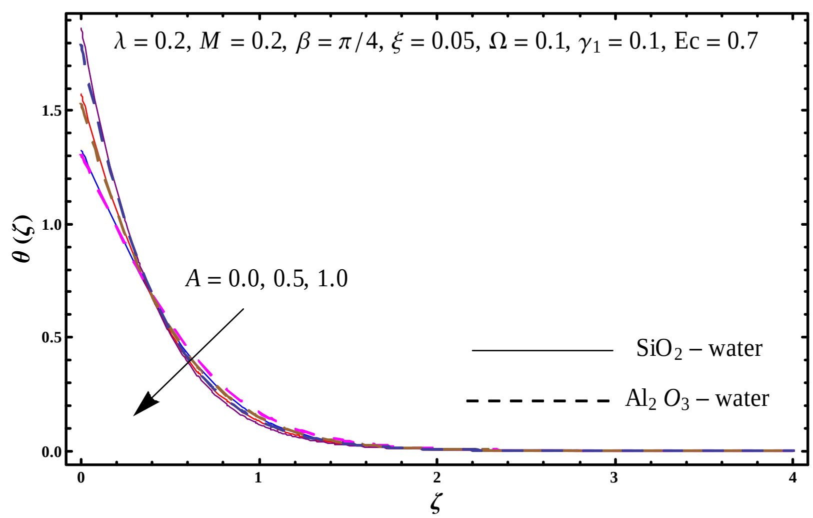

Fig. 2.16: Sketch of $\theta(\zeta)$ against A.

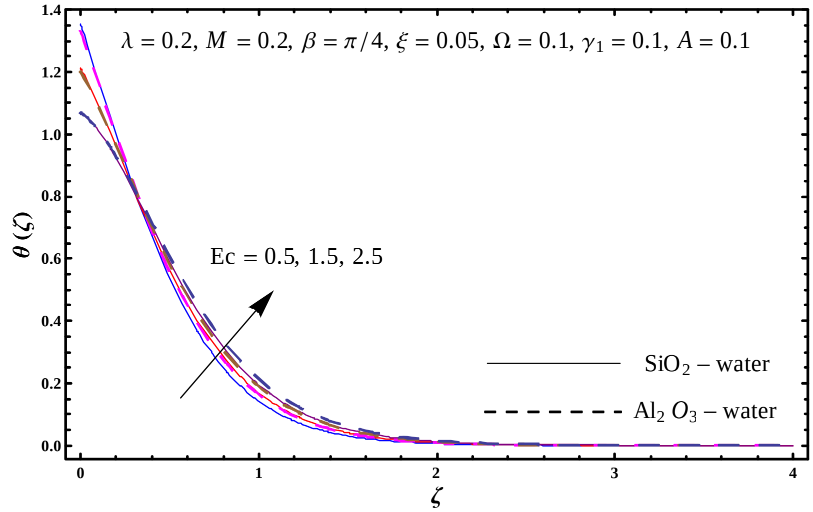

Fig. 2.17: Sketch of $\theta\left(\zeta\right)$ against Ec.

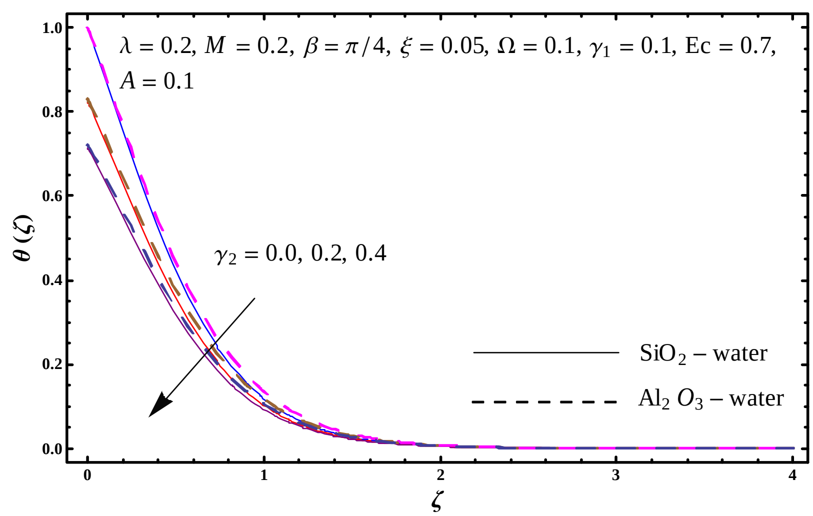

Fig. 2.18: Sketch of $\theta\left(\zeta\right)$ against γ_2.

Table 2.3: Values for skin friction coefficient $\left(\frac{\mathrm{Re}}{2}\right)^{1/2} C_f$ against λ, M, ξ, Ω, β and γ_1.

λ	M	ξ	Ω	β	γ_1	$-\left(\frac{\mathrm{Re}}{2}\right)^{1/2} C_f$	
						SiO_2−water	Al_2O_3−water
0.0	0.2	0.05	0.1	$\pi/4$	0.1	1.27202	1.30121
0.1						1.33674	1.36393
0.3						1.45547	1.47942
0.2	0.0	0.05	0.1	$\pi/4$	0.1	1.34984	1.37662
	0.1					1.37475	1.40083
	0.3					1.42291	1.44766
0.2	0.2	0.01	0.1	$\pi/4$	0.1	1.28334	1.28835
		0.02				1.31077	1.32083
		0.03				1.33896	1.35412
0.2	0.2	0.05	0.0	$\pi/4$	0.1	1.39021	1.41523
			0.2			1.41896	1.44564
			0.3			1.45026	1.47852
0.2	0.2	0.05	0.4	0	0.1	1.34883	1.37556
				$\pi/6$		1.37427	1.40032
				$\pi/3$		1.42336	1.44812
0.2	0.2	0.05	0.4	$\pi/4$	0.0	1.66943	1.70692
					0.2	1.20928	1.22793
					0.3	1.06948	1.08384

Table 2.4: Values for skin friction coefficient $\left(\frac{\mathrm{Re}}{2}\right)^{1/2} C_g$ against λ, M, ξ, Ω, β and γ_1.

λ	M	ξ	Ω	β	γ_1	$-\left(\frac{\mathrm{Re}}{2}\right)^{1/2} C_g$	
						SiO_2−water	Al_2O_3−water
0.0	0.2	0.05	0.1	$\pi/4$	0.1	0.10709	0.11537
0.1						0.09793	0.10591
0.3						0.08452	0.09189
0.2	0.0	0.05	0.1	$\pi/4$	0.1	0.16823	0.17455
	0.1					0.16292	0.16925
	0.3					0.15353	0.15982
0.2	0.2	0.01	0.1	$\pi/4$	0.1	0.07486	0.07641
		0.02				0.07872	0.08182
		0.03				0.08263	0.08726
0.2	0.2	0.05	0.0	$\pi/4$	0.1	0.01149	0.01605
			0.2			0.24212	0.25538
			0.3			0.38117	0.39903
0.2	0.2	0.05	0.4	0	0.1	0.15737	0.16365
				$\pi/6$		0.15762	0.16392
				$\pi/3$		0.15804	0.16436
0.2	0.2	0.05	0.4	$\pi/4$	0.0	0.09932	0.10783
					0.2	0.08382	0.09086
					0.3	0.07835	0.08491

Table 2.5: Values for local Nusselt number $\left(\frac{\mathrm{Re}}{2}\right)^{-1/2} Nu$ against λ, M, ξ, Ω, β, Ec, A and γ_1.

λ	M	ξ	Ω	β	Ec	A	γ_2	$-\left(\frac{\mathrm{Re}}{2}\right)^{-1/2} Nu$	
								SiO_2−water	Al_2O_3−water
0.0	0.2	0.05	0.1	$\pi/4$	0.7	0.1	0.2	2.20981	2.2439
0.1								2.08128	2.11787
0.3								1.85385	1.89375
0.2	0.0	0.05	0.1	$\pi/4$	0.7	0.1	0.2	2.01133	2.04963
	0.1							1.98425	2.02267
	0.3							1.93179	1.97037
0.2	0.2	0.01	0.1	$\pi/4$	0.7	0.1	0.2	2.02286	2.02972
		0.02						2.00818	2.02233
		0.03						1.99334	2.01521
0.2	0.2	0.05	0.0	$\pi/4$	0.7	0.1	0.2	1.97852	2.01883
			0.2					1.91405	1.94778
			0.3					1.84143	1.86877
0.2	0.2	0.05	0.4	0	0.7	0.1	0.2	2.01465	2.05315
				$\pi/6$				1.98583	2.02435
				$\pi/3$				1.93032	1.96882
0.2	0.2	0.05	0.4	$\pi/4$	0.8	0.1	0.2	1.88709	1.92533
					0.9			1.81104	1.84905
					1.0			1.73499	1.77276
0.2	0.2	0.05	0.4	$\pi/4$	0.7	0.0	0.2	1.71803	1.75586
						0.2		2.21481	2.25304
						0.3		2.47369	2.51068
0.2	0.2	0.05	0.4	$\pi/4$	0.7	0.1	0.0	1.33049	1.38925
							0.1	1.58605	1.64014
							0.3	2.57545	2.56746

Chapter 3

Rotating flow of carbon nanotubes subject to prescribed heat flux condition

This chapter intends to describe the three-dimensional flow of nanofluid in rotating frame. Carbon nanotubes (CNTs) are adopted. Disturbance in flow is generated by an exponentially stretching sheet. Prescribed heat flux condition is considered. Darcy-Forchheimer relation is employed to characterize the flow in porous space. System of dimensionless equations is obtained by utilizing adequate transformations. Solutions are computed by Optimal homotopy analysis algorithm (OHAM). Physical interpretation of emerging variables on flow fields and physical quantities is discussed.

3.1 Model development

We examine rotating flow of carbon nanotubes dispersed in water through porous space. Disturbance in flow in created by an exponentially stretching sheet. Darcy-Forchheimer expression is employed for flow through porous space. Here the fluid occupies the domain $z > 0$ and the stretching surface is aligned in $x-$direction. Surface is exponentially stretching with velocity $u_w(x) = u_0 e^{x/L}$ (see Fig. 3.1). Fluid is rotating with constant angular velocity ω about $z-$axis.

The boundary layer equations for 3D flow satisfy

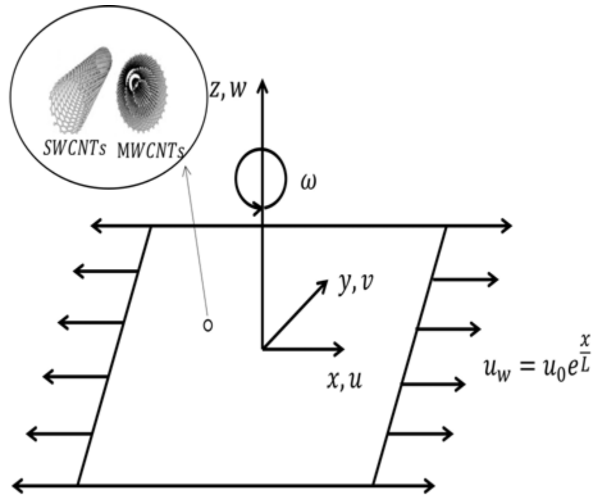

Fig. 3.1: Flow configuration.

$$\frac{\partial u}{\partial x}+\frac{\partial v}{\partial y}+\frac{\partial w}{\partial z}=0, \tag{3.1}$$

$$u\frac{\partial u}{\partial x}+v\frac{\partial u}{\partial y}+w\frac{\partial u}{\partial z}-2\omega v=\nu_{nf}\left(\frac{\partial^2 u}{\partial z^2}\right)-\frac{\nu_{nf}}{K^*}u-Fu\sqrt{u^2+v^2}, \tag{3.2}$$

$$u\frac{\partial v}{\partial x}+v\frac{\partial v}{\partial y}+w\frac{\partial v}{\partial z}+2\omega u=\nu_{nf}\left(\frac{\partial^2 v}{\partial z^2}\right)-\frac{\nu_{nf}}{K^*}v-Fv^2\sqrt{u^2+v^2}, \tag{3.3}$$

$$u\frac{\partial T}{\partial x}+v\frac{\partial T}{\partial y}+w\frac{\partial T}{\partial z}=\alpha_{nf}\frac{\partial^2 T}{\partial z^2}, \tag{3.4}$$

$$u=u_w(x)=u_0e^{x/L},\quad v=0,\quad w=0,\quad -k_{nf}\left(\frac{\partial T}{\partial z}\right)_w=T_0e^{\frac{(A+1)x}{2L}}\quad \text{at}\quad z=0, \tag{3.5}$$

$$u\to 0,\quad v\to 0,\quad T\to T_\infty\quad \text{as}\quad z\to\infty. \tag{3.6}$$

Xue suggested a theoretical model satisfying [45]

$$\left.\begin{array}{l} \mu_{nf}=\frac{\mu_f}{(1-\xi)^{2.5}},\ \nu_{nf}=\frac{\mu_{nf}}{\rho_{nf}},\ \alpha_{nf}=\frac{k_{nf}}{(\rho c_p)_{nf}},\ \rho_{nf}=\rho_f(1-\xi)+\rho_{CNT}\xi, \\ (\rho c_p)_{nf}=(\rho c_p)_f(1-\xi)+(\rho c_p)_{CNT}\xi,\ \frac{k_{nf}}{k_f}=\frac{(1-\xi)+2\xi\frac{k_{CNT}}{k_{CNT}-k_f}\ln\frac{k_{CNT}+k_f}{2k_f}}{(1-\xi)+2\xi\frac{k_f}{k_{CNT}-k_f}\ln\frac{k_{CNT}+k_f}{2k_f}}. \end{array}\right\} \tag{3.7}$$

Table 3.1: Thermophysical characteristics [45].

Physical properties	Base fluid	Nanoparticles	
	Water	$SWCNTs$	$MWCNTs$
$\rho\left(kg/m^3\right)$	997.1	2600	1600
$k\,(W/mK)$	0.613	6600	3000
$c_p\,(J/kgK)$	4179	425	796

Considering

$$\begin{aligned} u = u_0 e^{\frac{x}{L}} \frac{\partial f(\eta,\zeta)}{\partial \zeta},\ v = u_0 e^{\frac{x}{L}} g\left(\eta,\zeta\right),\ w = -\sqrt{\frac{\nu_f u_0}{2L}} e^{\frac{x}{2L}} \left(f + \zeta \frac{\partial f}{\partial \zeta} + 2\eta \frac{\partial f}{\partial \eta}\right), \\ T = T_\infty + \frac{T_0}{k_f} e^{Ax/2L} \sqrt{\frac{2\nu_f L}{u_0}} \theta\left(\eta,\zeta\right),\ \zeta = z\left(\frac{u_0}{2\nu_f L}\right)^{1/2} e^{\frac{x}{2L}},\ \eta = e^{x/L}. \end{aligned} \tag{3.8}$$

we have

$$\begin{aligned} \frac{1}{(1-\xi)^{2.5}\left(1-\xi+\frac{\rho_{CNT}}{\rho_f}\xi\right)} \left(\frac{\partial^3 f}{\partial \zeta^3} - 2\frac{\lambda}{\eta}\frac{\partial f}{\partial \zeta}\right) + f\frac{\partial^2 f}{\partial \zeta^2} + 4\frac{\Omega}{\eta} g - 2\left(\frac{\partial f}{\partial \zeta}\right)^2 - \\ 2F_r\left(\left(\frac{\partial f}{\partial \zeta}\right)^2 + \frac{1}{2}g^2\right) = 2\eta\left(\frac{\partial f}{\partial \zeta}\frac{\partial^2 f}{\partial \zeta \partial \eta} - \frac{\partial f}{\partial \eta}\frac{\partial^2 f}{\partial \zeta^2}\right), \end{aligned} \tag{3.9}$$

$$\begin{aligned} \frac{1}{(1-\xi)^{2.5}\left(1-\xi+\frac{\rho_{CNT}}{\rho_f}\xi\right)} \left(\frac{\partial^2 g}{\partial \zeta^2} - 2\frac{\lambda}{\eta} g\right) + f\frac{\partial g}{\partial \zeta} - 2\frac{\partial f}{\partial \zeta} g - 4\frac{\Omega}{\eta}\frac{\partial f}{\partial \zeta} - \\ 2F_r\left(g^2 + \frac{1}{2}\left(\frac{\partial f}{\partial \zeta}\right)^2\right) = 2\eta\left(\frac{\partial f}{\partial \zeta}\frac{\partial g}{\partial \eta} - \frac{\partial f}{\partial \eta}\frac{\partial g}{\partial \zeta}\right), \end{aligned} \tag{3.10}$$

$$\frac{1}{\left(1-\xi+\frac{(\rho c_p)_{CNT}}{(\rho c_p)_f}\xi\right)} \frac{k_{nf}}{k_f}\frac{\partial^2 \theta}{\partial \zeta^2} + \Pr f\frac{\partial \theta}{\partial \zeta} - \Pr A\theta \frac{\partial f}{\partial \zeta} = 2\Pr \eta\left(\frac{\partial f}{\partial \eta}\frac{\partial \theta}{\partial \zeta} - \frac{\partial \theta}{\partial \eta}\frac{\partial f}{\partial \zeta}\right), \tag{3.11}$$

$$f\left(\eta,0\right) = -2\eta\frac{\partial f\left(\eta,0\right)}{\partial \eta},\ \frac{\partial f\left(\eta,0\right)}{\partial \zeta} = 1,\ g\left(\eta,0\right) = 0,\ \frac{\partial \theta\left(\eta,0\right)}{\partial \zeta} = -\frac{k_f}{k_{nf}}, \tag{3.12}$$

$$\frac{\partial f\left(\eta,\infty\right)}{\partial \zeta} \to 0,\ g\left(\eta,\infty\right) \to 0,\ \theta\left(\eta,\infty\right) \to 0, \tag{3.13}$$

Here equation (3.1) is identically justified. Emerging flow parameters can be stated as:

$$\lambda = \frac{\nu_f L}{K^* u_0},\ F_r = \frac{C_b}{{K^*}^{1/2}} L,\ \Omega = \frac{\omega L}{u_0},\ \Pr = \frac{\nu_f}{\alpha_f}. \tag{3.14}$$

3.1.1 First order of truncation

In first order of truncation, the terms including $\frac{\partial(.)}{\partial\eta}$ are assumed to be very small and may be approximated by zero. Thus Eqs. (3.9) – (3.13) becomes

$$\frac{1}{(1-\xi)^{2.5}\left(1-\xi+\frac{\rho_{\breve{p}}}{\rho_f}\xi\right)}\left(f'''-2\frac{\lambda}{\eta}f'\right)-2f'^2+ff''+4\frac{\Omega}{\eta}g-2F_r\left(f'^2+\frac{1}{2}g^2\right)=0, \quad (3.15)$$

$$\frac{1}{(1-\xi)^{2.5}\left(1-\xi+\frac{\rho_{\breve{p}}}{\rho_f}\xi\right)}\left(g''-2\frac{\lambda}{\eta}g\right)-2f'g+fg'-4\frac{\Omega}{\eta}f'-2F_r\left(g^2+\frac{1}{2}f'^2\right)=0, \quad (3.16)$$

$$\frac{1}{\left(1-\xi+\frac{(\rho c_p)_{\breve{p}}}{(\rho c_p)_f}\xi\right)}\frac{k_{nf}}{k_f}\theta''+\Pr f\theta'-\Pr A\theta f'=0, \quad (3.17)$$

$$f(\eta,0)=0,\ f'(\eta,0)=1,\ g(\eta,0)=0,\ \theta'(\eta,0)=-\frac{k_f}{k_{nf}}, \quad (3.18)$$

$$f'(\eta,\infty)\to 0,\ g(\eta,\infty)\to 0,\ \theta(\eta,\infty)\to 0. \quad (3.19)$$

3.1.2 Second order of truncation

To approach non-similarity solutions of Eqs. (3.9) – (3.13) , we consider

$$f^*=\frac{\partial f}{\partial\eta},\ g^*=\frac{\partial g}{\partial\eta},\ \theta^*=\frac{\partial\theta}{\partial\eta}\text{ and }\frac{\partial f^*}{\partial\eta}=\frac{\partial g^*}{\partial\eta}=\frac{\partial\theta^*}{\partial\eta}=0. \quad (3.20)$$

Taking partial derivatives of Eqs. (3.9) – (3.13) with respect to η, we have

$$\begin{aligned}&\frac{1}{(1-\xi)^{2.5}\left(1-\xi+\frac{\rho_{\breve{p}}}{\rho_f}\xi\right)}\left(f^{*\prime\prime\prime}-2\frac{\lambda}{\eta}f^{*\prime}+2\frac{\lambda}{\eta^2}f'\right)-4f'f^{*\prime}+ff^{*\prime\prime}+f^*f''-\\&4\frac{\Omega}{\eta}g^*-4\frac{\Omega}{\eta^2}g-2F_r\left(f'f^{*\prime}+gg^*\right)=2\left(f'f^{*\prime}-f^*f''\right)+2\eta\left(f^{*\prime 2}-f^*f^{*\prime\prime}\right),\end{aligned} \quad (3.21)$$

$$\begin{aligned}&\frac{1}{(1-\xi)^{2.5}\left(1-\xi+\frac{\rho_{\breve{p}}}{\rho_f}\xi\right)}\left(g^{*\prime\prime}-2\frac{\lambda}{\eta}g^*+2\frac{\lambda}{\eta^2}g\right)-2f'g^*-2gf^{*\prime}+f^*g'+fg^{*\prime\prime}-\\&4\frac{\Omega}{\eta^2}f'-4\frac{\Omega}{\eta}f^{*\prime}-2F_r\left(2gg^*+f'f^{*\prime}\right)=2\left(f^*g'-g^*f'\right)+2\eta\left(f^*g^{*\prime}-f^{*\prime}g^*\right),\end{aligned} \quad (3.22)$$

$$\frac{1}{\left(1-\xi+\frac{(\rho c_p)_{\breve{p}}}{(\rho c_p)_f}\xi\right)}\frac{k_{nf}}{k_f}\theta^{*\prime\prime}+\Pr f^{*}\theta^{\prime}+\Pr f\theta^{*\prime}-\Pr A\theta^{*}f^{\prime}-\Pr A\theta f^{*\prime}=2\Pr\left(f^{*}\theta^{\prime}-\theta^{*}f^{\prime}\right)+$$
$$2\eta\Pr\left(f^{*}\theta^{*\prime}-\theta^{*}f^{*\prime}\right), \tag{3.23}$$

$$f^{*}(\eta,0)=0,\ f^{*\prime}(\eta,0)=0,\ g^{*}(\eta,0)=0,\ \theta^{*}(\eta,0)=0, \tag{3.24}$$

$$f^{*\prime}(\eta,\infty)\to 0,\ g^{*}(\eta,\infty)\to 0,\ \theta^{*}(\eta,\infty)\to 0, \tag{3.25}$$

in which η is the constant prescribed variable at any streamwise location.

3.2 Physical quantities

Expressions of physical quantities are

$$\left.\begin{array}{c}\left(\frac{\mathrm{Re}}{2}\right)^{1/2}C_f=\frac{1}{\sqrt{\eta}}\frac{1}{(1-\xi)^{2.5}}f^{\prime\prime}(\eta,0),\\ \left(\frac{\mathrm{Re}}{2}\right)^{1/2}C_g=\frac{1}{\sqrt{\eta}}\frac{1}{(1-\xi)^{2.5}}g^{\prime}(\eta,0),\\ \left(\frac{\mathrm{Re}}{2}\right)^{-1/2}Nu=\frac{\sqrt{\eta}\ln\eta}{\theta(\eta,0)},\end{array}\right\} \tag{3.26}$$

Here $\mathrm{Re}=\frac{u_0L}{\nu_f}$ symbolizes local Reynolds number.

3.3 OHAM Solutions

Obtained system of nonlinear equations is solved by employing OHAM. Initial approximations and operators satisfy

$$\mathcal{L}_f=\frac{d^3f}{d\zeta^3}-\frac{df}{d\zeta},\quad \mathcal{L}_g=\frac{d^2g}{d\zeta^2}-g,\quad \mathcal{L}_\theta=\frac{d^2\theta}{d\zeta^2}-\theta, \tag{3.27}$$

$$f_0(\zeta)=1-e^{-\zeta},\quad g_0(\zeta)=0,\quad \theta_0(\zeta)=\frac{1}{\frac{k_{nf}}{k_f}}e^{-\zeta}, \tag{3.28}$$

with characteristics

$$\mathcal{L}_f\left[\breve{J}_1^{*}+\breve{J}_2^{*}e^{\zeta}+\breve{J}_3^{*}e^{-\zeta}\right]=0,\ \mathcal{L}_g\left[\breve{J}_4^{*}e^{\zeta}+\breve{J}_5^{*}e^{-\zeta}\right]=0,\ \mathcal{L}_\theta\left[\breve{J}_6^{*}e^{\zeta}+\breve{J}_7^{*}e^{-\zeta}\right]=0. \tag{3.29}$$

3.4 Solutions convergence

The momentum and energy equations are solved by utilizing BVPh2.0. These expressions contain $\hbar_f$, $\hbar_g$ and $\hbar_\theta$ which plays significant role in computation of approximate series solutions. The optimal data of convergence control variables can be evaluated by taking minimum error. At mth-order of approximation, average squared residual error are given as [140] :

$$\varepsilon_m^f = \frac{1}{\breve{k}+1} \sum_{i=0}^{\breve{k}} \left[\mathcal{N}_f \left(\sum_{j=0}^{m} f(\zeta), \sum_{j=0}^{m} g(\zeta) \right)_{\zeta = i\delta\zeta} \right]^2, \tag{3.30}$$

$$\varepsilon_m^g = \frac{1}{\breve{k}+1} \sum_{i=0}^{\breve{k}} \left[\mathcal{N}_g \left(\sum_{j=0}^{m} f(\zeta), \sum_{j=0}^{m} g(\zeta) \right)_{\zeta = i\delta\zeta} \right]^2, \tag{3.31}$$

$$\varepsilon_m^\theta = \frac{1}{\breve{k}+1} \sum_{i=0}^{\breve{k}} \left[\mathcal{N}_\theta \left(\sum_{j=0}^{m} f(\zeta), \sum_{j=0}^{m} g(\zeta), \sum_{j=0}^{m} \theta(\zeta) \right)_{\zeta = i\delta\zeta} \right]^2, \tag{3.32}$$

$$\varepsilon_m^t = \varepsilon_m^f + \varepsilon_m^g + \varepsilon_m^\theta. \tag{3.33}$$

At 2nd order of approximations, the numerical data of convergence control variables in SWCNTs and MWCNTs cases are $\hbar_f = -0.987276$, $\hbar_g = -1.14483$, $\hbar_\theta = -0.536343$ and $\hbar_f = -0.922204$, $\hbar_g = -1.0583$ and $\hbar_\theta = -0.545242$. The total residual error in SWCNTs and MWCNTs cases are $\varepsilon_m^t = 6.74 \times 10^{-4}$ and $\varepsilon_m^t = 8.19 \times 10^{-4}$. Figs. 3.2 and 3.3 are plotted to characterize the total residual error in case of SWCNTs and MWCNTs. Individual average squared residual errors at 2nd order of deformation are provided in Tables 3.2 and 3.3. Decrease in average squared residual error is noted with higher order approximation.

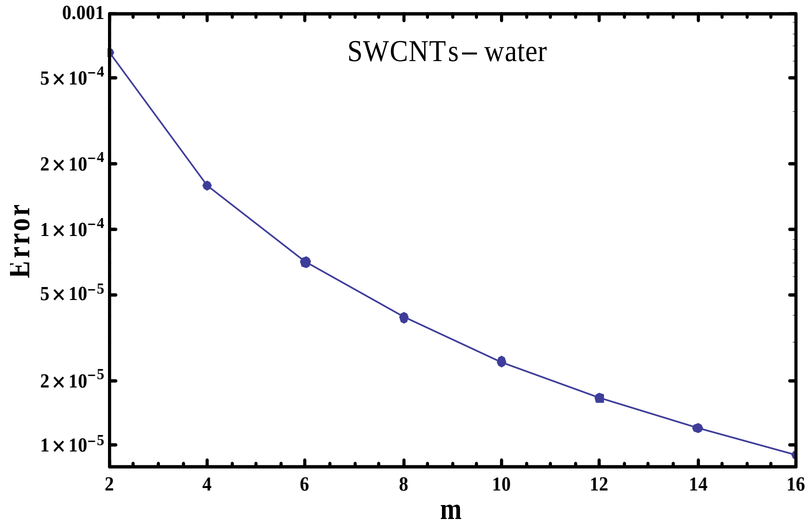

Fig. 3.2: Plot of total residual error for SWCNTs-water.

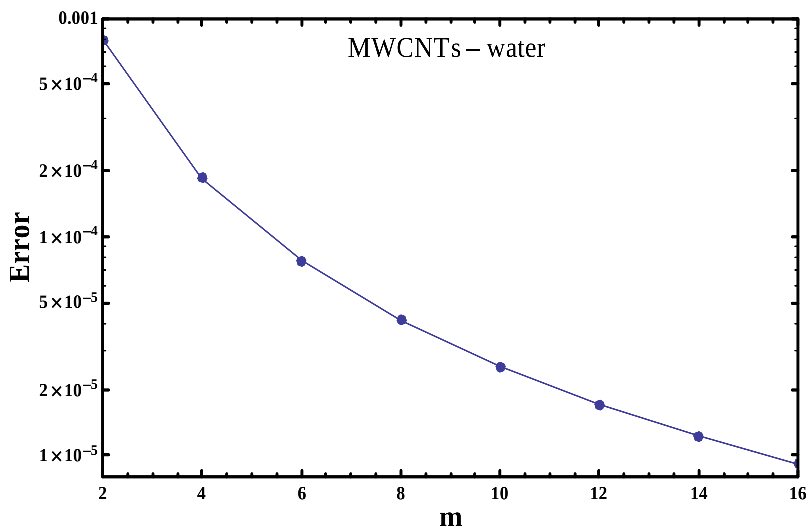

Fig. 3.3: Sketch of total residual error for MWCNTs-water.

Table 3.2: Optimal data of average squared residual errors for SWCNTs.

m	ε_m^f	ε_m^g	ε_m^θ
2	2.73×10^{-4}	1.48×10^{-4}	2.53×10^{-4}
6	3.14×10^{-5}	1.72×10^{-5}	2.37×10^{-5}
10	1.24×10^{-5}	5.73×10^{-6}	6.86×10^{-6}
14	6.84×10^{-6}	2.59×10^{-6}	2.81×10^{-6}
16	5.40×10^{-6}	1.86×10^{-6}	1.95×10^{-6}

Table 3.3: Optimal data of average squared residual errors for MWCNTs.

m	ε_m^f	ε_m^g	ε_m^θ
2	2.37×10^{-4}	1.82×10^{-4}	4.00×10^{-4}
6	2.83×10^{-5}	2.34×10^{-5}	2.78×10^{-5}
10	1.15×10^{-5}	8.29×10^{-6}	6.26×10^{-6}
14	6.44×10^{-6}	3.96×10^{-6}	2.14×10^{-6}
16	5.13×10^{-6}	2.92×10^{-6}	1.38×10^{-6}

3.5 Discussion

This section analyzes the characteristics of different emerging flow variables like (λ), (Ω), (A), (ξ) and (F_r) on the velocities $f'(\zeta)$ and $g(\zeta)$ and temperature $\theta(\zeta)$ fields. Velocity field $f'(\zeta)$ shows decreasing trend for higher (λ) in SWCNTs and MWCNTs situations (see Fig. 3.4). Physically fluid viscosity and (λ) varies directly so for larger (λ) the viscosity improves which lowers the velocity $f'(\zeta)$. Fig. 3.5 scrutinizes the change in velocity $f'(\zeta)$ for varying (F_r). Larger (F_r) produces resistance between the fluid particles which decreases velocity $f'(\zeta)$ in SWCNTs and MWCNTs. Fig. 3.6 elaborates the consequences of (ξ) for velocity field $f'(\zeta)$. Higher estimation of (ξ) produces higher velocity field $f'(\zeta)$ in SWCNTs and MWCNTs situations. Fig. 3.7 is portrayed to describe the behavior of (Ω) on $f'(\zeta)$. It has been analyzed that higher estimation of (Ω) causes higher rotation rate which leads to lower velocity field $f'(\zeta)$. Fig. 3.8 presents that larger (λ) produces lower velocity field $g(\zeta)$ in

SWCNTs and MWCNTs situations. Fig. 3.9 analyzed that velocity $g(\zeta)$ decreases for higher (F_r) in SWCNTs and MWCNTs situations. Behavior of (ξ) on velocity $g(\zeta)$ is analyzed in Fig. 3.10. It is analyzed that $g(\zeta)$ enhances via (ξ) in SWCNTs and MWCNTs situations. Physically an increase in volume fraction of nanoparticles causes more collisions between the nanoparticles which corresponds to higher velocity $g(\zeta)$. Fig. 3.11 illustrates the role of (Ω) on velocity field $g(\zeta)$. Local rotational parameter plays an important role in stimulating the flow along $y-$direction which produces oscillatory trend in $f'(\zeta)$. Fig. 3.12 captured the behavior of (λ) on temperature field $\theta(\zeta)$. By increasing (λ), more heat is produced due to the resistance between particles which causes stronger $\theta(\zeta)$ and thicker thermal layer thickness is observed in SWCNTs and MWCNTs situations. Fig. 3.13 is portrayed to deliberate the effect of (F_r) on temperature $\theta(\zeta)$. Larger estimation of (F_r) yield an increase of $\theta(\zeta)$ and its related layer thickness through SWCNTs and MWCNTs. Fig. 3.14 is portrayed to describe impact of (ξ) against $\theta(\zeta)$. Higher estimation of (ξ) yield weaker thermal field $\theta(\zeta)$ in SWCNTs and MWCNTs situations. Fig. 3.15 displayed that by enhancing (A), temperature $\theta(\zeta)$ is reduced in SWCNTs and MWCNTs. Figs. $3.16 - 3.19$ plotted the skin friction coefficients $\left(\frac{\mathrm{Re}}{2}\right)^{1/2} C_f$ and $\left(\frac{\mathrm{Re}}{2}\right)^{1/2} C_g$ for varying ξ, λ and F_r. $\left(\frac{\mathrm{Re}}{2}\right)^{1/2} C_f$ and $\left(\frac{\mathrm{Re}}{2}\right)^{1/2} C_g$ are incriminated for larger estimation of (ξ). Figs. 3.20 and 3.21 are for local heat transfer rate $\left(\frac{\mathrm{Re}}{2}\right)^{-1/2} Nu$ via distinct values of λ, ξ and F_r. Here magnitude of $\left(\frac{\mathrm{Re}}{2}\right)^{-1/2} Nu$ is higher for larger estimation of (ξ). Table 3.4 illustrates the validation of present results of skin friction coefficients with existing

[12] . A good agreement here is noticed.

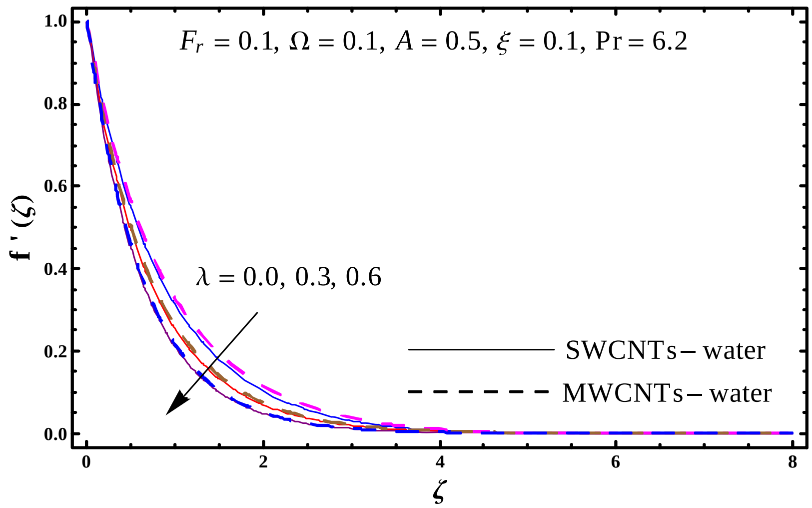

Fig. 3.4: Plot for $f'(\zeta)$ against λ.

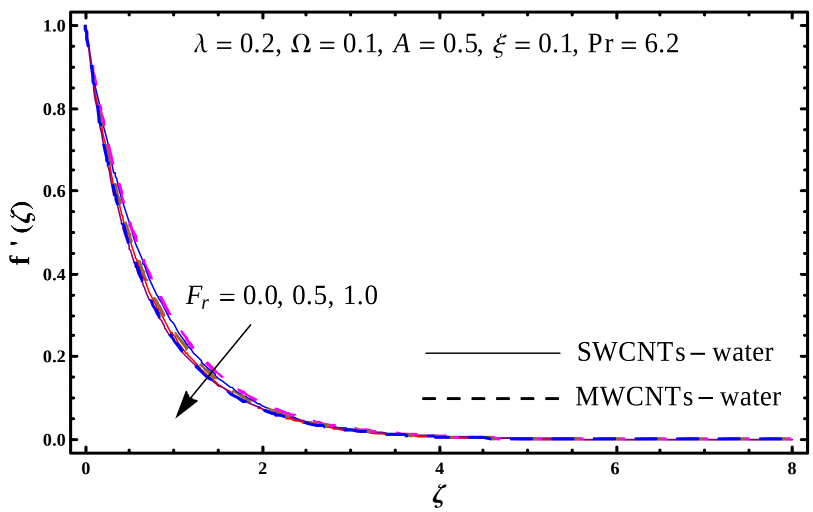

Fig. 3.5: Plot for $f'(\zeta)$ against F_r.

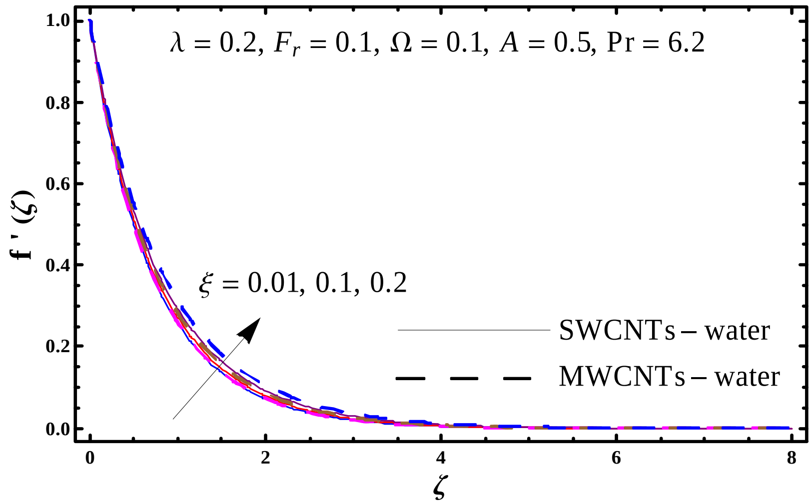

Fig. 3.6: Plot for $f'(\zeta)$ against ξ.

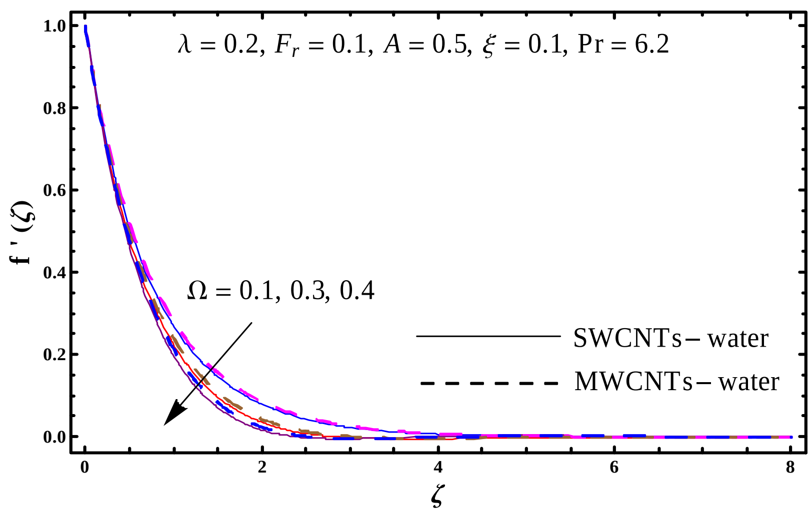

Fig. 3.7: Plot for $f'(\zeta)$ against Ω.

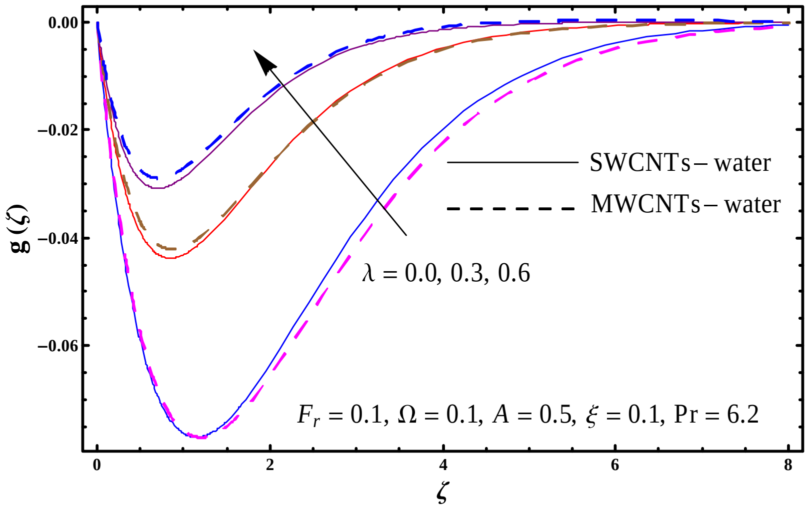

Fig. 3.8: Sketch for $g(\zeta)$ against λ.

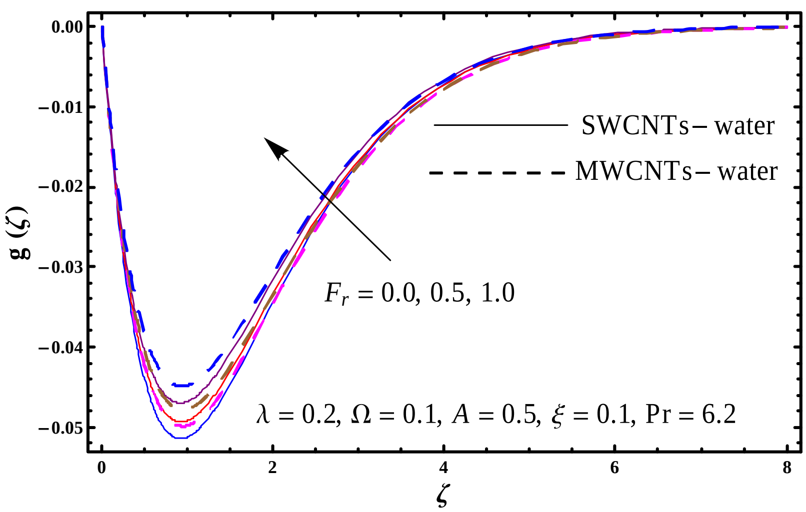

Fig. 3.9: Sketch for $g(\zeta)$ against F_r.

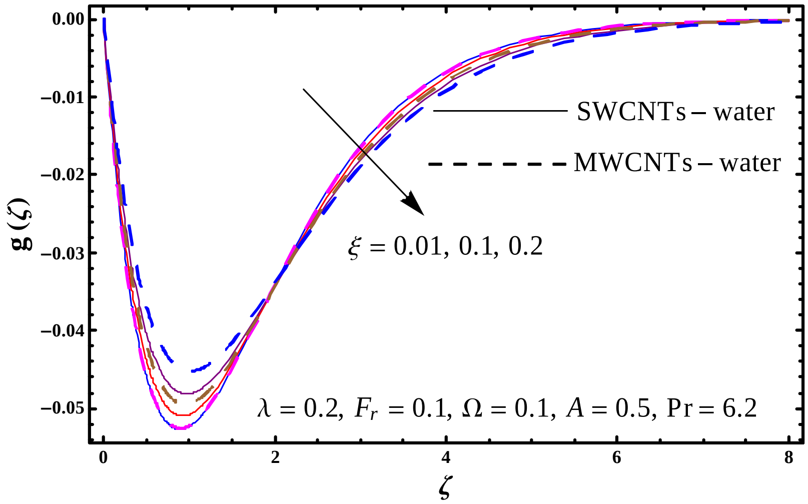

Fig. 3.10: Sketch for $g(\zeta)$ against ξ.

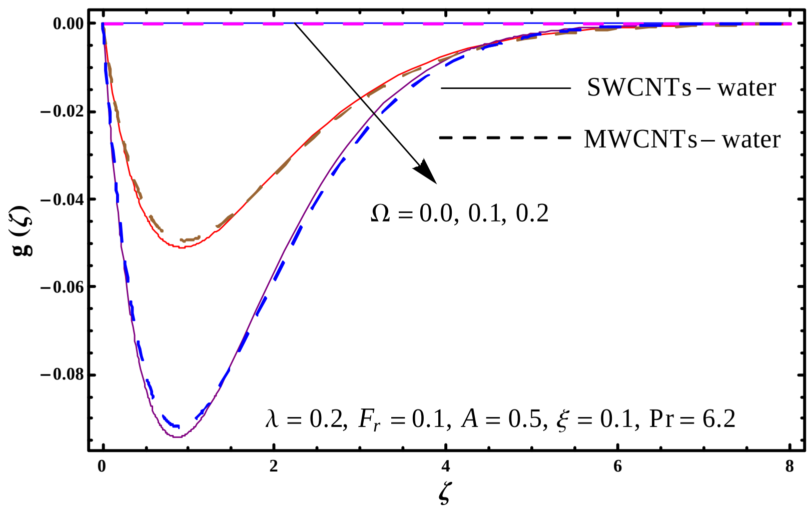

Fig. 3.11: Sketch for $g(\zeta)$ against Ω.

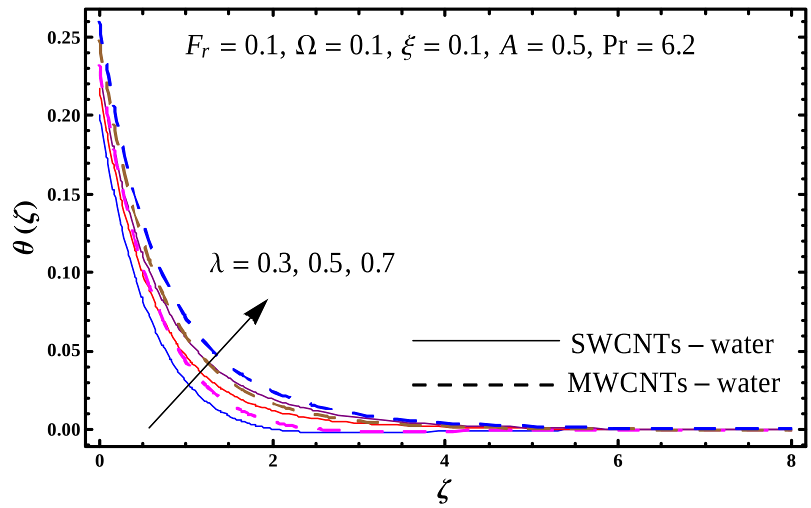

Fig. 3.12: Sketch for $\theta(\zeta)$ against λ.

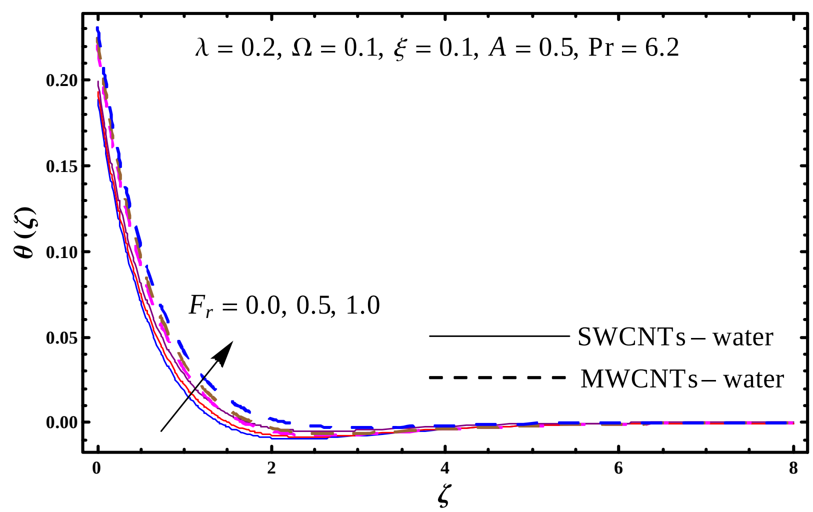

Fig. 3.13: Sketch for $\theta(\zeta)$ against F_r.

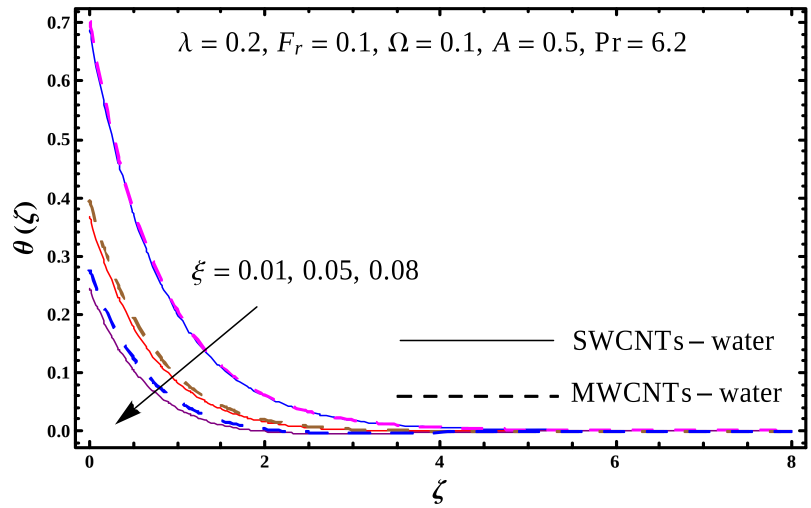

Fig. 3.14: Sketch for $\theta(\zeta)$ against ξ.

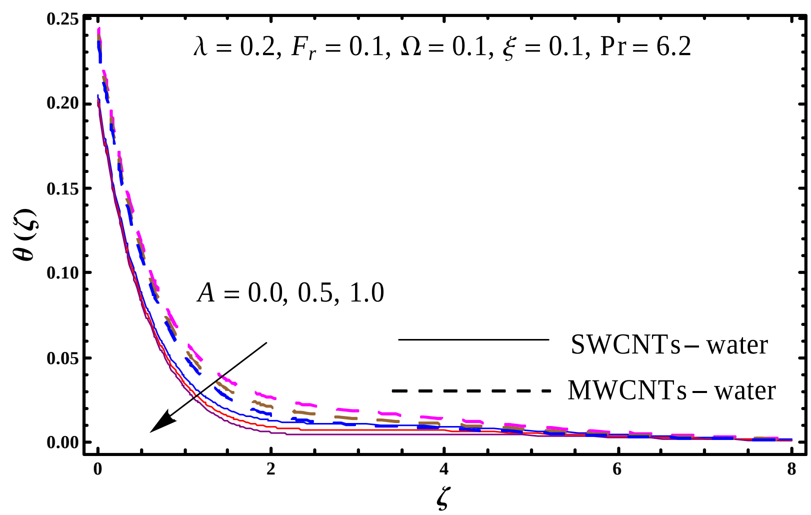

Fig. 3.15: Sketch for $\theta(\zeta)$ against A.

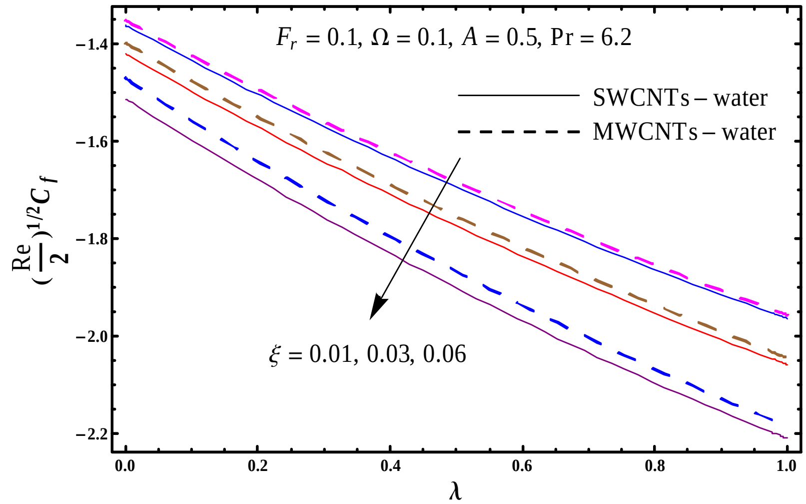

Fig. 3.16: Sketch for $\left(\frac{\mathrm{Re}}{2}\right)^{1/2} C_f$ against ξ and λ.

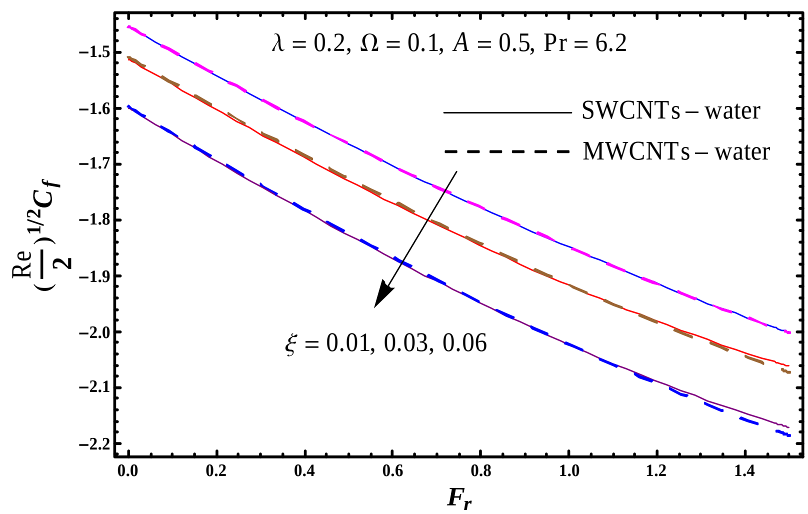

Fig. 3.17: Sketch of $\left(\frac{\mathrm{Re}}{2}\right)^{1/2} C_f$ against ξ and F_r.

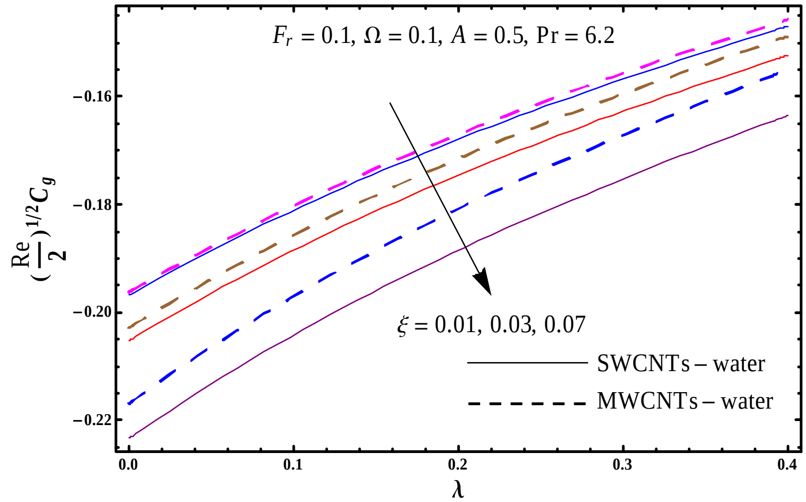

Fig. 3.18: Sketch of $\left(\frac{\mathrm{Re}}{2}\right)^{1/2} C_g$ against ξ and λ.

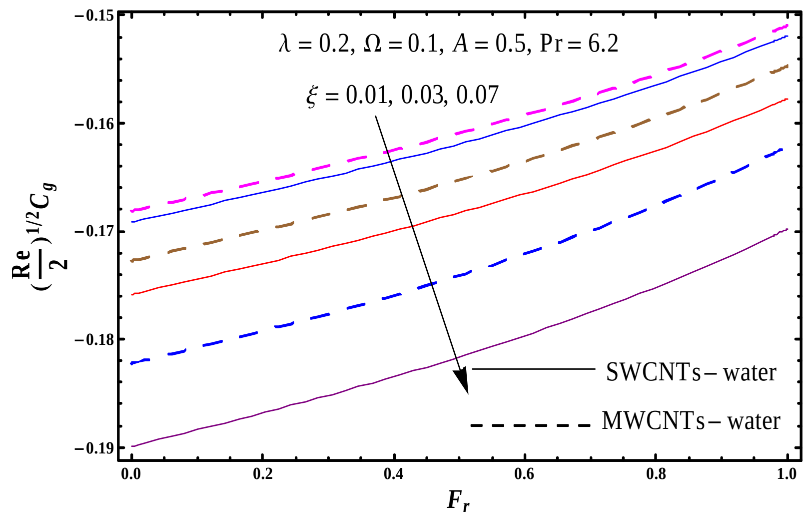

Fig. 3.19: Sketch of $\left(\frac{\mathrm{Re}}{2}\right)^{1/2} C_g$ against ξ and F_r.

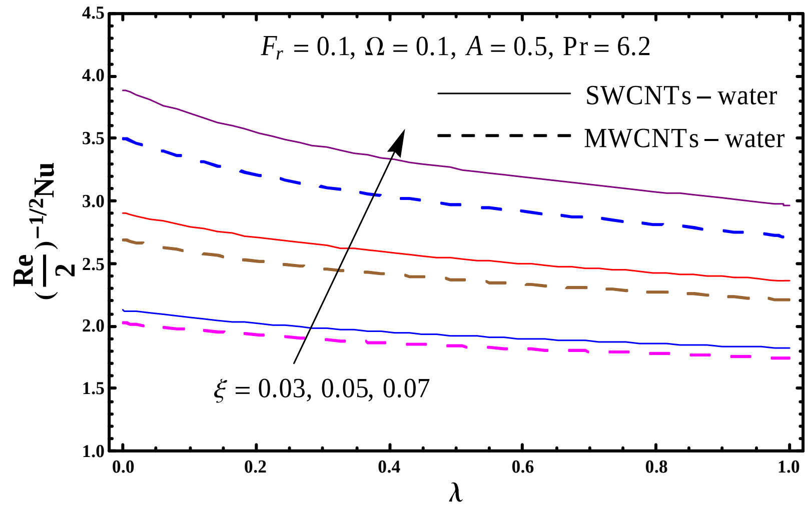

Fig. 3.20: Plot for $\left(\frac{\text{Re}}{2}\right)^{-1/2} Nu$ against ξ and λ.

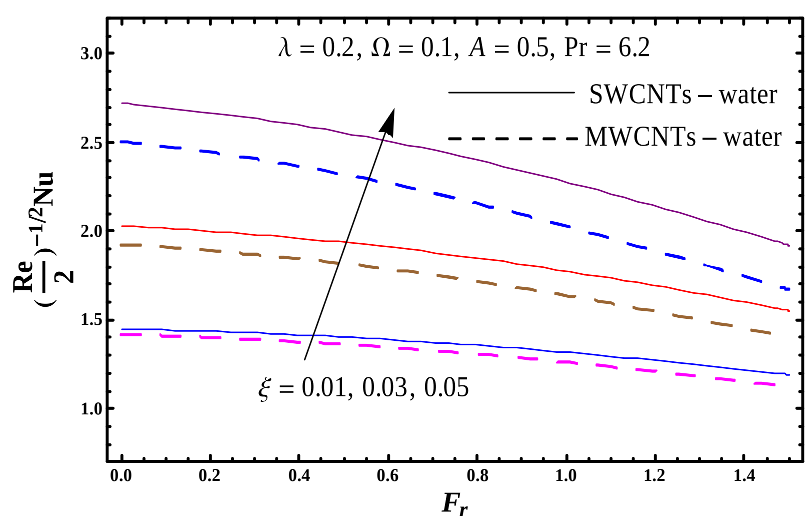

Fig. 3.21: Plot for $\left(\frac{\text{Re}}{2}\right)^{-1/2} Nu$ against ξ and F_r.

Table 3.4: Comparative values of $\left(\frac{\text{Re}}{2}\right)^{1/2} C_f$ and $\left(\frac{\text{Re}}{2}\right)^{1/2} C_g$ against distinct values of Ω when $\lambda = F_r = \xi = 0$.

Ω	$-\left(\frac{\text{Re}}{2}\right)^{1/2} C_f$			$-\left(\frac{\text{Re}}{2}\right)^{1/2} C_g$		
	Keller-box [12]	Shooting [12]	OHAM	Keller-box [12]	Shooting [12]	OHAM
0.0	1	1	1.28170	0	0	0
0.2	1.34742	1.34744	1.34632	0.37023	0.37020	0.36973
0.5	1.51941	1.51943	1.51852	0.76254	0.76252	0.76093
1.0	1.80251	1.80254	1.78883	1.21793	1.21793	1.19724

Chapter 4

Irreversibility analysis of carbon nanotubes subject to rotating frame

This chapter interprets the chemically reactive rotating flow of water-based carbon nanotubes. Homogeneous-heterogeneous reactions are considered. Heat transport is studied in presence of heat generation/absorption and viscous dissipation. Flow in porous space is investigated through nonlinear Darcy-Forchheimer relation. Carbon nanotubes of two types (namely single wall SWCNTs and multi wall MWCNTs) are utilized. Optimal solutions are derived by Optimal homotopy analysis method (OHAM). Roles of sundry parameters on flow fields, physical quantities and entropy generation rate are interpreted. It is witnessed that rate of entropy generation increases through homogeneous and heterogeneous reaction parameters.

4.1 Model development

Here rotating flow of carbon nanotubes dispersed in water past an exponentially stretched surface is considered. Homogeneous-heterogeneous reactions and viscous dissipation are accounted. Darcy-Forchheimer expression is employed to specify the porous space. Cartesian coordinate frame is chosen such that flow is in $z-$direction and the surface is stretched in $x-$direction. The viscous fluid filling half space $z > 0$ rotates uniformly with constant angular velocity ω

(see Fig. 4.1). Let $u_w(s) = u_0 e^{x/L}$ denotes the stretching velocity.

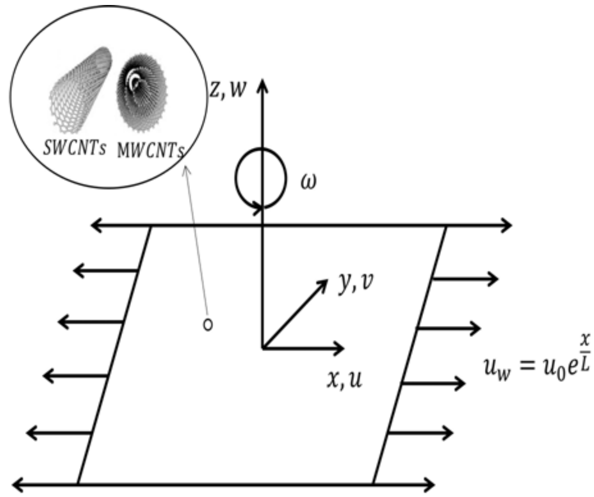

Fig. 4.1: Flow configuration.

In cubic autocatalysis, the characteristics of homogeneous reaction is defined as

$$C_1 + 2C_2 \rightarrow 3C_2, \quad rate = k_c c_1 c_2^2.$$

The first-order isothermal reaction at catalyst surface is

$$C_1 \rightarrow C_2, \quad rate = k_s c_1,$$

Resulting equations are

$$\frac{\partial u}{\partial x} + \frac{\partial v}{\partial y} + \frac{\partial w}{\partial z} = 0, \tag{4.1}$$

$$u\frac{\partial u}{\partial x} + v\frac{\partial u}{\partial y} + w\frac{\partial u}{\partial z} - 2\omega v = \nu_{nf}\frac{\partial^2 u}{\partial z^2} - \frac{\nu_{nf}}{K^*}u - Fu\sqrt{u^2 + v^2}, \tag{4.2}$$

$$u\frac{\partial v}{\partial x} + v\frac{\partial v}{\partial y} + w\frac{\partial v}{\partial z} - 2\omega u = \nu_{nf}\frac{\partial^2 v}{\partial z^2} - \frac{\nu_{nf}}{K^*}v - Fv\sqrt{u^2 + v^2}, \tag{4.3}$$

$$u\frac{\partial T}{\partial x} + v\frac{\partial T}{\partial y} + w\frac{\partial T}{\partial z} = \alpha_{nf}\frac{\partial^2 T}{\partial z^2} + \frac{Q}{(\rho c_p)_{nf}}(T - T_\infty) + \frac{\mu_{nf}}{(\rho c_p)_{nf}}\left(\left(\frac{\partial u}{\partial z}\right)^2 + \left(\frac{\partial v}{\partial z}\right)^2\right), \tag{4.4}$$

$$u\frac{\partial c_1}{\partial x} + v\frac{\partial c_1}{\partial y} + w\frac{\partial c_1}{\partial z} = \breve{D}_{C_1}\frac{\partial^2 c_1}{\partial z^2} - k_c c_1 c_2^2, \tag{4.5}$$

$$u\frac{\partial c_2}{\partial x}+v\frac{\partial c_2}{\partial y}+w\frac{\partial c_2}{\partial z}=\breve{D}_{C_2}\frac{\partial^2 c_2}{\partial z^2}+k_c c_1 c_2^2, \tag{4.6}$$

$$u=u_w=u_0e^{x/L},\ v=w=0,\ T=T_w=T_\infty+T_0e^{\frac{Ax}{2L}},\ \breve{D}_{C_1}\frac{\partial c_1}{\partial z}=k_sc_1,\ \breve{D}_{C_2}\frac{\partial c_2}{\partial z}=-k_sc_1 \text{ at } z=0, \tag{4.7}$$

$$u\to 0,\ v\to 0,\ T\to T_\infty,\ c_1\to c_0e^{Bx/2L},\ c_2\to 0 \text{ as } z\to\infty. \tag{4.8}$$

By Xue model [45] we have

$$\left.\begin{aligned}&\mu_{nf}=\tfrac{\mu_f}{(1-\xi)^{2.5}},\ \nu_{nf}=\tfrac{\mu_{nf}}{\rho_{nf}},\ \alpha_{nf}=\tfrac{k_{nf}}{(\rho c_p)_{nf}},\ \rho_{nf}=\rho_f(1-\xi)+\rho_{CNT}\xi,\\ &(\rho c_p)_{nf}=(\rho c_p)_f(1-\xi)+(\rho c_p)_{CNT}\xi,\ \tfrac{k_{nf}}{k_f}=\frac{(1-\xi)+2\xi\frac{k_{CNT}}{k_{CNT}-k_f}\ln\frac{k_{CNT}+k_f}{2k_f}}{(1-\xi)+2\xi\frac{k_f}{k_{CNT}-k_f}\ln\frac{k_{CNT}+k_f}{2k_f}}.\end{aligned}\right\} \tag{4.9}$$

Table 4.1: Thermophysical characteristics [45].

Physical characteristics	Base fluid	Nanoparticles	
	Water	SWCNTs	MWCNTs
$\rho\left(kg/m^3\right)$	997.1	2600	1600
$k\,(W/mK)$	0.613	6600	3000
$c_p\,(J/kgK)$	4179	425	796

Selecting

$$\begin{aligned}&u=u_0e^{\frac{x}{L}}\tfrac{\partial f(\eta,\zeta)}{\partial\zeta},\ v=u_0e^{\frac{x}{L}}g(\eta,\zeta),\ w=-\sqrt{\tfrac{\nu_fu_0}{2L}}e^{\frac{x}{2L}}\left(f+\zeta\tfrac{\partial f}{\partial\zeta}+2\eta\tfrac{\partial f}{\partial\eta}\right),\ \eta=e^{x/L},\\ &T=T_\infty+T_0e^{Ax/2L}\theta(\eta,\zeta),c_1=c_0e^{Bx/2L}\phi(\eta,\zeta),\ c_2=c_0e^{Bx/2L}h(\eta,\zeta),\ \zeta=z\left(\tfrac{u_0}{2\nu_fL}\right)^{1/2}e^{\frac{x}{2L}}.\end{aligned} \tag{4.10}$$

we have

$$\begin{aligned}&\frac{1}{(1-\xi)^{2.5}\left(1-\xi+\frac{\rho_{CNT}}{\rho_f}\xi\right)}\left(\frac{\partial^3 f}{\partial\zeta^3}-2\frac{\lambda}{\eta}\frac{\partial f}{\partial\zeta}\right)+f\frac{\partial^2 f}{\partial\zeta^2}+4\frac{\Omega}{\eta}g-2\left(\frac{\partial f}{\partial\zeta}\right)^2-\\ &2F_r\left(\left(\frac{\partial f}{\partial\zeta}\right)^2+\frac{1}{2}g^2\right)=2\eta\left(\frac{\partial f}{\partial\zeta}\frac{\partial^2 f}{\partial\zeta\partial\eta}-\frac{\partial f}{\partial\eta}\frac{\partial^2 f}{\partial\zeta^2}\right),\end{aligned} \tag{4.11}$$

$$\begin{aligned}&\frac{1}{(1-\xi)^{2.5}\left(1-\xi+\frac{\rho_{CNT}}{\rho_f}\xi\right)}\left(\frac{\partial^2 g}{\partial\zeta^2}-2\frac{\lambda}{\eta}g\right)+f\frac{\partial g}{\partial\zeta}-2\frac{\partial f}{\partial\zeta}g-4\frac{\Omega}{\eta}\frac{\partial f}{\partial\zeta}-\\ &2F_r\left(g^2+\frac{1}{2}\left(\frac{\partial f}{\partial\zeta}\right)^2\right)=2\eta\left(\frac{\partial f}{\partial\zeta}\frac{\partial g}{\partial\eta}-\frac{\partial f}{\partial\eta}\frac{\partial g}{\partial\zeta}\right),\end{aligned} \tag{4.12}$$

$$\frac{1}{\left(1-\xi+\frac{(\rho c_p)_{CNT}}{(\rho c_p)_f}\xi\right)}\frac{k_{nf}}{k_f}\left(\frac{\partial^2\theta}{\partial\zeta^2}+2\Pr Q^*\theta+\frac{2\eta^{2-\frac{A}{2}}Br}{(1-\xi)^{2.5}}\left(\left(\frac{\partial^2 f}{\partial\zeta^2}\right)^2+\left(\frac{\partial g}{\partial\zeta}\right)^2\right)\right)+\Pr f\frac{\partial\theta}{\partial\zeta}- \\ \Pr A\theta\frac{\partial f}{\partial\zeta}=2\Pr\eta\left(\frac{\partial f}{\partial\eta}\frac{\partial\theta}{\partial\zeta}-\frac{\partial\theta}{\partial\eta}\frac{\partial f}{\partial\zeta}\right), \tag{4.13}$$

$$\frac{1}{Sc}\frac{\partial^2\phi}{\partial\zeta^2}+f\frac{\partial\phi}{\partial\zeta}-B\frac{\partial f}{\partial\zeta}\phi-2\frac{\hat{K}}{\eta^{1-B}}\phi h^2=2\eta\left(\frac{\partial f}{\partial\zeta}\frac{\partial\phi}{\partial\eta}-\frac{\partial f}{\partial\eta}\frac{\partial\phi}{\partial\zeta}\right), \tag{4.14}$$

$$\frac{\Psi}{Sc}\frac{\partial^2 h}{\partial\zeta^2}+f\frac{\partial h}{\partial\zeta}-B\frac{\partial f}{\partial\zeta}h+2\frac{\hat{K}}{\eta^{1-B}}\phi h^2=2\eta\left(\frac{\partial f}{\partial\zeta}\frac{\partial h}{\partial\eta}-\frac{\partial f}{\partial\eta}\frac{\partial h}{\partial\zeta}\right), \tag{4.15}$$

$$f(\eta,0)=-2\eta\frac{\partial f(\eta,0)}{\partial\eta},\ \frac{\partial f(\eta,0)}{\partial\zeta}=1,\ g(\eta,0)=0,\ \theta(\eta,0)=1, \\ \frac{\partial\phi(\eta,0)}{\partial\zeta}=\frac{\hat{K}_s}{\sqrt{\eta}}\phi(\eta,0),\ \frac{\partial h(\eta,0)}{\partial\zeta}=-\Psi\frac{\hat{K}_s}{\sqrt{\eta}}\phi(\eta,0), \tag{4.16}$$

$$\frac{\partial f(\eta,\infty)}{\partial\zeta}\to 0,\ g(\eta,\infty)\to 0,\ \theta(\eta,\infty)\to 0,\ \phi(\eta,\infty)\to 1,\ h(\eta,\infty)\to 0, \tag{4.17}$$

Here equation (4.1) is trivially justified. Considering same diffusion coefficients of chemical species C_1 and C_2 i.e. $\breve{D}_{C_1}=\breve{D}_{C_2}$ (or $\check{\delta}=1$) and thus

$$h+\phi=1, \tag{4.18}$$

From Eqs. (4.14) and (4.15), we have

$$\frac{1}{Sc}\frac{\partial^2\phi}{\partial\zeta^2}+f\frac{\partial\phi}{\partial\zeta}+B\frac{\partial f}{\partial\zeta}(1-\phi)-2\frac{\hat{K}}{\eta^{1-B}}\phi(1-\phi)^2=2\eta\left(\frac{\partial f}{\partial\zeta}\frac{\partial\phi}{\partial\eta}-\frac{\partial f}{\partial\eta}\frac{\partial\phi}{\partial\zeta}\right), \tag{4.19}$$

with boundary condition

$$\frac{\partial\phi(\eta,0)}{\partial\zeta}=\hat{K}_s\phi(\eta,0),\ \phi(\eta,\infty)\to 1. \tag{4.20}$$

We define

$$\lambda=\frac{\nu_f L}{K^* u_0},\ \Omega=\frac{\omega L}{u_0},\ F_r=\frac{C_b}{K^{*1/2}}L,\ Q^*=\frac{Q_0}{(\rho c_p)_f}\frac{L}{u_0},\ \hat{K}=\frac{k_c c_0^2 L}{u_0}, \\ Ec=\frac{u_0^2}{T_0(c_p)_f},\ \hat{K}_s=\left(\frac{2\nu_f L}{u_0}\right)^{1/2}\frac{k_s}{\breve{D}_{C_1}},\ \Psi=\frac{\breve{D}_{C_1}}{\breve{D}_{C_2}},\ \Pr=\frac{\nu_f}{\alpha_f},\ Sc=\frac{\nu_f}{\breve{D}_{C_1}}. \tag{4.21}$$

4.1.1 First order of truncation

In first order of truncation, the terms including $\frac{\partial(.)}{\partial\eta}$ are assumed to be very small and may be approximated by zero. We have

$$\frac{1}{(1-\xi)^{2.5}\left(1-\xi+\frac{\rho_{\breve{p}}}{\rho_f}\xi\right)}\left(f'''-2\frac{\lambda}{\eta}f'\right)-2f'^2+ff''+4\frac{\Omega}{\eta}g-2F_r\left(f'^2+\frac{1}{2}g^2\right)=0, \quad (4.22)$$

$$\frac{1}{(1-\xi)^{2.5}\left(1-\xi+\frac{\rho_{\breve{p}}}{\rho_f}\xi\right)}\left(g''-2\frac{\lambda}{\eta}g\right)-2f'g+fg'-4\frac{\Omega}{\eta}f'-2F_r\left(g^2+\frac{1}{2}f'^2\right)=0, \quad (4.23)$$

$$\frac{1}{\left(1-\xi+\frac{(\rho c_p)_{\breve{p}}}{(\rho c_p)_f}\xi\right)}\left(\frac{k_{nf}}{k_f}\theta''+\frac{2}{\eta}Q^*\Pr\theta+2\eta^{2-\frac{A}{2}}\frac{Br}{(1-\xi)^{2.5}}\left(f''^2+g'^2\right)\right)+\Pr f\theta'-\Pr A\theta f'=0, \quad (4.24)$$

$$\frac{1}{Sc}\phi''+f\phi'+Bf'(1-\phi)-2\frac{\hat{K}}{\eta^{1-B}}\phi(1-\phi)^2=0, \quad (4.25)$$

$$f(\eta,0)=0,\ f'(\eta,0)=1,\ g(\eta,0)=0,\ \theta(\eta,0)=1,\ \phi'(\eta,0)=\frac{\hat{K}_s}{\sqrt{\eta}}\phi(\eta,0), \quad (4.26)$$

$$f'(\eta,\infty)\to 0,\ g(\eta,\infty)\to 0,\ \theta(\eta,\infty)\to 0,\ \phi(\eta,\infty)\to 1. \quad (4.27)$$

4.1.2 Second order of truncation

For non-similarity solutions of Eqs. $(4.11)-(4.20)$, one may express that

$$f^*=\frac{\partial f}{\partial\eta},\ g^*=\frac{\partial g}{\partial\eta},\ \theta^*=\frac{\partial\theta}{\partial\eta},\ \phi^*=\frac{\partial\phi}{\partial\eta}\text{ and }\frac{\partial f^*}{\partial\eta}=\frac{\partial g^*}{\partial\eta}=\frac{\partial\theta^*}{\partial\eta}=\frac{\partial\phi^*}{\partial\eta}=0. \quad (4.28)$$

Taking partial derivatives of Eqs. $(4.11)-(4.20)$ with respect to η, we obtain

$$\begin{aligned}&\frac{1}{(1-\xi)^{2.5}\left(1-\xi+\frac{\rho_{\breve{p}}}{\rho_f}\xi\right)}\left(f^{*\prime\prime\prime}-2\frac{\lambda}{\eta}f^{*\prime}+2\frac{\lambda}{\eta^2}f'\right)-4f'f^{*\prime}+ff^{*\prime\prime}+f^*f''-\\&4\frac{\Omega}{\eta}g^*-4\frac{\Omega}{\eta^2}g-2F_r\left(f'f^{*\prime}+gg^*\right)=2\left(f'f^{*\prime}-f^*f''\right)+2\eta\left(f^{*\prime 2}-f^*f^{*\prime\prime}\right),\end{aligned} \quad (4.29)$$

$$\begin{aligned}&\frac{1}{(1-\xi)^{2.5}\left(1-\xi+\frac{\rho_{\breve{p}}}{\rho_f}\xi\right)}\left(g^{*\prime\prime}-2\frac{\lambda}{\eta}g^*+2\frac{\lambda}{\eta^2}g\right)-2f'g^*-2gf^{*\prime}+f^*g'+fg^{*\prime\prime}-\\&4\frac{\Omega}{\eta^2}f'-4\frac{\Omega}{\eta}f^{*\prime}-2F_r\left(2gg^*+f'f^{*\prime}\right)=2\left(f^*g'-g^*f'\right)+2\eta\left(f^*g^{*\prime}-f^{*\prime}g^*\right),\end{aligned} \quad (4.30)$$

$$\frac{1}{\left(1-\xi+\frac{(\rho c_p)_{\breve{p}}}{(\rho c_p)_f}\xi\right)}\left(\begin{array}{c}\frac{k_{nf}}{k_f}\theta^{*\prime\prime}-\frac{2}{\eta^2}\Pr Q^*\theta+\frac{2}{\eta}\Pr Q^*\theta^*+2\left(2-\frac{A}{2}\right)\frac{\eta^{1-\frac{A}{2}}Br}{(1-\xi)^{2.5}}\left(f''^2+g'^2\right)+\\ \frac{2\eta^{2-\frac{A}{2}}Br}{(1-\xi)^{2.5}}\left(2f''f^{*\prime\prime}+2g'g^{*\prime}\right)\end{array}\right)$$

$$\Pr f^*\theta'+\Pr f\theta^{*\prime}-\Pr A\theta^* f'-\Pr A\theta f^{*\prime}=2\Pr\left(f^*\theta'-\theta^* f'\right)+2\eta\Pr\left(f^*\theta^{*\prime}-\theta^* f^{*\prime}\right), \tag{4.31}$$

$$\begin{array}{c}\frac{1}{Sc}\phi^{*\prime\prime}+f\phi^{*\prime}+f^*\phi'-2\frac{\hat{K}}{\eta^{1-B}}\left(\phi^*+3\phi^2\phi^*-4\phi\phi^*-\frac{1-B}{\eta}\phi\left(1-\phi^2\right)\right)+\\ Bf^{*\prime}(1-\phi)-Bf'\phi^{*\prime}=2\left(f^*\phi'-\phi^* f'\right)+2\eta\left(f^*\phi^{*\prime}-\phi^* f^{*\prime}\right),\end{array} \tag{4.32}$$

$$f^*(\eta,0)=0,\ f^{*\prime}(\eta,0)=0,\ g^*(\eta,0)=0,\ \theta^*(\eta,0)=0,\ \phi^{*\prime}(\eta,0)=-\frac{1}{2}\frac{\hat{K}_s}{\eta^{3/2}}\phi(\eta,0)+\frac{\hat{K}_s}{\eta^{1/2}}\phi^*(\eta,0), \tag{4.33}$$

$$f^{*\prime}(\eta,\infty)\to 0,\ g^*(\eta,\infty)\to 0,\ \theta^*(\eta,\infty)\to 0,\ \phi^*(\eta,\infty)\to 0, \tag{4.34}$$

in which η is the constant prescribed variable at any streamwise location.

4.2 Entropy generation

Entropy generation for considered flow problem is

$$\begin{array}{c}S'''_{gen}=\underbrace{\frac{k_{nf}}{T_m^2}\left(\frac{\partial T}{\partial z}\right)^2}_{Heat\ transfer\ irreversibility}+\underbrace{\frac{\mu_{nf}}{T_m}\left(\left(\frac{\partial u}{\partial z}\right)^2+\left(\frac{\partial v}{\partial z}\right)^2\right)}_{Viscous\ dissipation\ irreversibility}+\\ \underbrace{\frac{Q}{T_m}(T-T_\infty)}_{Heat\ generation/absorption\ irreversibility}+\\ \underbrace{\frac{\breve{R}\breve{D}_{C_1}}{T_m}\left(\frac{\partial c_1}{\partial z}\frac{\partial T}{\partial z}\right)+\frac{\breve{R}\breve{D}_{C_1}}{c_1}\left(\frac{\partial c_1}{\partial z}\right)^2+\frac{\breve{R}\breve{D}_{C_2}}{T_m}\left(\frac{\partial c_2}{\partial z}\frac{\partial T}{\partial z}\right)+\frac{\breve{R}\breve{D}_{C_2}}{c_2}\left(\frac{\partial c_2}{\partial z}\right)^2}_{mass\ diffusion\ irreversibility\ of\ \hom ogeneous-heterogeneous\ reactions},\end{array} \tag{4.35}$$

Applying transformations (4.10), above equation reduces to

$$\begin{array}{c}N_g(\zeta)=\frac{k_{nf}}{k_f}\alpha_1\eta^{1+\frac{A}{2}}\theta'^2+\frac{Br\eta^{3-\frac{A}{2}}}{(1-\xi)^{2.5}}\left(f''^2+g'^2\right)+2Q^*\Pr\eta\theta+\eta^{1+\frac{B}{2}}\left(L_1-L_2\right)\theta'\phi'+\\ \frac{\phi'^2}{\alpha_1\eta^{\frac{A}{2}}}\left(\frac{L_1}{\phi}+\frac{L_2}{1-\phi}\right)\eta^{1+\frac{B}{2}},\end{array} \tag{4.36}$$

where

$$\alpha_1=\frac{T_0}{T_m},\ Br=Ec\Pr,\ L_1=\frac{\breve{R}\breve{D}_{C_1}c_0}{k_f},\ L_2=\frac{\breve{R}\breve{D}_{C_2}c_0}{k_f},\ N_g=\frac{2\nu_f L\alpha_1}{k_f u_0}S'''_{gen}. \tag{4.37}$$

4.3 Physical quantities

Expressions of skin friction coefficients and local Nusselt number satisfy

$$\left.\begin{aligned} \left(\tfrac{\mathrm{Re}}{2}\right)^{1/2} C_f &= \tfrac{1}{\sqrt{\eta}} \tfrac{1}{(1-\xi)^{2.5}} f''(\eta,0)\,, \\ \left(\tfrac{\mathrm{Re}}{2}\right)^{1/2} C_g &= \tfrac{1}{\sqrt{\eta}} \tfrac{1}{(1-\xi)^{2.5}} g'(\eta,0)\,, \\ \left(\tfrac{\mathrm{Re}}{2}\right)^{-1/2} Nu &= -\tfrac{k_{nf}}{k_f} \sqrt{\eta} \ln \eta \theta'(\eta,0)\,, \end{aligned}\right\} \tag{4.38}$$

in which $\mathrm{Re}_x = \frac{u_0 L}{\nu_f}$ depicts local Reynolds number.

4.4 OHAM solutions

It is found that a nonlinear system is involved in formulation. OHAM employed for computations. For that

$$f_0(\zeta) = 1 - e^{-\zeta}, \quad g_0(\zeta) = 0, \quad \theta_0(\zeta) = e^{-\zeta}, \quad \phi_0(\zeta) = 1 - \frac{1}{2} e^{-\frac{\hat{K}_s}{\sqrt{\eta}}\zeta}, \tag{4.39}$$

$$\mathcal{L}_f = \frac{d^3 f}{d\zeta^3} - \frac{df}{d\zeta}, \quad \mathcal{L}_g = \frac{d^2 g}{d\zeta^2} - g, \quad \mathcal{L}_\theta = \frac{d^2\theta}{d\zeta^2} - \theta, \quad \mathcal{L}_\phi = \frac{d^2\phi}{d\zeta^2} - \phi, \tag{4.40}$$

with

$$\begin{gathered} \mathcal{L}_f\left[\breve{J}_1^* + \breve{J}_2^* e^{\zeta} + \breve{J}_3^* e^{-\zeta}\right] = 0,\ \mathcal{L}_g\left[\breve{J}_4^* e^{\zeta} + \breve{J}_5^* e^{-\zeta}\right] = 0, \\ \mathcal{L}_\theta\left[\breve{J}_6^* e^{\zeta} + \breve{J}_7^* e^{-\zeta}\right] = 0,\ \mathcal{L}_\phi\left[\breve{J}_8^* e^{\zeta} + \breve{J}_9^* e^{-\zeta}\right] = 0. \end{gathered} \tag{4.41}$$

4.5 Solutions convergence

BVPh2.0 is utilized for the solutions. The solutions consists of $\hbar_f$, $\hbar_g$, $\hbar_\theta$ and $\hbar_\phi$. Optimal data of $\hbar_f$, $\hbar_g$, $\hbar_\theta$ and $\hbar_\phi$ can be determined by taking minimum error. For saving CPU time, average squared residual error has been computed at mth-order of deformation i.e.

$$\varepsilon_m^f = \frac{1}{\breve{k}+1} \sum_{j=0}^{\breve{k}} \left[\mathcal{N}_f \left(\sum_{i=0}^{m} f(\zeta), \sum_{i=0}^{m} g(\zeta) \right)_{\zeta = j\delta\zeta} \right]^2, \tag{4.42}$$

$$\varepsilon_m^g = \frac{1}{\breve{k}+1} \sum_{j=0}^{\breve{k}} \left[\mathcal{N}_g \left(\sum_{i=0}^{m} f(\zeta), \sum_{i=0}^{m} g(\zeta) \right)_{\zeta = j\delta\zeta} \right]^2, \tag{4.43}$$

$$\varepsilon_m^\theta = \frac{1}{\breve{k}+1}\sum_{j=0}^{\breve{k}}\left[\mathcal{N}_\theta\left(\sum_{i=0}^{m} f(\zeta), \sum_{i=0}^{m} g(\zeta), \sum_{i=0}^{m}\theta(\zeta)\right)_{\zeta=j\delta\zeta}\right]^2, \tag{4.44}$$

$$\varepsilon_m^\phi = \frac{1}{\breve{k}+1}\sum_{j=0}^{\breve{k}}\left[\mathcal{N}_\phi\left(\sum_{i=0}^{m} f(\zeta), \sum_{i=0}^{m}\phi(\zeta)\right)_{\zeta=j\delta\zeta}\right]^2, \tag{4.45}$$

$$\varepsilon_m^t = \varepsilon_m^f + \varepsilon_m^g + \varepsilon_m^\theta + \varepsilon_m^\phi. \tag{4.46}$$

The optimal values of convergence control variables at 2nd order of deformation for SWCNTs and MWCNTs yield $\hbar_f = -0.255005$, $\hbar_g = -0.288118$, $\hbar_\theta = -0.406414$, $\hbar_\phi = -2.02207$ and $\hbar_f = -0.242898$, $\hbar_g = -0.277511$, $\hbar_\theta = -0.434528$, $\hbar_\phi = -2.03455$ respectively. The total averaged squared residual error in SWCNTs and MWCNTs cases are $\varepsilon_m^t = 0.16$ and $\varepsilon_m^t = 0.16$ respectively. Total residual errors in SWCNTs and MWCNTs case are illustrated in Figs. 4.2 and 4.3. Numerical values of individual average squared residual error at 2nd order of deformation for SWCNTs and MWCNTs cases are deliberated in Tables 4.2 and 4.3. Clearly average squared residual error decreases for higher order deformations.

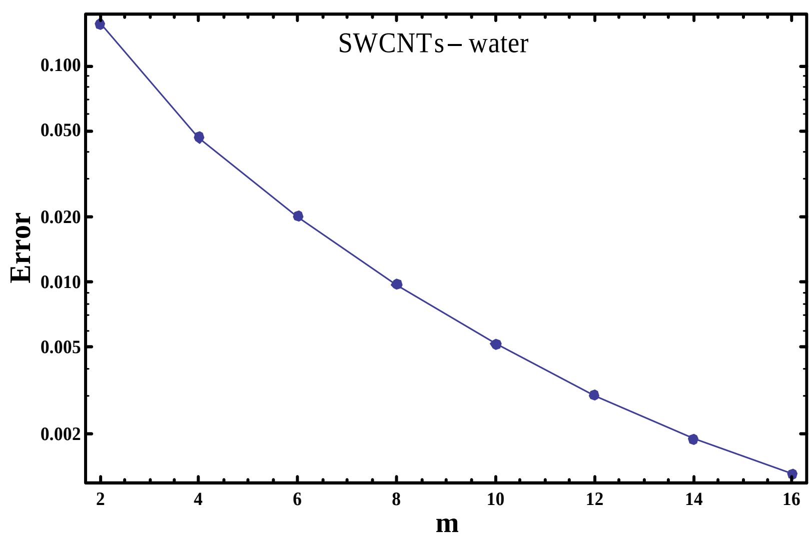

Fig. 4.2: Total residual error for SWCNTs-water.

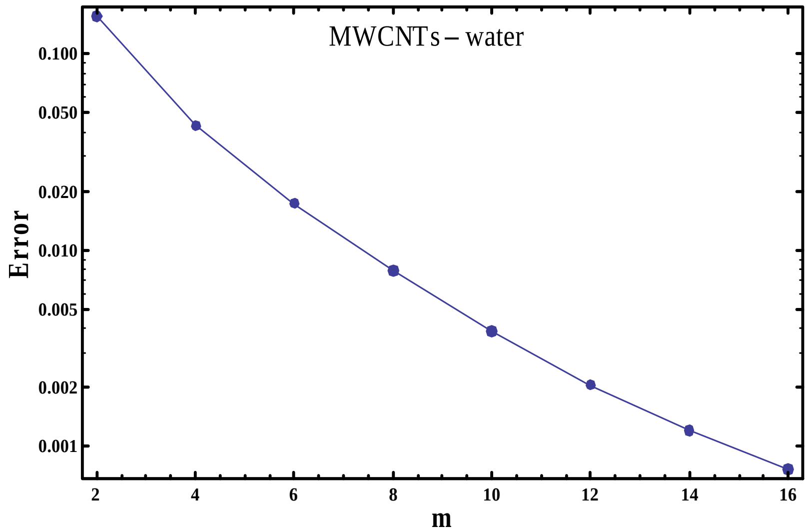

Fig. 4.3: Total residual error for MWCNTs-water.

Table 4.2: Optimal convergence control parameters and total average squared residual errors in SWCNTs case.

m	ε_m^f	ε_m^g	ε_m^θ	ε_m^ϕ
2	5.17×10^{-2}	4.43×10^{-3}	0.10×10^{-1}	1.49×10^{-4}
6	5.06×10^{-3}	3.23×10^{-4}	1.58×10^{-2}	6.22×10^{-5}
10	8.02×10^{-4}	4.62×10^{-4}	4.61×10^{-3}	4.28×10^{-5}
14	2.42×10^{-4}	1.19×10^{-5}	1.71×10^{-3}	3.53×10^{-5}
16	1.60×10^{-4}	7.29×10^{-6}	1.17×10^{-3}	3.31×10^{-5}

Table 4.3: Optimal convergence control parameters and total average squared residual errors in MWCNTs case.

m	ε_m^f	ε_m^g	ε_m^θ	ε_m^ϕ
2	4.89×10^{-2}	4.23×10^{-3}	1.06×10^{-1}	1.56×10^{-4}
6	4.57×10^{-3}	2.99×10^{-4}	1.35×10^{-2}	6.84×10^{-5}
10	7.37×10^{-4}	4.48×10^{-5}	3.29×10^{-3}	4.88×10^{-5}
14	2.34×10^{-4}	1.35×10^{-5}	9.83×10^{-4}	4.13×10^{-5}
16	1.57×10^{-4}	8.56×10^{-6}	6.04×10^{-4}	3.92×10^{-5}

4.6 Discussion

This section inspects the behavior of velocities $f'(\zeta)$, $g(\zeta)$, temperature $\theta(\zeta)$ and concentration $\phi(\zeta)$ fields for emerging flow variables. Characteristics of (ξ) on $f'(\zeta)$ is captured in Fig. 4.4. Here $f'(\zeta)$ enhances through (ξ) in both SWCNTs and MWCNTs. Fig. 4.5 sketches (Ω) effect for $f'(\zeta)$. Higher (Ω) give rise to an augmentation in $f'(\zeta)$ regarding SWCNTs and MWCNTs. From Figs. 4.6 and 4.7, it is recognized that $f'(\zeta)$ decreases for larger (λ) and (F_r) in SWCNTs and MWCNTs cases. Fig. 4.8 elaborates consequences of (ξ) on velocity $g(\zeta)$. Here $g(\zeta)$ decays for higher estimation of (ξ) in SWCNTs and MWCNTs situations. By increasing (Ω), an enhancement in $g(\zeta)$ is noticed in SWCNTs and MWCNTs situations (see Fig. 4.9). Velocity $g(\zeta)$ against (λ) is shown in Fig. 4.10. Larger (λ) indicates decrease in $g(\zeta)$ for both cases of SWCNTs and MWCNTs. Aspects of (F_r) on $g(\zeta)$ is elaborated in Fig. 4.11. $g(\zeta)$ depict decreasing trend for higher (F_r) in SWCNTs and MWCNTs situations. From Figs. 4.12 and 4.13, it is recognized that larger (ξ) and (Ω) show an enhancement in temperature $\theta(\zeta)$ in SWCNTs and MWCNTs. Fig. 4.14 depicts the behavior of $\theta(\zeta)$ against (λ). Here $\theta(\zeta)$ enhances against (λ) in SWCNTs and MWCNTs cases. Fig. 4.15 indicates that how $\theta(\zeta)$ gets affected with change in (F_r). Higher values of (F_r) yields $\theta(\zeta)$ enhancement and related layer thickness. Fig. 4.16 addresses temperature field $\theta(\zeta)$ for (Q^*). Here $(Q^* > 0)$ represents heat generation and $(Q^* < 0)$ for heat absorption. Clearly both $\theta(\zeta)$ and related layer thickness are increased for higher estimation of (Q^*) in SWCNTs and MWCNTs situations. Fig. 4.17 is portrayed for impact of (Br) on $\theta(\zeta)$. An augmentation in $\theta(\zeta)$ is noticed for higher (Br) in SWCNTs and MWCNTs. Fig. 4.18 elaborates the change in $\theta(\zeta)$ for distinct values of (A). Higher (A) yield weaker $\theta(\zeta)$ in SWCNTs and MWCNTs cases. Fig. 4.19 elucidates that $\phi(\zeta)$ is weaker for larger (ξ) in SWCNTs and MWCNTs situations. Fig. 4.20 characterized the consequences of (Ω) on concentration $\phi(\zeta)$. An increment in (Ω) shows enhancement in $\phi(\zeta)$ in SWCNTs and MWCNTs situations. Concentration field $\phi(\zeta)$ is reduced for larger (λ) and (F_r) in both SWCNTs and MWCNTs (see Figs. 4.21 and 4.22). Role of (Q^*) on concentration $\phi(\zeta)$ is presented in Fig. 4.23. Higher (Q^*) correspond to weaker $\phi(\zeta)$ in both SWCNTs and MWCNTs. Concentration $\phi(\zeta)$ via (B) is displayed in Fig. 4.24. Note that $\phi(\zeta)$ and associated layer thickness are increasing function of (B). Fig. 4.25 portrays variation of

$\left(\hat{K}\right)$ on concentrations $\phi(\zeta)$. It is noticed that $\phi(\zeta)$ reduces for higher $\left(\hat{K}\right)$ in both SWCNTs and MWCNTs. Fig. 4.26 addressed concentration $\phi(\zeta)$ for $\left(\hat{K}_s\right)$. Higher $\left(\hat{K}_s\right)$ give rise to stronger $\phi(\zeta)$ in SWCNTs and MWCNTs. Fig. 4.27 illustrates that concentration $\phi(\zeta)$ is higher for larger (Sc) in SWCNTs and MWCNTs cases. Curves of $N_g(\zeta)$ against (Q^*) is displayed in Fig. 4.28. $N_g(\zeta)$ enhances against (Q^*) in both SWCNTs and MWCNTs cases. Aspects of $N_g(\zeta)$ through $\left(\hat{K}\right)$ and $\left(\hat{K}_s\right)$ are portrayed in Figs. 4.29 and 4.30. Similar trend of $N_g(\zeta)$ is observed through $\left(\hat{K}\right)$ and $\left(\hat{K}_s\right)$ in both SWCNTs and MWCNTs case. Impact for (Br) on $N_g(\zeta)$ is elaborated in Fig. 4.31. An augmentation in $N_g(\zeta)$ is witnessed through (Br) in both SWCNTs and MWCNTs situations. Similar trend of $N_g(\zeta)$ is noted for (L_1) and (L_2) in both SWCNTs and MWCNTs cases (see Figs. 4.32 and 4.33). Fig. 4.34 captured the consequences of (α_1) on $N_g(\zeta)$. An enhancement is noticed for (α_1) in both SWCNTs and MWCNTs situations.. Roles of (Ω), (λ) and (F_r) on skin friction coefficients $\left(\frac{\mathrm{Re}}{2}\right)^{1/2} C_f$ and $\left(\frac{\mathrm{Re}}{2}\right)^{1/2} C_g$ are elaborated in Figs. 4.35 – 4.38. Magnitudes of $\left(\frac{\mathrm{Re}}{2}\right)^{1/2} C_f$ and $\left(\frac{\mathrm{Re}}{2}\right)^{1/2} C_g$ are enhanced for higher estimation of (Ω), (λ) and (F_r) in SWCNTs and MWCNTs. From Figs. 4.39 and 4.40, here local heat transfer rate is increased against (Ω), (λ) and (F_r) in both case of SWCNTs and MWCNTs.

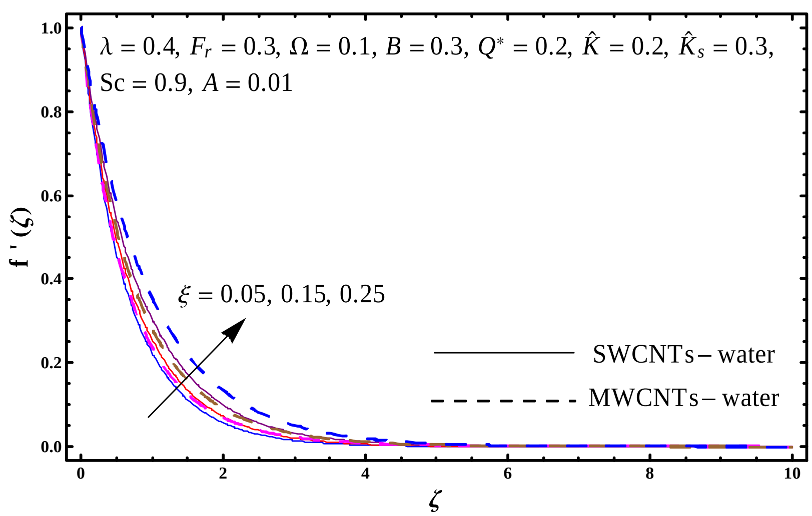

Fig. 4.4: Plot for $f'(\zeta)$ against ξ.

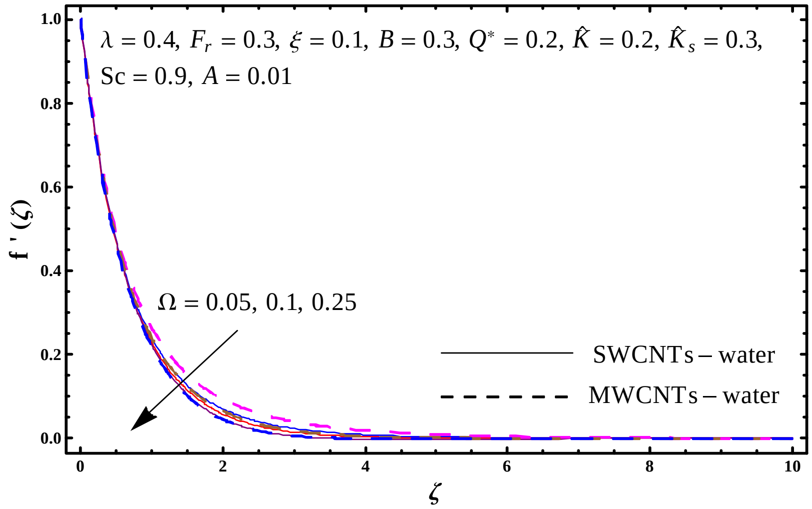

Fig. 4.5: Plot for $f'(\zeta)$ against Ω.

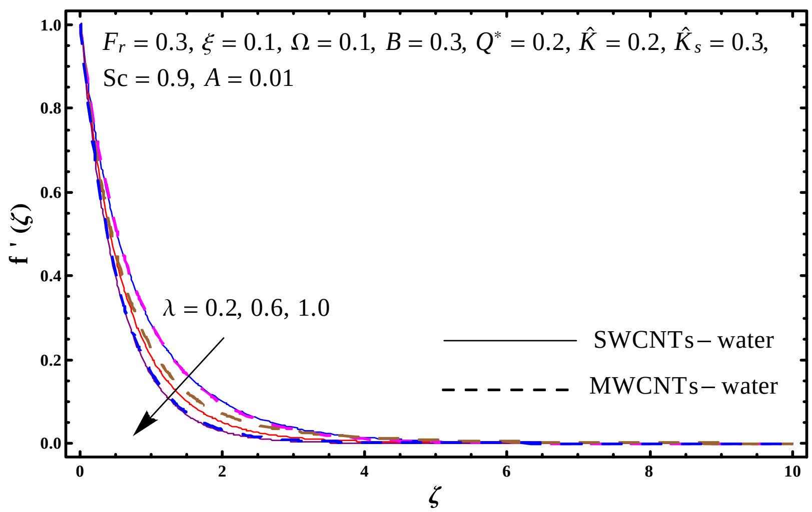

Fig. 4.6: Plot for $f'(\zeta)$ against λ.

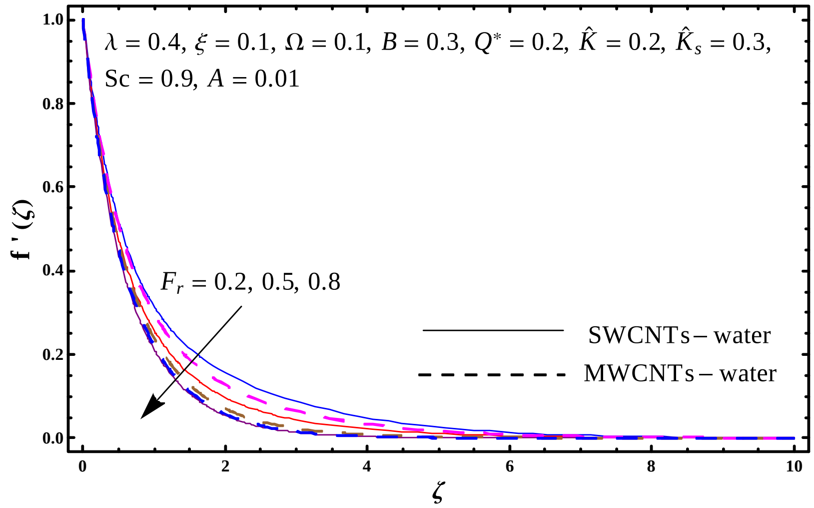

Fig. 4.7: Plot for $f'(\zeta)$ against F_r.

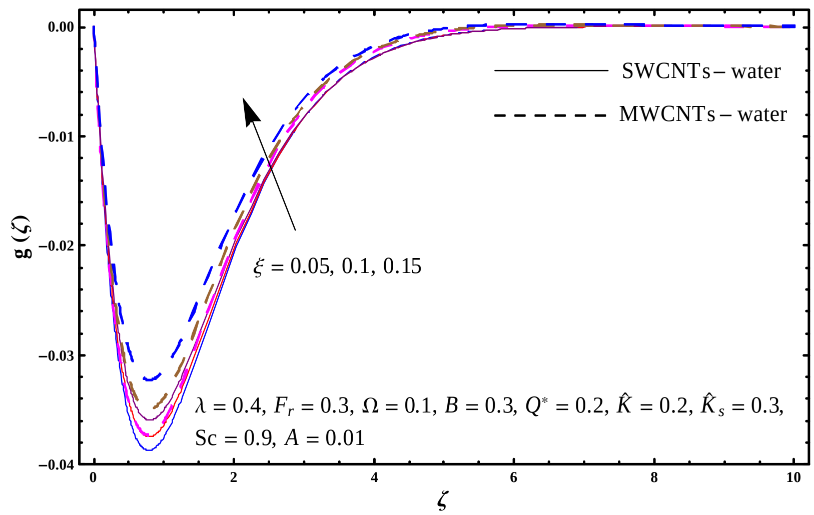

Fig. 4.8: Sketch for $g(\zeta)$ against ξ.

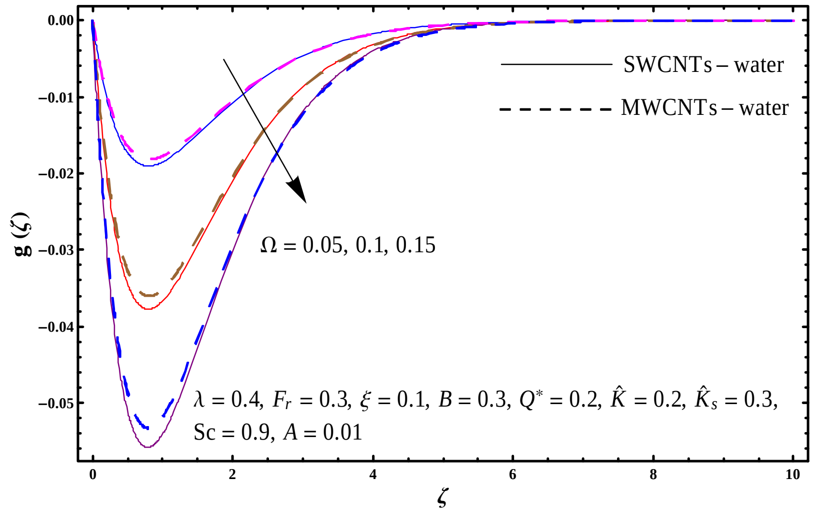

Fig. 4.9: Sketch of $g(\zeta)$ against Ω.

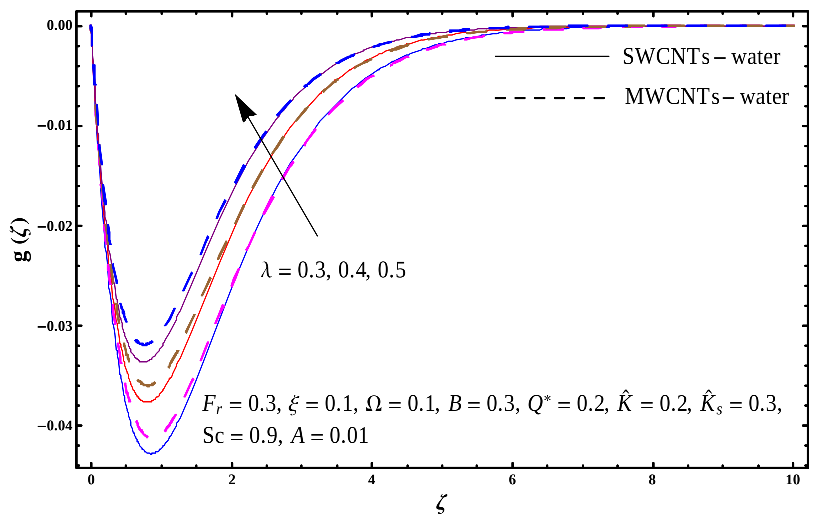

Fig. 4.10: Plot for $g(\zeta)$ against λ.

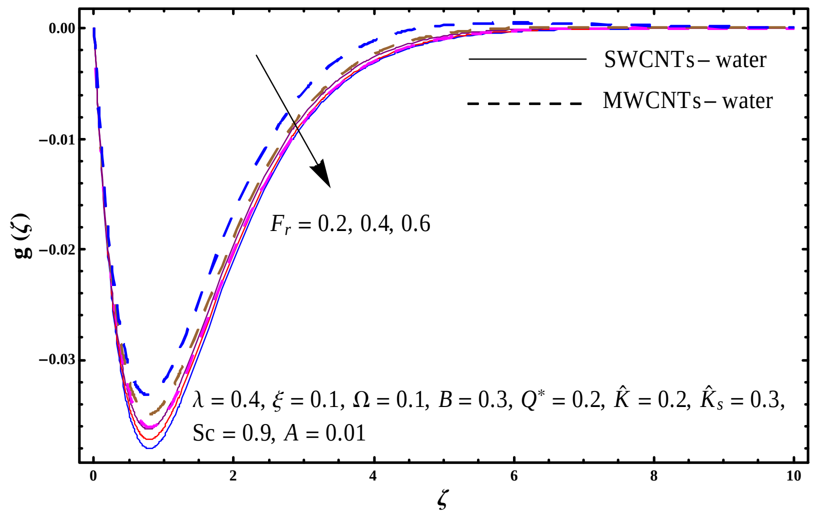

Fig. 4.11: Plot for $g(\zeta)$ against F_r.

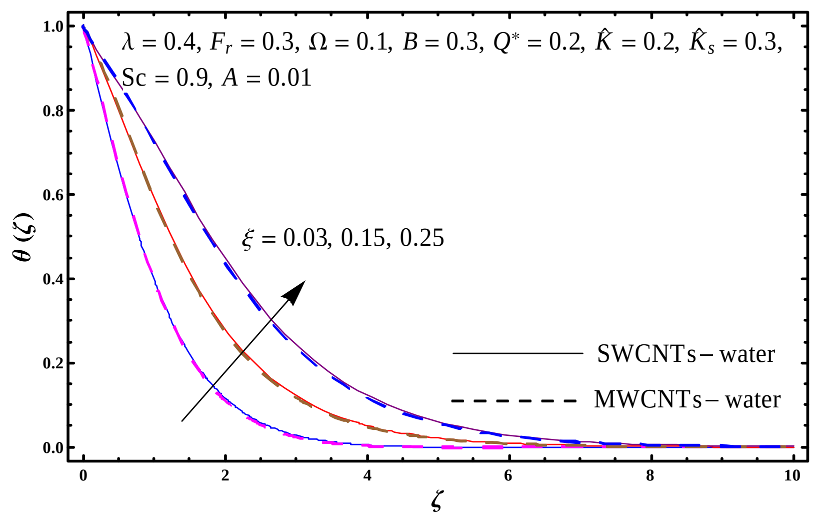

Fig. 4.12: Sketch for $\theta(\zeta)$ against ξ.

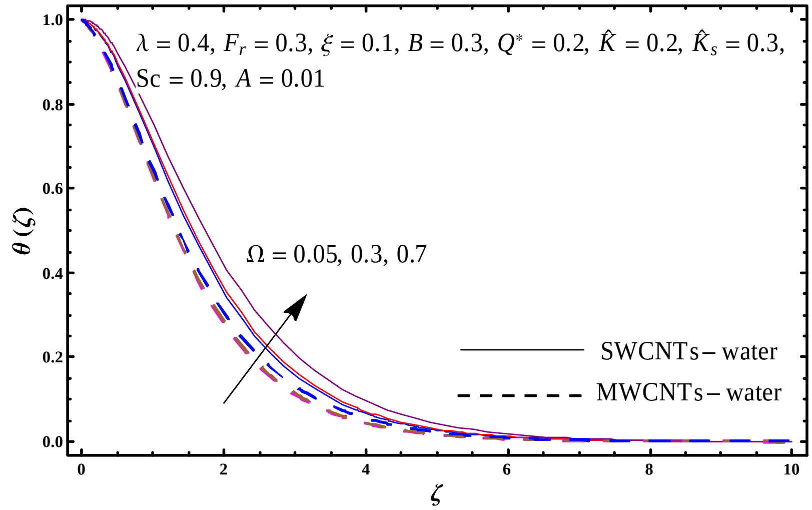

Fig. 4.13: Plot for $\theta(\zeta)$ against Ω.

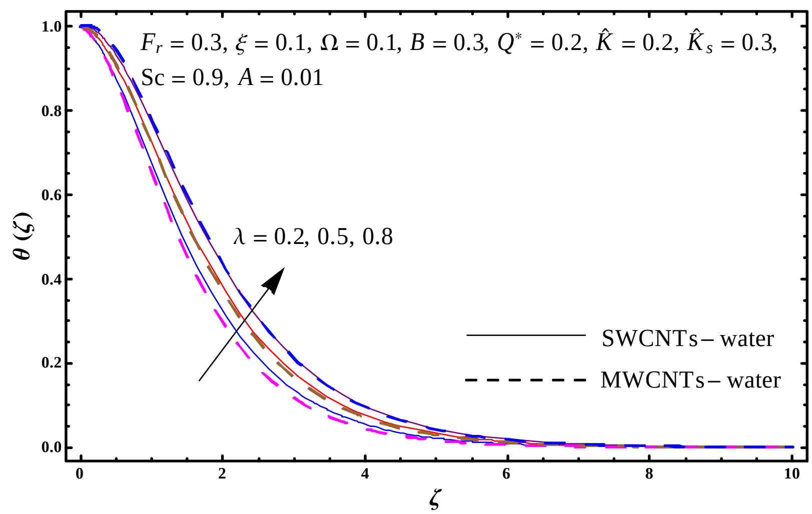

Fig. 4.14: Plot for $\theta(\zeta)$ against λ.

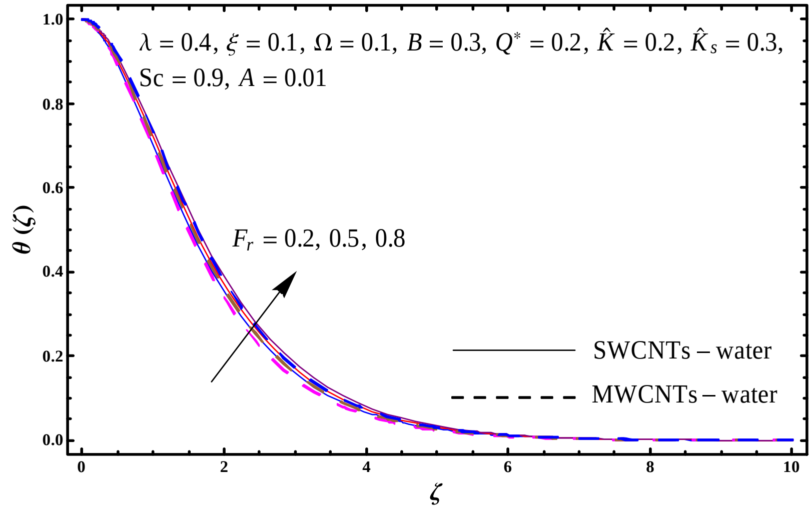

Fig. 4.15: Sketch for $\theta(\zeta)$ against F_r.

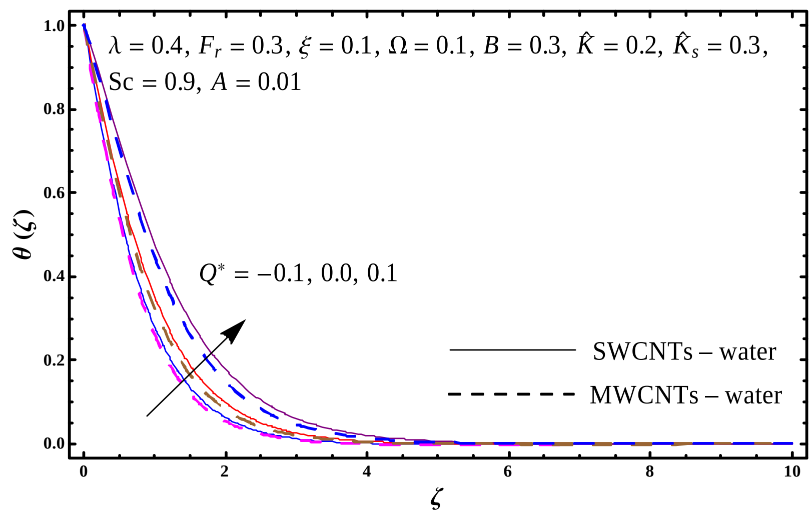

Fig. 4.16: Plot for $\theta(\zeta)$ against Q^*.

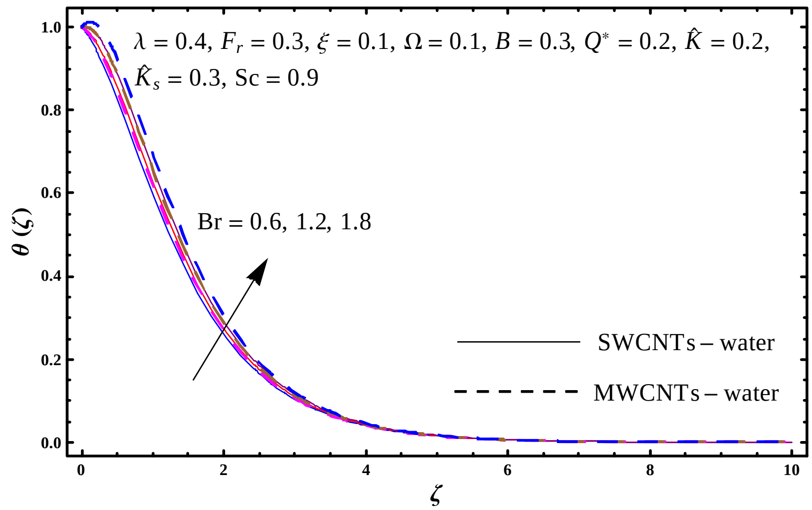

Fig. 4.17: Sketch for $\theta(\zeta)$ against Br.

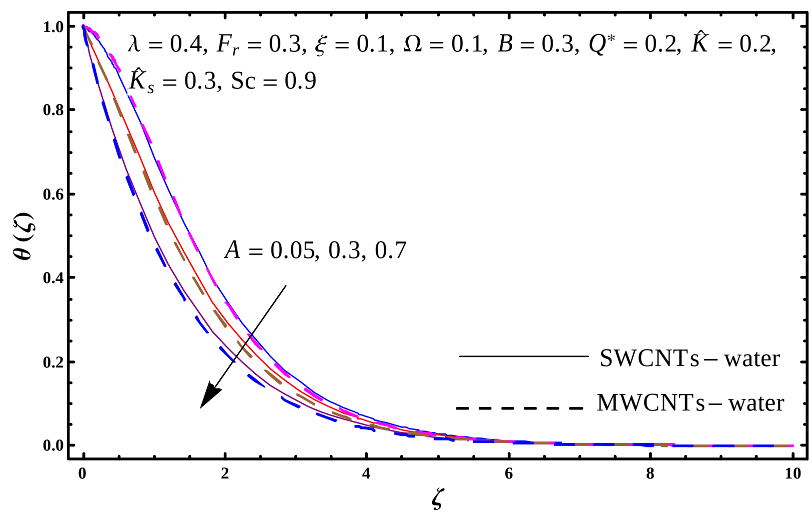

Fig. 4.18: Plot for $\theta(\zeta)$ against A.

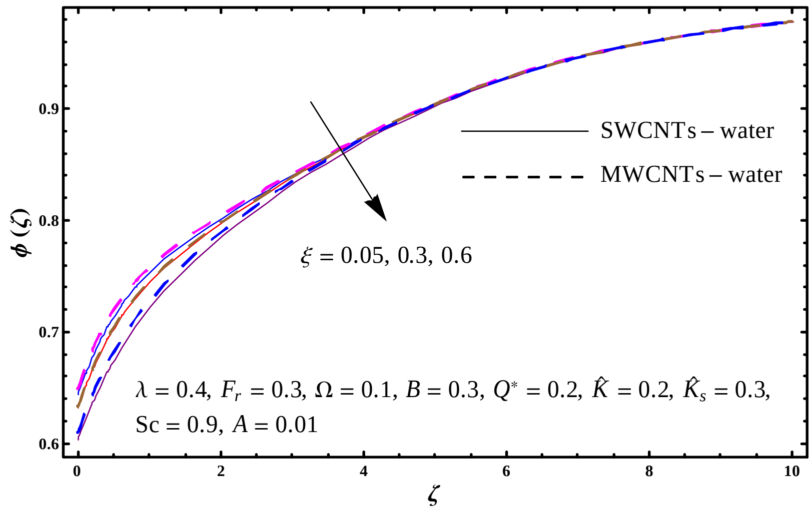

Fig. 4.19: Plot for $\phi(\zeta)$ against ξ.

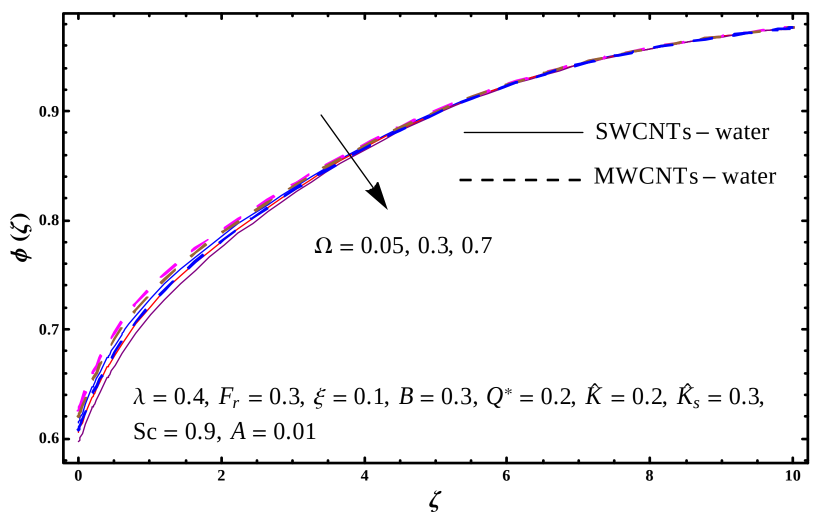

Fig. 4.20: Plot for $\phi(\zeta)$ against Ω.

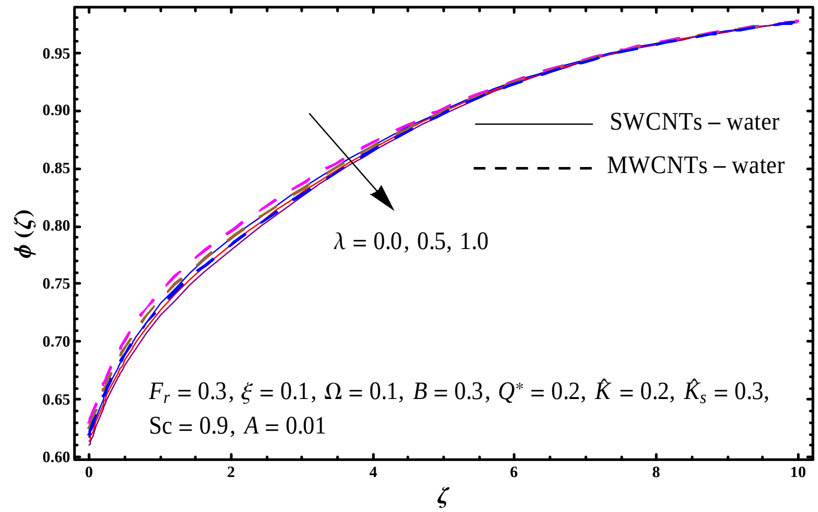

Fig. 4.21: Plot for $\phi(\zeta)$ against λ.

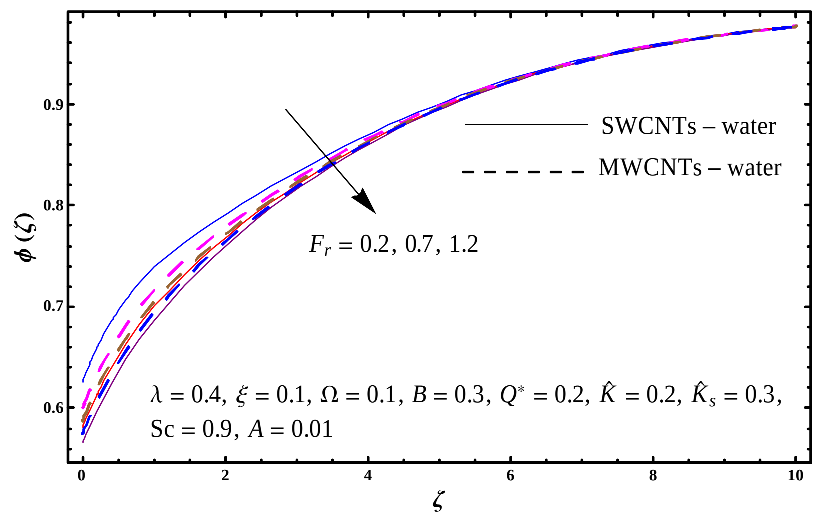

Fig. 4.22: Plot for $\phi(\zeta)$ against F_r.

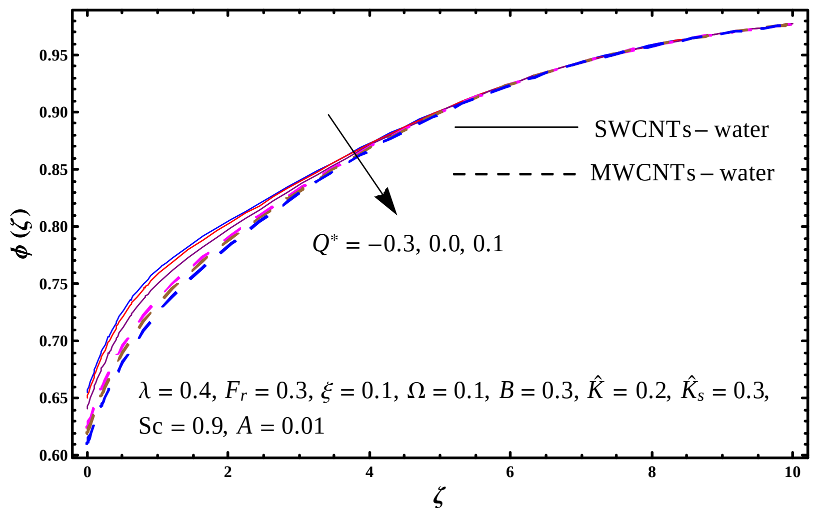

Fig. 4.23: Sketch for $\phi(\zeta)$ against Q^*.

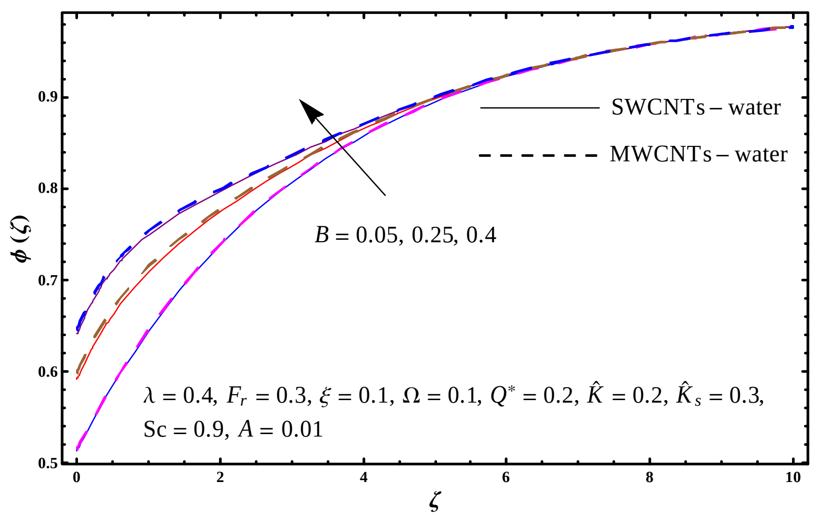

Fig. 4.24: Sketch for $\phi(\zeta)$ against B.

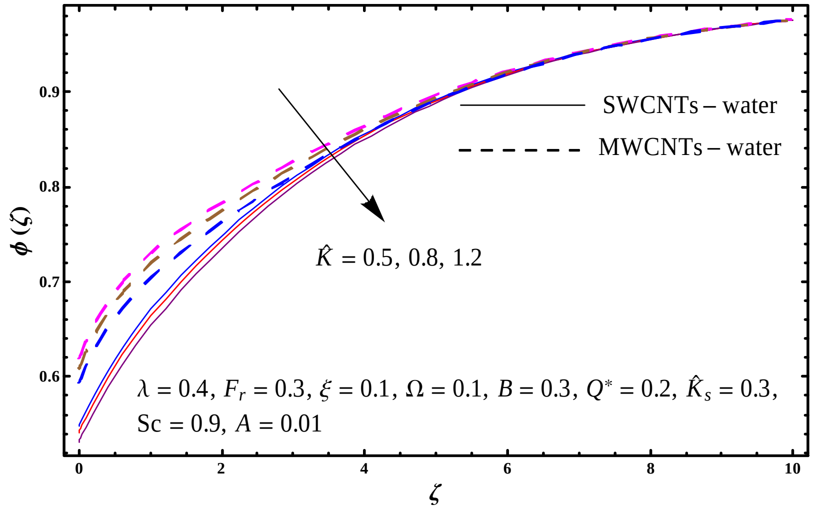

Fig. 4.25: Plot for $\phi(\zeta)$ against $\hat{K}$.

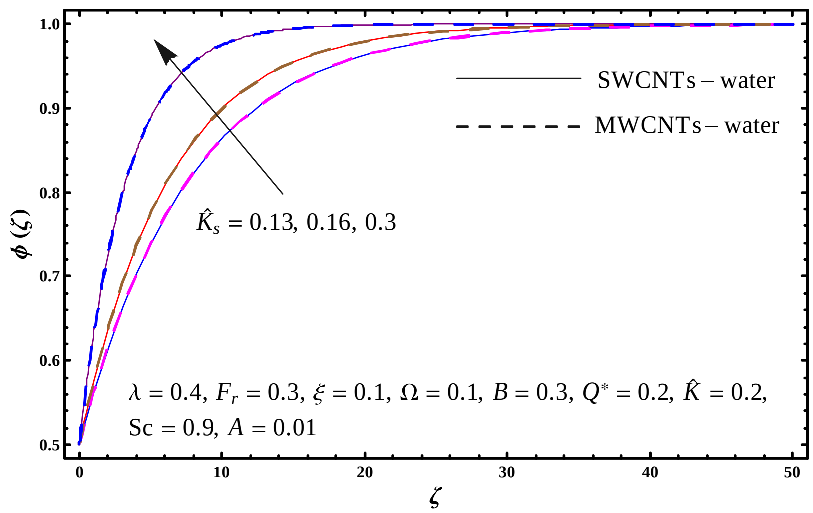

Fig. 4.26: Plot for $\phi(\zeta)$ against $\hat{K}_s$.

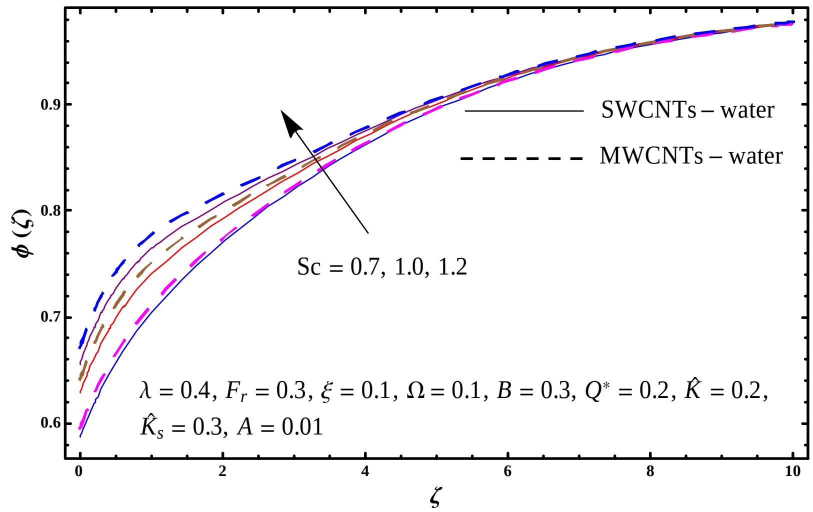

Fig. 4.27: Sketch for $\phi(\zeta)$ against Sc.

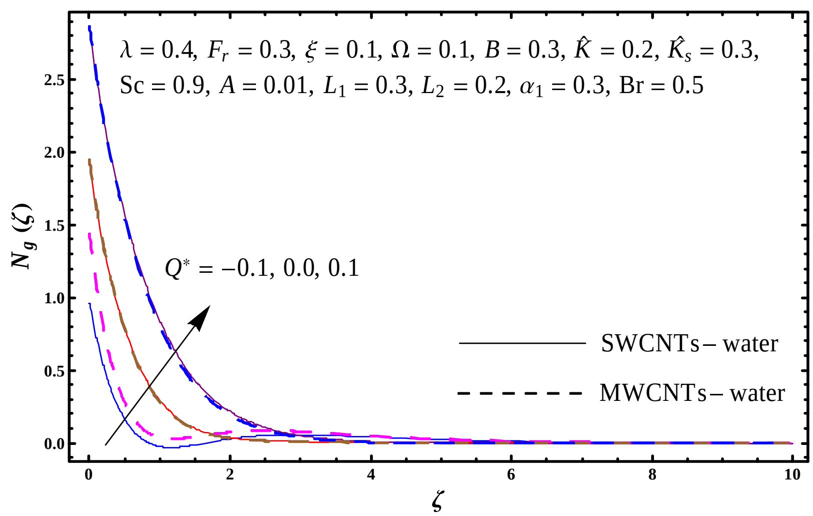

Fig. 4.28: Plot for $N_g(\zeta)$ against Q^*.

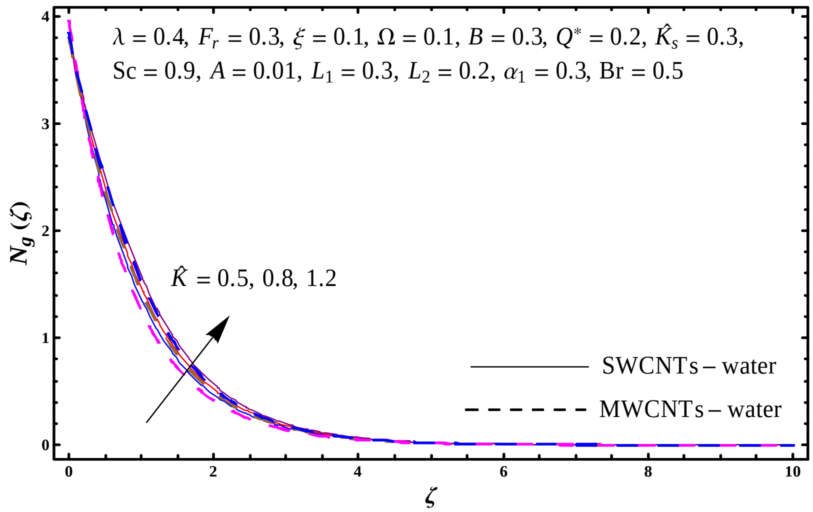

Fig. 4.29: Plot for $N_g(\zeta)$ against $\hat{K}$.

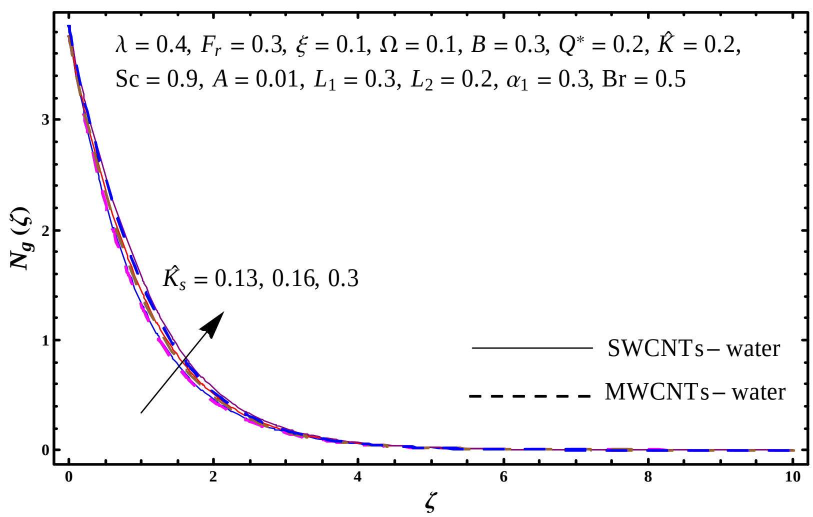

Fig. 4.30: Sketch for $N_g(\zeta)$ against $\hat{K}_s$.

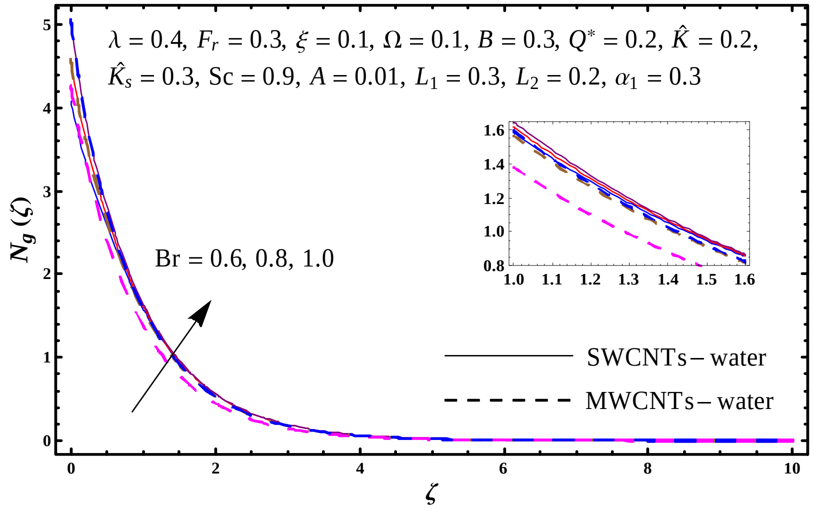

Fig. 4.31: Sketch for $N_g(\zeta)$ against Br.

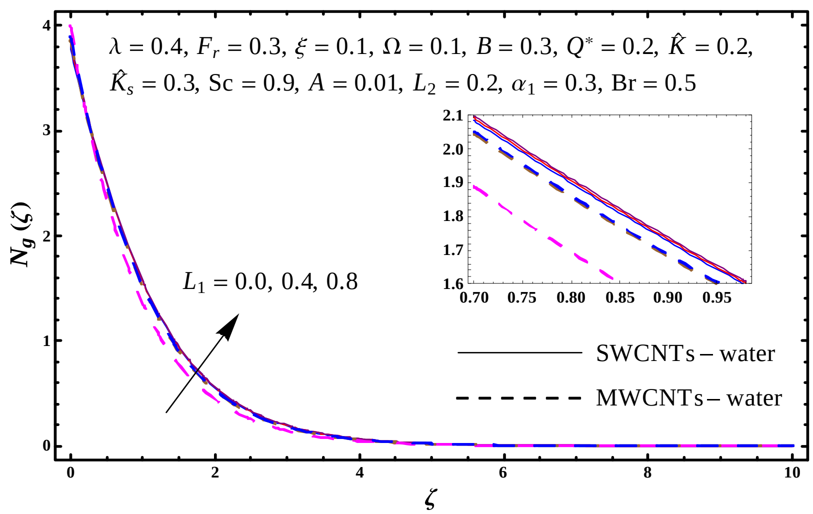

Fig. 4.32: Plot for $N_g(\zeta)$ against L_1.

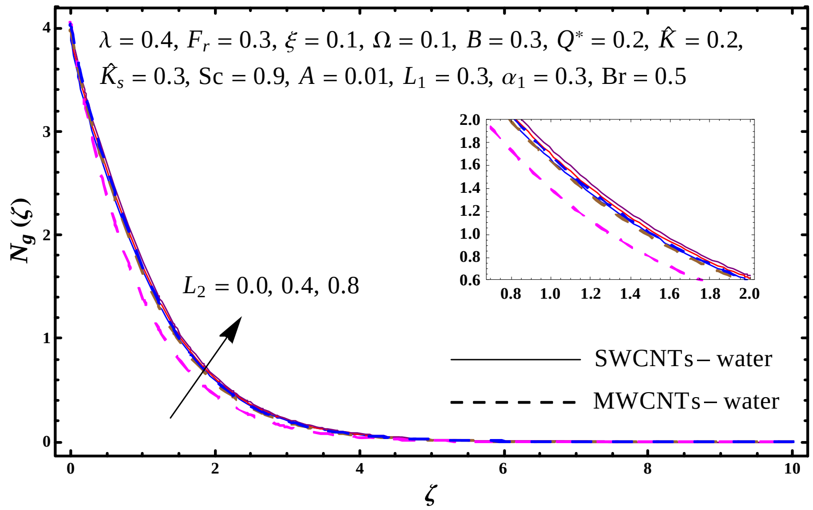

Fig. 4.33: Plot for $N_g(\zeta)$ against L_1.

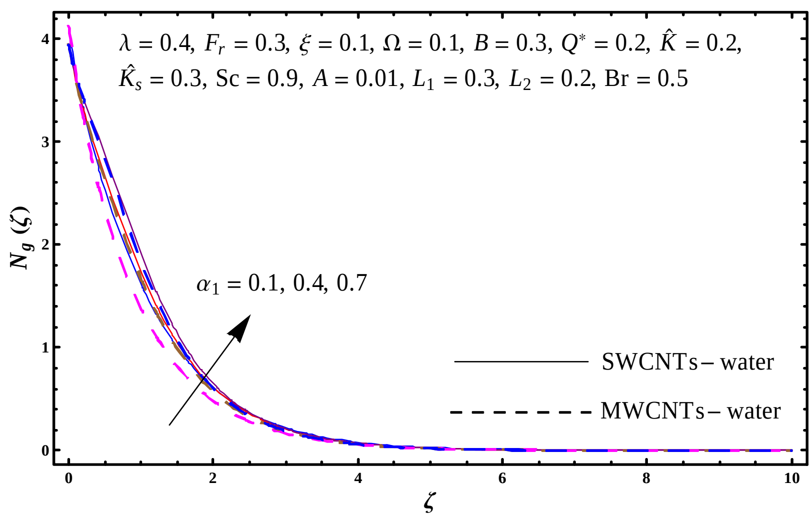

Fig. 4.34: Sketch for $N_g(\zeta)$ against α_1.

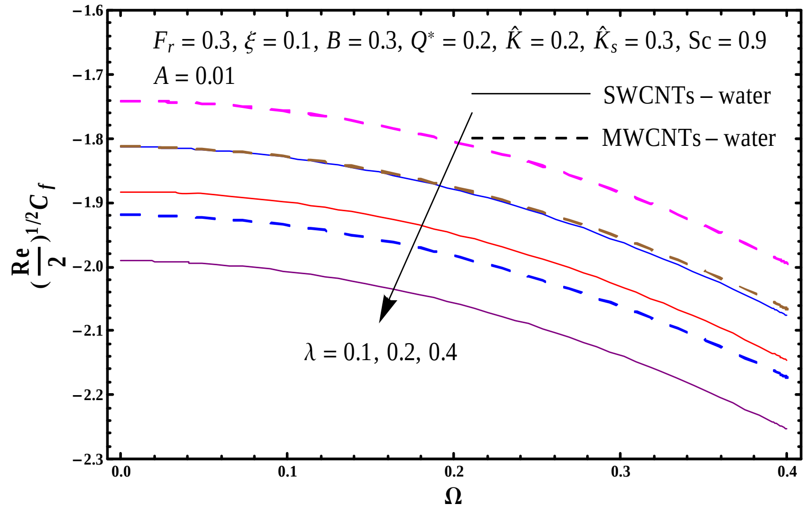

Fig. 4.35: Sketch for $\left(\frac{\text{Re}}{2}\right)^{1/2} C_f$ against Ω and λ.

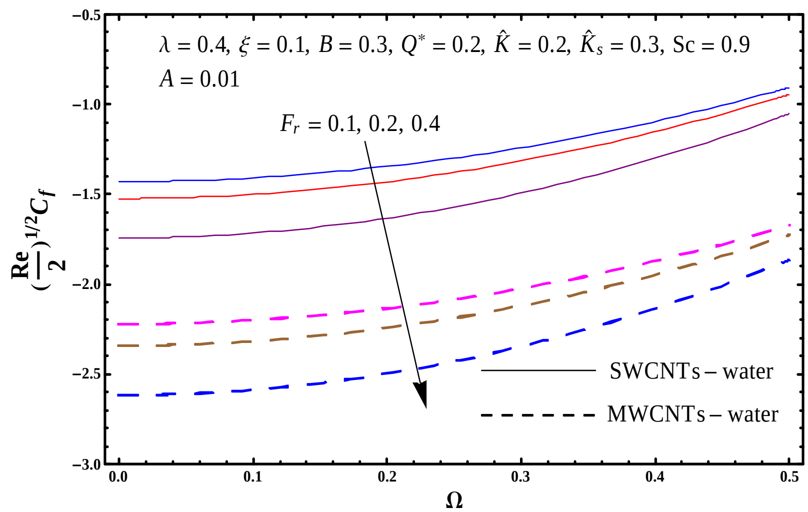

Fig. 4.36: Sketch of $\left(\frac{\text{Re}}{2}\right)^{1/2} C_f$ against Ω and F_r.

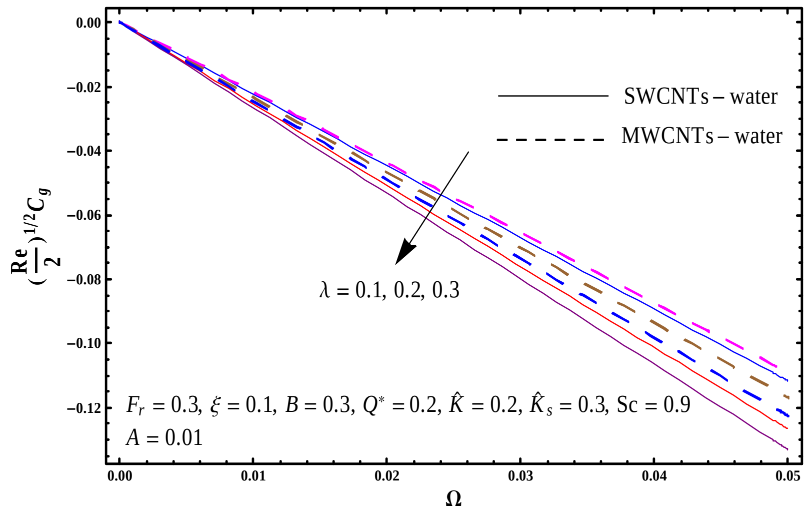

Fig. 4.37: Sketch of $\left(\frac{\text{Re}}{2}\right)^{1/2} C_g$ against Ω and λ.

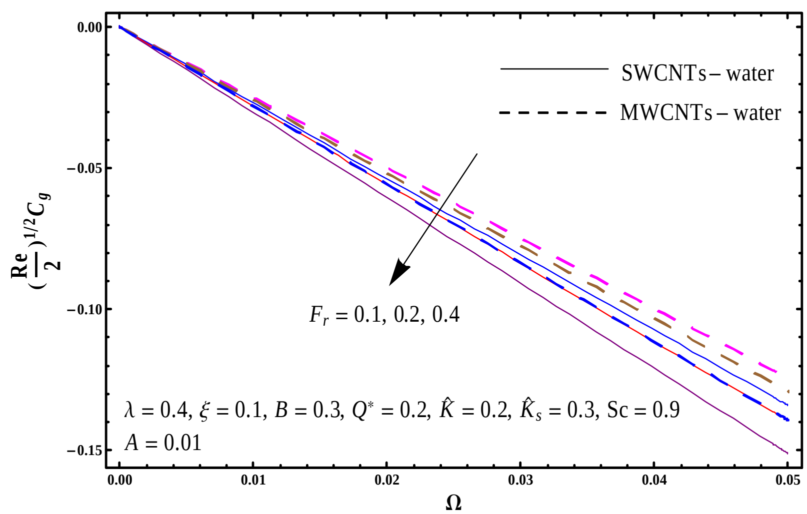

Fig. 4.38: Sketch of $\left(\frac{\text{Re}}{2}\right)^{1/2} C_g$ against Ω and F_r.

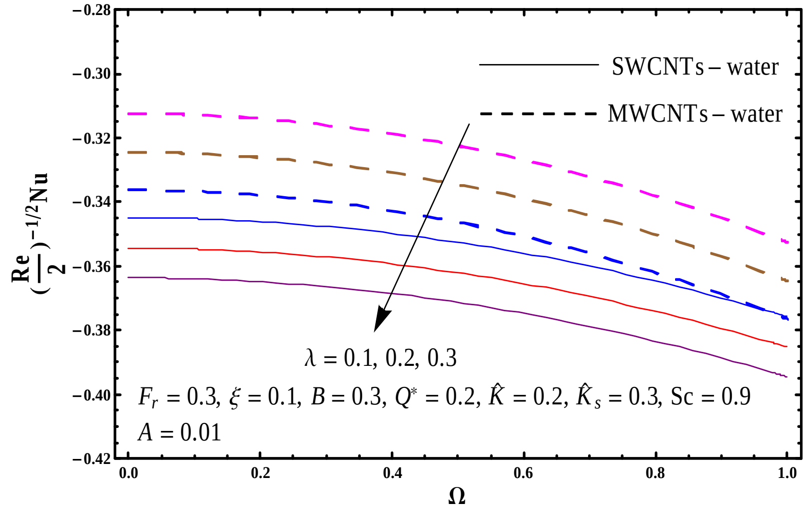

Fig. 4.39: Plot for $\left(\frac{\mathrm{Re}}{2}\right)^{-1/2} Nu$ against Ω and λ.

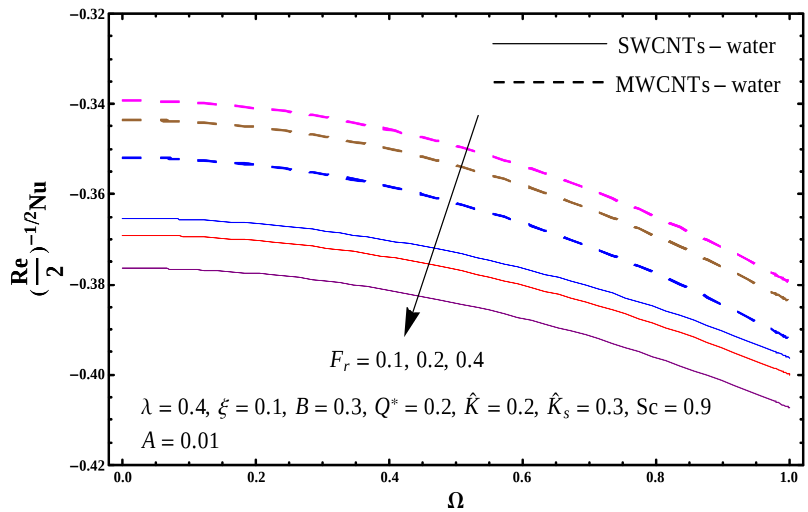

Fig. 4.40: Sketch of $\left(\frac{\mathrm{Re}}{2}\right)^{-1/2} Nu$ against Ω and F_r.

Chapter 5

Flow of carbon nanotubes induced by curved stretching sheet

This chapter provides a numerical study for Darcy-Forchheimer flow of carbon-water nanofluid. Flow is induced by an exponential stretched curved sheet. Viscous liquid is described by Darcy-Forchheimer relation in porous space. Numerical arrangements of governing frameworks are set up by NDSolve procedure. Outcomes of different sundry parameters on temperature and velocity are examined. Skin friction and heat transfer rate are also shown and analyzed.

5.1 Model development

We assume flow of carbon-water nanofluid. Flow is induced by an exponential extending bended sheet coiled in circle of radius R (see Figure 5.1). Permeable space by Darcy-Forchheimer model is considered. Here $u_w(s) = u_0 e^{s/L}$ depicts the exponential velocity with $u_0 > 0$. Resulting relations are

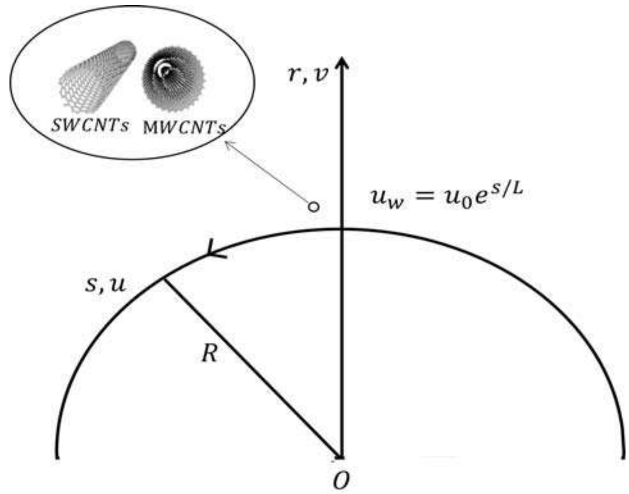

Fig. 5.1: Flow configuration.

$$\frac{\partial}{\partial r}\left((r+R)\,v\right)+R\frac{\partial u}{\partial s}=0, \tag{5.1}$$

$$\frac{u^2}{r+R}=\frac{1}{\rho_{nf}}\frac{\partial p}{\partial r}, \tag{5.2}$$

$$\begin{aligned} v\frac{\partial u}{\partial r}+\frac{R}{r+R}u\frac{\partial u}{\partial s}+\frac{uv}{r+R} &= -\frac{1}{\rho_{nf}}\frac{R}{r+R}\frac{\partial p}{\partial s}+ \\ \nu_{nf}\left(\frac{\partial^2 u}{\partial r^2}+\frac{1}{r+R}\frac{\partial u}{\partial r}-\frac{u}{(r+R)^2}\right) &- \frac{\nu_{nf}}{K^*}u-Fu^2\ , \end{aligned} \tag{5.3}$$

$$v\frac{\partial T}{\partial r}+u\frac{\partial T}{\partial s}\frac{R}{r+R}=\alpha_{nf}\left(\frac{\partial^2 T}{\partial r^2}+\frac{1}{r+R}\frac{\partial T}{\partial r}\right), \tag{5.4}$$

$$u=u_0e^{s/L},\quad v=0,\quad T=T_w=T_\infty+T_0e^{As/2L}\quad \text{at}\quad r=0, \tag{5.5}$$

$$u\to 0,\quad \frac{\partial u}{\partial r}\to 0,\quad T\to T_\infty\quad \text{as}\quad r\to\infty. \tag{5.6}$$

Xue [45] model gives:

$$\left.\begin{aligned} &\mu_{nf}=\frac{\mu_f}{(1-\xi)^{2.5}},\ \nu_{nf}=\frac{\mu_{nf}}{\rho_{nf}},\ \alpha_{nf}=\frac{k_{nf}}{(\rho c_p)_{nf}},\ \rho_{nf}=\rho_f\,(1-\xi)+\rho_{CNT}\xi, \\ &(\rho c_p)_{nf}=(\rho c_p)_f\,(1-\xi)+(\rho c_p)_{CNT}\,\xi,\ \frac{k_{nf}}{k_f}=\frac{(1-\xi)+2\xi\frac{k_{CNT}}{k_{CNT}-k_f}\ln\frac{k_{CNT}+k_f}{2k_f}}{(1-\xi)+2\xi\frac{k_f}{k_{CNT}-k_f}\ln\frac{k_{CNT}+k_f}{2k_f}}. \end{aligned}\right\} \tag{5.7}$$

Table 5.1: Thermophysical features of carbon nanotubes and water [45].

Physical properties	Water	Nanoparticles	
		$SWCNTs$	$MWCNTs$
$\rho\left(kg/m^3\right)$	997.1	2600	1600
$k\,(W/mK)$	0.613	6600	3000
$c_p\,(J/kgK)$	4179	425	796

Consider

$$\begin{gathered} u=u_0 e^{s/L}\frac{\partial f(\eta,\zeta)}{\partial\zeta},\ v=-\frac{R}{r+R}\sqrt{\frac{u_0\nu_f e^{s/L}}{2L}}\left(f+2\eta\frac{\partial f}{\partial\eta}+\zeta\frac{\partial f}{\partial\zeta}\right),\ \zeta=\left(\frac{u_0 e^{s/L}}{2\nu_f L}\right)^{1/2} r, \\ T=T_\infty+T_0 e^{\frac{As}{2L}}\theta\left(\eta,\zeta\right),\ p=\rho_f u_0^2 e^{2s/L}H\left(\eta,\zeta\right),\ \eta=e^{s/L}. \end{gathered} \tag{5.8}$$

Now, Eq. (5.1) is trivially verified and Eqs. (5.2) – (5.7) yield

$$\frac{1}{\left(1-\xi+\frac{\rho_{CNT}}{\rho_f}\xi\right)}\frac{\partial H}{\partial\zeta}=\frac{1}{\sqrt{\eta}}\frac{1}{\zeta+K}\left(\frac{\partial f}{\partial\zeta}\right)^2, \tag{5.9}$$

$$\begin{gathered} \frac{1}{(1-\xi)^{2.5}\left(1-\xi+\frac{\rho_{CNT}}{\rho_f}\xi\right)}\left(\frac{\partial^3 f}{\partial\zeta^3}+\frac{1}{\sqrt{\eta}}\frac{1}{\zeta+K}\frac{\partial^2 f}{\partial\zeta^2}-\frac{1}{\eta}\frac{1}{(\zeta+K)^2}\frac{\partial f}{\partial\zeta}-2\frac{\lambda}{\eta}\frac{\partial f}{\partial\zeta}\right)-2F_r\left(\frac{\partial f}{\partial\zeta}\right)^2- \\ \frac{K}{\zeta+K}\left(\frac{2K+\zeta}{\zeta+K}\left(\frac{\partial f}{\partial\zeta}\right)^2-f^2\frac{\partial^2 f}{\partial\zeta^2}-\frac{1}{\zeta+K}f\frac{\partial f}{\partial\zeta}\right)=-\frac{1}{(1-\xi)+\frac{\rho_{CNT}}{\rho_f}\xi}\frac{K}{\zeta+K}\left(4H+2\eta\frac{\partial H}{\partial\eta}+\zeta\frac{\partial H}{\partial\zeta}\right)- \\ \frac{\eta K}{K+\zeta}\left(2\frac{\partial f}{\partial\eta}\frac{\partial f}{\partial\zeta}-\frac{2}{\zeta+K}\frac{\partial f}{\partial\eta}\frac{\partial f}{\partial\zeta}-\frac{\partial^2 f}{\partial\zeta^2}\frac{\partial f}{\partial\eta}\right), \end{gathered} \tag{5.10}$$

$$\begin{gathered} \frac{1}{\Pr}\frac{1}{1-\xi+\frac{(\rho c_p)_{CNT}}{(\rho c_p)_f}\xi}\left(\frac{k_{nf}}{k_f}\left(\frac{\partial^2\theta}{\partial\zeta^2}+\frac{1}{\sqrt{\eta}}\frac{1}{\zeta+K}\frac{\partial\theta}{\partial\zeta}\right)\right)+ \\ \frac{K}{\zeta+K}\left(f\frac{\partial\theta}{\partial\zeta}-A\theta\frac{\partial f}{\partial\zeta}\right)=2\frac{\eta K}{\zeta+K}\left(\frac{\partial\theta}{\partial\eta}\frac{\partial f}{\partial\zeta}-\frac{\partial\theta}{\partial\zeta}\frac{\partial f}{\partial\eta}\right), \end{gathered} \tag{5.11}$$

$$f\left(\eta,0\right)=-2\eta\frac{\partial f\left(\eta,0\right)}{\partial\eta},\ \frac{\partial f\left(\eta,0\right)}{\partial\zeta}=1,\ \theta\left(\eta,0\right)=1, \tag{5.12}$$

$$\frac{\partial f\left(\eta,\infty\right)}{\partial\zeta}\to 0,\ \frac{\partial^2 f\left(\eta,\infty\right)}{\partial\zeta^2}\to 0,\ \theta\left(\eta,\infty\right)\to 0, \tag{5.13}$$

Here η is the constant prescribed variable at any streamwise location. To attain similar solutions we assume that the terms including $\frac{\partial(.)}{\partial\eta}$ are sufficiently small and may be approximated by zero.

Thus, we have

$$\frac{1}{\left(1-\xi+\frac{\rho_{CNT}}{\rho_f}\xi\right)}H' = \frac{1}{\sqrt{\eta}}\frac{1}{\zeta+K}f'^2, \tag{5.14}$$

$$\begin{gathered}\frac{1}{(1-\xi)^{2.5}\left(1-\xi+\frac{\rho_{CNT}}{\rho_f}\xi\right)}\left(f''' + \frac{1}{\sqrt{\eta}}\frac{1}{\zeta+K}f'' - \frac{1}{\eta}\frac{1}{(\zeta+K)^2}f' - 2\frac{\lambda}{\eta}f'\right) - 2F_r f'^2 - \\ \frac{K}{\zeta+K}\left(\frac{2K+\zeta}{\zeta+K}f'^2 - f^2 f'' - \frac{1}{\zeta+K}ff''\right) = -\frac{1}{(1-\xi)+\frac{\rho_{CNT}}{\rho_f}\xi}\frac{K}{\zeta+K}\left(4H+\zeta H'\right),\end{gathered} \tag{5.15}$$

$$\frac{1}{\Pr}\frac{1}{1-\xi+\frac{(\rho c_p)_{CNT}}{(\rho c_p)_f}\xi}\frac{k_{nf}}{k_f}\left(\theta'' + \frac{1}{\sqrt{\eta}}\frac{1}{\zeta+K}\theta'\right) + \frac{K}{\zeta+K}\left(f\theta' - A\theta f'\right) = 0\ . \tag{5.16}$$

Eqs. (5.14) and (5.15) after elimination of H give

$$\begin{gathered}\frac{1}{(1-\xi)^{2.5}\left(1-\xi+\frac{\rho_{CNT}}{\rho_f}\xi\right)}\left(\begin{array}{c} f^{iv} + \frac{1}{\eta}\frac{1}{\zeta+K}f''' + \frac{1}{\sqrt{\eta}}\frac{1}{\zeta+K}f''' - \frac{1}{\eta}\frac{1}{(\zeta+K)^2}f'' - \\ 2\frac{\lambda}{\eta}\left(f'' + \frac{1}{\zeta+K}f'\right)\end{array}\right) + \\ \frac{K}{\zeta+K}\left(ff''' + \frac{1}{\zeta+K}ff'' - \frac{1}{(\zeta+K)^2}ff' + \frac{2K+\zeta}{(\zeta+K)^2}f'^2 - \frac{1}{\sqrt{\eta}}\frac{4\zeta+5K}{(\zeta+K)^2}f'^2 - \frac{3K+\zeta}{\zeta+K}f'f'' - \frac{1}{\sqrt{\eta}}\frac{2\zeta}{\zeta+K}f'f''\right) - \\ 2F_r\left(2f'f'' + \frac{1}{\zeta+K}f'^2\right) = 0,\end{gathered} \tag{5.17}$$

$$f(\eta,0) = 0,\ \ f'(\eta,0) = 1,\ \ \theta(\eta,0) = 1, \tag{5.18}$$

$$f'(\eta,\infty) \to 0,\ \ f''(\eta,\infty) \to 0,\ \ \theta(\eta,\infty) \to 0. \tag{5.19}$$

Emerging flow variables are:

$$K = \left(\frac{u_0}{2\nu_f L}\right)^{1/2} R,\ \ \lambda = \frac{\nu_f L}{K^* u_0},\ \ F_r = \frac{C_b L}{K^{*1/2}},\ \ \Pr = \frac{\nu_f}{\alpha_f}\ . \tag{5.20}$$

5.2 Physical quantities

Skin friction coefficient and local Nusselt number are

$$\left.\begin{array}{c}\left(\frac{\mathrm{Re}}{2}\right)^{1/2} C_f = \frac{1}{\eta}\frac{1}{(1-\xi)^{2.5}}\left(\sqrt{\eta}f''(\eta,0) - \frac{1}{K}f'(\eta,0)\right), \\ \left(\frac{\mathrm{Re}}{2}\right)^{-1/2} Nu = -\frac{k_{nf}}{k_f}\sqrt{\eta}\ln\eta\,\theta'(\eta,0),\end{array}\right\} \tag{5.21}$$

with $\mathrm{Re} = \frac{u_0 L}{\nu_f}$ as local Reynolds number.

5.3 Discussion

Local-similar arrangements of system of nonlinear equations are figured numerically by utilizing NDSolve method. This portion outlines impacts of (ξ) , (λ), (K), (F_r) and (A) on velocity $f'(\zeta)$ and temperature $\theta(\zeta)$ fields. The outcomes are accomplished for SWCNTs and MWCNTs. Features of (ξ) on velocity $f'(\zeta)$ are plotted in Fig. 5.2. Larger (ξ) causes higher velocity field $f'(\zeta)$ for SWCNTs and MWCNTs. Fig. 5.3 is interpreted to analyze outcome for (K) on velocity field $f'(\zeta)$. It is analyzed that an increment in (K) shows higher velocity field $f'(\zeta)$ for both SWCNTs and MWCNTs. In Fig. 5.4, it is clearly examined that lower velocity field $f'(\zeta)$ is generated by using larger (λ) for both SWCNTs and MWCNTs. Outcome of (F_r) on $f'(\zeta)$ is shown in Fig. 5.5. Here $f'(\zeta)$ reduces for higher (F_r) for both SWCNTs and MWCNTs. Fig. 5.6 shows impact of (ξ) on $\theta(\zeta)$. It is revealed that increment in (ξ) enhances temperature $\theta(\zeta)$ for SWCNTs and MWCNTs. The variation of (K) on temperature field $\theta(\zeta)$ is depicted in Fig. 5.7. By increasing (K), a reduction in temperature field $\theta(\zeta)$ for SWCNTs and MWCNTs is observed. Fig. 5.8 depicts that how (λ) affects temperature field $\theta(\zeta)$. Here higher (λ) leads to enhancement in temperature $\theta(\zeta)$ for SWCNTs and MWCNTs. Fig. 5.9 displays that larger (F_r) yields stronger temperature field $\theta(\zeta)$ for SWCNTs and MWCNTs. Fig. 5.10 is sketched to characterize the consequences of (A) on temperature field $\theta(\zeta)$. Clearly higher (A) cause weaker $\theta(\zeta)$ for SWCNTs and MWCNTs. Skin friction coefficient $\left(\frac{\mathrm{Re}}{2}\right)^{1/2} C_f$ for various pertinent flow variables such as (ξ), (K) and (λ) is plotted in Figs. 5.11 and 5.12. Here skin friction is higher for increasing estimations of (ξ) for both SWCNTs and MWCNTs. Figs. 5.13 and 5.14 elucidate local Nusselt number $\left(\frac{\mathrm{Re}}{2}\right)^{-1/2} Nu$ for SWCNTs and MWCNTs. We concluded that local Nusselt number is increased for higher (ξ) , (K) and (λ). Table 5.2 is developed to validate present outcomes with existing outcomes by Okechi et al. [20]. Here we examined that present NDSolve solution is in good agreement with the existing solution by

Okechi et al. [20].

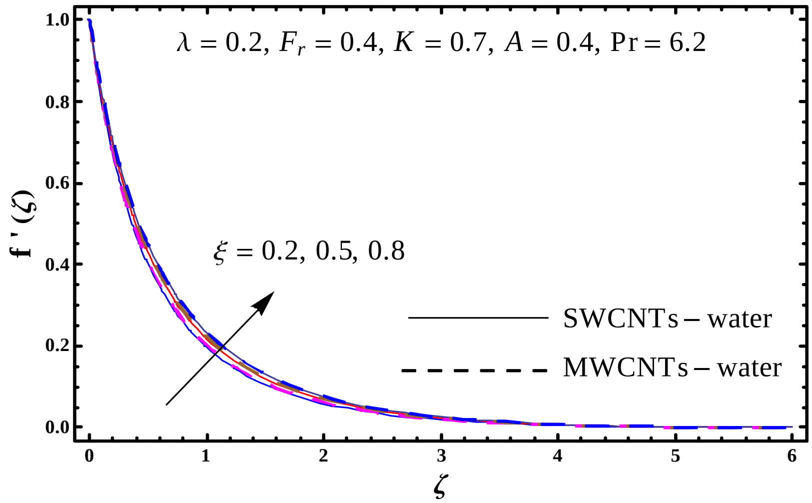

Fig. 5.2: Sketch of $f'(\zeta)$ against ξ.

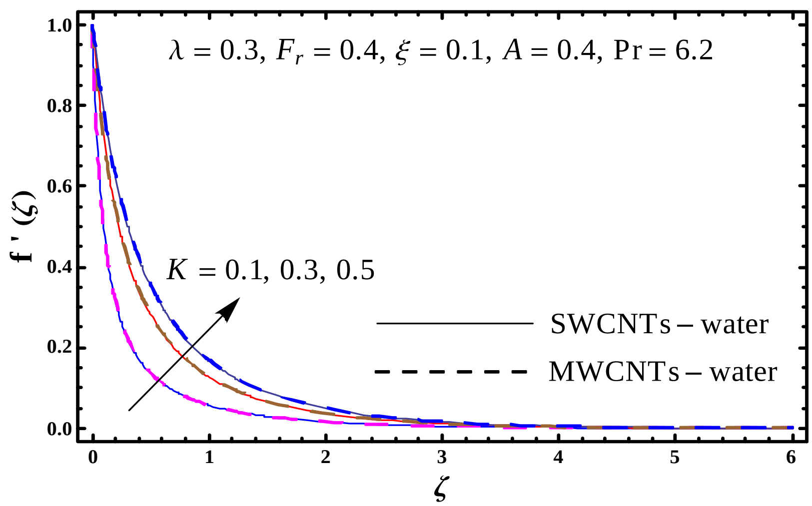

Fig. 5.3: Sketch for $f'(\zeta)$ versus K.

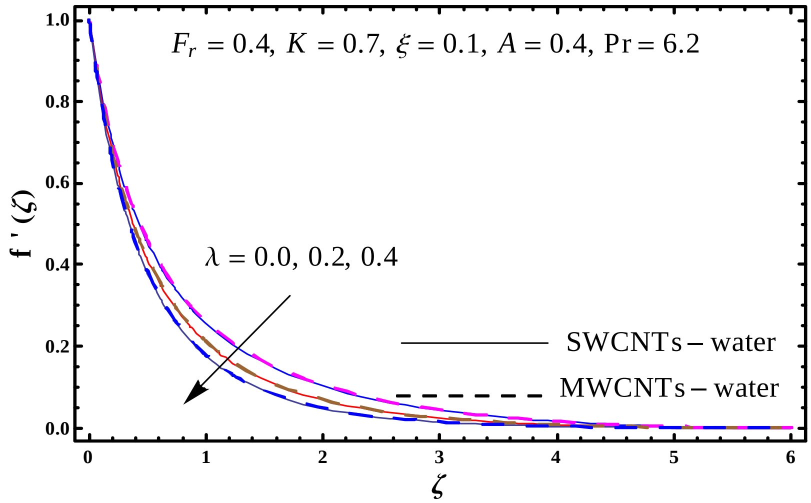

Fig. 5.4: Sketch for $f'(\zeta)$ versus λ.

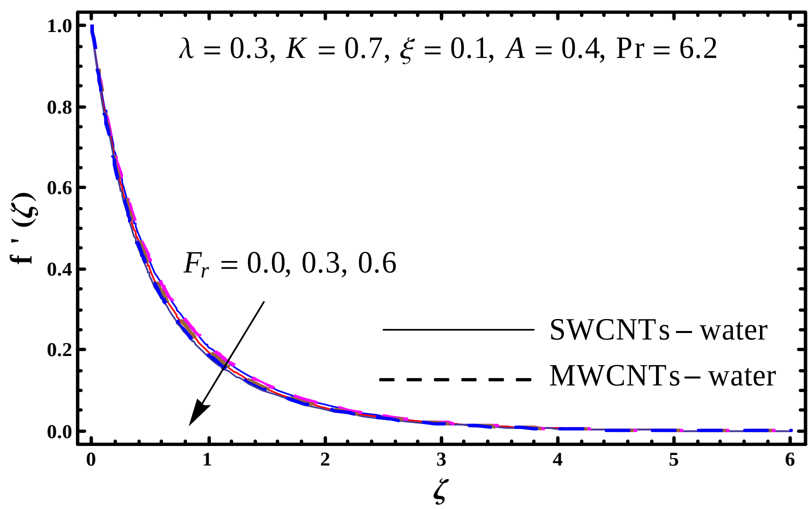

Fig. 5.5: Sketch for $f'(\zeta)$ versus F_r.

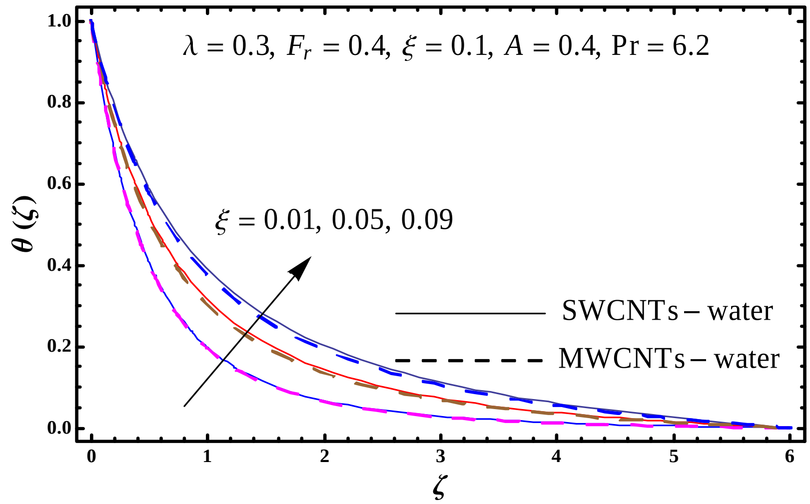

Fig. 5.6: Sketch for $\theta(\zeta)$ versus ξ.

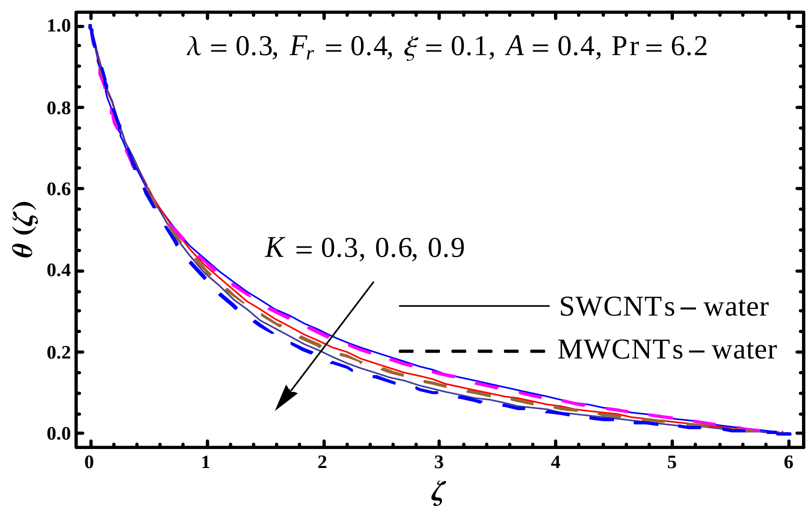

Fig. 5.7: Sketch for $\theta(\zeta)$ versus K.

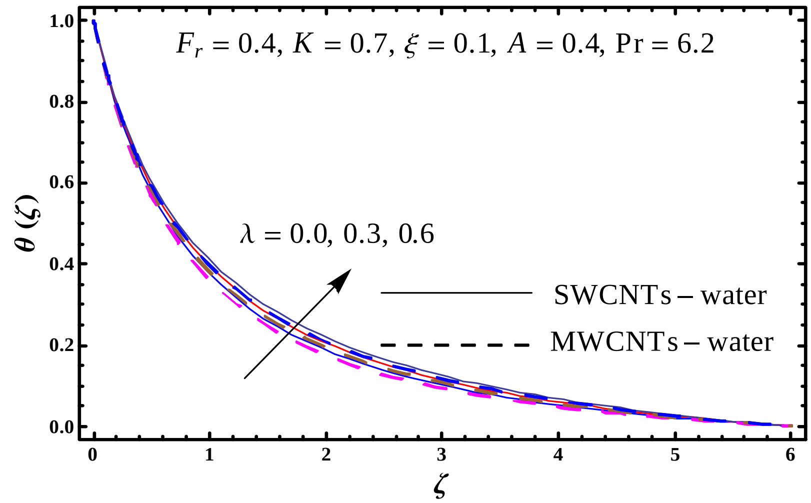

Fig. 5.8: Sketch for $\theta(\zeta)$ versus λ.

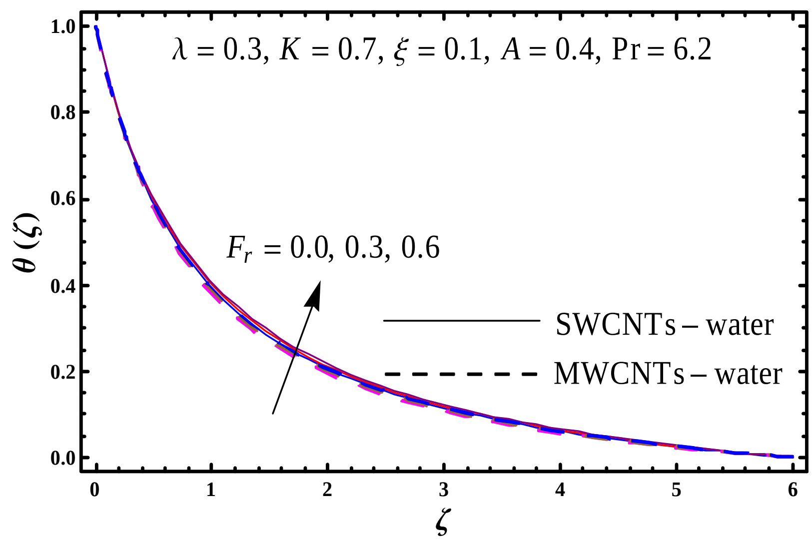

Fig. 5.9: Sketch for $\theta(\zeta)$ versus F_r.

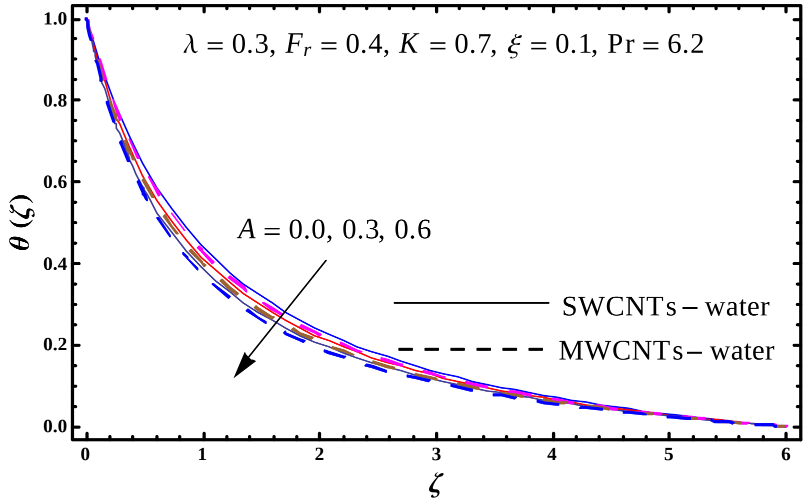

Fig. 5.10: Sketch for $\theta(\zeta)$ versus A.

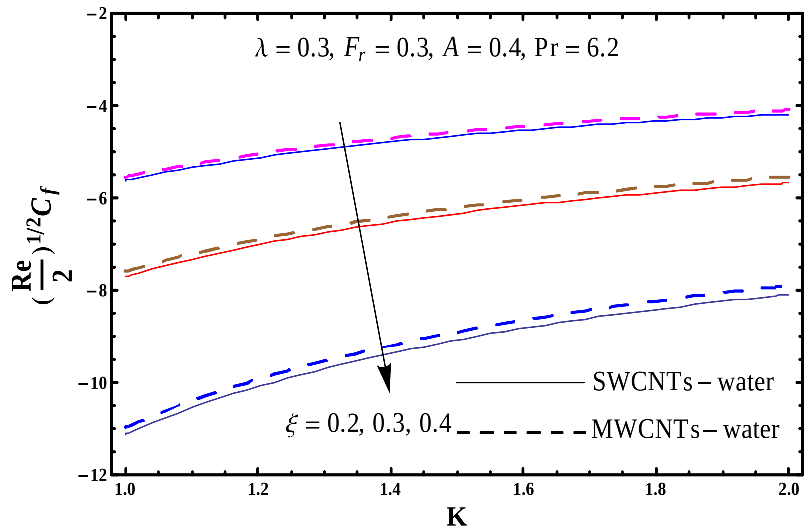

Fig. 5.11: Sketch for $\left(\frac{\mathrm{Re}}{2}\right)^{1/2} C_f$ versus ξ and K.

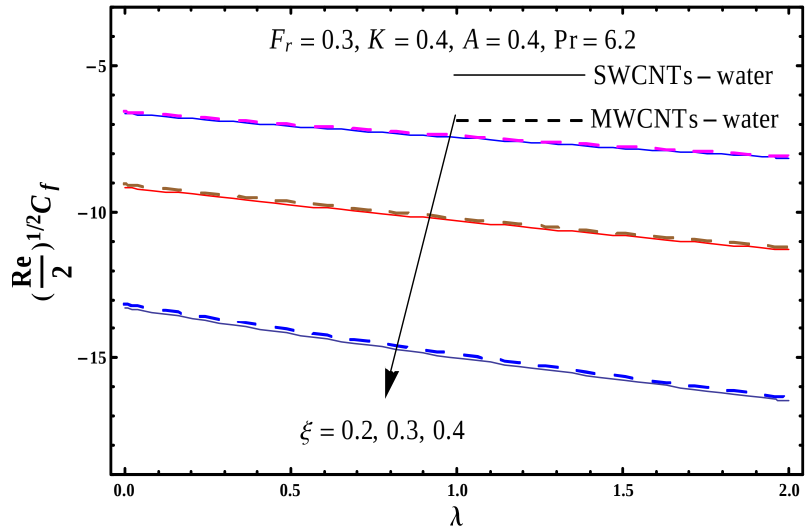

Fig. 5.12: Sketch for $\left(\frac{\mathrm{Re}}{2}\right)^{1/2} C_f$ versus ξ and λ.

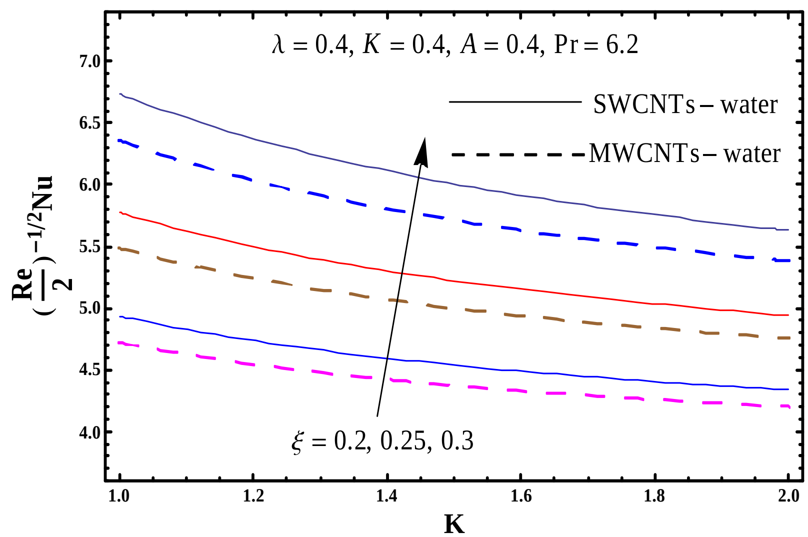

Fig. 5.13: Sketch for $\left(\frac{\mathrm{Re}}{2}\right)^{-1/2} Nu$ versus ξ and K.

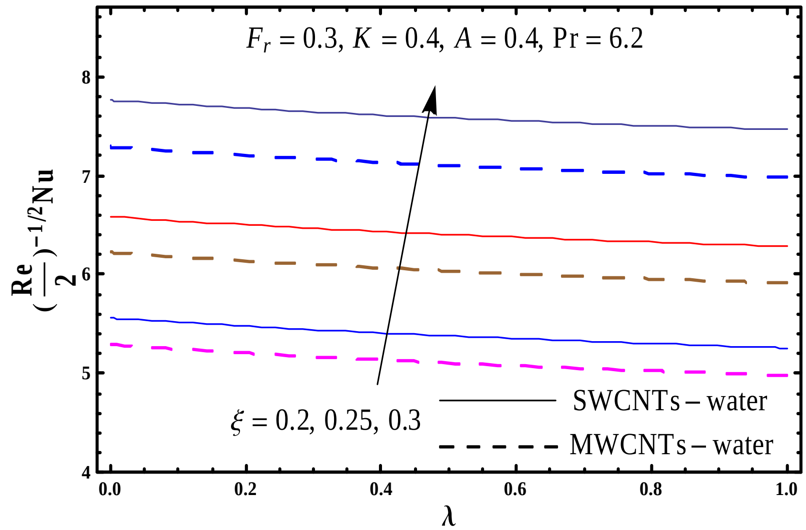

Fig. 5.14: Sketch of $\left(\frac{\mathrm{Re}}{2}\right)^{-1/2} Nu$ against ξ and λ.

Table 5.2: Comparative data of $-\left(\frac{\mathrm{Re}}{2}\right)^{1/2} C_f$ for varying K when $\xi = \lambda = F_r = 0$.

	$-\left(\frac{\mathrm{Re}}{2}\right)^{1/2} C_f$	
K	NDSolve	Okechi et al. [20]
5	1.41962	1.41964
10	1.34672	1.34673
20	1.31353	1.31352

Chapter 6

Impact of heat flux condition in Darcy-Forchheimer nanofluid flow

Flow of water-based carbon nanotubes past an exponentially stretching curved sheet is modelled. Analysis is carried out for imposed flux condition and heat generation/absorption. Darcy-Forchheimer expression is used to characterize the flow in porous space. Carbon nanotubes of two types (recognized as SWCNT and MWCNT) are utilized. Adequate transformations correspond to system of coupled differential equations. The resulting nonlinear system is solved by NDSolve technique. Influences of various pertinent variables for quantities of interest are examined.

6.1 Formulation

Flow of carbon nanotubes dispersed in water induced by curved sheet stretched exponentially coiled in a circle of radius R (see Fig. 6.1) is considered. An incompressible fluid filling porous space is studied by Darcy-Forchheimer relation. Non-uniform heat generation/absorption is accounted. Thermal radiation is not considered. Here $u_w(s) = u_0 e^{s/L}$ is the stretching velocity with $u_0 > 0$. Governing expressions are:

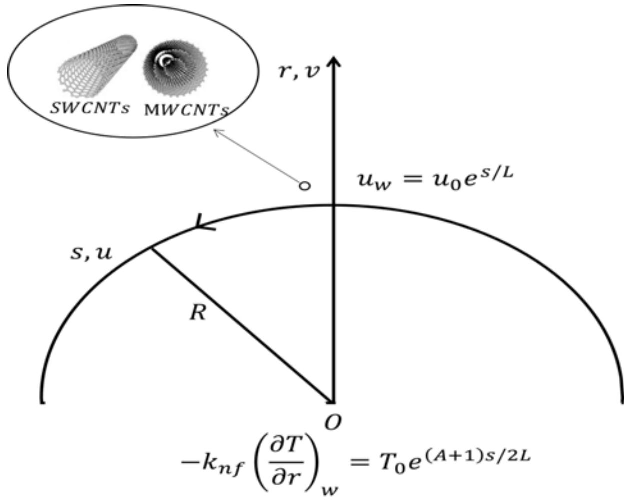

Fig. 6.1: Flow configuration [17].

$$\frac{\partial}{\partial r}\left((r+R)\,v\right) + R\frac{\partial u}{\partial s} = 0, \tag{6.1}$$

$$\frac{u^2}{r+R} = \frac{1}{\rho_{nf}}\frac{\partial p}{\partial r}, \tag{6.2}$$

$$\begin{aligned} v\frac{\partial u}{\partial r} + \frac{R}{r+R}u\frac{\partial u}{\partial s} + \frac{uv}{r+R} &= -\frac{1}{\rho_{nf}}\frac{R}{r+R}\frac{\partial p}{\partial s} \\ &+\nu_{nf}\left(\frac{\partial^2 u}{\partial r^2} + \frac{1}{r+R}\frac{\partial u}{\partial r} - \frac{u}{(r+R)^2}\right) - \frac{\nu_{nf}}{K^*}u - Fu^2, \end{aligned} \tag{6.3}$$

$$v\frac{\partial T}{\partial r} + u\frac{\partial T}{\partial s}\frac{R}{r+R} = \alpha_{nf}\left(\frac{\partial^2 T}{\partial r^2} + \frac{1}{r+R}\frac{\partial T}{\partial r}\right) + \frac{Q}{(\rho c_p)_{nf}}\left(T - T_\infty\right). \tag{6.4}$$

The prescribed conditions are:

$$u = u_0 e^{s/L}, \quad v = 0, \quad -k_{nf}\left(\frac{\partial T}{\partial r}\right)_w = T_0 e^{(A+1)s/2L} \quad \text{at} \quad r = 0, \tag{6.5}$$

$$u \to 0, \quad \frac{\partial u}{\partial r} \to 0, \quad T \to T_\infty \quad \text{as} \quad r \to \infty. \tag{6.6}$$

The theoretical model suggested by Xue [45] gives:

$$\left.\begin{array}{c} \mu_{nf}=\frac{\mu_f}{(1-\xi)^{2.5}},\ \nu_{nf}=\frac{\mu_{nf}}{\rho_{nf}},\ \alpha_{nf}=\frac{k_{nf}}{(\rho c_p)_{nf}},\ \rho_{nf}=\rho_f\left(1-\xi\right)+\rho_{CNT}\xi, \\ (\rho c_p)_{nf}=(\rho c_p)_f\left(1-\xi\right)+(\rho c_p)_{CNT}\,\xi,\ \frac{k_{nf}}{k_f}=\frac{(1-\xi)+2\xi\frac{k_{CNT}}{k_{CNT}-k_f}\ln\frac{k_{CNT}+k_f}{2k_f}}{(1-\xi)+2\xi\frac{k_f}{k_{CNT}-k_f}\ln\frac{k_{CNT}+k_f}{2k_f}}. \end{array}\right\} \tag{6.7}$$

Table 6.1: Thermophysical characteristics of water and CNTs [45].

Physical characteristics	Base fluid	Nanoparticles	
	Water	$SWCNTs$	$MWCNTs$
$\rho\left(kg/m^3\right)$	997.1	2600	1600
$k\,(W/mK)$	0.613	6600	3000
$c_p\,(J/kgK)$	4179	425	796

We consider

$$\begin{array}{c} u=u_0e^{s/L}\frac{\partial f(\eta,\zeta)}{\partial\zeta},\ v=-\frac{R}{r+R}\sqrt{\frac{u_0\nu_f e^{s/L}}{2L}}\left(f+2\eta\frac{\partial f}{\partial\eta}+\zeta\frac{\partial f}{\partial\zeta}\right),\ \zeta=\left(\frac{u_0e^{s/L}}{2\nu_f L}\right)^{1/2}r, \\ T=T_\infty+\frac{T_0}{k_f}e^{\frac{As}{2L}}\sqrt{\frac{2\nu_f L}{u_0}}\theta\left(\eta,\zeta\right),\ p=\rho_f u_0^2e^{2s/L}H\left(\eta,\zeta\right),\ \eta=e^{s/L}. \end{array} \tag{6.8}$$

Equation (6.1) is trivially verified and Eqs. (6.2) – (6.7) yield

$$\frac{1}{\left(1-\xi+\frac{\rho_{CNT}}{\rho_f}\xi\right)}\frac{\partial H}{\partial\zeta}=\frac{1}{\sqrt{\eta}}\frac{1}{\zeta+K}\left(\frac{\partial f}{\partial\zeta}\right)^2, \tag{6.9}$$

$$\begin{array}{c} \frac{1}{(1-\xi)^{2.5}\left(1-\xi+\frac{\rho_{CNT}}{\rho_f}\xi\right)}\left(\frac{\partial^3 f}{\partial\zeta^3}+\frac{1}{\sqrt{\eta}}\frac{1}{\zeta+K}\frac{\partial^2 f}{\partial\zeta^2}-\frac{1}{\eta}\frac{1}{(\zeta+K)^2}\frac{\partial f}{\partial\zeta}-2\frac{\lambda}{\eta}\frac{\partial f}{\partial\zeta}\right)-2F_r\left(\frac{\partial f}{\partial\zeta}\right)^2- \\ \frac{K}{\zeta+K}\left(\frac{2K+\zeta}{\zeta+K}\left(\frac{\partial f}{\partial\zeta}\right)^2-f^2\frac{\partial^2 f}{\partial\zeta^2}-\frac{1}{\zeta+K}f\frac{\partial f}{\partial\zeta}\right)=-\frac{1}{(1-\xi)+\frac{\rho_{CNT}}{\rho_f}\xi}\frac{K}{\zeta+K}\left(4H+2\eta\frac{\partial H}{\partial\eta}+\zeta\frac{\partial H}{\partial\zeta}\right)- \\ \frac{\eta K}{K+\zeta}\left(2\frac{\partial f}{\partial\eta}\frac{\partial f}{\partial\zeta}-\frac{2}{\zeta+K}\frac{\partial f}{\partial\eta}\frac{\partial f}{\partial\zeta}-\frac{\partial^2 f}{\partial\zeta^2}\frac{\partial f}{\partial\eta}\right), \end{array} \tag{6.10}$$

$$\begin{array}{c} \frac{1}{\Pr}\frac{1}{1-\xi+\frac{(\rho c_p)_{CNT}}{(\rho c_p)_f}\xi}\left(\frac{k_{nf}}{k_f}\left(\frac{\partial^2\theta}{\partial\zeta^2}+\frac{1}{\sqrt{\eta}}\frac{1}{\zeta+K}\frac{\partial\theta}{\partial\zeta}\right)+2\Pr\frac{Q^*}{\eta}\theta\right)+ \\ \frac{K}{\zeta+K}\left(f\frac{\partial\theta}{\partial\zeta}-A\theta\frac{\partial f}{\partial\zeta}\right)=2\frac{\eta K}{\zeta+K}\left(\frac{\partial\theta}{\partial\eta}\frac{\partial f}{\partial\zeta}-\frac{\partial\theta}{\partial\zeta}\frac{\partial f}{\partial\eta}\right), \end{array} \tag{6.11}$$

$$f\left(\eta,0\right)=-2\eta\frac{\partial f\left(\eta,0\right)}{\partial\eta},\ \frac{\partial f\left(\eta,0\right)}{\partial\zeta}=1,\ \frac{\partial\theta\left(\eta,0\right)}{\partial\zeta}=-\frac{k_f}{k_{nf}}, \tag{6.12}$$

$$\frac{\partial f(\eta,\infty)}{\partial \zeta}\to 0,\ \frac{\partial^2 f(\eta,\infty)}{\partial \zeta^2}\to 0,\ \theta(\eta,\infty)\to 0, \tag{6.13}$$

Here η is the constant prescribed variable at any streamwise location. To attain similar solutions, we assume that the terms including $\frac{\partial(.)}{\partial\eta}$ are sufficiently small and may be approximated by zero. Thus, we have

$$\frac{1}{\left(1-\xi+\frac{\rho_{CNT}}{\rho_f}\xi\right)}H' = \frac{1}{\sqrt{\eta}}\frac{1}{\zeta+K}f'^2, \tag{6.14}$$

$$\begin{gathered}\frac{1}{(1-\xi)^{2.5}\left(1-\xi+\frac{\rho_{CNT}}{\rho_f}\xi\right)}\left(f'''+\frac{1}{\sqrt{\eta}}\frac{1}{\zeta+K}f''-\frac{1}{\eta}\frac{1}{(\zeta+K)^2}f'-2\frac{\lambda}{\eta}f'\right)-2F_r f'^2-\\ \frac{K}{\zeta+K}\left(\frac{2K+\zeta}{\zeta+K}f'^2-f^2f''-\frac{1}{\zeta+K}ff''\right)=-\frac{1}{(1-\xi)+\frac{\rho_{CNT}}{\rho_f}\xi}\frac{K}{\zeta+K}\left(4H+\zeta H'\right),\end{gathered} \tag{6.15}$$

$$\frac{1}{\Pr}\frac{1}{1-\xi+\frac{(\rho c_p)_{CNT}}{(\rho c_p)_f}\xi}\left(\frac{k_{nf}}{k_f}\left(\theta''+\frac{1}{\sqrt{\eta}}\frac{1}{\zeta+K}\theta'\right)+2\Pr\frac{Q^*}{\eta}\theta\right)+\frac{K}{\zeta+K}\left(f\theta'-A\theta f'\right)=0. \tag{6.16}$$

Eqs. (6.14) and (6.15) after elimination of H give

$$\begin{gathered}\frac{1}{(1-\xi)^{2.5}\left(1-\xi+\frac{\rho_{CNT}}{\rho_f}\xi\right)}\left(\begin{array}{c} f^{iv}+\frac{1}{\eta}\frac{1}{\zeta+K}f'''+\frac{1}{\sqrt{\eta}}\frac{1}{\zeta+K}f'''-\frac{1}{\eta}\frac{1}{(\zeta+K)^2}f''-\\ 2\frac{\lambda}{\eta}\left(f''+\frac{1}{\zeta+K}f'\right)\end{array}\right)+\\ \frac{K}{\zeta+K}\left(ff'''+\frac{1}{\zeta+K}ff''-\frac{1}{(\zeta+K)^2}ff'+\frac{2K+\zeta}{(\zeta+K)^2}f'^2-\frac{1}{\sqrt{\eta}}\frac{4\zeta+5K}{(\zeta+K)^2}f'^2-\frac{3K+\zeta}{\zeta+K}f'f''-\frac{1}{\sqrt{\eta}}\frac{2\zeta}{\zeta+K}f'f''\right)-\\ 2F_r\left(2f'f''+\frac{1}{\zeta+K}f'^2\right)=0,\end{gathered} \tag{6.17}$$

$$f(\eta,0)=0,\ f'(\eta,0)=1,\ \theta'(\eta,0)=-\frac{k_f}{k_{nf}}, \tag{6.18}$$

$$f'(\eta,\infty)\to 0,\ f''(\eta,\infty)\to 0,\ \theta(\eta,\infty)\to 0. \tag{6.19}$$

Involved flow variables are:

$$\lambda=\frac{\nu_f L}{K^* u_0},\ F_r=\frac{C_b L}{K^{*1/2}},\ K=\left(\frac{u_0}{2\nu_f L}\right)^{1/2}R,\ Q^*=\frac{QL}{u_0(\rho c_p)_f},\ \Pr=\frac{\nu_f}{\alpha_f}. \tag{6.20}$$

6.2 Quantities of interest

Coefficient of skin friction and local Nusselt number are

$$\left.\begin{aligned} \left(\tfrac{\mathrm{Re}}{2}\right)^{1/2} C_f = \tfrac{1}{\eta}\tfrac{1}{(1-\xi)^{2.5}}\left(\sqrt{\eta} f''(\eta,0) - \tfrac{1}{K} f'(\eta,0)\right), \\ \left(\tfrac{\mathrm{Re}}{2}\right)^{-1/2} Nu = \tfrac{\sqrt{\eta}\ln\eta}{\theta(\eta,0)}, \end{aligned}\right\} \tag{6.21}$$

in which $\mathrm{Re} = \frac{u_0 L}{\nu_f}$ depicts local Reynolds number.

6.3 Discussion

The local similar solutions of obtained system of equations are computed by employing shooting technique. The behaviors of sundry variables on velocity $f'(\zeta)$ and temperature $\theta(\zeta)$ are interpreted here. The results are attained for two classes of carbon nanotubes (namely single walled carbon nanotubes (SWCNTs) and multi walled carbon nanotubes (MWCNTs). Fig. 6.2 portrayed the velocity $f'(\zeta)$ for (K). Here higher estimation of (K) enhances the velocity field $f'(\zeta)$ for SWCNTs and MWCNTs situations. Fig. 6.3 interprets that velocity $f'(\zeta)$ enhances for larger estimation of (ξ) in SWCNTs and MWCNTs situations. It is revealed from Fig. 6.4 that velocity $f'(\zeta)$ reduces for increasing (F_r) for SWCNTs and MWCNTs. Curves of velocity field $f'(\zeta)$ for (λ) estimations is interpreted in Fig. 6.5. It is analyzed that velocity $f'(\zeta)$ decays for larger (λ) in SWCNTs and MWCNTs situations. Outcome of (K) on $\theta(\zeta)$ is interpreted in Fig. 6.6. Higher (K) constitute weaker temperature field $\theta(\zeta)$ in SWCNTs and MWCNTs cases. Characteristics of (ξ) on $\theta(\zeta)$ are displayed through Fig. 6.7. Here stronger temperature field $\theta(\zeta)$ is observed for larger estimation of (ξ) in SWCNTs and MWCNTs situations. Behavior of temperature field $\theta(\zeta)$ for (F_r) is shown in Fig. 6.8. Clearly temperature $\theta(\zeta)$ enhances via (F_r). Stronger $\theta(\zeta)$ and more related layer thickness is noticed through (λ) for SWCNTs and MWCNTs cases (see Fig. 6.9). Fig. 6.10 depicts outcome for (Q^*) on temperature $\theta(\zeta)$. Clearly $(Q^* > 0)$ leads to heat generation and $(Q^* < 0)$ corresponds to heat absorption. For higher estimation of (Q^*) the temperature field $\theta(\zeta)$ shows increasing trend in SWCNTs and MWCNTs situations. Fig. 6.11 interprets that an increase in (A) yields weaker temperature field $\theta(\zeta)$ in SWCNTs and MWCNTs situations. Table 6.2 is constructed to illustrate skin friction coefficient $-\left(\frac{\mathrm{Re}}{2}\right)^{1/2} C_f$ for numerous values of (K), (λ), (ξ) and (F_r). It is observed that $-\left(\frac{\text{Re}}{2}\right)^{1/2} C_f$ reduces for higher (λ), (F_r) and (K) in SWCNTs and MWCNTs situations. Numerical data of $\left(\frac{\text{Re}}{2}\right)^{-1/2} Nu$ for numerous values of (F_r), (K), (Q^*), (A), (λ) and (ξ) is elaborated in Table 6.3. An augmentation in $\left(\frac{\text{Re}}{2}\right)^{-1/2} Nu$ is analyzed through (λ), (ξ) and (A) in SWCNTs and MWCNTs situations. Table 6.4 provides the validation of present results with existing by Okechi et al. [20] under some special cases. Presented analysis agree very well with Okechi et al. [20].

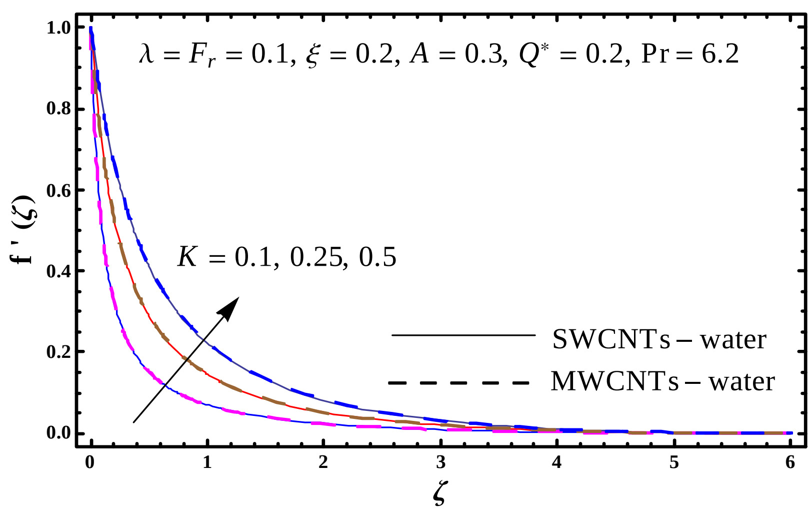

Fig. 6.2: Sketch of $f'(\zeta)$ against K.

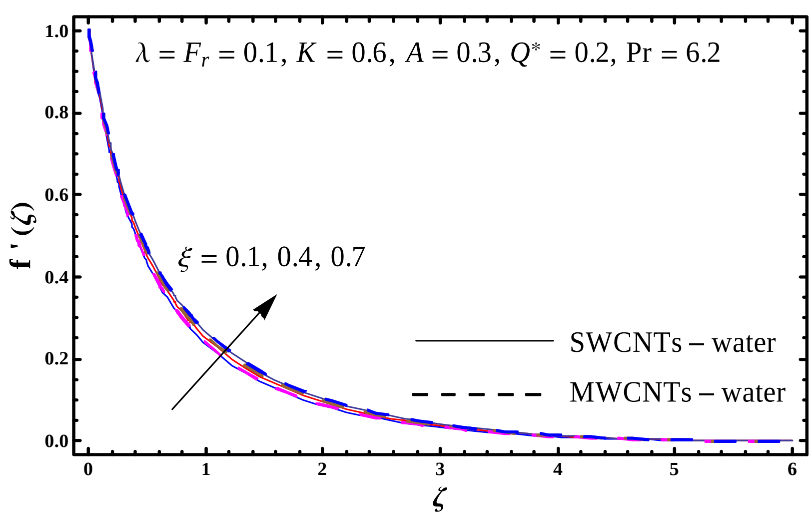

Fig. 6.3: Plot for $f'(\zeta)$ against ξ.

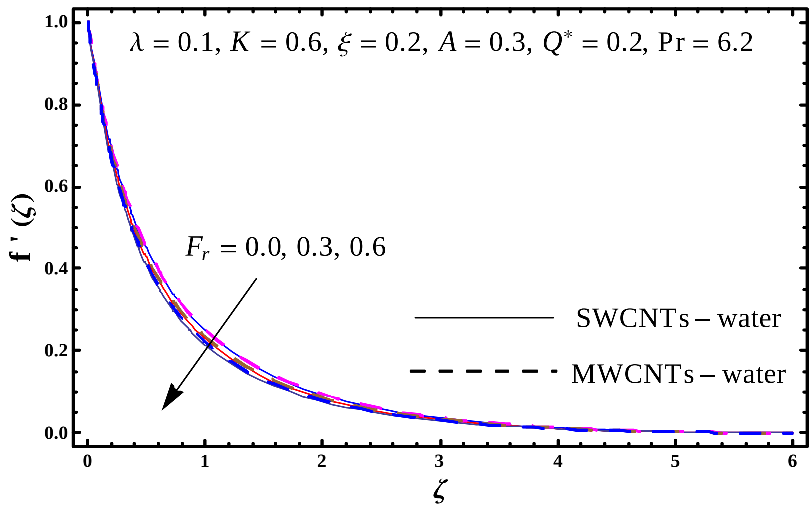

Fig. 6.4: Plot for $f'(\zeta)$ against F_r.

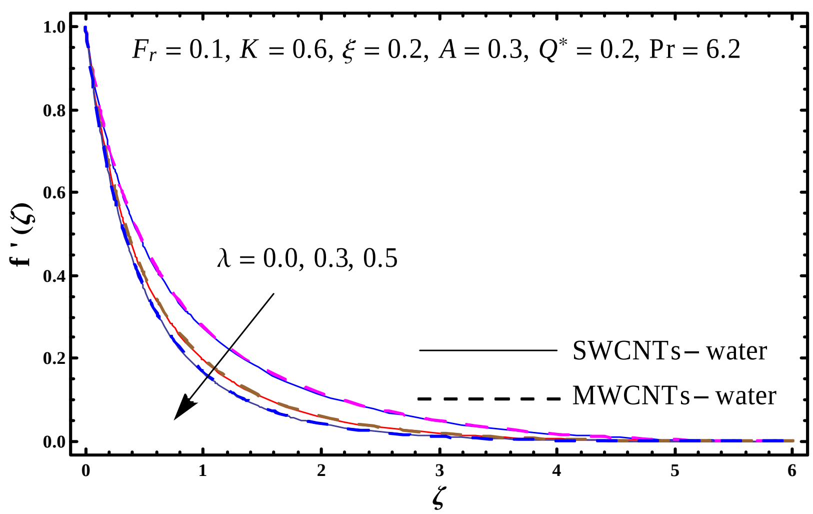

Fig. 6.5: Sketch of $f'(\zeta)$ against λ.

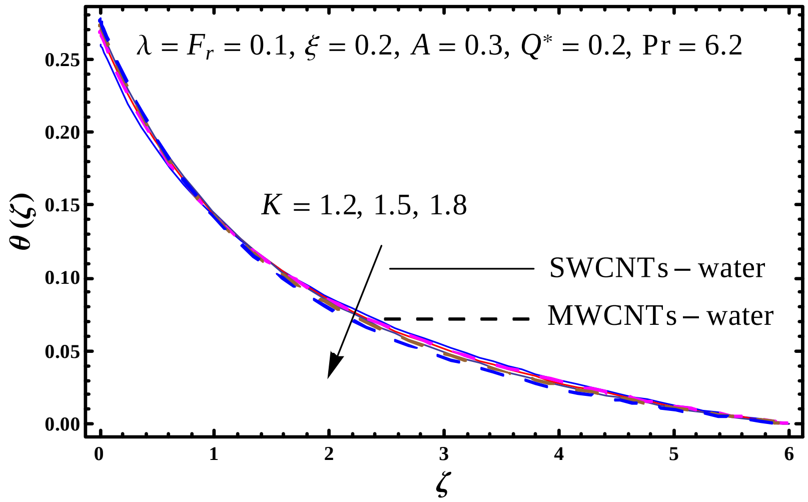

Fig. 6.6: Plot for $\theta(\zeta)$ against K.

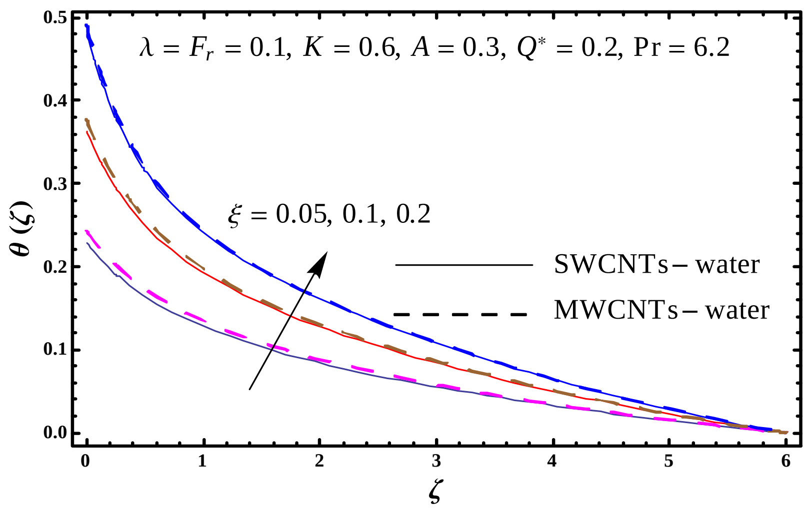

Fig. 6.7: Plot for $\theta(\zeta)$ against ξ.

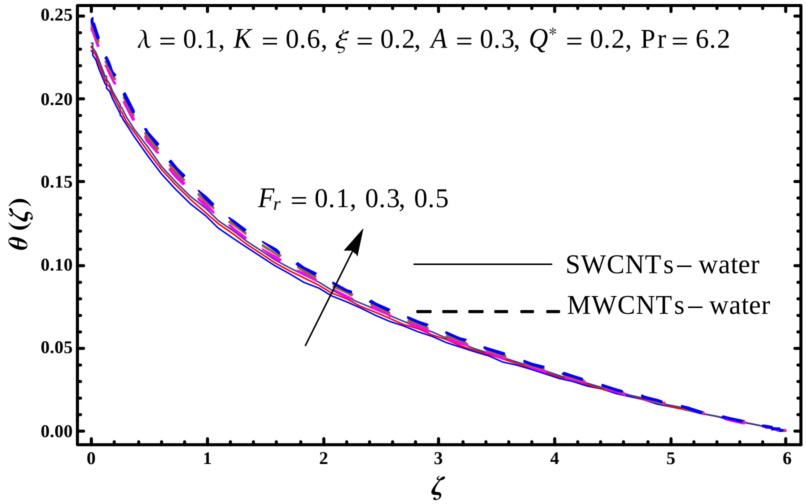

Fig. 6.8: Plot for $\theta(\zeta)$ against F_r.

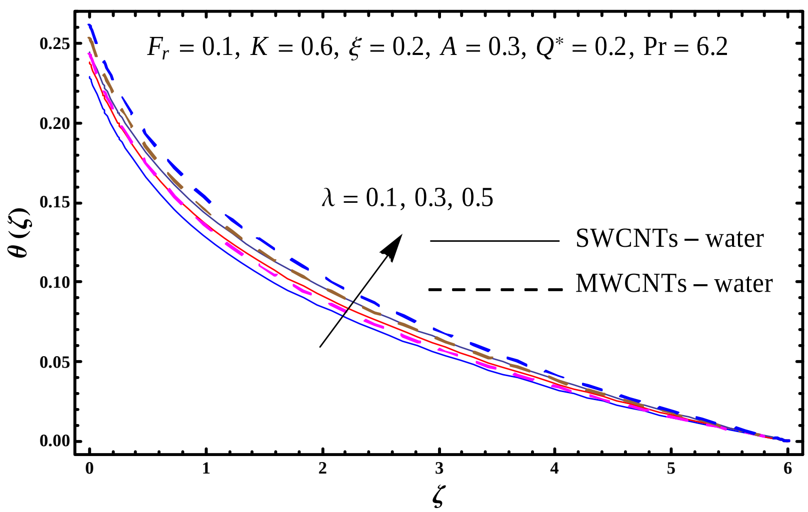

Fig. 6.9: Plot for $\theta(\zeta)$ against λ.

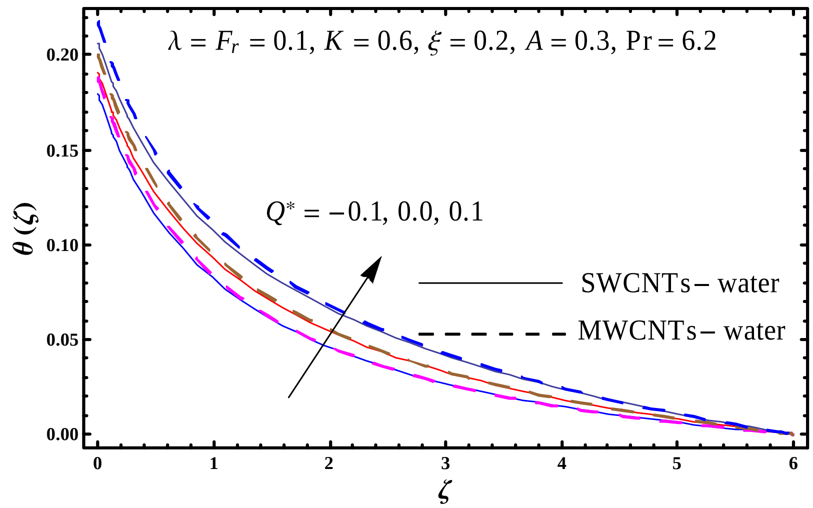

Fig. 6.10: Plot for $\theta(\zeta)$ against Q^*.

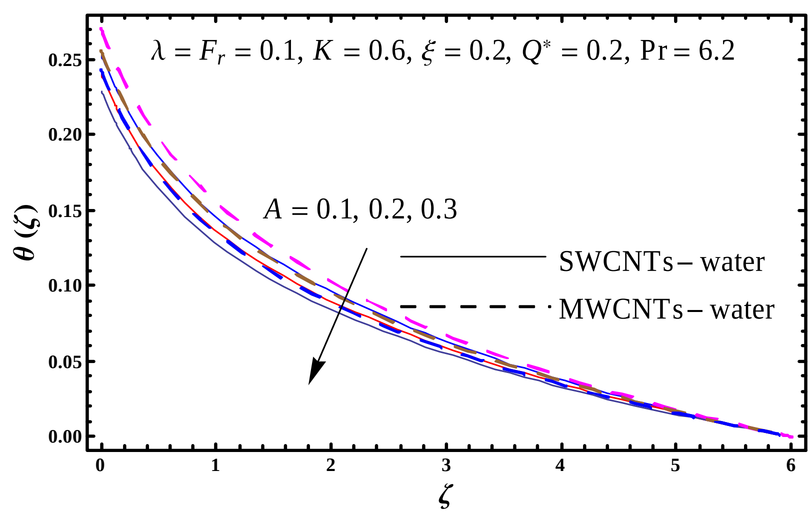

Fig. 6.11: Plot for $\theta(\zeta)$ against A.

Table 6.2: Numerical data of $-\left(\frac{\mathrm{Re}}{2}\right)^{1/2} C_f$ for various values of ξ, λ, F_r and K.

ξ	λ	F_r	K	$-\left(\frac{\mathrm{Re}}{2}\right)^{1/2} C_f$	
				SWCNTs	MWCNTs
0.01	0.1	0.1	0.6	0.04434	0.07564
0.1				0.36564	0.38611
0.2				0.54443	0.59501
0.2	0.2	0.1	0.6	0.61885	0.12284
	0.3			0.12821	0.02032
	0.4			0.05439	0.00493
0.2	0.1	0.2	0.6	0.63233	0.67710
		0.3		0.51760	0.58713
		0.4		0.45857	0.50308
0.2	0.1	0.1	0.7	1.52993	0.59638
			0.8	1.36500	0.55251
			0.9	1.25715	0.49249

Table 6.3: Values for $\left(\frac{\text{Re}}{2}\right)^{-1/2} Nu$ against various values of λ, F_r, Q^*, A, ξ and K.

λ	F_r	ξ	Q^*	A	K	$\left(\frac{\text{Re}}{2}\right)^{-1/2} Nu$	
						SWCNTs	MWCNTs
0.2	0.1	0.2	0.1	0.3	0.6	3.36296	3.09644
0.3						4.83869	3.64728
0.4						5.44634	5.13991
0.1	0.2	0.2	0.1	0.3	0.6	3.48793	3.23967
	0.3					3.45115	3.20464
	0.4					3.41711	3.17192
0.1	0.1	0.01	0.1	0.3	0.6	2.29168	2.26971
		0.1				2.58148	2.52452
		0.2				2.99048	2.86827
0.1	0.1	0.2	0.2	0.3	0.6	3.37912	3.08438
			0.3			1.68195	1.08041
			0.5			1.57049	0.97028
0.1	0.1	0.2	0.1	0.4	0.6	3.76823	3.52554
				0.5		4.00299	3.76717
				0.6		4.23246	4.00261
0.1	0.1	0.2	0.1	0.3	0.7	3.49251	3.28944
					0.8	2.97679	3.30772
					0.9	2.93339	3.32725

Table 6.4: Comparison for $-\left(\frac{\text{Re}}{2}\right)^{1/2} C_f$ against K when $F_r = Q^* = \xi = \lambda = 0$.

K	$-\left(\frac{\text{Re}}{2}\right)^{1/2} C_f$	
	Present results	Okechi et al. [20]
10	1.34682	1.34673
30	1.30283	1.30284
50	1.29443	1.29442
100	1.28872	1.28812
200	1.28561	1.28501

Chapter 7

Outcome of entropy generation in hybrid nanomaterial

Salient characteristics of hybrid nanofluid (MoS_2-SiO_2/water) is analyzed. Variable aspects of permeability and porosity in porous medium are considered. Heat transfer analysis is studied with additional aspects of heat generation/absorption, nonlinear radiation and dissipation. Disturbance in flow is caused by an exponentially stretched curved sheet. Adequate transformations lead to ordinary differential system. Entropy generation is examined. Comparative analysis is done for nanofluid (MoS_2-water and SiO_2-water) and hybrid (MoS_2-SiO_2/water) nanofluid.

7.1 Model development

Here flow of hybrid nanofluid by Darcy-Forchheimer-Brinkman porous is analyzed. Viscous dissipation, heat generation/absorption and non-linear thermal radiation are also taken. Disturbance is flow is created by a curved stretching sheet. Sheet is stretched with an exponential velocity $u_w(s) = u_0 e^{s/L}$ (see Fig. 7.1). Here curvilinear coordinates frame is adopted. Relevant equations for considered problem are:

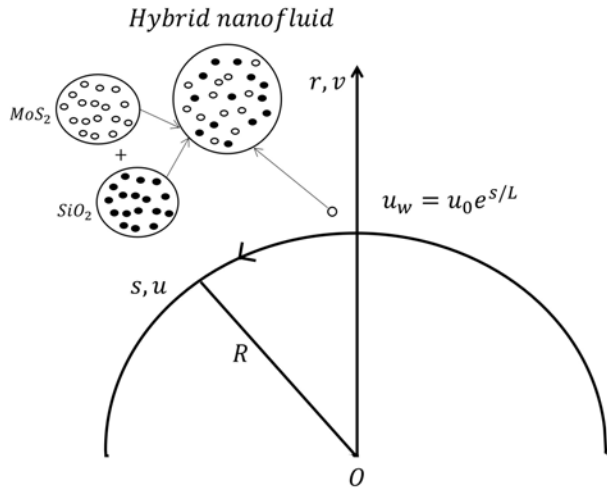

Fig. 7.1: Flow configuration [17].

$$\frac{\partial}{\partial r}\left((r+R)\,v\right)+R\frac{\partial u}{\partial s}=0, \tag{7.1}$$

$$\frac{u^2}{r+R}=\frac{1}{\rho_{hnf}}\frac{\partial p}{\partial r}, \tag{7.2}$$

$$\begin{aligned} v\tfrac{\partial u}{\partial r}+\tfrac{R}{r+R}u\tfrac{\partial u}{\partial s}+\tfrac{uv}{r+R} = -\tfrac{1}{\rho_{hnf}}\tfrac{R}{r+R}\tfrac{\partial p}{\partial s}+ \\ \nu_{hnf}\left(\tfrac{\partial^2 u}{\partial r^2}+\tfrac{1}{r+R}\tfrac{\partial u}{\partial r}-\tfrac{u}{(r+R)^2}\right)-\nu_{hnf}\tfrac{\varepsilon(r)}{K^*(r)}u-\tfrac{C_b\varepsilon^2(r)}{(K^*(r))^{1/2}}u^2, \end{aligned} \tag{7.3}$$

$$\begin{aligned} v\tfrac{\partial T}{\partial r}+u\tfrac{\partial T}{\partial s}\tfrac{R}{r+R}=\alpha_{hnf}\left(\tfrac{\partial^2 T}{\partial r^2}+\tfrac{1}{r+R}\tfrac{\partial T}{\partial r}\right)+\tfrac{\mu_{hnf}}{(\rho c_p)_{hnf}}\left(\tfrac{\partial u}{\partial r}-\tfrac{u}{r+R}\right)^2+ \\ \tfrac{Q}{(\rho c_p)_{hnf}}\left(T-T_\infty\right)-\tfrac{1}{(\rho c_p)_{hnf}}\tfrac{\partial}{\partial r}\left(-\tfrac{16\tilde{\sigma}}{3\epsilon}T^3\tfrac{\partial T}{\partial r}\right)+\tfrac{\mu_{hnf}}{(\rho c_p)_{hnf}}\tfrac{\varepsilon(r)}{K^*(r)}u^2+ \\ \tfrac{\rho_{hnf}}{(\rho c_p)_{hnf}}\tfrac{C_b\varepsilon^2(r)}{(K^*(r))^{1/2}}u^3, \end{aligned} \tag{7.4}$$

$$u=u_0e^{s/L},\quad v=0,\quad T=T_f=T_\infty+T_0e^{As/2L}\quad \text{at}\quad r=0, \tag{7.5}$$

$$u\to 0,\quad \frac{\partial u}{\partial r}\to 0,\quad T\to T_\infty\quad \text{as}\quad r\to\infty, \tag{7.6}$$

where

$$K^*\left(r\right)=K_\infty\left(1+de^{-\frac{r}{\gamma}}\right), \tag{7.7}$$

$$\varepsilon\left(r\right)=\varepsilon_\infty\left(1+d^*e^{-\frac{r}{\gamma}}\right). \tag{7.8}$$

Model for hybrid nanofluid is [55] :

$$\left.\begin{array}{c}\mu_{hnf}=\frac{\mu_f}{(1-\xi_1-\xi_2)^{2.5}},\ \nu_{hnf}=\frac{\mu_{hnf}}{\rho_{hnf}},\ \rho_{hnf}=\rho_f\left(1-\xi_1-\xi_2\right)+\rho_1\xi_1+\rho_2\xi_2,\\ \alpha_{hnf}=\frac{k_{hnf}}{(\rho c_p)_{hnf}},\ \ (\rho c_p)_{hnf}=(\rho c_p)_f\left(1-\xi_1-\xi_2\right)+(\rho c_p)_1\xi_1+(\rho c_p)_2\xi_2,\\ \frac{k_{hnf}}{k_f}=\frac{\xi_1k_1+\xi_2k_2+2\xi k_f+2\xi(\xi_1k_1+\xi_2k_2)-2(\xi_1+\xi_2)^2k_f}{\xi_1k_1+\xi_2k_2+2\xi k_f-\xi(\xi_1k_1+\xi_2k_2)+(\xi_1+\xi_2)^2k_f}.\end{array}\right\}\tag{7.9}$$

Here ξ_1 signifies solid volume fraction of $\mathrm{Si}\,O_2$, ξ_2 the solid volume fraction of MoS_2, ρ_1 the density of $\mathrm{Si}\,O_2$, ρ_2 the density of MoS_2, k_1 the thermal conductivity of $\mathrm{Si}\,O_2$ and k_2 the thermal conductivity of MoS_2. Following Table [55] consists of characteristics of base liquids and nanoparticles.

Physical properties	Base fluid	Nanoparticles	
	H_2O	$\mathrm{Si}\,O_2$	MoS_2
$\rho\left(kg/m^3\right)$	997.1	2650	5060
$k\,(W/mK)$	0.613	1.5	34.5
$c_p\,(J/kgK)$	4179	730	397.746

Considering

$$\begin{array}{c}u=u_0e^{s/L}\frac{\partial f(\eta,\zeta)}{\partial\zeta},\ v=-\frac{R}{r+R}\sqrt{\frac{u_0\nu_fe^{s/L}}{2L}}\left(f+2\eta\frac{\partial f}{\partial\eta}+\zeta\frac{\partial f}{\partial\zeta}\right),\ \zeta=\left(\frac{u_0e^{s/L}}{2\nu_fL}\right)^{1/2}r,\\ T=T_\infty+T_0e^{\frac{As}{2L}}\theta\left(\eta,\zeta\right),\ p=\rho_fu_0^2e^{2s/L}H\left(\eta,\zeta\right),\ \eta=e^{s/L}.\end{array}\tag{7.10}$$

we have

$$\frac{1}{\left(1-\xi_1-\xi_2+\frac{\rho_1}{\rho_f}\xi_1+\frac{\rho_2}{\rho_f}\xi_2\right)}\frac{\partial H}{\partial\zeta}=\frac{1}{\zeta+K}\left(\frac{\partial f}{\partial\zeta}\right)^2,\tag{7.11}$$

$$\begin{array}{c}\frac{1}{(1-\xi_1-\xi_2)^{2.5}\left(1-\xi_1-\xi_2+\frac{\rho_1}{\rho_f}\xi_1+\frac{\rho_2}{\rho_f}\xi_2\right)}\left(\begin{array}{c}\frac{\partial^3f}{\partial\zeta^3}+\frac{1}{\sqrt{\eta}}\frac{1}{\zeta+K}\frac{\partial^2f}{\partial\zeta^2}-\\ \frac{1}{\eta}\frac{1}{(\zeta+K)^2}\frac{\partial f}{\partial\zeta}-2\frac{\lambda}{\eta}\frac{1+d^*e^{-\zeta}}{1+de^{-\zeta}}\frac{\partial f}{\partial\zeta}\end{array}\right)-2F_r\frac{\left(1+d^*e^{-\zeta}\right)^2}{\sqrt{1+de^{-\zeta}}}\left(\frac{\partial f}{\partial\zeta}\right)^2+\\ \frac{K}{\zeta+K}\left(\frac{\zeta+2K}{\zeta+K}\left(\frac{\partial f}{\partial\zeta}\right)^2-f\frac{\partial^2f}{\partial\zeta^2}-\frac{1}{\zeta+K}f\frac{\partial f}{\partial\zeta}\right)=-\frac{1}{\left(1-\xi_1-\xi_2+\frac{\rho_1}{\rho_f}\xi_1+\frac{\rho_2}{\rho_f}\xi_2\right)}\frac{K}{\zeta+K}\left(4H+2\eta\frac{\partial H}{\partial\eta}+\zeta H'\right)+\\ \frac{\eta K}{K+\zeta}\left(2\frac{\partial f}{\partial\eta}\frac{\partial f}{\partial\zeta}-\frac{2}{\zeta+K}\frac{\partial f}{\partial\eta}\frac{\partial f}{\partial\zeta}-\frac{\partial^2f}{\partial\zeta^2}\frac{\partial f}{\partial\eta}\right),\end{array}\tag{7.12}$$

$$\frac{1}{\left(1-\xi_1-\xi_2+\frac{(\rho c_p)_1}{(\rho c_p)_f}\xi_1+\frac{(\rho c_p)_2}{(\rho c_p)_f}\xi_2\right)}\frac{k_{hnf}}{k_f}\left(\frac{\partial^2\theta}{\partial\zeta^2}+\frac{1}{\sqrt{\eta}}\frac{1}{\zeta+K}\frac{\partial\theta}{\partial\zeta}\right)+\Pr\frac{K}{\zeta+K}\left(f\frac{\partial\theta}{\partial\zeta}-A\theta\frac{\partial f}{\partial\zeta}\right)+$$

$$\frac{1}{\left(1-\xi_1-\xi_2+\frac{(\rho c_p)_1}{(\rho c_p)_f}\xi_1+\frac{(\rho c_p)_2}{(\rho c_p)_f}\xi_2\right)}\left(\begin{array}{c} 2\frac{Q^*}{\eta}\Pr\theta-\frac{4}{3}Rd\Pr\frac{\partial}{\partial\zeta}\left(\left((1+(\theta_w-1)\theta)^3\right)\frac{\partial\theta}{\partial\zeta}\right)+\\ \frac{Br}{(1-\xi_1-\xi_2)^{2.5}}\left(\begin{array}{c}\eta^{2-\frac{A}{2}}\left(\frac{\partial^2 f}{\partial\zeta^2}-\frac{1}{\sqrt{\eta}}\frac{1}{\zeta+K}\frac{\partial f}{\partial\zeta}\right)^2+\\ 2\lambda\eta^{-\frac{A}{2}}\frac{1+d^*e^{-\zeta}}{1+de^{-\zeta}}\left(\frac{\partial f}{\partial\zeta}\right)^2\end{array}\right)+\\ 2F_rBr\eta^{-\frac{A}{2}}\left(1-\xi_1-\xi_2+\frac{\rho_1}{\rho_f}\xi_1+\frac{\rho_2}{\rho_f}\xi_2\right)\frac{\left(1+d^*e^{-\zeta}\right)^2}{\sqrt{1+de^{-\zeta}}}\left(\frac{\partial f}{\partial\zeta}\right)^3\end{array}\right)=$$

$$2\eta\left(\frac{\partial f}{\partial\zeta}\frac{\partial\theta}{\partial\eta}-\frac{\partial\theta}{\partial\zeta}\frac{\partial f}{\partial\eta}\right), \tag{7.13}$$

$$f(\eta,0)=-2\eta\frac{\partial f(\eta,0)}{\partial\eta},\ \frac{\partial f(\eta,0)}{\partial\zeta}=1,\ \theta(\eta,0)=1, \tag{7.14}$$

$$\frac{\partial f(\eta,\infty)}{\partial\zeta}\to 0,\ \frac{\partial^2 f(\eta,\infty)}{\partial\zeta^2}\to 0,\ \theta(\eta,\infty)\to 0. \tag{7.15}$$

Here η is the constant prescribed variable at any streamwise location. To attain similar solutions, we assume that the terms including $\frac{\partial(.)}{\partial\eta}$ are sufficiently small and may be approximated by zero. Therefore one obtains

$$\frac{1}{\left(1-\xi_1-\xi_2+\frac{\rho_1}{\rho_f}\xi_1+\frac{\rho_2}{\rho_f}\xi_2\right)}H'=\frac{1}{\sqrt{\eta}}\frac{1}{\zeta+K}f'^2, \tag{7.16}$$

$$\frac{1}{(1-\xi_1-\xi_2)^{2.5}\left(1-\xi_1-\xi_2+\frac{\rho_1}{\rho_f}\xi_1+\frac{\rho_2}{\rho_f}\xi_2\right)}\left(\begin{array}{c} f'''+\frac{1}{\sqrt{\eta}}\frac{1}{\zeta+K}f''-\\ \frac{1}{\eta}\frac{1}{(\zeta+K)^2}f'-2\lambda\frac{1+d^*e^{-\zeta}}{1+de^{-\zeta}}f'\end{array}\right)-2F_r\frac{\left(1+d^*e^{-\zeta}\right)^2}{\sqrt{1+de^{-\zeta}}}f'^2+$$
$$\frac{K}{\zeta+K}\left(\frac{\zeta+2K}{\zeta+K}f'^2-ff''-\frac{1}{\zeta+K}ff'\right)=-\frac{1}{\left(1-\xi_1-\xi_2+\frac{\rho_1}{\rho_f}\xi_1+\frac{\rho_2}{\rho_f}\xi_2\right)}\frac{K}{\zeta+K}\left(4H+\zeta H'\right), \tag{7.17}$$

$$\frac{1}{\left(1-\xi_1-\xi_2+\frac{(\rho c_p)_1}{(\rho c_p)_f}\xi_1+\frac{(\rho c_p)_2}{(\rho c_p)_f}\xi_2\right)}\frac{k_{hnf}}{k_f}\left(\theta''+\frac{1}{\sqrt{\eta}}\frac{1}{\zeta+K}\theta'\right)+\Pr\frac{K}{\zeta+K}\left(f\theta'-A\theta f'\right)+$$
$$\frac{1}{\left(1-\xi_1-\xi_2+\frac{(\rho c_p)_1}{(\rho c_p)_f}\xi_1+\frac{(\rho c_p)_2}{(\rho c_p)_f}\xi_2\right)}\left(\begin{array}{c} 2\frac{Q^*}{\eta}\Pr\theta-\frac{4}{3}Rd\Pr\left(\left((1+(\theta_w-1)\theta)^3\right)\theta'\right)'+\\ \frac{Br}{(1-\xi_1-\xi_2)^{2.5}}\left(\begin{array}{c}\eta^{2-\frac{A}{2}}\left(f''-\frac{1}{\sqrt{\eta}}\frac{1}{\zeta+K}f'\right)^2+\\ 2\lambda\eta^{-\frac{A}{2}}\frac{1+d^*e^{-\zeta}}{1+de^{-\zeta}}f'^2\end{array}\right)+\\ 2F_rBr\eta^{-\frac{A}{2}}\left(1-\xi_1-\xi_2+\frac{\rho_1}{\rho_f}\xi_1+\frac{\rho_2}{\rho_f}\xi_2\right)\frac{\left(1+d^*e^{-\zeta}\right)^2}{\sqrt{1+de^{-\zeta}}}f'^3\end{array}\right)=0. \tag{7.18}$$

Here Eq. (7.1) is trivially verified. Eqs. (7.16) and (7.17) after omission of H yield

$$\frac{1}{(1-\xi_1-\xi_2)^{2.5}\left(1-\xi_1-\xi_2+\frac{\rho_1}{\rho_f}\xi_1+\frac{\rho_2}{\rho_f}\xi_2\right)}\left(\begin{array}{c} f^{iv}+\frac{1}{\eta}\frac{1}{\zeta+K}f'''+\frac{1}{\sqrt{\eta}}\frac{1}{\zeta+K}f'''-\frac{1}{\eta}\frac{1}{(\zeta+K)^2}f''+ \\ \frac{1}{\eta}\frac{1}{(\zeta+K)^3}f'-2\frac{\lambda}{\eta}\left(\begin{array}{c}\frac{1+d^*e^{-\zeta}}{1+de^{-\zeta}}f''+\frac{1}{\zeta+K}\frac{1+d^*e^{-\zeta}}{1+de^{-\zeta}}f'- \\ e^{-\zeta}\frac{d+d^*}{\left(1+de^{-\zeta}\right)^2}f'\end{array}\right)\end{array}\right)+$$

$$\frac{K}{\zeta+K}\left(\begin{array}{c} ff'''+\frac{1}{\zeta+K}ff''-\frac{1}{(\zeta+K)^2}ff'+ \\ \frac{2K+\zeta}{(\zeta+K)^2}f'^2-\frac{1}{\sqrt{\eta}}\frac{4\zeta+5K}{(\zeta+K)^2}f'^2 \\ -\frac{3K+\zeta}{\zeta+K}f'f''-\frac{1}{\sqrt{\eta}}\frac{2\zeta}{\zeta+K}f'f''\end{array}\right)-2F_r\left(\begin{array}{c} 2\frac{\left(1+d^*e^{-\zeta}\right)^2}{\sqrt{1+de^{-\zeta}}}f'f''+\left(\frac{\left(1+d^*e^{-\zeta}\right)^2}{\sqrt{1+de^{-\zeta}}}\right)'f'^2+ \\ \frac{1}{\zeta+K}\frac{\left(1+d^*e^{-\zeta}\right)^2}{\sqrt{1+de^{-\zeta}}}f'^2\end{array}\right)=0, \tag{7.19}$$

$$f(\eta,0)=0,\ f'(\eta,0)=1,\ \theta(\eta,0)=1, \tag{7.20}$$

$$f'(\eta,\infty)\to 0,\ f''(\eta,\infty)\to 0,\ \theta(\eta,\infty)\to 0. \tag{7.21}$$

Here

$$\begin{array}{c} Pe=\mathrm{Re}\,\mathrm{Pr},\ \frac{1}{\gamma}=\sqrt{\frac{\alpha_f}{\nu_f}}\frac{Pe^{1/2}}{\sqrt{2}L},\ \mathrm{Re}=\frac{u_0L}{\nu_f},\ \lambda=\frac{\nu_fL\varepsilon_\infty}{K_\infty u_0},\ K=\left(\frac{u_0}{2\nu_fL}\right)^{1/2}R, \\ F_r=\frac{C_b\varepsilon_\infty^2L}{\sqrt{K_\infty}},\ Rd=\frac{4\tilde{\sigma}T_\infty^3}{\epsilon k_f},\ \theta_w=\frac{T_f}{T_\infty},\ Q^*=\frac{QL}{u_0(\rho c_p)_f},\ Ec=\frac{u_0^2}{T_0(c_p)_f}, \\ \mathrm{Pr}=\frac{\nu_f}{\alpha_f},\ Br=\mathrm{Pr}\,Ec. \end{array} \tag{7.22}$$

7.2 Entropy generation

Entropy generation expression for considered flow problem is

$$S'''_{gen}=\underbrace{\frac{k_{hnf}}{T_m^2}\left(\frac{\partial T}{\partial r}\right)^2}_{Thermal\ irreversibility}+\underbrace{\frac{\mu_{hnf}}{T_m}\left(\frac{\partial u}{\partial r}-\frac{u}{r+R}\right)^2}_{Viscous\ dissipation\ irreversibility}+\underbrace{\frac{Q}{T_m}(T-T_\infty)}_{Heat\ generation/absorption\ irreversibility}+$$
$$\underbrace{\frac{1}{T_m}\frac{\partial}{\partial r}\left(-\frac{16\tilde{\sigma}}{3\epsilon}T^3\frac{\partial T}{\partial r}\right)}_{Thermal\ radiation\ irreversibility}+\underbrace{\frac{\mu_{hnf}}{T_m}\frac{\varepsilon(r)}{K^*(r)}u^2+\frac{C_b\varepsilon^2(r)\rho_{hnf}}{T_mK^{*1/2}}u^3}_{Porous\ dissipation\ irreversibility}, \tag{7.23}$$

Applying transformations (7.10) , above expression reduces to

$$N_g(\zeta) = \frac{k_{hnf}}{k_f}\alpha_1\eta^{1+\frac{A}{2}}\theta'^2 + 2\Pr Q^*\theta + \frac{4}{3}\eta Rd\left(\left(1+(\theta_w-1)\theta\right)^3\theta'\right)' + \frac{Br}{(1-\xi_1-\xi_2)^{2.5}}\left(\eta^{3-\frac{A}{2}}\left(f'' - \frac{1}{\zeta+K}f'\right)^2 + 2\lambda\eta^{2-\frac{A}{2}}\frac{1+d^*e^{-\zeta}}{1+de^{\zeta}}f'^2\right) + 2F_r Br\eta^{3-\frac{A}{2}}\left(1-\xi_1-\xi_2+\frac{\rho_1}{\rho_f}\xi_1+\frac{\rho_2}{\rho_f}\xi_2\right)\frac{\left(1+d^*e^{-\zeta}\right)^2}{\sqrt{1+de^{-\zeta}}}f'^3, \tag{7.24}$$

where

$$\alpha_1 = \frac{\Delta T}{T_m},\ N_g = \frac{S'''_{gen}}{\alpha_1}\frac{2\nu_f L}{u_0 k_f}. \tag{7.25}$$

7.3 Physical quantities

The following expressions of coefficient of skin friction and local Nusselt number hold

$$\left.\begin{array}{c} \left(\frac{\mathrm{Re}}{2}\right)^{1/2}C_f = \frac{1}{\eta}\frac{1}{(1-\xi_1-\xi_2)^{2.5}}\left(\sqrt{\eta}f''(\eta,0) - \frac{1}{K}f'(\eta,0)\right), \\ \left(\frac{\mathrm{Re}}{2}\right)^{-1/2}Nu = -\sqrt{\eta}\ln\eta\left(\frac{k_{hnf}}{k_f} + \frac{4}{3}\theta_w^3 Rd\right)\theta'(\eta,0). \end{array}\right\} \tag{7.26}$$

7.4 Discussion

This section interprets the characteristics of velocity $f'(\zeta)$, temperature $\theta(\zeta)$ and entropy generation rate $N_g(\zeta)$ through (K), (λ), (d), (d^*), (F_r), (Br), (A), (θ_w), (Rd) and (Q^*). Comparison is made between hybrid nanofluid (MoS_2-SiO_2/water) and nanofluid (MoS_2/water and SiO_2/ water). The consequences of $f'(\zeta)$ against (K) are in Fig. 7.2. An enhancement in is observed through for both hybrid nanofluid and nanomaterial. Physically the bend of the curved stretching sheet contributes in accelerating the flow. The impact of (λ) on $f'(\zeta)$ is illustrated in Fig. 7.3. Here $f'(\zeta)$ is a decreasing function of (ξ) for both hybrid nanofluid and nanomaterial. Reverse trend of $f'(\zeta)$ is noted for (d) and (d^*) in both hybrid nanofluid and nanomaterial (see Figs. 7.4 and 7.5). Fig. 7.6 is plotted for the features of $f'(\zeta)$ through (F_r). Higher estimation of (F_r) lead to a reduction in $f'(\zeta)$ for both hybrid nanofluid (MoS_2-SiO_2/water) and nanomaterial (MoS_2/water and SiO_2/ water). Fig. 7.7 addressed $\theta(\zeta)$ against (K). By increasing (K) reduction is observed in $\theta(\zeta)$ for both hybrid nanofluid and nanomaterial. Fig. 7.8 captured consequences of $\theta(\zeta)$ against (λ). Here enhancement in $\theta(\zeta)$ is analyzed through higher (λ) for both hybrid nanofluid and nanomaterial. Behaviors of $\theta(\zeta)$ through (d) and (d^*) is portrayed in Figs. 7.9 and 7.10. An enhancement in $\theta(\zeta)$ is observed through (d^{*}) while opposite trend is seen against (d) for both hybrid nanofluid and nanomaterial. Aspects of $\theta(\zeta)$ against (F_r) is deliberated in Fig. 7.11. Higher (F_r) produces resilience in the fluid motion due to which more heat is produced which strengthens the thermal field $\theta(\zeta)$ for both hybrid nanofluid (MoS_2-SiO_2/water) and nanofluid (MoS_2/water and SiO_2/ water). Fig. 7.12 cleared that $\theta(\zeta)$ is an increasing function of (Br) for both hybrid nanofluid and nanomaterial. Physically (Br) has a direct relation with heat generation by fluid friction which causes stronger $\theta(\zeta)$. Significant behavior of $\theta(\zeta)$ through (A) is drawn in Fig. 7.13. Higher (A) produces weaker $\theta(\zeta)$ in both hybrid nanofluid and nanomaterial. Curves of $\theta(\zeta)$ against (Rd) is elucidated in Fig. 7.14. Higher estimation of (Rd) strengthen $\theta(\zeta)$ and more related layer thickness for both hybrid nanofluid and nanomaterial. Variation of $\theta(\zeta)$ through (θ_w) is shown in Fig. 7.15. Here higher (θ_w) enhance $\theta(\zeta)$ for both hybrid nanofluid (MoS_2-SiO_2/water) and nanomaterial (MoS_2/water and SiO_2/ water). Role of (Q^{*}) on $\theta(\zeta)$ is highlighted in Fig. 7.16. Here an augmentation in $\theta(\zeta)$ is observed through (Q^{*}) for both hybrid nanofluid and nanomaterial. Influence of (K) on $N_g(\zeta)$ is depicted in Fig. 7.17. Entropy generation rate decreases due to higher (K) for both hybrid nanofluid and nanomaterial. Fig. 7.18 and 7.19 analyzed the behavior of $N_g(\zeta)$ against (Br) and (Rd). Similar trend of $N_g(\zeta)$ is witnessed through (Br) and (Rd) for both hybrid nanofluid and nanomaterial. Fig. 7.20 illustrates that $N_g(\zeta)$ increases for higher (θ_w) for both hybrid nanofluid (MoS_2-SiO_2/water) and nanomaterial (MoS_2/water and SiO_2/ water). Impact of (Q^{*}) on $N_g(\zeta)$ is sketched in Fig. 7.21. Higher (Q^{*}) produces augmentation in $N_g(\zeta)$ due to rise in surface temperature for both hybrid nanofluid and nanomaterial. Consequences of (α_1) on $N_g(\zeta)$ is highlighted in Fig. 7.22. Here $N_g(\zeta)$ is an increasing function of (α_1) for both hybrid nanofluid and nanomaterial. Contribution of involved variables on skin friction coefficient $\left(\frac{\mathrm{Re}}{2}\right)^{1/2} C_f$ is displayed in Table 7.2. Reduction in $\left(\frac{\mathrm{Re}}{2}\right)^{1/2} C_f$ is seen through (K), (d) and (F_r) for both hybrid nanofluid and nanofluid. Significant behavior of $\left(\frac{\mathrm{Re}}{2}\right)^{-1/2} Nu$ through influential parameters is shown in Table 7.3. Here (K), (d), (Rd) and (θ_w) strengthen the $\left(\frac{\mathrm{Re}}{2}\right)^{-1/2} Nu$ for both hybrid nanofluid and nanomaterial. Table 7.4 is drawn to compare the values of skin friction coefficient with Okechi et al. [20]. Comparison is excellent.

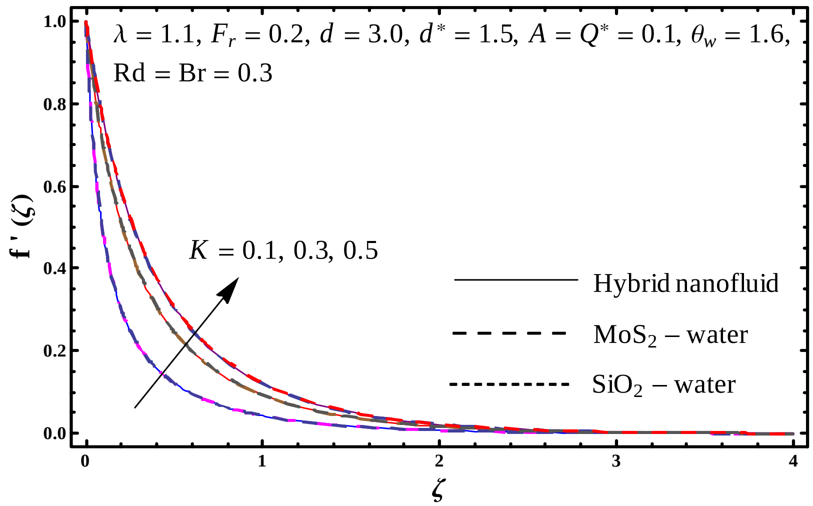

Fig. 7.2: Sketch of $f'(\zeta)$ against K.

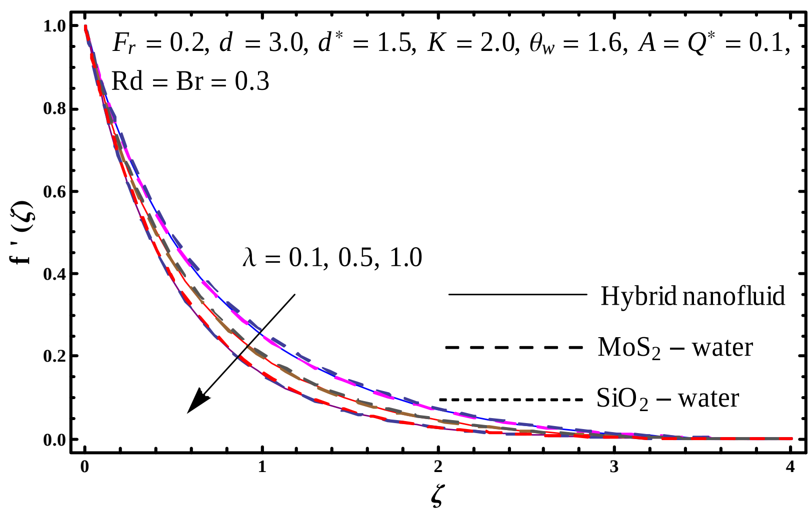

Fig. 7.3: Plot for $f'(\zeta)$ against λ.

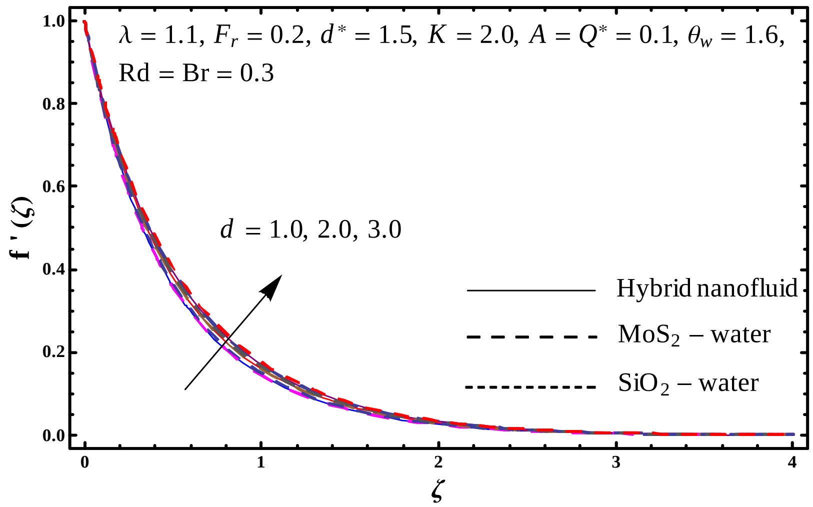

Fig. 7.4: Plot for $f'(\zeta)$ against d.

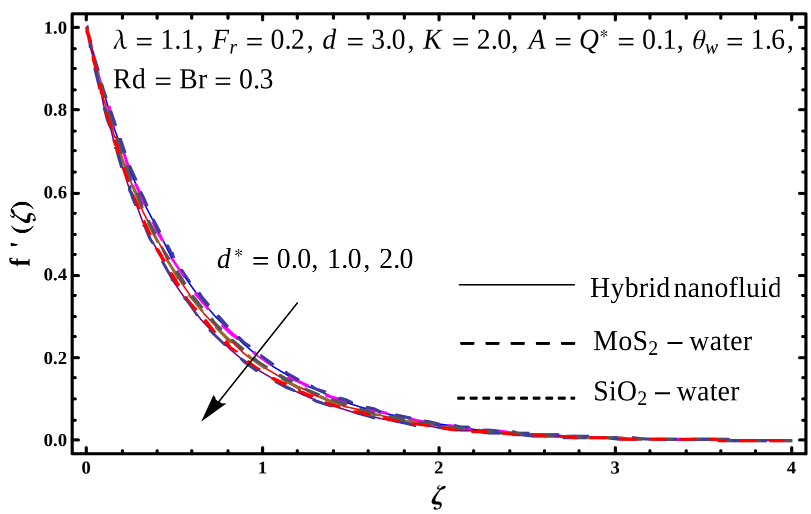

Fig. 7.5: Plot for $f'(\zeta)$ against d^*.

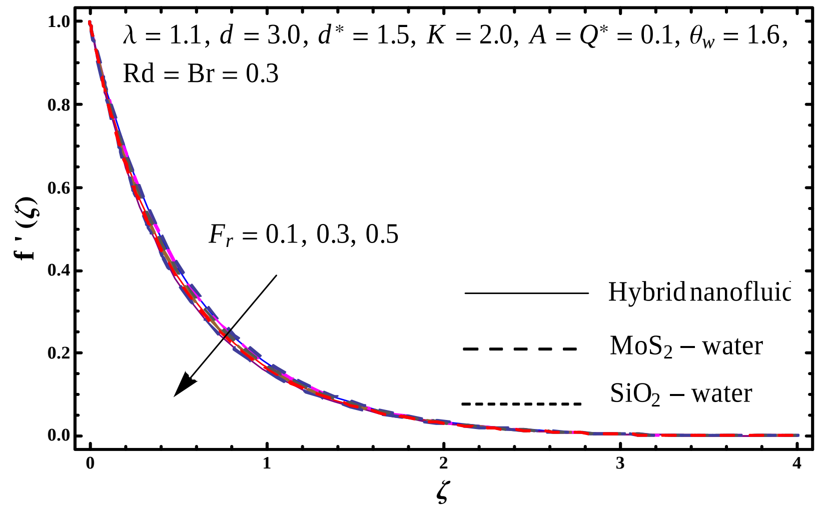

Fig. 7.6: Plot for $f'(\zeta)$ against F_r.

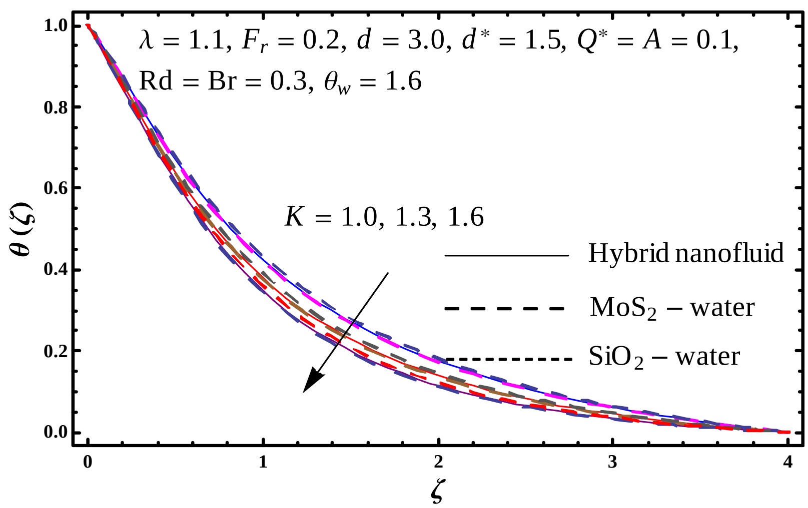

Fig. 7.7: Plot for $\theta(\zeta)$ against K.

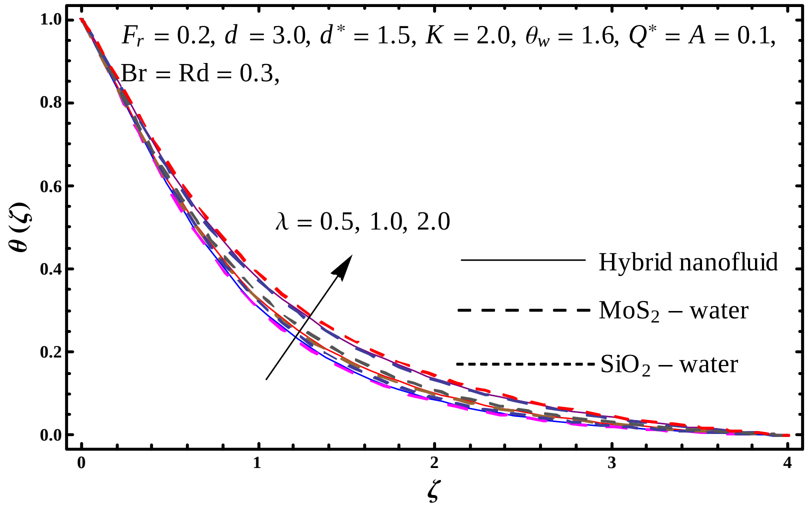

Fig. 7.8: Plot for $\theta(\zeta)$ against λ.

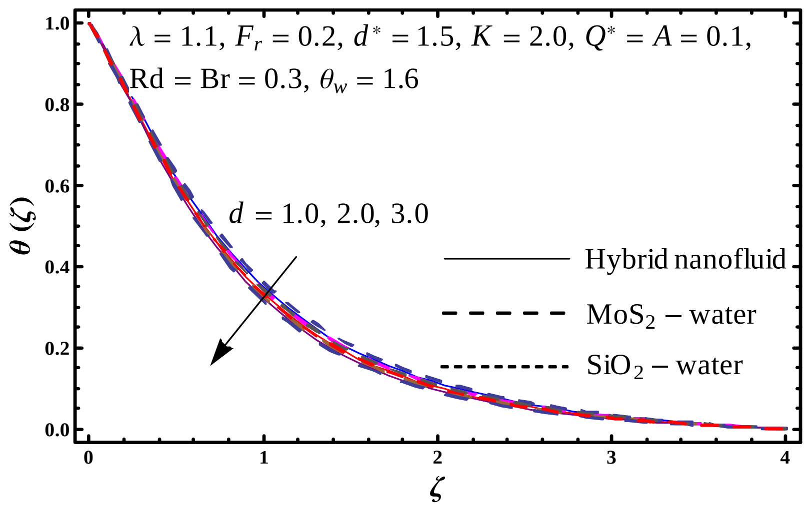

Fig. 7.9: Plot for $\theta(\zeta)$ against d.

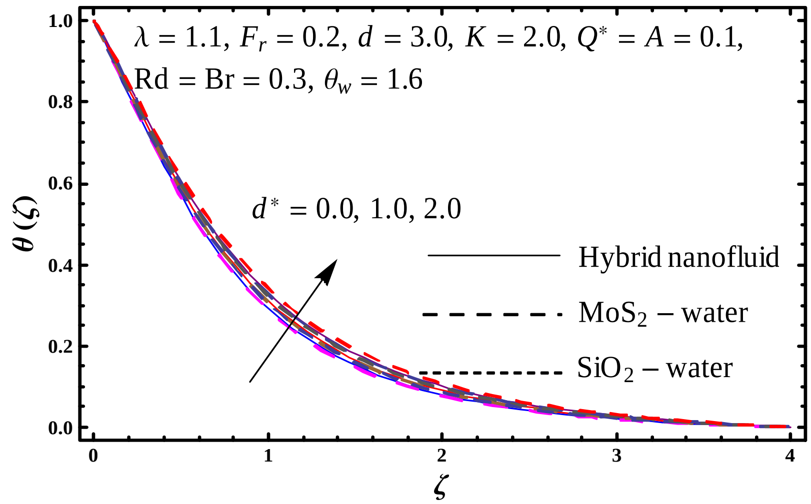

Fig. 7.10: Plot for $\theta(\zeta)$ against d^*.

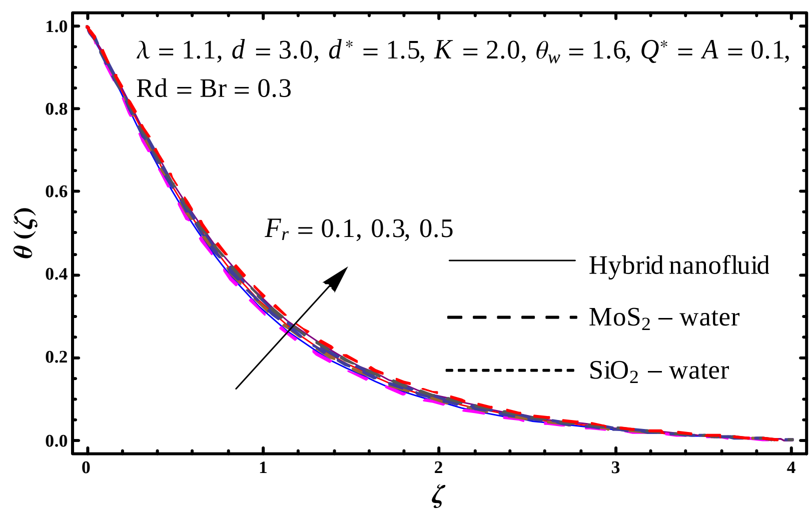

Fig. 7.11: Plot for $\theta(\zeta)$ against F_r.

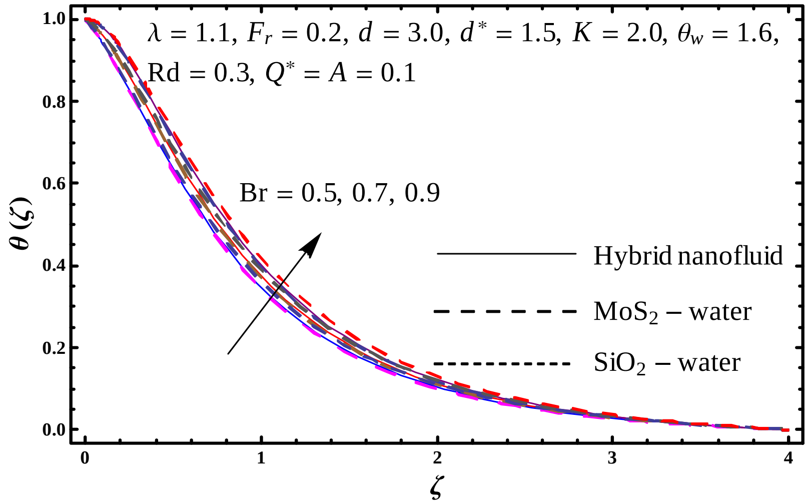

Fig. 7.12: Plot for $\theta(\zeta)$ against Br.

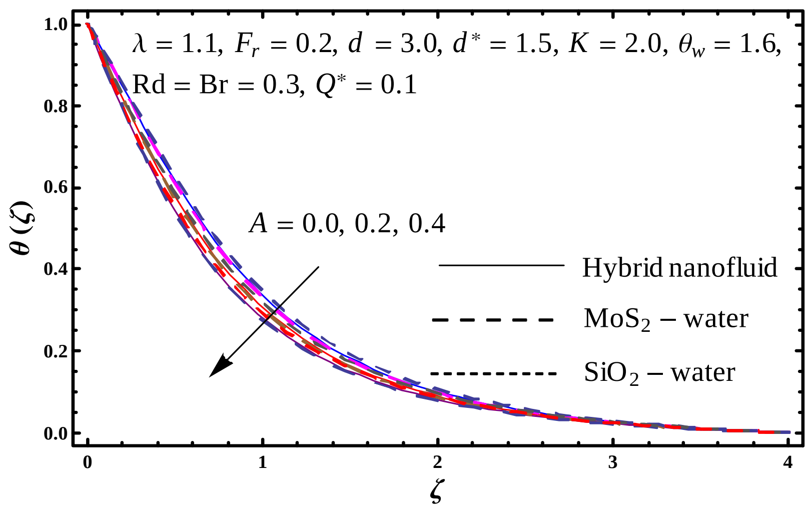

Fig. 7.13: Plot for $\theta(\zeta)$ against A.

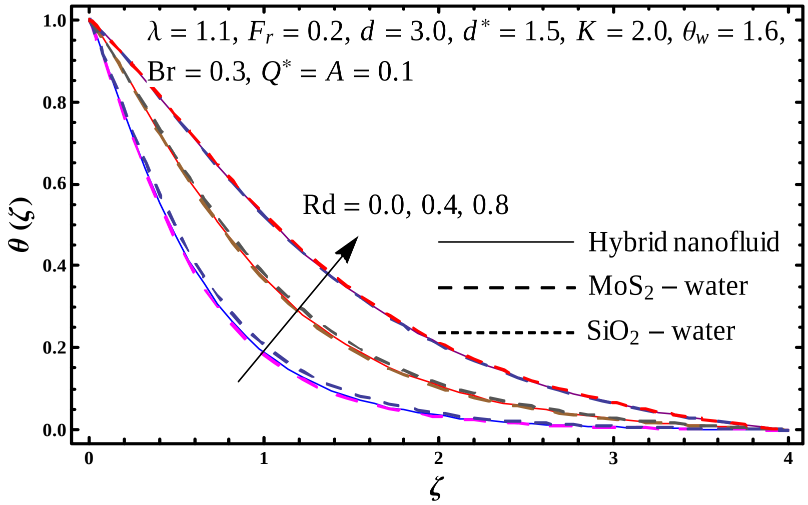

Fig. 7.14: Plot for $\theta(\zeta)$ against Rd.

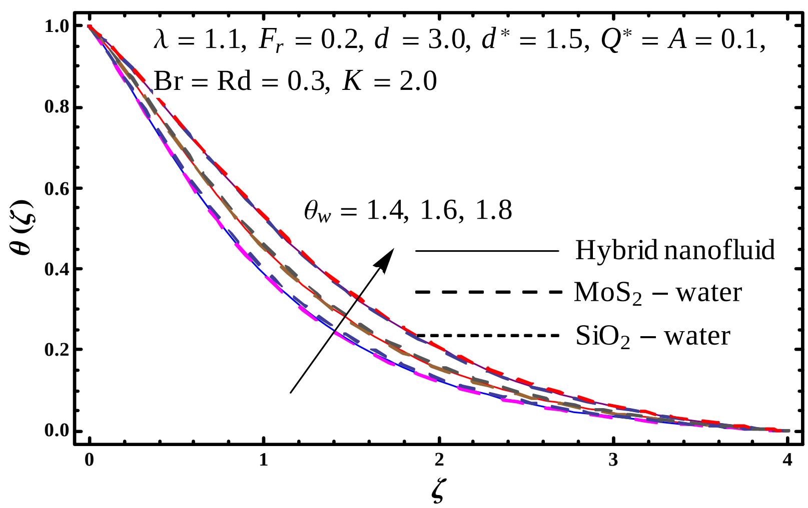

Fig. 7.15: Plot for $\theta(\zeta)$ against θ_w.

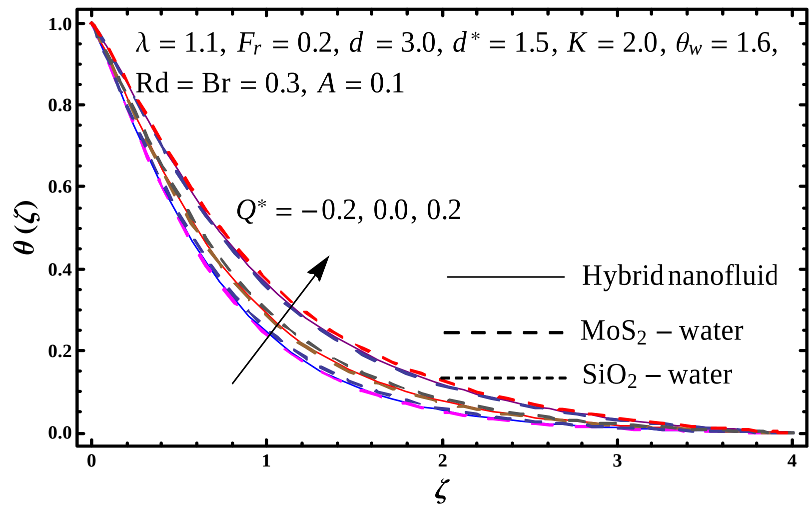

Fig. 7.16: Plot for $\theta(\zeta)$ against Q^{*}.

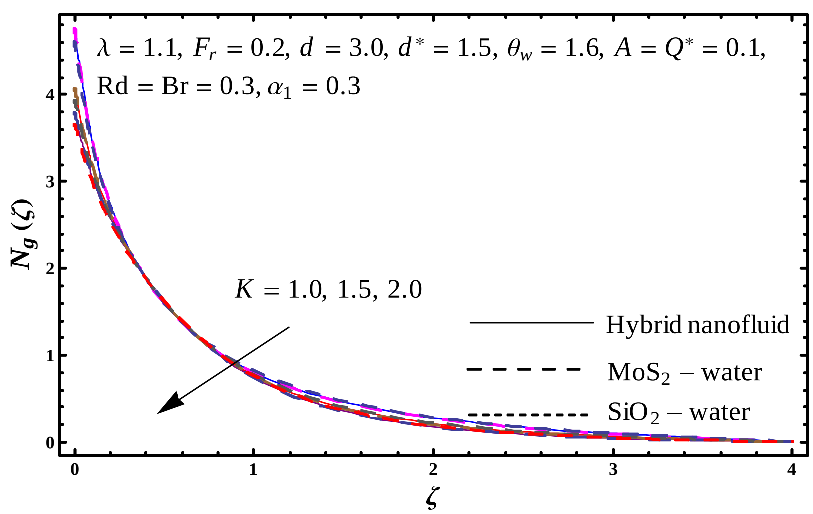

Fig. 7.17: Plot for $N_g(\zeta)$ against K.

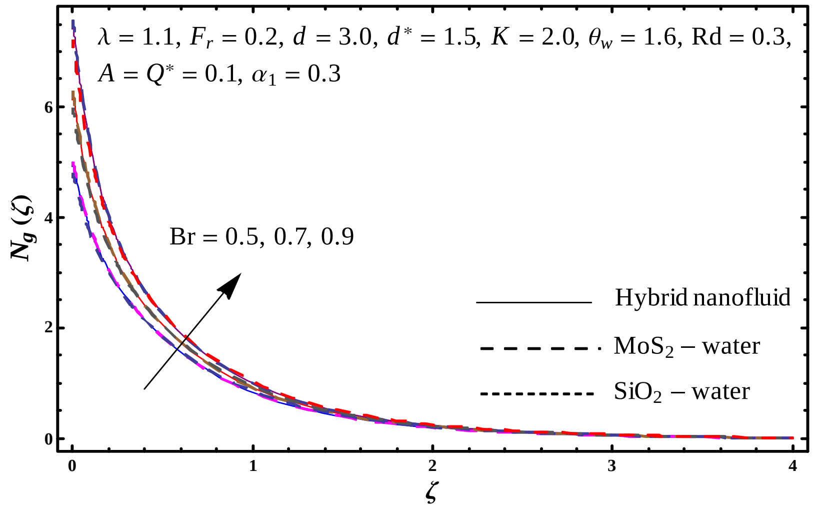

Fig. 7.18: Plot for $N_g(\zeta)$ against Br.

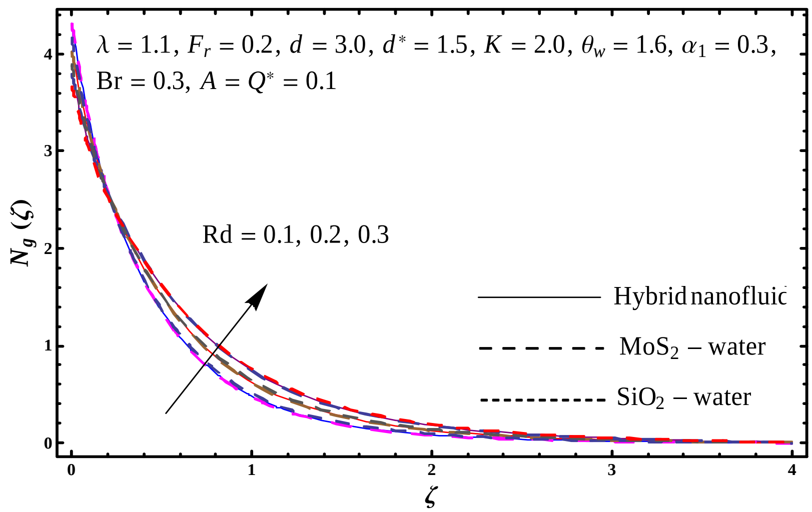

Fig. 7.19: Plot for $N_g(\zeta)$ against Rd.

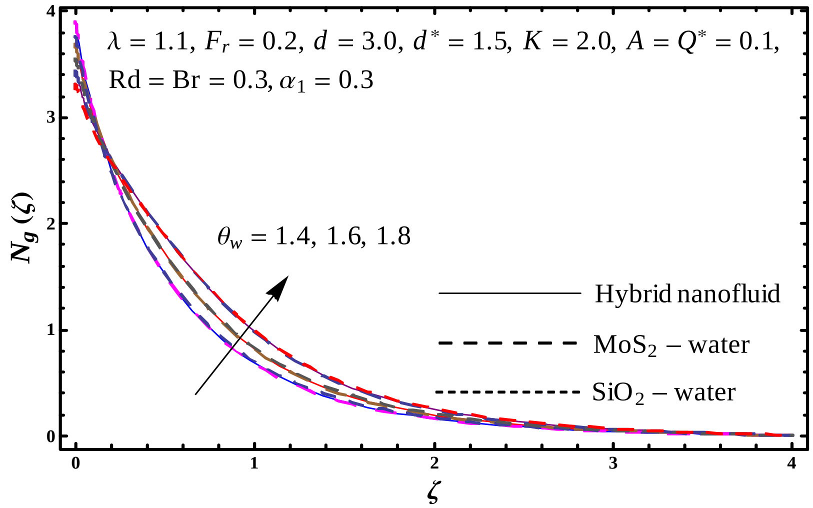

Fig. 7.20: Plot for $N_g(\zeta)$ against θ_w.

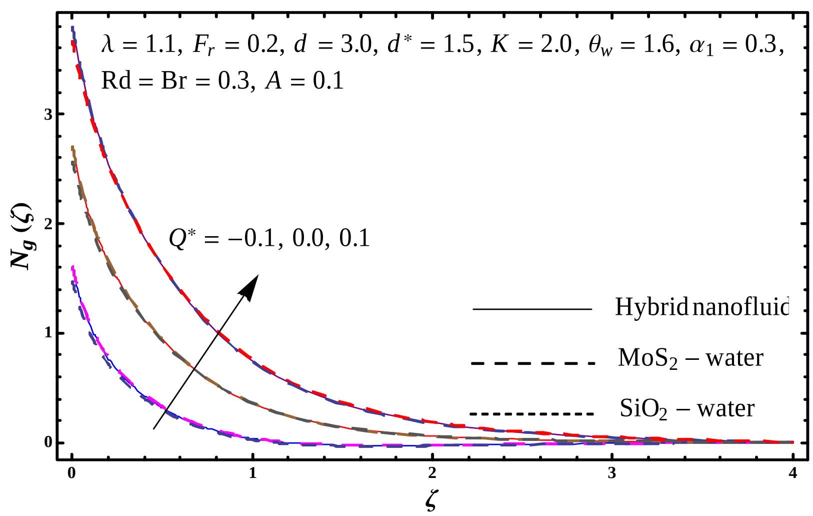

Fig. 7.21: Plot for $N_g(\zeta)$ against Q^*.

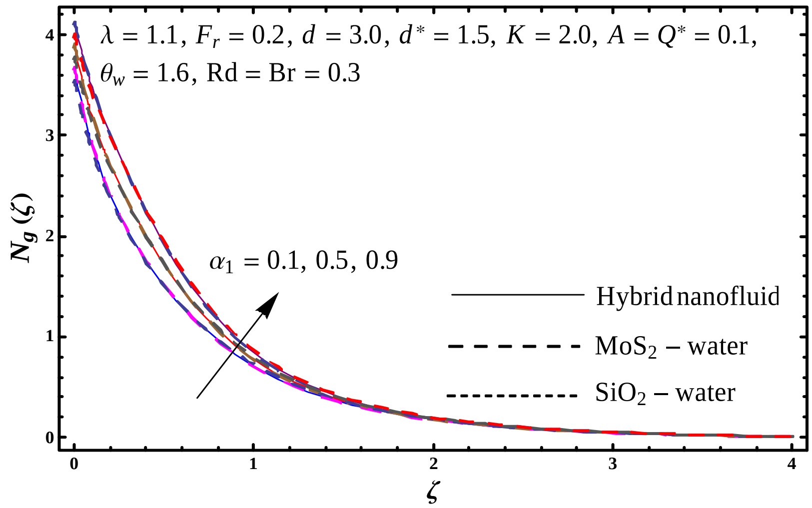

Fig. 7.22: Sketch of $N_g\,(\zeta)$ against α_1.

Table 7.2: Skin friction coefficient $\left(\frac{\mathrm{Re}}{2}\right)^{1/2} C_f$ for K, λ, d, d^* and F_r.

K	λ	d	d^*	F_r	$-\left(\frac{\mathrm{Re}}{2}\right)^{1/2} C_f$		
					Hybrid nanofluid	MoS_2-water	SiO_2-water
1.0	1.1	3.0	1.5	0.2	3.84238	3.85225	3.79266
1.3					3.41971	3.43047	3.36545
1.5					3.23852	3.24971	3.18205
2.0	0.5	3.0	1.5	0.2	2.77804	2.79077	2.71364
	1.0				3.04036	3.05193	2.98189
	2.0				3.46423	3.47433	3.41334
2.0	1.1	1.0	1.5	0.2	3.24720	3.25959	3.18459
		2.0			3.06787	3.07997	3.00672
		3.0			2.95453	2.96646	2.89425
2.0	1.1	3.0	0.0	0.2	2.64363	2.65338	2.59446
			1.0		2.84189	2.85292	2.78613
			2.0		3.07546	3.08842	3.00990
2.0	1.1	3.0	1.5	0.0	2.74260	2.75107	2.69994
				0.1	2.85047	2.86073	2.79873
				0.3	3.05515	3.06865	2.98681

Table 7.3: Local Nusselt number $\left(\frac{\mathrm{Re}}{2}\right)^{-1/2} Nu$ for K, λ, d, d^{*}, F_r, Br, Rd, θ_w and Q^{*}.

K	λ	d	d^{*}	F_r	Br	Rd	θ_w	Q^{*}	$\left(\frac{\mathrm{Re}}{2}\right)^{-1/2} Nu$		
									Hybrid nanofluid	MoS_2-water	SiO_2-water
1.0	1.1	3.0	1.5	0.2	0.3	0.3	1.6	0.1	0.78812	0.77888	0.78773
1.3									0.95609	0.94689	0.96164
1.6									1.06312	1.05373	1.07280
2.0	0.5	3.0	1.5	0.2	0.3	0.3	1.6	0.1	1.12602	1.11725	1.13271
	1.0								1.10578	1.09692	1.11589
	2.0								0.94486	0.93801	0.94759
2.0	1.1	1.0	1.5	0.2	0.3	0.3	1.6	0.1	0.95681	0.94929	0.96096
		2.0							1.07907	1.07021	1.08903
		3.0							1.15619	1.14646	1.16977
2.0	1.1	3.0	0.0	0.2	0.3	0.3	1.6	0.1	1.36447	1.35379	1.38047
			1.0						1.23024	1.22030	1.24414
			2.0						1.07829	1.06870	1.09196
2.0	1.1	3.0	1.5	0.0	0.3	0.3	1.6	0.1	1.28077	1.27229	1.28646
				0.1					1.21696	1.20783	1.22679
				0.3					1.09811	1.08785	1.11512
2.0	1.1	3.0	1.5	0.2	0.5	0.3	1.6	0.1	0.75746	0.75223	0.74922
					0.6				0.55799	0.55499	0.53882
					0.7				0.35843	0.35767	0.32834
2.0	1.1	3.0	1.5	0.2	0.3	0.0	1.6	0.1	1.09425	1.08172	1.11263
						0.4			1.19772	1.18872	1.21607
						0.8			1.25805	1.24707	1.27647
2.0	1.1	3.0	1.5	0.2	0.3	0.3	1.4	0.1	1.18662	1.17787	1.19835
							1.6		1.19562	1.18716	1.20711
							1.8		1.19871	1.19025	1.21112
2.0	1.1	3.0	1.5	0.2	0.3	0.3	1.6	−0.2	1.55119	1.53599	1.57635
								0.0	1.30480	1.29301	1.32259
								0.2	0.97895	0.97161	0.98815

Table 7.4: Skin friction coefficient $-\left(\frac{\mathrm{Re}}{2}\right)^{1/2} C_f$ for distinct values of K.

K	$-\left(\frac{\mathrm{Re}}{2}\right)^{1/2} C_f$	
	Okechi et al. [20]	Present
5	1.41962	1.457033
10	1.34671	1.368192
20	1.31351	1.328104
30	1.30282	1.315362
40	1.29750	1.309121
50	1.29444	1.305391
100	1.28812	1.298042
200	1.28502	1.294433
1000	1.28263	1.291524

Chapter 8

Nanofluid flow by rotating disk with slip conditions

This chapter intends to illustrate the velocity and thermal slip effects in Darcy-Forchheimer flow by a rotating disk. Viscous dissipation is considered. Carbon nanotubes of two types (recognized as SWCNTs and MWCNTs) are utilized. Suitable variables are introduced for conversion of partial differential expressions into ordinary differential system. Computation of nonlinear system is arranged by Optimal homotopic analysis technique (OHAM). Behaviors of involved variables on quantities of interest are graphically examined.

8.1 Model development

Flow of carbon nanotubes saturating porous medium is analyzed. Rotating disk at $z = 0$ creates the flow. Velocity and temperature slip conditions are implemented. Viscous dissipation is also accounted. Disk rotates subject to constant angular frequency ω. Here $(u,\ v,\ w)$ denote velocity components along $(r,\ \psi,\ z)$. Relevant equations for 3D flow satisfy

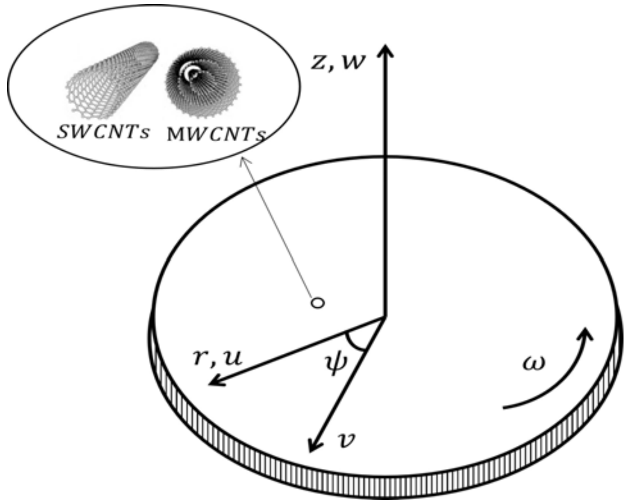

Fig. 8.1: Flow configuration.

$$\frac{\partial u}{\partial r}+\frac{u}{r}+\frac{\partial w}{\partial z}=0, \tag{8.1}$$

$$u\frac{\partial u}{\partial r}-\frac{v^2}{r}+w\frac{\partial u}{\partial z}=\nu_{nf}\left(\frac{\partial^2 u}{\partial z^2}\right)-\frac{\nu_{nf}}{K^*}u-Fu\sqrt{u^2+v^2}, \tag{8.2}$$

$$u\frac{\partial v}{\partial r}+\frac{uv}{r}+w\frac{\partial v}{\partial z}=\nu_{nf}\left(\frac{\partial^2 v}{\partial z^2}\right)-\frac{\nu_{nf}}{K^*}v-Fv\sqrt{u^2+v^2}, \tag{8.3}$$

$$u\frac{\partial T}{\partial r}+w\frac{\partial T}{\partial z}=\alpha_{nf}\left(\frac{\partial^2 T}{\partial z^2}\right)-\frac{\mu_{nf}}{(\rho c_p)_{nf}}\left[\left(\frac{\partial v}{\partial z}\right)^2+\left(\frac{\partial u}{\partial z}\right)^2\right], \tag{8.4}$$

$$u=N_1\frac{\partial u}{\partial z},\quad v=r\omega+N_1\frac{\partial v}{\partial z},\quad w=0,\quad T=T_w+N_2\frac{\partial T}{\partial z}\quad \text{at}\quad z=0, \tag{8.5}$$

$$u\to 0,\quad v\to 0,\quad T\to T_\infty,\quad \text{as}\quad z\to\infty. \tag{8.6}$$

By Xue model [45] one has

$$\left.\begin{array}{l}\mu_{nf}=\frac{\mu_f}{(1-\xi)^{2.5}},\ \nu_{nf}=\frac{\mu_{nf}}{\rho_{nf}},\ \alpha_{nf}=\frac{k_{nf}}{(\rho c_p)_{nf}},\ \rho_{nf}=\rho_f(1-\xi)+\rho_{CNT}\xi,\\ (\rho c_p)_{nf}=(\rho c_p)_f(1-\xi)+(\rho c_p)_{CNT}\,\xi,\ \frac{k_{nf}}{k_f}=\frac{(1-\xi)+2\xi\frac{k_{CNT}}{k_{CNT}-k_f}\ln\frac{k_{CNT}+k_f}{2k_f}}{(1-\xi)+2\xi\frac{k_f}{k_{CNT}-k_f}\ln\frac{k_{CNT}+k_f}{2k_f}}.\end{array}\right\} \tag{8.7}$$

Table 8.1: Characteristics for water and CNTs [45].

Physical properties	Water	Nanoparticles	
		$SWCNTs$	$MWCNTs$
ρ $\left(kg/m^3\right)$	997.1	2600	1600
k (W/mK)	0.613	6600	3000
c_p (J/kgK)	4179	425	796

We set

$$u = r\omega\frac{\partial f(\eta,\zeta)}{\partial\zeta},\ v = r\omega g(\eta,\zeta),\ w = -\sqrt{\frac{\omega\nu_f}{2}}\left(f + \eta\frac{\partial f}{\partial\eta}\right),$$
$$\theta(\eta,\zeta) = \frac{T-T_\infty}{T_w-T_\infty},\ \zeta = \left(\frac{2\omega}{\nu_f}\right)^{1/2} z,\ \eta = \frac{r}{\bar{R}}. \tag{8.8}$$

Equation (8.1) is trivially verified and Eqs. (8.2) – (8.7) yield

$$\frac{1}{(1-\xi)^{2.5}\left(1-\xi+\frac{\rho_{CNT}}{\rho_f}\xi\right)}\left(2\frac{\partial^3 f}{\partial\zeta^3} - \lambda\frac{\partial f}{\partial\zeta}\right) + 2f\frac{\partial^2 f}{\partial\zeta^2} - \left(\frac{\partial f}{\partial\zeta}\right)^2 + g^2 - F_r\eta\left(\left(\frac{\partial f}{\partial\zeta}\right)^2 + \frac{1}{2}g^2\right) =$$
$$\eta\left(\frac{\partial f}{\partial\zeta}\frac{\partial^2 f}{\partial\zeta\partial\eta} - \frac{\partial f}{\partial\eta}\frac{\partial^2 f}{\partial\zeta^2}\right), \tag{8.9}$$

$$\frac{1}{(1-\xi)^{2.5}\left(1-\xi+\frac{\rho_{CNT}}{\rho_f}\xi\right)}\left(2\frac{\partial^2 g}{\partial\zeta^2} - \lambda g\right) + 2f\frac{\partial g}{\partial\zeta} - 2g\frac{\partial f}{\partial\zeta} - F_r\eta\left(g^2 + \frac{1}{2}\left(\frac{\partial f}{\partial\zeta}\right)^2\right) =$$
$$\eta\left(\frac{\partial f}{\partial\eta}\frac{\partial g}{\partial\zeta} - \frac{\partial f}{\partial\zeta}\frac{\partial g}{\partial\eta}\right), \tag{8.10}$$

$$\frac{2}{\Pr}\frac{1}{1-\xi+\frac{(\rho c_p)_{CNT}}{(\rho c_p)_f}\xi}\frac{k_{nf}}{k_f}\frac{\partial^2\theta}{\partial\zeta^2} + 2f\frac{\partial\theta}{\partial\zeta} + \frac{2Ec\eta^2}{(1-\xi)^{2.5}\left(1-\xi+\frac{(\rho c_p)_{CNT}}{(\rho c_p)_f}\xi\right)}\left(\left(\frac{\partial^2 f}{\partial\zeta^2}\right)^2 + \left(\frac{\partial g}{\partial\zeta}\right)^2\right) =$$
$$\eta\left(\frac{\partial f}{\partial\zeta}\frac{\partial\theta}{\partial\eta} - \frac{\partial f}{\partial\eta}\frac{\partial\theta}{\partial\zeta}\right), \tag{8.11}$$

$$2f(\eta,0) = -\eta\frac{\partial f(\eta,0)}{\partial\eta},\ \frac{\partial f(\eta,0)}{\partial\zeta} = \gamma_1\frac{\partial^2 f(\eta,0)}{\partial\zeta},\ g(\eta,0) = 1 + \gamma_1\frac{\partial g(\eta,0)}{\partial\zeta},$$
$$\theta(\eta,0) = 1 + \gamma_2\frac{\partial\theta(\eta,0)}{\partial\zeta}, \tag{8.12}$$

$$\frac{\partial f(\eta,\infty)}{\partial\zeta} \to 0,\ g(\eta,\infty) \to 0,\ \theta(\eta,\infty) \to 0. \tag{8.13}$$

We set variables as

$$\gamma_1 = N_1\sqrt{\frac{2\omega}{\nu_f}},\ \gamma_2 = N_2\sqrt{\frac{2\omega}{\nu_f}},\ F_r = \frac{C_b}{K^{*1/2}}\bar{R},\ \lambda = \frac{\nu_f}{\omega K^*},$$
$$Ec = \frac{\bar{R}^2\omega^2}{(T_w-T_\infty)(c_p)_f},\ \Pr = \frac{\nu_f}{\alpha_f}. \tag{8.14}$$

8.1.1 First order of truncation

In first order of truncation, the terms including $\frac{\partial(.)}{\partial\eta}$ are assumed to be very small and may be approximated by zero. We have

$$\frac{1}{(1-\xi)^{2.5}\left(1-\xi+\frac{\rho_{CNT}}{\rho_f}\xi\right)}\left(2f'''-\lambda f'\right)+2ff''-f'^2+g^2-F_r\eta\left(f'^2+\frac{1}{2}g^2\right)=0, \tag{8.15}$$

$$\frac{1}{(1-\xi)^{2.5}\left(1-\xi+\frac{\rho_{CNT}}{\rho_f}\xi\right)}\left(2g''-\lambda g\right)+2fg'-2gf'-F_r\eta\left(g^2+\frac{1}{2}f'^2\right)=0, \tag{8.16}$$

$$\frac{2}{\Pr}\frac{1}{1-\xi+\frac{(\rho c_p)_{CNT}}{(\rho c_p)_f}\xi}\frac{k_{nf}}{k_f}\theta''+2f\theta'+\frac{2Ec\eta^2}{(1-\xi)^{2.5}\left(1-\xi+\frac{(\rho c_p)_{CNT}}{(\rho c_p)_f}\xi\right)}\left(f''^2+g'^2\right)=0, \tag{8.17}$$

$$f(\eta,0)=0,\ f'(\eta,0)=\gamma_1 f''(\eta,0),\ g(\eta,0)=1+\gamma_1 g'(\eta,0),\ \theta(\eta,0)=1+\gamma_2\theta'(\eta,0), \tag{8.18}$$

$$f'(\eta,\infty)\to 0,\ g(\eta,\infty)\to 0,\ \theta(\eta,\infty)\to 0. \tag{8.19}$$

8.1.2 Second order of truncation

In order to approach non-similarity solutions of Eqs. $(8.9)-(8.13)$, we write

$$f^*=\frac{\partial f}{\partial\eta},\ g^*=\frac{\partial g}{\partial\eta},\ \theta^*=\frac{\partial\theta}{\partial\eta}\text{ and }\frac{\partial f^*}{\partial\eta}=\frac{\partial g^*}{\partial\eta}=\frac{\partial\theta^*}{\partial\eta}=0. \tag{8.20}$$

Taking partial derivatives of Eqs. $(8.9)-(8.13)$ with respect to η, we have

$$\frac{1}{(1-\xi)^{2.5}\left(1-\xi+\frac{\rho_{CNT}}{\rho_f}\xi\right)}\left(2f^{*\prime\prime\prime}-\lambda f^{*\prime}\right)+2f^*f''+2ff^{*\prime\prime}-2ff^{*\prime}+2gg^*-F_r\left(f'^2+\tfrac{1}{2}g^2\right)- \\ F_r\eta\left(2f'f^{*\prime}+gg^*\right)=f'f^{*\prime}-f^*f''+\eta\left(f^{*\prime 2}-f^*f^{*\prime\prime}\right), \tag{8.21}$$

$$\frac{1}{(1-\xi)^{2.5}\left(1-\xi+\frac{\rho_{CNT}}{\rho_f}\xi\right)}\left(2g^{*\prime\prime}-\lambda g^*\right)+2f^*g'+2fg^{*\prime}-2g^*f'-2gf^{*\prime}-F_r\left(g^2+\tfrac{1}{2}f'^2\right)- \\ F_r\eta\left(2gg^*+f'f^{*\prime}\right)=f^*g'-f'g^*+\eta\left(f^*g^{*\prime}-g^*f^{*\prime}\right), \tag{8.22}$$

$$\frac{2}{\Pr}\frac{1}{1-\xi+\frac{(\rho c_p)_{CNT}}{(\rho c_p)_f}\xi}\frac{k_{nf}}{k_f}\theta^{*\prime\prime}+2f^*\theta'+2f\theta^{*\prime}+\frac{2Ec\eta^2}{(1-\xi)^{2.5}\left(1-\xi+\frac{(\rho c_p)_{CNT}}{(\rho c_p)_f}\xi\right)}\left(2f''f^{*\prime\prime}+2g'g^{*\prime}\right)+$$
$$\frac{4Ec\eta}{(1-\xi)^{2.5}\left(1-\xi+\frac{(\rho c_p)_{CNT}}{(\rho c_p)_f}\xi\right)}\left(f''^2+g'^2\right)=f'\theta^*-f^*\theta'+\eta\left(f^{*\prime}\theta^*-\theta^{*\prime}f^*\right), \tag{8.23}$$

$$f^*(\eta,0)=0,\ \ f^{*\prime}(\eta,0)=\gamma_1 f^{*\prime\prime}(\eta,0),\ \ g^*(\eta,0)=\gamma_1 g^{*\prime}(\eta,0),\ \ \theta^*(\eta,0)=\gamma_2\theta^{*\prime}(\eta,0), \tag{8.24}$$

$$f^{*\prime}(\eta,\infty)\to 0,\ \ g^*(\eta,\infty)\to 0,\ \ \theta^*(\eta,\infty)\to 0. \tag{8.25}$$

8.2 Physical quantities

Coefficients of skin friction and local Nusselt number obey

$$\left.\begin{array}{l}\left(\frac{\mathrm{Re}}{2}\right)^{1/2}C_f=\frac{1}{\eta}\frac{1}{(1-\xi)^{5/2}}f''(\eta,0),\\ \left(\frac{\mathrm{Re}}{2}\right)^{1/2}C_g=\frac{1}{\eta}\frac{1}{(1-\xi)^{5/2}}g'(\eta,0),\\ \left(\frac{\mathrm{Re}}{2}\right)^{-1/2}Nu=-\eta\frac{k_{nf}}{k_f}\theta'(\eta,0),\end{array}\right\} \tag{8.26}$$

Here $\mathrm{Re}=\frac{\bar{R}^2\omega}{\nu_f}$ shows local Reynolds number. It is observed that present investigation reduces to classical Von-Karman flow when $\lambda=F_r=\gamma_1=\gamma_2=Ec=0$.

8.3 OHAM Solutions

The optimal series arrangement of nonlinear system is developed by optimal homotopic analysis algorithm (OHAM). We select

$$f_0(\zeta)=0,\quad g_0(\zeta)=\frac{1}{1+\gamma_1}e^{-\zeta},\quad \theta_0(\zeta)=\frac{1}{1+\gamma_2}e^{-\zeta}, \tag{8.27}$$

$$\mathcal{L}_f=\frac{d^3f}{d\zeta^3}-\frac{df}{d\zeta},\quad \mathcal{L}_g=\frac{d^2g}{d\zeta^2}-g,\quad \mathcal{L}_\theta=\frac{d^2\theta}{d\zeta^2}-\theta, \tag{8.28}$$

$$\mathcal{L}_f\left[\breve{J}_1^*+\breve{J}_2^*e^{\zeta}+J_3^*e^{-\zeta}\right]=0,\ \mathcal{L}_g\left[\breve{J}_4^*e^{\zeta}+\breve{J}_5^*e^{-\zeta}\right]=0,\ \mathcal{L}_\theta\left[\breve{J}_6^*e^{\zeta}+\breve{J}_7^*e^{-\zeta}\right]=0. \tag{8.29}$$

The deformation problems of zeroth and mth-order are easily defined in view of above operators by BVPH2.0 of Mathematica.

8.4 Solutions convergence

BVPh2.0 is utilized for computation of optimal solutions. These solution expressions contain $\hbar_f$, $\hbar_g$ and $\hbar_\theta$ which play important role in homotopic expressions. The optimal values of $\hbar_f$, $\hbar_g$ and $\hbar_\theta$ can be computed by taking minimum error. Average squared residual error is given as

$$\varepsilon_m^f = \frac{1}{\breve{k}+1}\sum_{j=0}^{\breve{k}}\left[\mathcal{N}_f\left(\sum_{i=0}^{m} f(\zeta), \sum_{i=0}^{m} g(\zeta)\right)_{\zeta=j\delta\zeta}\right]^2, \tag{8.30}$$

$$\varepsilon_m^g = \frac{1}{\breve{k}+1}\sum_{j=0}^{\breve{k}}\left[\mathcal{N}_g\left(\sum_{i=0}^{m} f(\zeta), \sum_{i=0}^{m} g(\zeta)\right)_{\zeta=j\delta\zeta}\right]^2, \tag{8.31}$$

$$\varepsilon_m^\theta = \frac{1}{\breve{k}+1}\sum_{j=0}^{\breve{k}}\left[\mathcal{N}_\theta\left(\sum_{i=0}^{m} f(\zeta), \sum_{i=0}^{m} g(\zeta), \sum_{i=0}^{m} \theta(\zeta)\right)_{\zeta=j\delta\zeta}\right]^2. \tag{8.32}$$

Following Liao [140] :

$$\varepsilon_m^t = \varepsilon_m^f + \varepsilon_m^g + \varepsilon_m^\theta. \tag{8.33}$$

At 2nd order of deformations, the optimal data of convergence control variables in SWCNTs and MWCNTs cases are $\hbar_f = -0.790686$, $\hbar_g = -0.609323$, $\hbar_\theta = -0.493612$ and $\hbar_f = -0.710962$, $\hbar_g = -0.556358$, $\hbar_\theta = -0.484269$ while total averaged squared residual error in SWCNTs and MWCNTs cases are $\varepsilon_m^t = 4.97 \times 10^{-2}$ and $\varepsilon_m^t = 5.52 \times 10^{-2}$ respectively. Plots of total residual error for both cases of CNTs (SWCNTs and MWCNTs) are shown in Figs. 8.2 and 8.3. Numerical data of average squared residual errors in case of SWCNTs and MWCNTs at $m = 2$ are presented in Tables 8.2 and 8.3. Clearly averaged squared residual error decreases for higher order deformations.

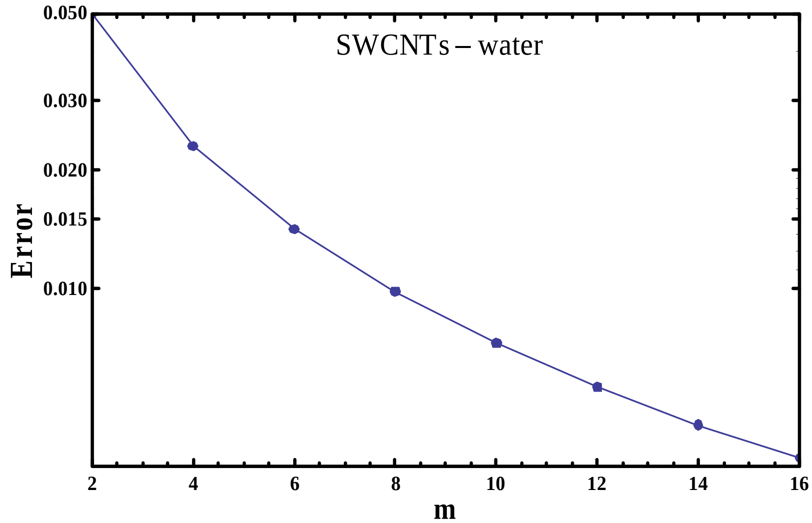

Fig. 8.1: Total residual error for SWCNTs-water.

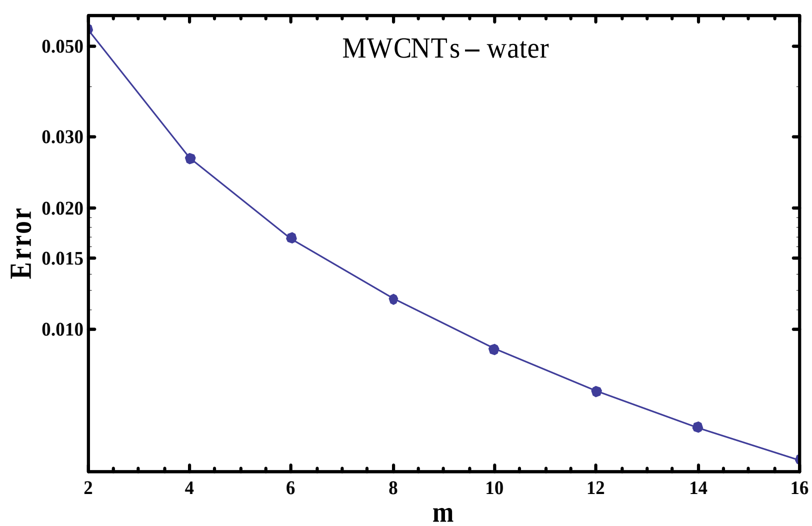

Fig. 8.2: Total residual error for MWCNTs-water.

Table 8.2: Total average squared residual errors in SWCNTs case.

m	ε_m^f	ε_m^g	ε_m^θ
2	3.94×10^{-3}	2.46×10^{-2}	4.79×10^{-3}
6	3.16×10^{-3}	2.08×10^{-2}	5.97×10^{-4}
10	3.02×10^{-3}	1.88×10^{-2}	3.46×10^{-4}
14	2.88×10^{-3}	1.75×10^{-2}	2.28×10^{-4}
16	2.82×10^{-3}	1.69×10^{-2}	1.90×10^{-4}

Table 8.3: Total average squared residual errors in MWCNTs case.

m	ε_m^f	ε_m^g	ε_m^θ
2	3.61×10^{-3}	2.69×10^{-2}	5.33×10^{-3}
6	2.97×10^{-3}	2.26×10^{-2}	4.95×10^{-4}
10	2.85×10^{-3}	2.05×10^{-2}	1.01×10^{-4}
14	2.73×10^{-3}	1.90×10^{-2}	2.06×10^{-5}
16	2.68×10^{-3}	1.84×10^{-2}	9.80×10^{-6}

8.5 Discussion

Main attention is to analyze velocities $f'(\zeta)$, $g(\zeta)$ and temperature $\theta(\zeta)$ for sundry variables like (λ), (F_r), (γ_1), (ξ), (γ_2) and (Ec). Outcomes are obtained for two cases of carbon nanotubes (recognized as SWCNTs and MWCNTs). Fig. 8.4 addresses velocity field $f'(\zeta)$ for (ξ). By increasing (ξ), the fluid becomes viscous and resistance between fluid particles increases which depicts lower $f'(\zeta)$. It is also analyzed that $f'(\zeta)$ is less for MWCNTs than SWCNTs. Figs. 8.5 and 8.6 declared the consequences of $f'(\zeta)$ against (λ) and (F_r). Here $f'(\zeta)$ is a decreasing function of (λ) and (F_r) in both SWCNTs and MWCNTs cases. From Fig. 8.7, the $f'(\zeta)$ is reduced via higher estimation of (γ_1) in SWCNTs and MWCNTs situations. Physically, higher (γ_1) cause more resistance between fluid particles and rotating disk which consequently yields lower velocity. Velocity field $g(\zeta)$ and associated layer thickness are increasing functions of (ξ) (see Fig. 8.8). Similar behavior is noticed in SWCNTs and MWCNTs situations. Fig. 8.9

portrayed the variation of $f'(\zeta)$ against (λ). Higher estimation of (λ) produces lower $f'(\zeta)$ for both SWCNTs and MWCNTs. From Fig. 8.10, it is analyzed that higher (F_r) yields reduction in $f'(\zeta)$ in both SWCNTs and MWCNTs cases. Fig. 8.11 is delineated for behavior of (γ_1) on $g(\zeta)$. Larger (γ_1) indicate decrease in $g(\zeta)$ for SWCNTs and MWCNTs cases. More $\theta(\zeta)$ is observed by higher (ξ) in both SWCNTs and MWCNTs situations (see Fig. 8.12). Role of (Ec) on $\theta(\zeta)$ is shown in Fig. 8.13. An increment in (Ec) causes more fluid friction between adjacent layers of fluid due to which conversion from kinetic energy into heat energy occurs. This conversion produces enhancement in $\theta(\zeta)$ for SWCNTs and MWCNTs cases. Fig. 8.14 characterized consequences of (γ_2) on $\theta(\zeta)$. It is recognized that for higher estimation of (γ_2), the heat transfer from surface towards adjacent layers of fluid decreases which yields weaker temperature $\theta(\zeta)$ in SWCNTs and MWCNTs cases. Features of (ξ), (γ_1) and (F_r) on skin friction coefficients $\left(\frac{\mathrm{Re}}{2}\right)^{1/2} C_f$ and $\left(\frac{\mathrm{Re}}{2}\right)^{1/2} C_g$ are interpreted in Figs. 8.15 − 8.18. It is reported that $\left(\frac{\mathrm{Re}}{2}\right)^{1/2} C_f$ and $\left(\frac{\mathrm{Re}}{2}\right)^{1/2} C_g$ depict increasing trend for higher estimation of (ξ), (γ_1) and (F_r). Figs. 8.19 and 8.20 are interpreted to scrutinize the impact of (ξ), (γ_2) and (Ec) on local Nusselt number $-\left(\frac{\mathrm{Re}}{2}\right)^{-1/2} Nu$. Local Nusselt number has increasing trend against higher (γ_2) and (Ec). Validation of current results with existing numerical results by Naqvi et al. [33] is depicted in Table 8.4 when $\xi = 0$. Reasonable agreement with results of Naqvi et al. [33] is found.

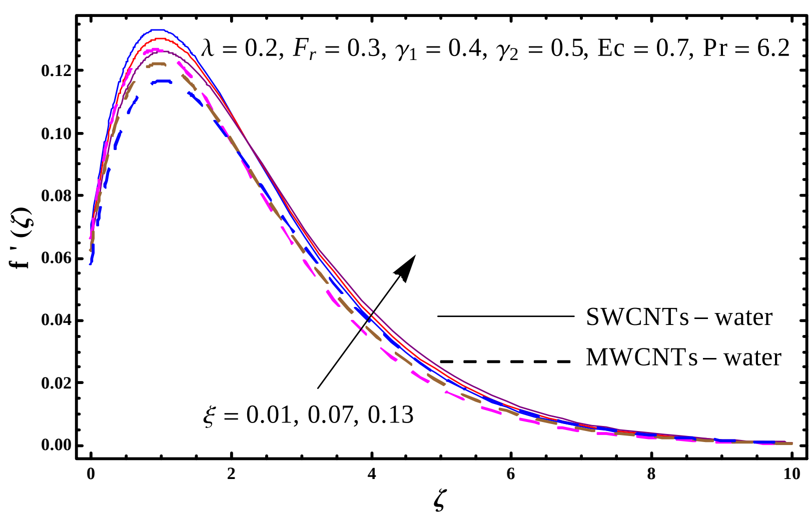

Fig. 8.4: Plot for $f'(\zeta)$ against ξ.

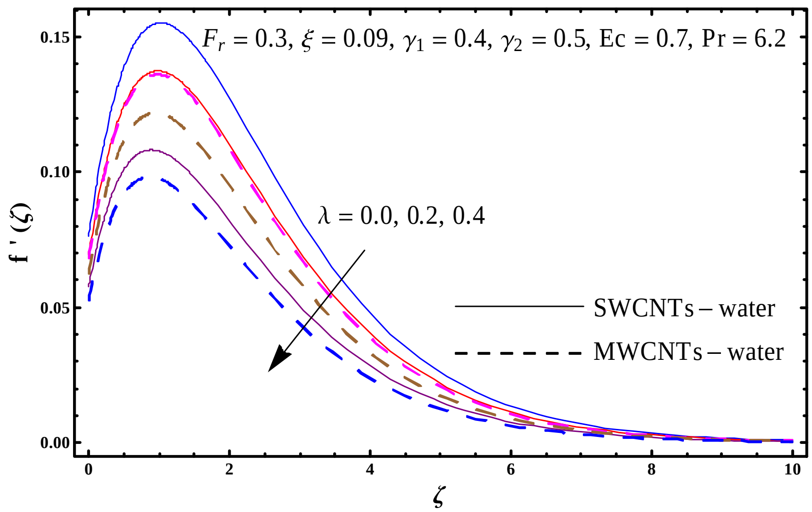

Fig. 8.5: Plot for $f'(\zeta)$ against λ.

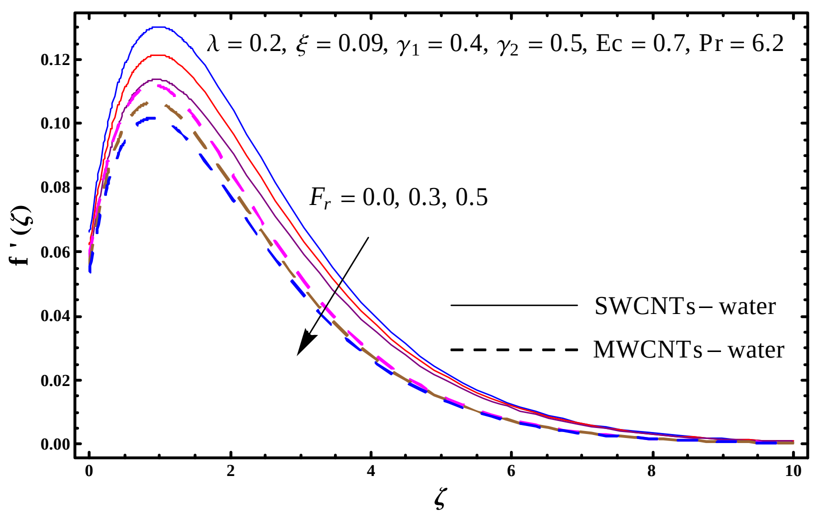

Fig. 8.6: Plot for $f'(\zeta)$ against F_r.

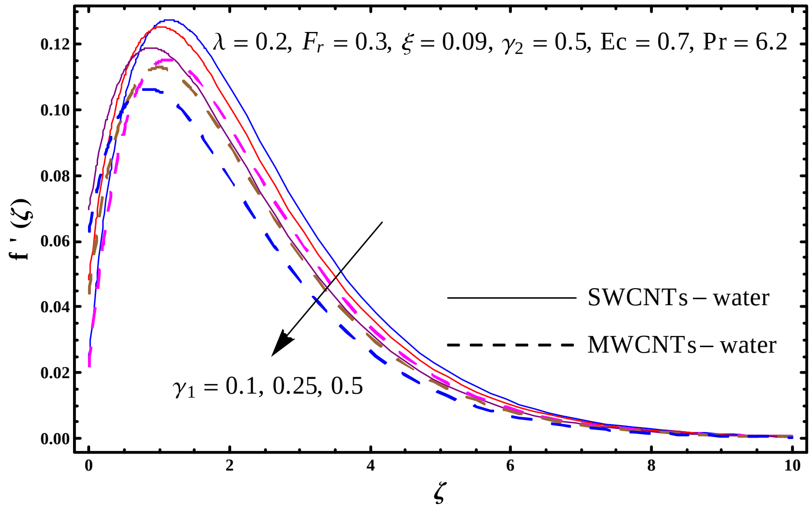

Fig. 8.7: Plot for $f'(\zeta)$ against γ_1.

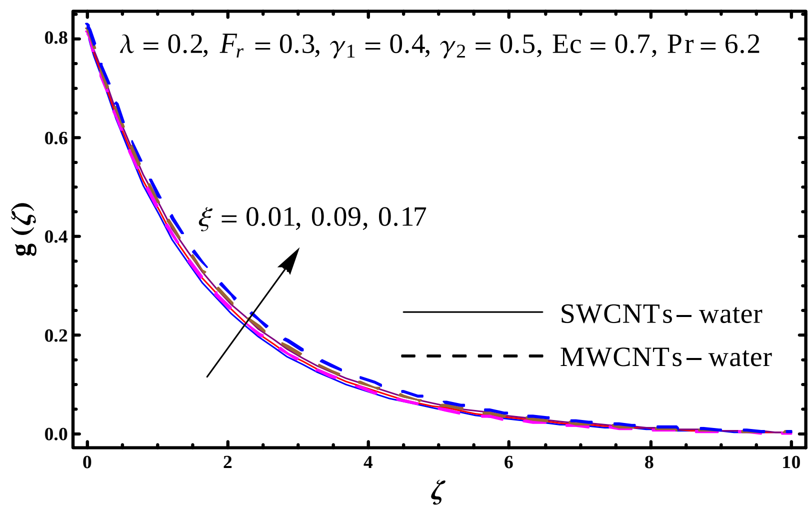

Fig. 8.8: Sketch of $g(\zeta)$ against ξ.

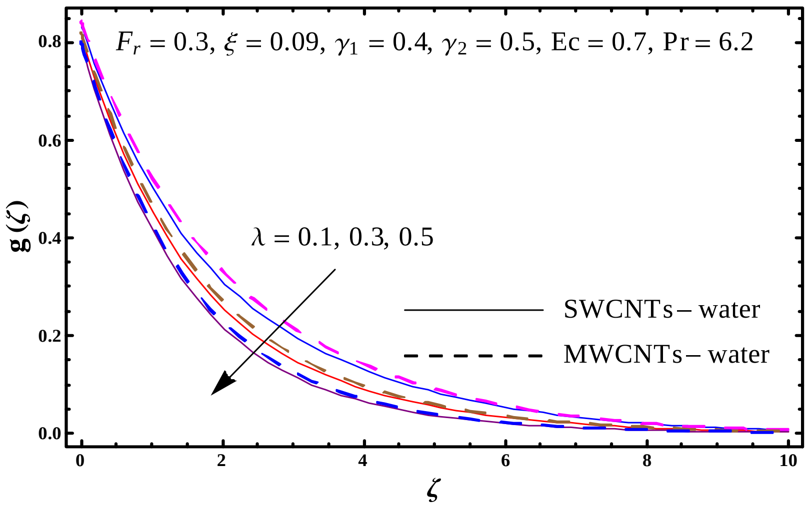

Fig. 8.9: Sketch of $g(\zeta)$ against λ.

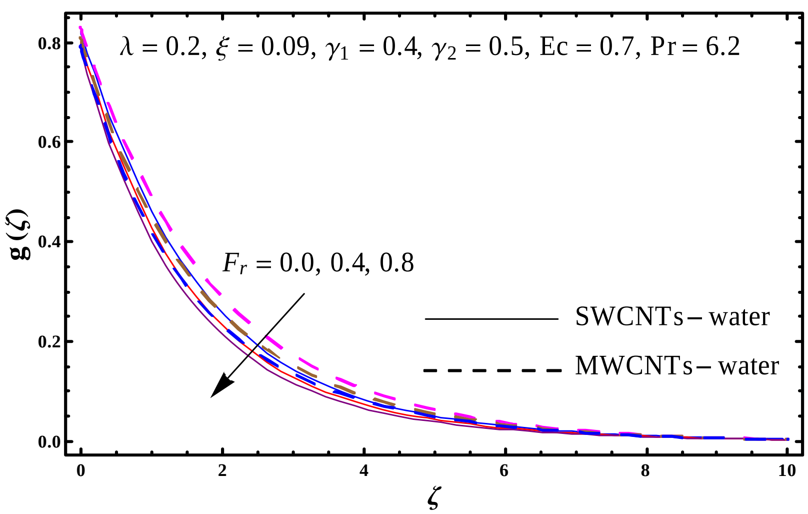

Fig. 8.10: Sketch of $g(\zeta)$ against F_r.

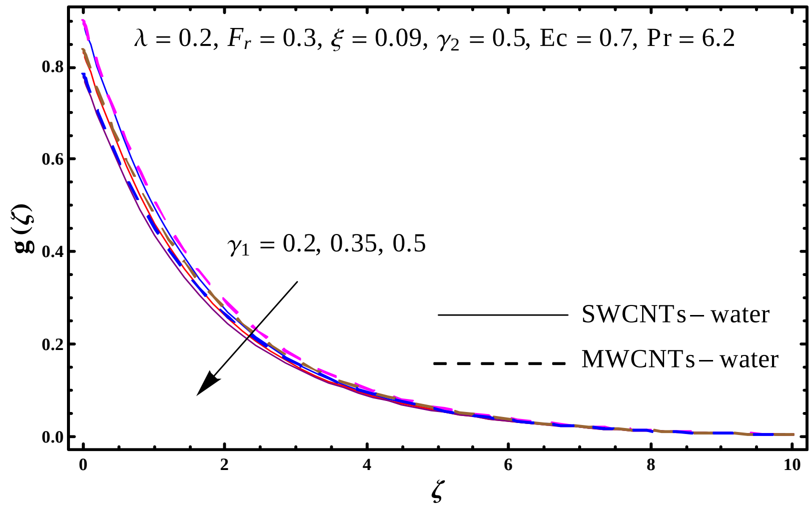

Fig. 8.11: Sketch of $g(\zeta)$ against γ_1.

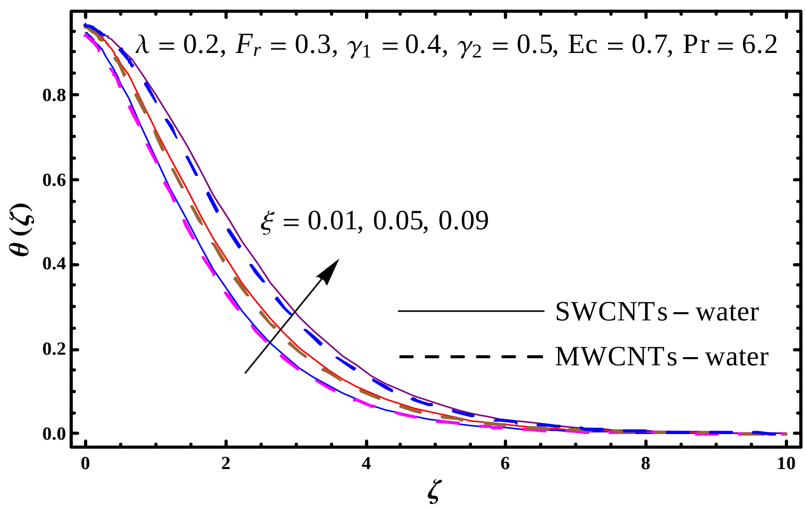

Fig. 8.12: Plot for $\theta(\zeta)$ against ξ.

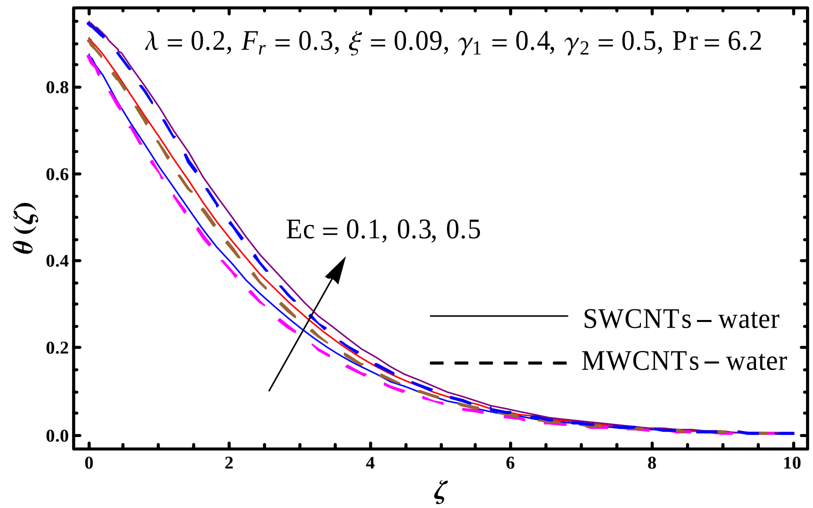

Fig. 8.13: Plot for $\theta(\zeta)$ against Ec.

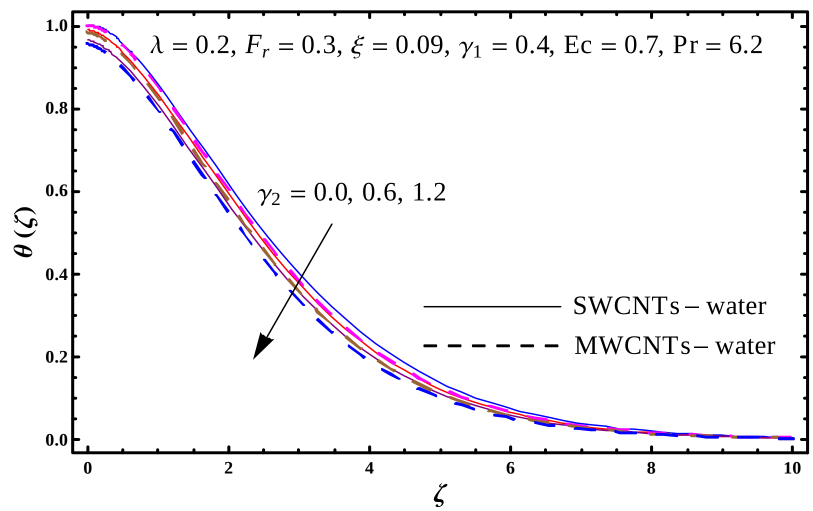

Fig. 8.14: Plot for $\theta(\zeta)$ against γ_2.

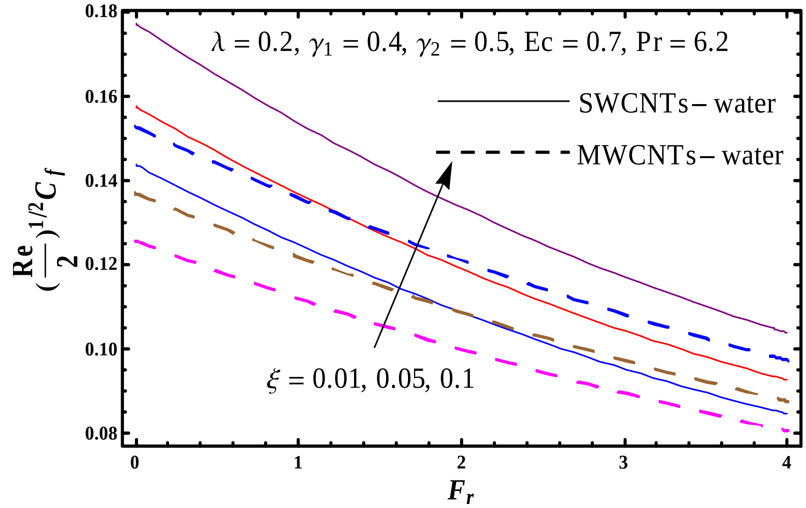

Fig. 8.15: Plot for $\left(\frac{\mathrm{Re}}{2}\right)^{1/2} C_f$ against ξ and F_r.

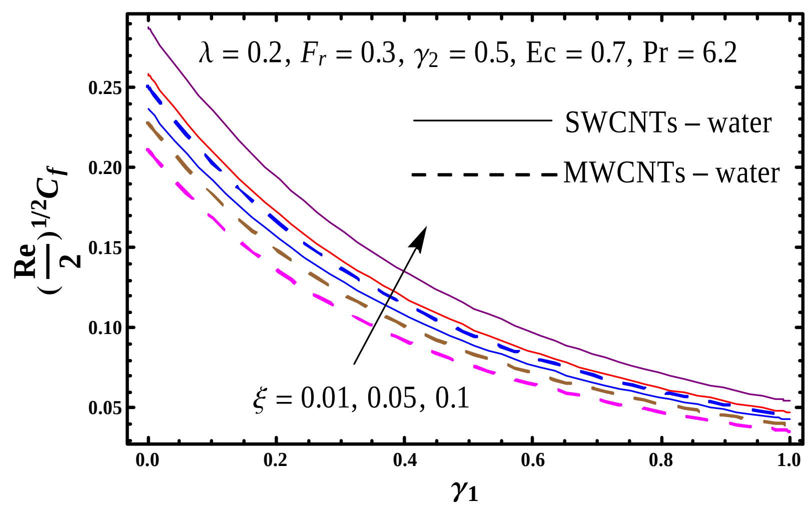

Fig. 8.16: Plot for $\left(\frac{\mathrm{Re}}{2}\right)^{1/2} C_f$ against ξ and γ_1.

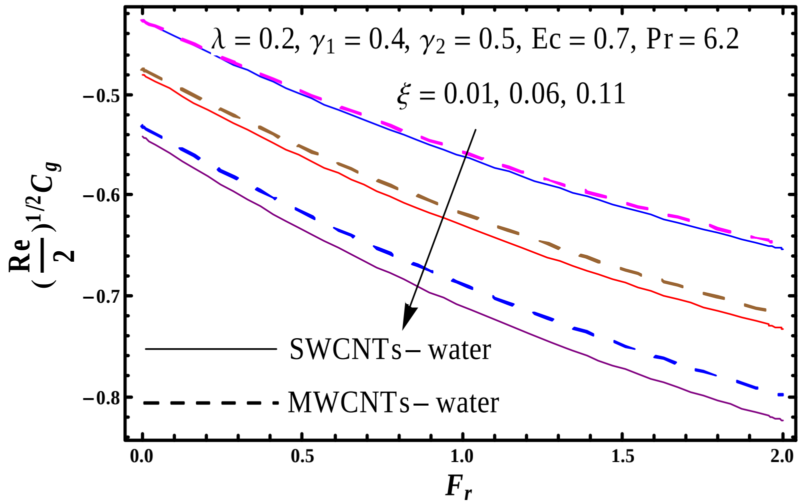

Fig. 8.17: Plot for $\left(\frac{\mathrm{Re}}{2}\right)^{1/2} C_g$ against ξ and F_r.

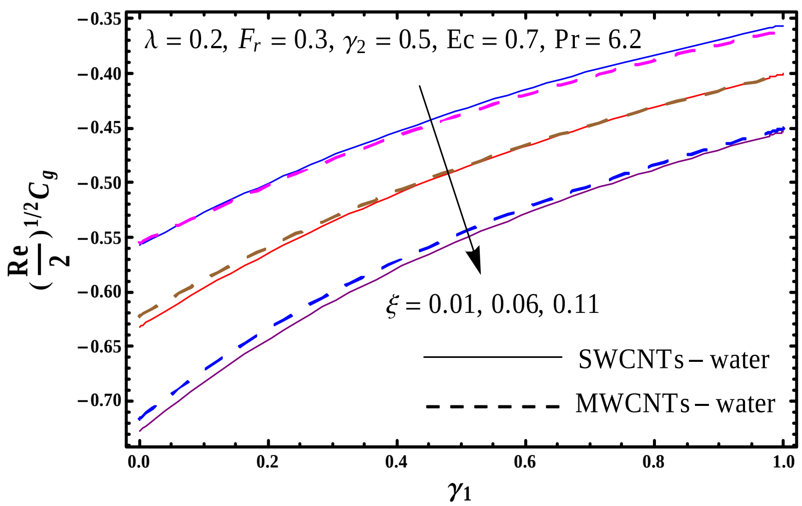

Fig. 8.18: Plot for $\left(\frac{\mathrm{Re}}{2}\right)^{1/2} C_g$ against ξ and γ_1.

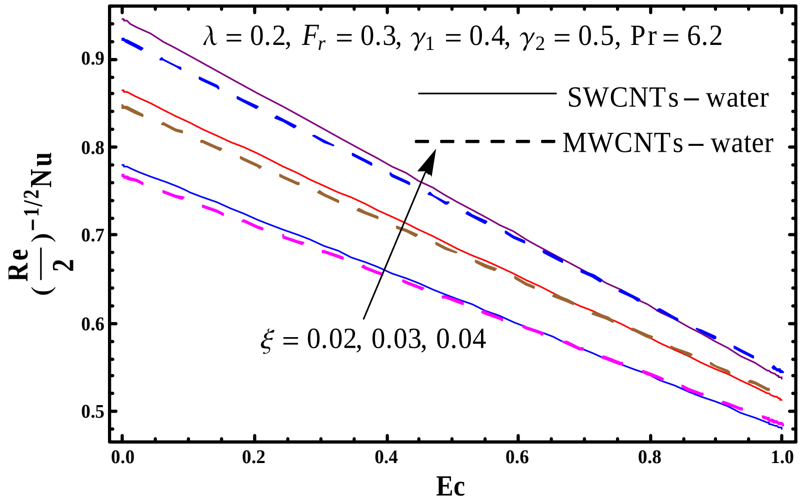

Fig. 8.19: Plot for $\left(\frac{\text{Re}}{2}\right)^{-1/2} Nu$ against ξ and Ec.

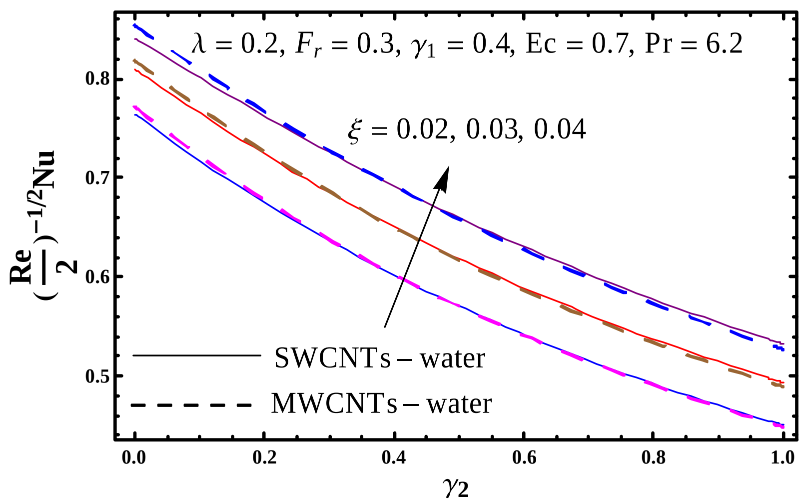

Fig. 8.20: Plot for $\left(\frac{\text{Re}}{2}\right)^{-1/2} Nu$ against ξ and γ_2.

Table 8.4: Skin friction coefficients for distinct λ, F_r and γ_1 when $\xi = 0$.

λ	F_r	γ_1	$\left(\frac{\mathrm{Re}}{2}\right)^{1/2} C_f$		$-\left(\frac{\mathrm{Re}}{2}\right)^{1/2} C_g$	
			OHAM	Naqvi et al. [33]	OHAM	Naqvi et al. [33]
0.0	0.2	0.2	0.27961	0.30051	0.48585	0.64605
0.5			0.18428	0.26436	0.57798	0.74946
1.2			0.13822	0.23697	0.72787	0.83632
0.2	0.0	0.2	0.23575	0.33311	0.23113	0.63023
	0.5		0.21077	0.22813	0.55613	0.77968
	1.0		0.19005	0.14961	0.62742	0.96925
0.2	0.2	0.0	0.30222	0.43478	0.55473	0.78139
		0.5	0.15323	0.17157	0.44021	0.56649
		1.0	0.09813	0.09212	0.35495	0.43068

Chapter 9

Unsteady flow of nanomaterial subject to variable characteristics

This chapter analyzed the salient characteristics of activation energy and porous space on unsteady flow of nanofluid. Darcy-Forchheimer relation with variable porosity and permeability is accounted. Disturbance in flow is caused by a stretchable rotating disk. Nanofluid properties are due to Brownian motion and thermophoresis. Heat transfer in flow of nanofluids are more prominent in industries and technological advances. Transportation, atomic reactors, hardware, vitality and medication are few such processes. Appropriate transformations are adopted for reduction purpose. Numerical solutions of resulting nonlinear system are computed. Graphs are plotted to interpret outcomes for velocities, temperature and concentration. Physical quantities are analyzed through numerical results.

9.1 Model development

Unsteady three dimensional flow by stretchable rotating disk is examined. Darcy-Forchheimer relation with variable properties is considered. Concentration expression is subject to an activation energy. Attributes of Brownian motion and thermophoresis are analyzed. Time dependent angular velocity is $\omega'(t)=\frac{\omega}{1-bt}$ (see Fig. 9.1). Cylindrical coordinate frame $(r,\ \psi,\ z)$ is adopted.

Relevant equations for the problems are:

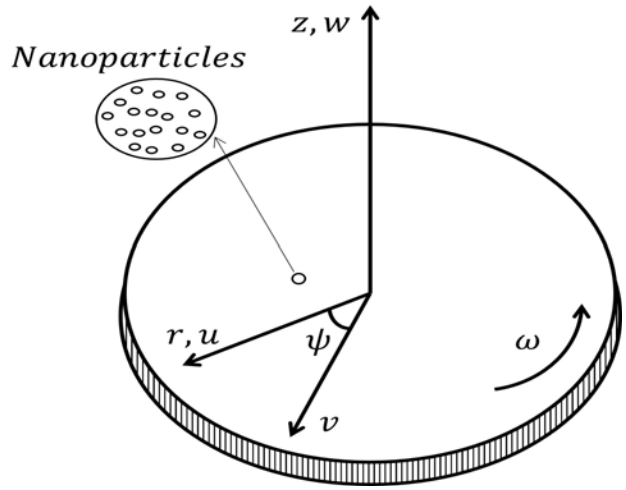

Fig. 9.1: Flow configuration [27].

$$\frac{\partial u}{\partial r} + \frac{u}{r} + \frac{\partial w}{\partial z} = 0, \tag{9.1}$$

$$\frac{\partial u}{\partial t} + u\frac{\partial u}{\partial r} + w\frac{\partial u}{\partial z} - \frac{v^2}{r} = -\frac{1}{\rho}\frac{\partial p}{\partial r} + \nu\left(\frac{\partial^2 u}{\partial z^2}\right) - \frac{\nu\varepsilon(z)}{K^*(z)}u - \frac{C_b\varepsilon^2(z)}{\sqrt{K^*(z)}}u\sqrt{u^2+v^2}, \tag{9.2}$$

$$\frac{\partial v}{\partial t} + u\frac{\partial v}{\partial r} + w\frac{\partial v}{\partial z} + \frac{uv}{r} = \nu\left(\frac{\partial^2 v}{\partial z^2}\right) - \frac{\nu\varepsilon(z)}{K^*(z)}v - \frac{C_b\varepsilon^2(z)}{\sqrt{K^*(z)}}v\sqrt{u^2+v^2}, \tag{9.3}$$

$$\frac{\partial T}{\partial t} + u\frac{\partial T}{\partial r} + w\frac{\partial T}{\partial z} = \alpha\left(\frac{\partial^2 T}{\partial z^2}\right) + \frac{(\rho c)_p}{(\rho c)_f}\left(D_B\left(\frac{\partial T}{\partial z}\frac{\partial C}{\partial z}\right) + \frac{D_T}{T_\infty}\left(\frac{\partial T}{\partial z}\right)^2\right), \tag{9.4}$$

$$\begin{gathered}\frac{\partial C}{\partial t} + u\frac{\partial C}{\partial r} + w\frac{\partial C}{\partial z} = D_B\left(\frac{\partial^2 C}{\partial z^2}\right) + \frac{D_T}{T_\infty}\left(\frac{\partial^2 T}{\partial z^2}\right) - \\ k_r^2\left(C - C_\infty\right)\left(\frac{T}{T_\infty}\right)^m e^{-\frac{E_a}{kT}},\end{gathered} \tag{9.5}$$

$$u = \frac{u_0 r}{1-bt}, \quad v = \frac{r\omega}{1-bt}, \quad w = 0, \quad T = T_w, \quad C = C_w \quad \text{at} \quad z = 0, \tag{9.6}$$

$$u \to 0, \ \ v \to 0, \ \ T \to T_\infty, \ \ C \to C_\infty \ \ as \ \ z \to \infty, \tag{9.7}$$

where [81]

$$K^*(z) = K_\infty\left(1 + de^{-\frac{z}{\gamma}}\right), \tag{9.8}$$

$$\varepsilon(z) = \varepsilon_\infty\left(1 + d^* e^{-\frac{z}{\gamma}}\right). \tag{9.9}$$

Considering

$$u=\frac{r\omega}{1-bt}\frac{\partial f(\eta,\zeta,\tau)}{\partial\zeta},\ v=\frac{r\omega}{1-bt}g\left(\eta,\zeta,\tau\right),\ w=-\sqrt{\frac{\omega v}{1-bt}}\left(2f+\eta\frac{\partial f}{\partial\eta}\right),\ p=\frac{\rho\nu\omega}{1-bt}P\left(\eta,\zeta,\tau\right), \\ \theta\left(\eta,\zeta,\tau\right)=\frac{T-T_\infty}{T_w-T_\infty},\ \phi\left(\eta,\zeta,\tau\right)=\frac{C-C_\infty}{C_w-C_\infty},\ \zeta=z\sqrt{\frac{\omega}{\nu(1-bt)}},\ \eta=\frac{r}{R},\ \tau=bt. \tag{9.10}$$

we have

$$\frac{\partial^3 f}{\partial\zeta^3}-\left(\frac{\partial f}{\partial\zeta}\right)^2+2f\frac{\partial^2 f}{\partial\zeta^2}+g^2-S\left(\frac{\partial f}{\partial\zeta}+(1-\tau)\frac{\partial^2 f}{\partial\zeta\partial\tau}+\frac{\zeta}{2}\frac{\partial^2 f}{\partial\zeta^2}\right)- \\ \lambda\left(1-\tau\right)\left(\frac{1+d^*e^{-\zeta}}{1+de^{-\zeta}}\right)\frac{\partial f}{\partial\zeta}-F_r\eta\frac{\left(1+d^*e^{-\zeta}\right)^2}{\sqrt{1+de^{-\zeta}}}\left(\left(\frac{\partial f}{\partial\zeta}\right)^2+\frac{1}{2}g^2\right)=\eta\left(\frac{\partial f}{\partial\zeta}\frac{\partial^2 f}{\partial\zeta\partial\eta}-\frac{\partial f}{\partial\eta}\frac{\partial^2 f}{\partial\zeta^2}\right), \tag{9.11}$$

$$\frac{\partial^2 g}{\partial\zeta^2}-2\frac{\partial f}{\partial\zeta}g+2f\frac{\partial g}{\partial\zeta}-S\left(g+(1-\tau)\frac{\partial g}{\partial\tau}+\frac{\zeta}{2}\frac{\partial g}{\partial\zeta}\right)- \\ \lambda\left(1-\tau\right)\left(\frac{1+d^*e^{-\zeta}}{1+de^{-\zeta}}\right)g-F_r\eta\frac{\left(1+d^*e^{-\zeta}\right)^2}{\sqrt{1+de^{-\zeta}}}\left(g^2+\frac{1}{2}\left(\frac{\partial f}{\partial\zeta}\right)^2\right)=\eta\left(\frac{\partial f}{\partial\zeta}\frac{\partial g}{\partial\eta}-\frac{\partial f}{\partial\eta}\frac{\partial g}{\partial\zeta}\right), \tag{9.12}$$

$$\frac{\partial^2\theta}{\partial\zeta^2}+2\Pr f\frac{\partial\theta}{\partial\zeta}-S\Pr\left((1-\tau)\frac{\partial\theta}{\partial\tau}+\frac{\zeta}{2}\frac{\partial\theta}{\partial\zeta}\right)+N_b\Pr\frac{\partial\theta}{\partial\zeta}\frac{\partial\phi}{\partial\zeta}+ \\ N_t\Pr\left(\frac{\partial\theta}{\partial\zeta}\right)^2=\eta\Pr\left(\frac{\partial f}{\partial\zeta}\frac{\partial\theta}{\partial\eta}-\frac{\partial f}{\partial\eta}\frac{\partial\theta}{\partial\zeta}\right), \tag{9.13}$$

$$\frac{\partial^2\phi}{\partial\zeta^2}+2Scf\frac{\partial\phi}{\partial\zeta}-SSc\left((1-\tau)\frac{\partial\phi}{\partial\tau}+\frac{\zeta}{2}\frac{\partial\phi}{\partial\zeta}\right)+\frac{N_t}{N_b}\frac{\partial^2\theta}{\partial\zeta^2}- \\ \Lambda\left(1-\tau\right)Sc\left(1+\alpha_1\theta\right)^m e^{\left(\frac{-E}{1+\alpha_1\theta}\right)}\phi=\eta Sc\left(\frac{\partial f}{\partial\zeta}\frac{\partial\phi}{\partial\eta}-\frac{\partial f}{\partial\eta}\frac{\partial\phi}{\partial\zeta}\right), \tag{9.14}$$

$$f\left(\eta,0,\tau\right)=-2\eta\frac{\partial f\left(\eta,0,\tau\right)}{\partial\eta},\ \frac{\partial f\left(\eta,0,\tau\right)}{\partial\zeta}=\delta,\ g\left(\eta,0,\tau\right)=1,\ \theta\left(\eta,0,\tau\right)=1,\ \phi\left(\eta,0,\tau\right)=1, \tag{9.15}$$

$$\frac{\partial f\left(\eta,\infty,\tau\right)}{\partial\zeta}\to 0,\ g\left(\eta,\infty,\tau\right)\to 0,\ \theta\left(\eta,\infty,\tau\right)\to 0,\ \phi\left(\eta,\infty,\tau\right)\to 0, \tag{9.16}$$

Here incompressibility equation is trivially verified and η is the constant prescribed variable at any streamwise location. To attain similar solutions, we assume that the terms including $\frac{\partial(.)}{\partial\eta}$ are sufficiently small and may be approximated by zero. Thus, we have

$$f'''-f'^2+2ff''+g^2-S\left(f'+\frac{\zeta}{2}f''\right)-\lambda\left(1-\tau\right)\left(\frac{1+d^*e^{-\zeta}}{1+de^{-\zeta}}\right)f'- \\ F_r\eta\frac{\left(1+d^*e^{-\zeta}\right)^2}{\sqrt{1+de^{-\zeta}}}\left(f'^2+\frac{1}{2}g^2\right)=0, \tag{9.17}$$

$$g''-2f'g+2fg'-S\left(g+\frac{\zeta}{2}g'\right)-\lambda\left(1-\tau\right)\left(\frac{1+d^*e^{-\zeta}}{1+de^{-\zeta}}\right)g- \\ F_r\eta\frac{\left(1+d^*e^{-\zeta}\right)^2}{\sqrt{1+de^{-\zeta}}}\left(g^2+\frac{1}{2}f'^2\right)=0, \tag{9.18}$$

$$\theta'' + 2\Pr f\theta' - S\Pr\frac{\zeta}{2}\theta' + N_b\Pr\theta'\phi' + N_t\Pr\theta'^2 = 0, \tag{9.19}$$

$$\phi'' + 2Scf\phi' - SSc\frac{\zeta}{2}\phi' + \frac{N_t}{N_b}\theta'' - \Lambda\left(1-\tau\right)Sc\left(1+\alpha_1\theta\right)^m e^{\left(\frac{-E}{1+\alpha_1\theta}\right)}\phi = 0, \tag{9.20}$$

$$f\left(\eta,0,\tau\right) = 0,\ f'\left(\eta,0,\tau\right) = \delta,\ g\left(\eta,0,\tau\right) = 1,\ \theta\left(\eta,0,\tau\right) = 1,\ \phi\left(\eta,0,\tau\right) = 1, \tag{9.21}$$

$$f'\left(\eta,\infty,\tau\right) \to 0,\ g\left(\eta,\infty,\tau\right) \to 0,\ \theta\left(\eta,\infty,\tau\right) \to 0,\ \phi\left(\eta,\infty,\tau\right) \to 0. \tag{9.22}$$

Emerging parameters are stated as

$$\begin{gathered} S = \tfrac{b}{\omega},\ \delta = \tfrac{u_0}{\omega},\ \lambda = \tfrac{\nu_f\varepsilon_\infty}{\omega K_\infty},\ \mathrm{Re} = \tfrac{\bar{R}^2\omega}{\nu},\ F_r = \tfrac{C_b\varepsilon_\infty^2\bar{R}}{\sqrt{K_\infty}},\ Pe = \mathrm{Re}_r\Pr,\ \tfrac{1}{\gamma} = \sqrt{\tfrac{\alpha}{\nu}}\tfrac{Pe^{1/2}}{\bar{R}}, \\ N_b = \tfrac{\tau D_B}{\nu}\left(C_w - C_\infty\right),\ N_t = \tfrac{\tau D_T}{T_\infty\nu}\left(T_w - T_\infty\right),\ \Pr = \tfrac{\nu}{\alpha},\ Sc = \tfrac{\nu}{D_B}, \\ \Lambda = k_r^2\left(\tfrac{1-bt}{\omega}\right),\ \alpha_1 = \tfrac{T_w - T_\infty}{T_\infty},\ E = \tfrac{E_a}{\breve{k}T_\infty}. \end{gathered} \tag{9.23}$$

9.2 Physical quantities

Coefficients of skin friction and local Nusselt and Sherwood numbers take the form

$$\left.\begin{array}{c} \left(\frac{\mathrm{Re}}{2}\right)^{1/2} C_f = \frac{1}{\eta}f''\left(\eta,0,\tau\right), \\ \left(\frac{\mathrm{Re}}{2}\right)^{1/2} C_g = \frac{1}{\eta}g'\left(\eta,0,\tau\right), \\ \left(\frac{\mathrm{Re}}{2}\right)^{-1/2} Nu = -\eta\theta'\left(\eta,0,\tau\right), \\ \left(\frac{\mathrm{Re}}{2}\right)^{-1/2} Sh = -\eta\phi'\left(\eta,0,\tau\right). \end{array}\right\} \tag{9.19}$$

9.3 Discussion

Purpose of this section is to interpret the graphical description of sundry variables such as (S), (δ), (λ), (F_r), (d), (d^*), (N_b), (N_t), $(\Pr)$, (Λ), (α_1), (E) and (Sc) on velocities $f'(\zeta)$ and $g(\zeta)$, thermal $\theta(\zeta)$ and concentration $\phi(\zeta)$ fields. Fig. 9.2 is sketched to scrutinize the behavior of $f'(\zeta)$ through (S). An enhancement in $f'(\zeta)$ is observed through higher (S). Fig. 9.3 elaborates the characteristics of (λ) on $f'(\zeta)$. Here $f'(\zeta)$ is lower for (λ). Figs. 9.4 and 9.5 highlighted the impacts of (d) and (d^*) on $f'(\zeta)$. It is seen that $f'(\zeta)$ possesses opposite trend for (d) and (d^*). Fig. 9.6 witnessed that (F_r) lowers the velocity $f'(\zeta)$. Plot of $f'(\zeta)$ against (δ) is illustrated in Fig. 9.7. Clearly $f'(\zeta)$ is enhanced for higher (δ). Fig. 9.8 elaborated the role of (S) on $g(\zeta)$. It is seen that higher estimation of (S) correspond to more velocity $g(\zeta)$.

Attributes of $g(\zeta)$ against (λ) is presented in Fig. 9.9. Higher $g(\zeta)$ is observed through (λ). An increment in (d) and (d^*) produces opposite trend in velocity $g(\zeta)$ (see Figs. 9.10 and 9.11). Fig. 9.12 presents variations of $g(\zeta)$ for (F_r). Reduction in $g(\zeta)$ is noted through higher (F_r). Fig. 9.13 presents estimation of $\theta(\zeta)$ for (S). Here higher estimation of (S) gives lower $\theta(\zeta)$ and less related layer thickness. Outcome of (N_b) on thermal field $\theta(\zeta)$ is plotted in Fig. 9.14. Clearly higher (N_b) strengthen the thermal field $\theta(\zeta)$. Features of $\theta(\zeta)$ through (N_t) is displayed in Fig. 9.15. $\theta(\zeta)$ shows decreasing behavior for (N_t). Fig. 9.16 sketched the attributes of $\phi(\zeta)$ for (S). Reduction in $\phi(\zeta)$ is seen through higher (S). Characteristics of (N_b) and (N_t) on $\phi(\zeta)$ are portrayed in Figs. 9.17 and 9.18. Opposite trend of $\phi(\zeta)$ is noted through (N_b) and (N_t). Fig. 9.19 displayed behavior of $\phi(\zeta)$ against (Sc). Clearly higher estimation of (Sc) lowers $\phi(\zeta)$. Similar trend of $\phi(\zeta)$ is seen through (Λ) and (α_1) (see Figs. 9.20 and 9.21). Fig. 9.22 displayed behavior of (E) on $\phi(\zeta)$. Higher (E) leads to stronger $\phi(\zeta)$ and more associated layer thickness. Role of (m) on $\phi(\zeta)$ is elaborated in Fig. 9.23. Here concentration $\phi(\zeta)$ is a decreasing function of (m). Table 9.1 is developed to analyze significant behavior of skin friction coefficients for involved variables. Skin friction coefficients reduces through (d) while reverse behavior is seen through (B), (F_r) and (d^*). Higher values of local Nusselt number are noted via (S) and $(\Pr)$ (see Table 9.2). Table 9.3 illustrated behavior of local Sherwood number against emerging flow variables. Clearly local Sherwood number through (N_b), (Λ), (α_1), (Sc) and (m) enhances. Comparison of present results with existing [28, 34] are presented in Tables

9.4 and 9.5. An agreement with present results is found with [28, 34].

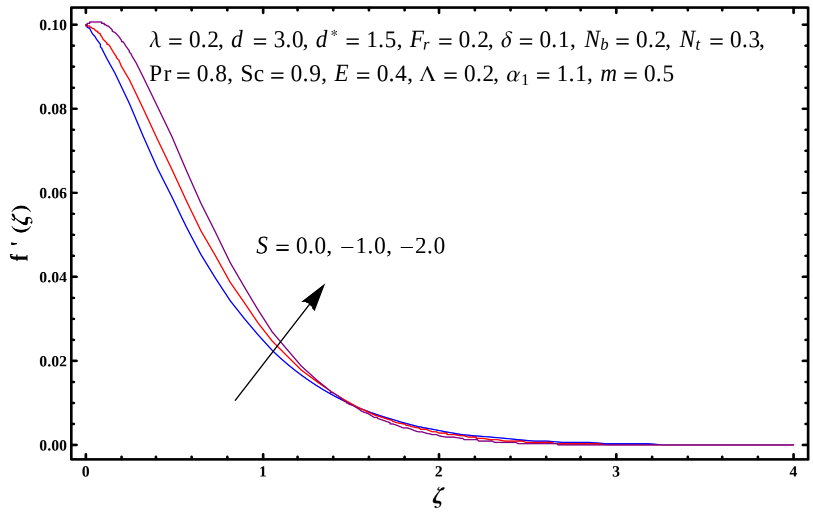

Fig. 9.2: Sketch of $f'(\zeta)$ against S.

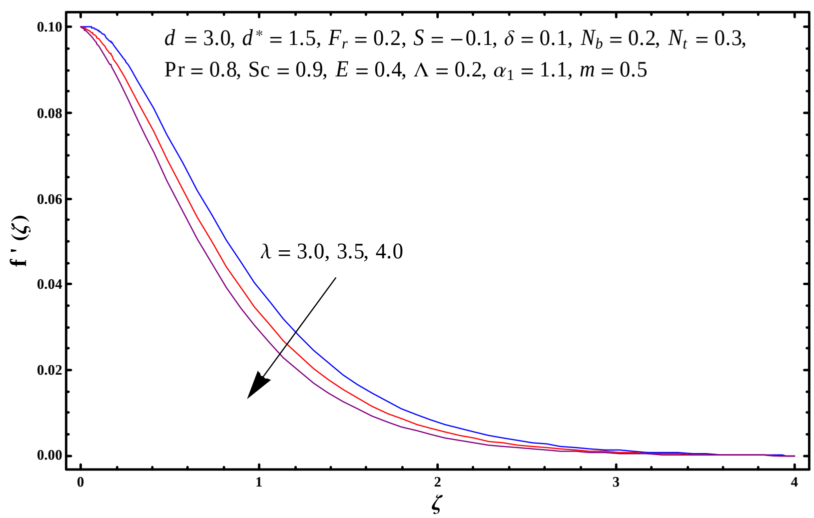

Fig. 9.3: Plot for $f'(\zeta)$ against λ.

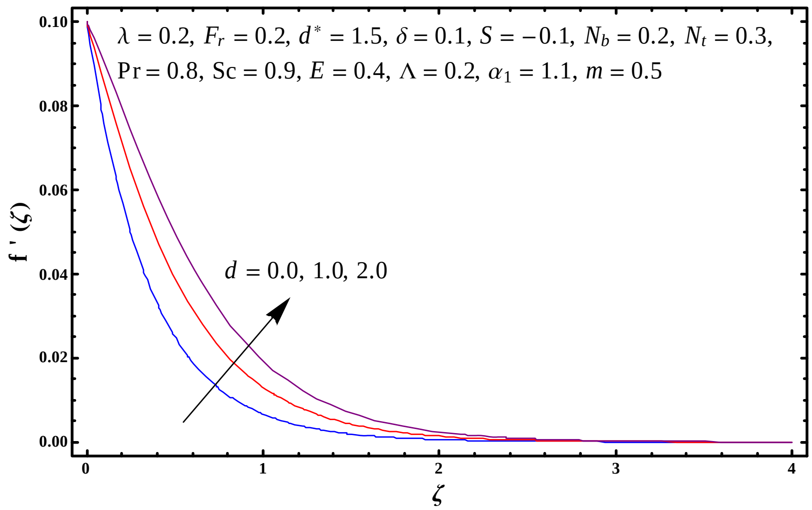

Fig. 9.4: Plot for $f'(\zeta)$ against d.

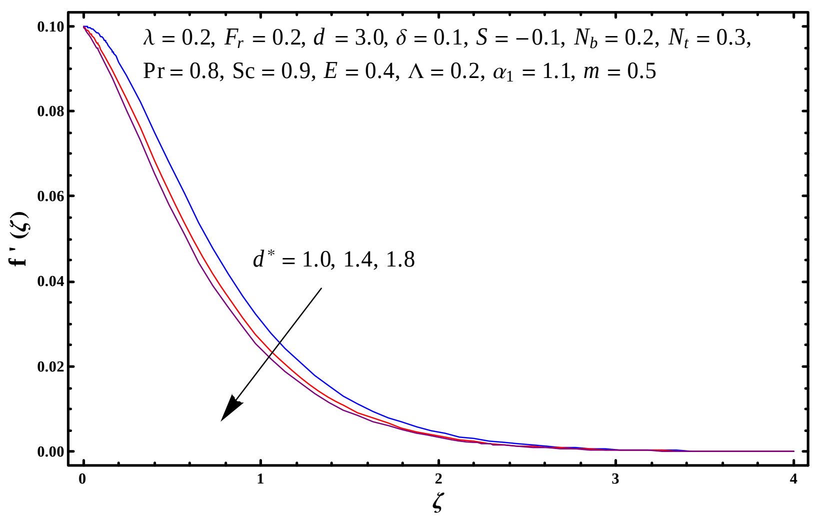

Fig. 9.5: Plot for $f'(\zeta)$ against d^*.

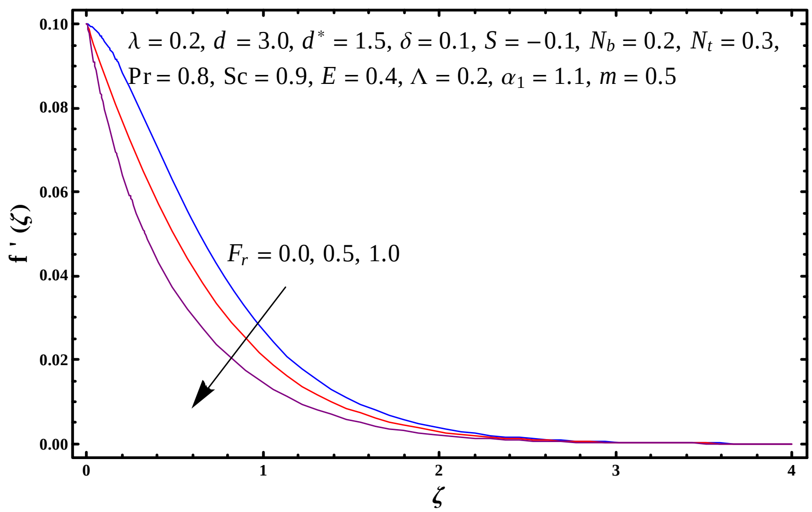

Fig. 9.6: Plot for $f'(\zeta)$ versus F_r.

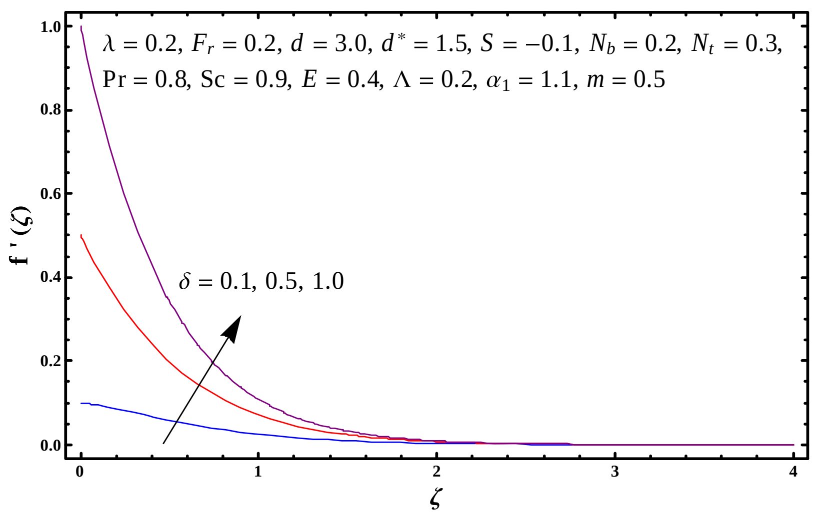

Fig. 9.7: Sketch of $f'(\zeta)$ versus δ.

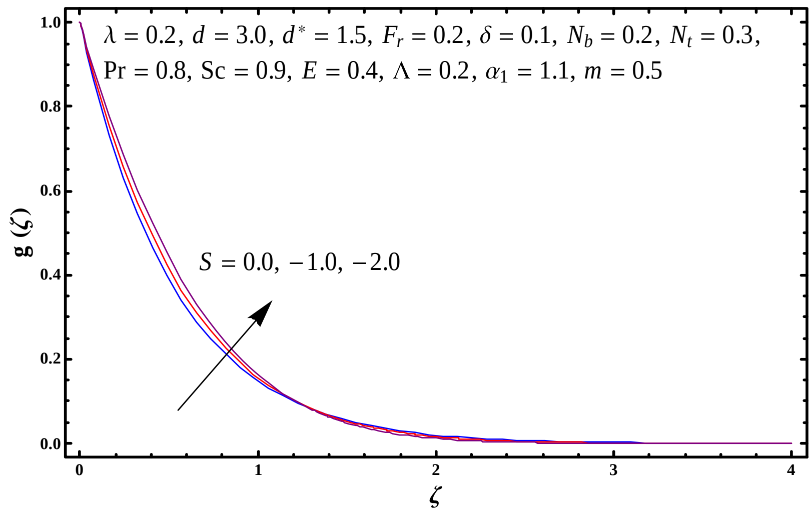

Fig. 9.8: Sketch of $g(\zeta)$ versus S.

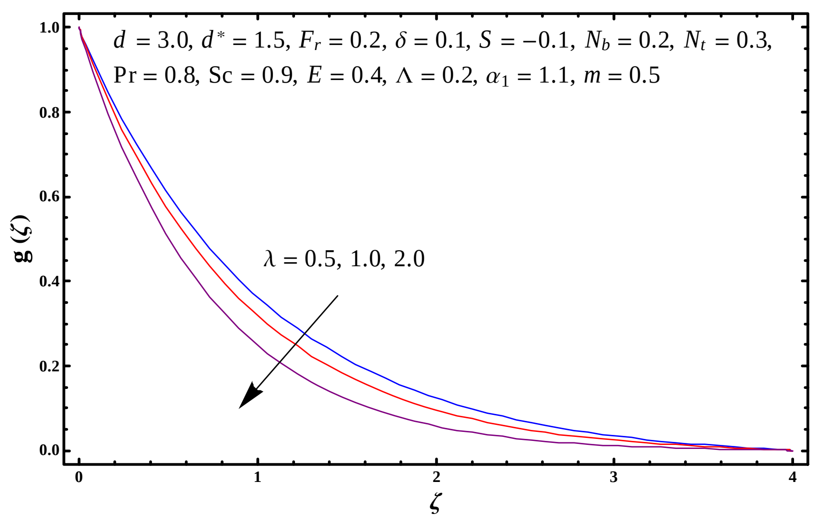

Fig. 9.9: Sketch of $g(\zeta)$ versus λ.

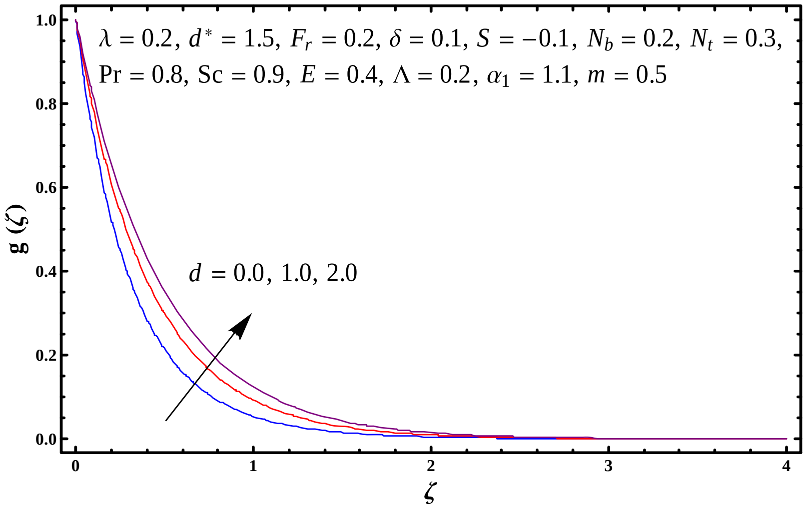

Fig. 9.10: Sketch of $g(\zeta)$ versus d.

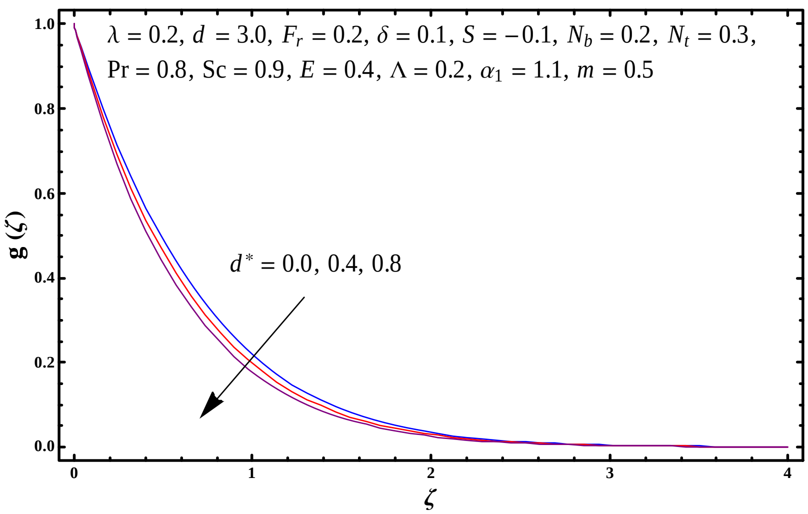

Fig. 9.11: Sketch of $g(\zeta)$ against d^*.

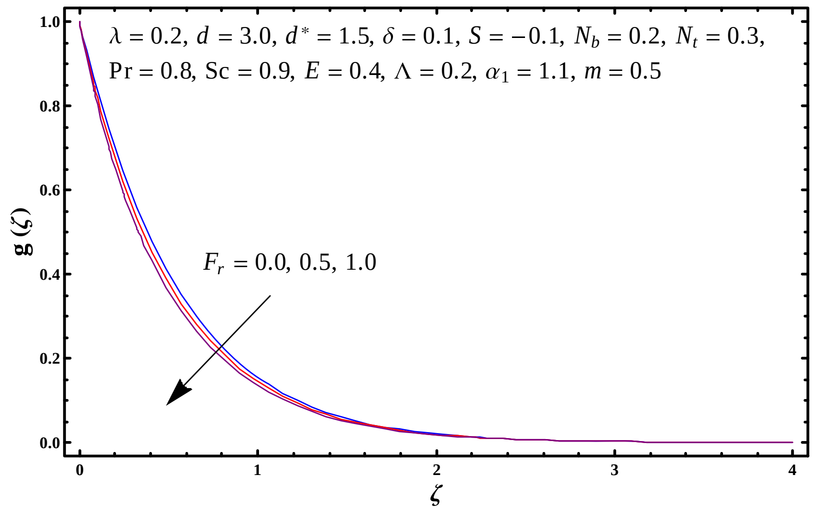

Fig. 9.12: Plot for $g(\zeta)$ against F_r.

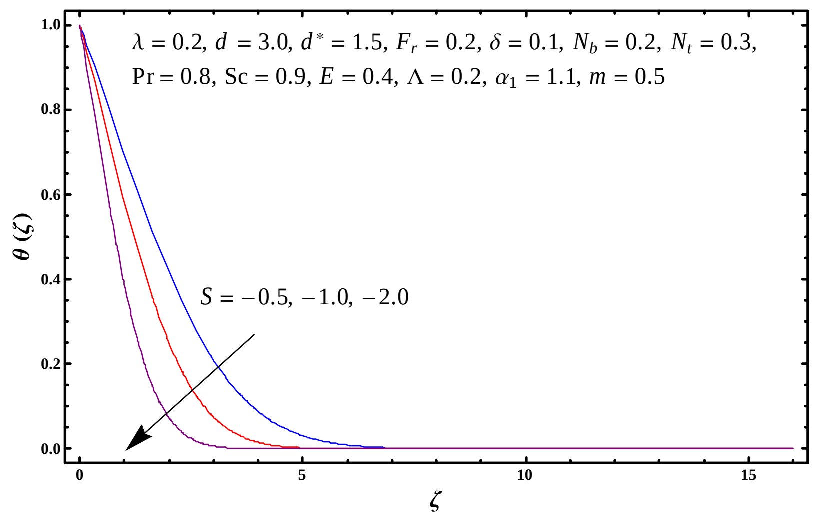

Fig. 9.13: Plot for $\theta(\zeta)$ against S.

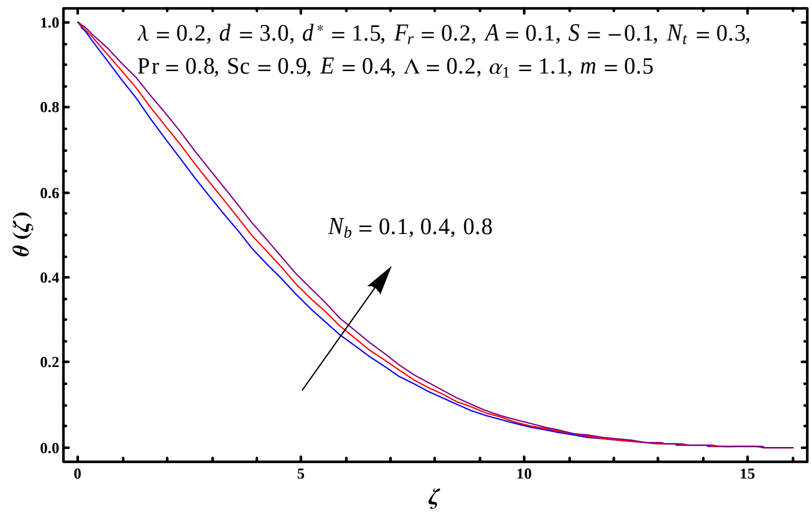

Fig. 9.14: Plot for $\theta\,(\zeta)$ against N_b.

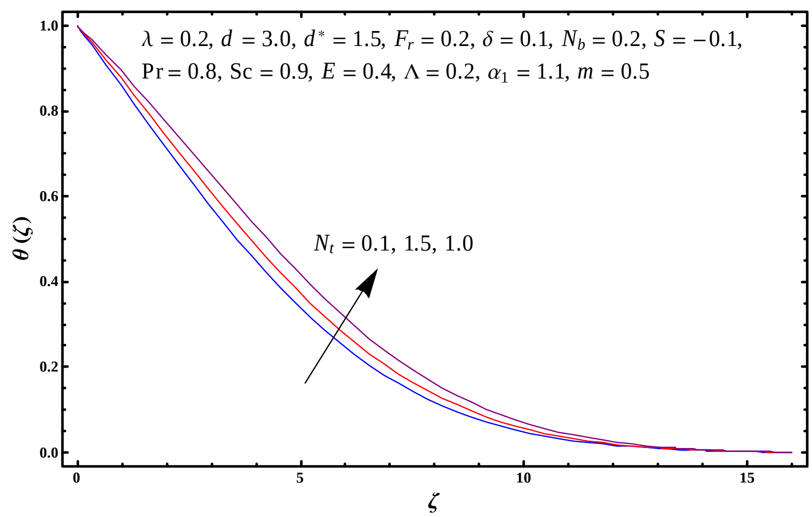

Fig. 9.15: Sketch of $\theta\,(\zeta)$ against N_t.

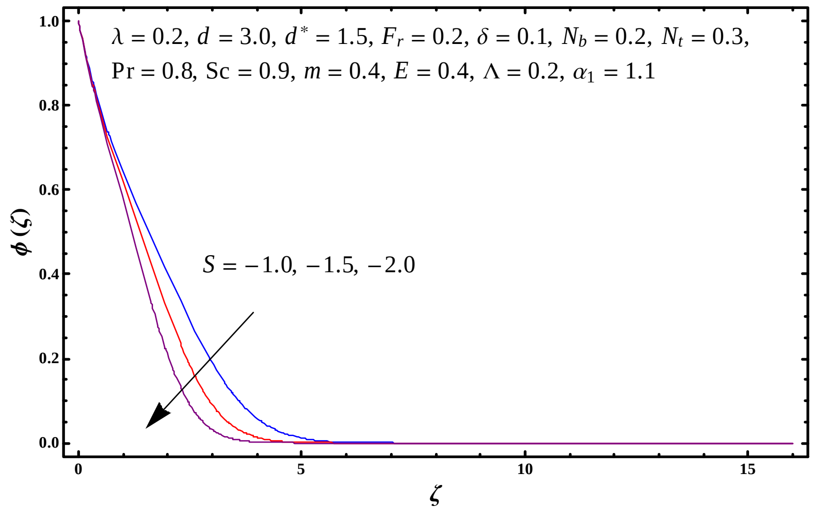

Fig. 9.16: Sketch of $\phi(\zeta)$ against S.

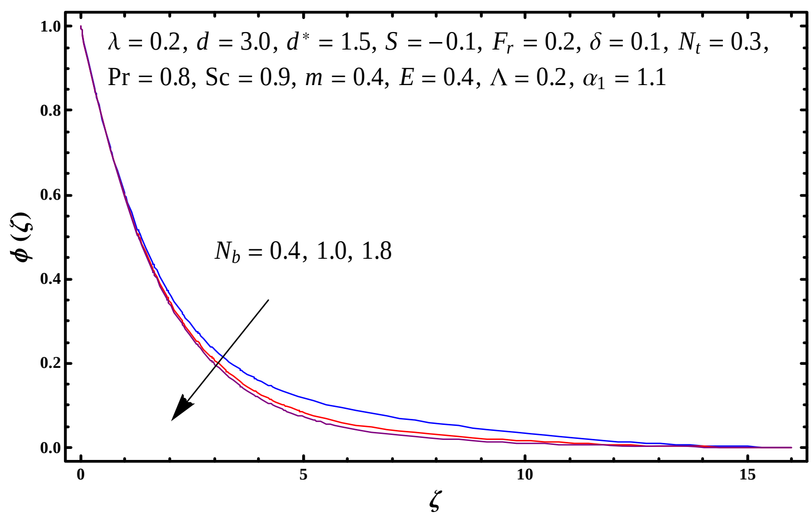

Fig. 9.17: Sketch of $\phi(\zeta)$ against N_b.

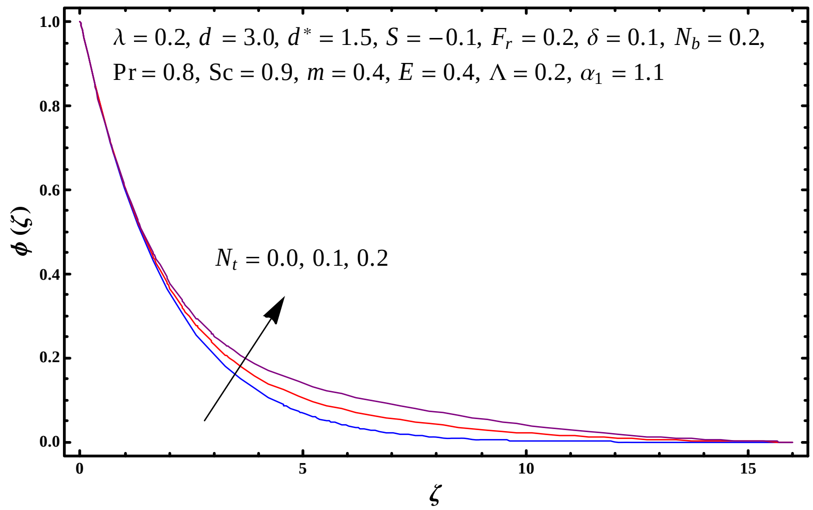

Fig. 9.18: Sketch of $\phi(\zeta)$ against N_t.

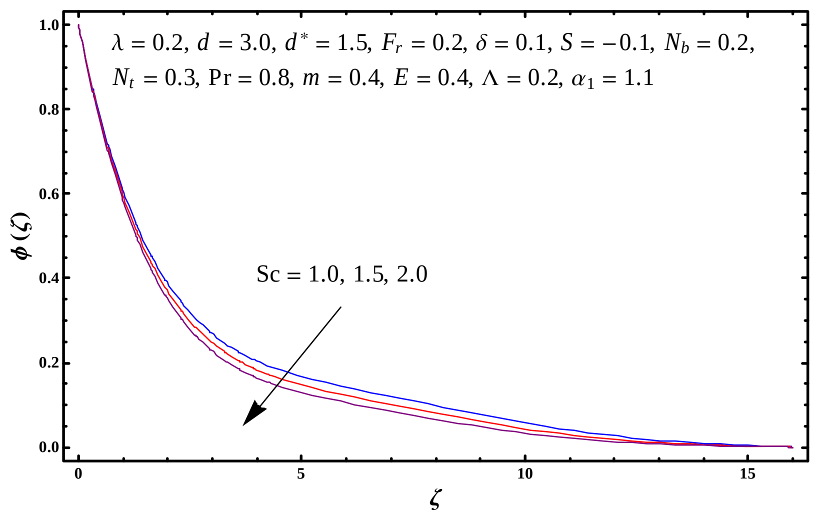

Fig. 9.19: Sketch for $\phi(\zeta)$ against Sc.

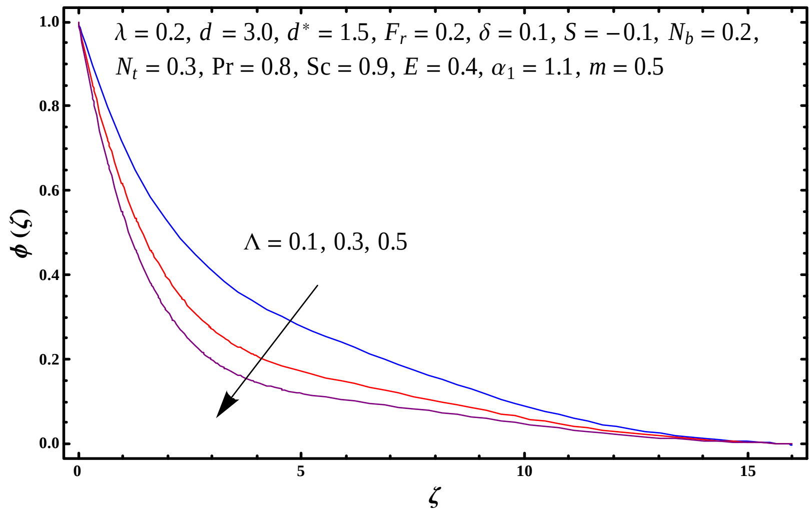

Fig. 9.20: Sketch of $\phi(\zeta)$ against Λ.

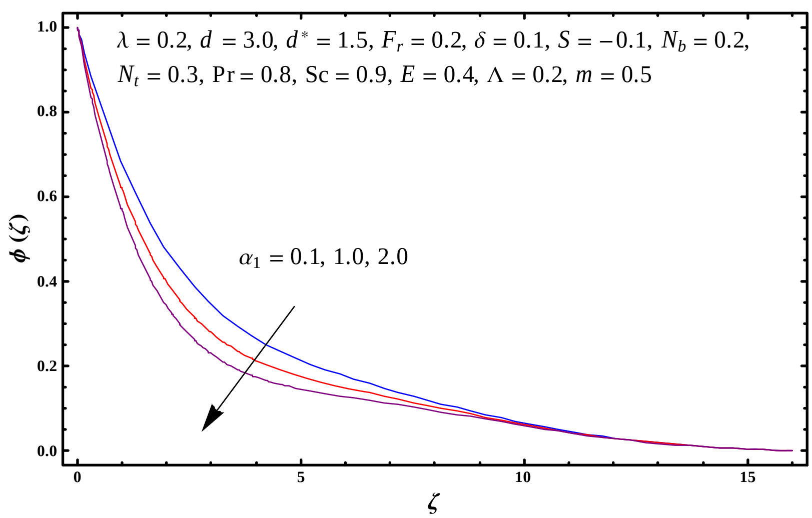

Fig. 9.21: Plot for $\phi(\zeta)$ against α_1.

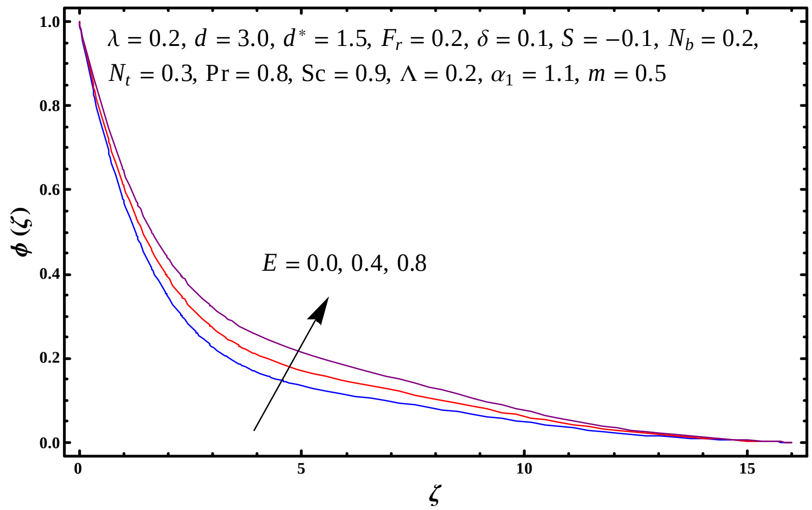

Fig. 9.22: Plot for $\phi(\zeta)$ against E.

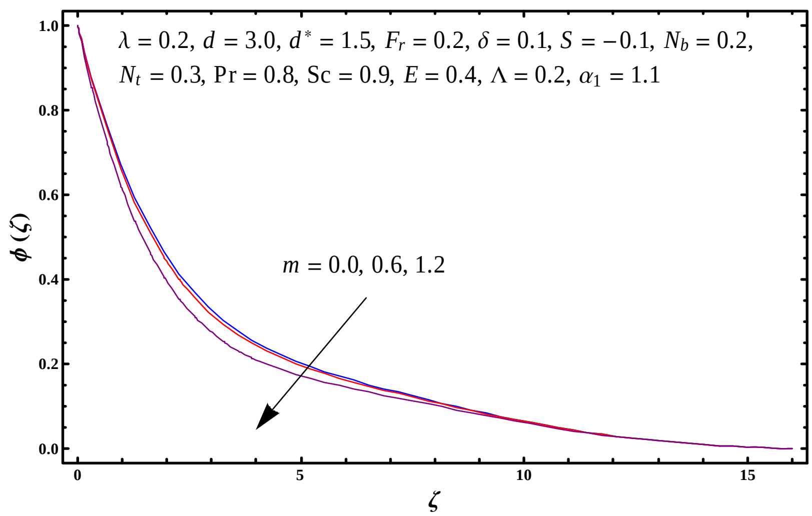

Fig. 9.23: Sketch of $\phi(\zeta)$ against m.

Table 9.1: Skin friction coefficients $\left(\frac{\mathrm{Re}}{2}\right)^{1/2} C_f$ and $\left(\frac{\mathrm{Re}}{2}\right)^{1/2} C_g$ against S, d, λ, d^*, δ and F_r.

S	λ	d	d^*	F_r	δ	$-\left(\frac{\mathrm{Re}}{2}\right)^{1/2} C_f$	$-\left(\frac{\mathrm{Re}}{2}\right)^{1/2} C_g$
0.0	0.2	3.0	1.5	0.2	0.1	0.23799	1.94439
−1.0						0.36466	1.80939
−2.0						0.45900	1.67553
−0.1	1.0	3.0	1.5	0.2	0.1	−0.14353	1.12722
	1.1					−0.13369	1.15367
	1.2					−0.12440	1.17972
−0.1	0.2	0.0	1.5	0.2	0.1	0.27884	3.36512
		1.0				0.15476	2.49785
		2.0				0.08891	2.10607
−0.1	0.2	3.0	0.0	0.2	0.1	0.00179	1.32595
			0.3			0.00964	1.44002
			0.6			0.01811	1.55137
0.2	0.2	0.4	1.5	0.0	0.1	0.02727	1.77506
				0.1		0.03061	1.82371
				0.3		0.03844	1.91813
−0.1	0.2	3.0	1.5	0.2	0.2	0.23278	1.92553
					0.3	0.43019	1.97928
					0.4	0.63621	2.03269

Table 9.2: Local Nusselt number $\left(\frac{\mathrm{Re}}{2}\right)^{-1/2} Nu$ against S, N_b, N_t and Pr.

S	N_b	N_t	Pr	$\left(\frac{\mathrm{Re}}{2}\right)^{-1/2} Nu$
0.0	0.2	0.3	0.8	0.04825
−0.2				0.18298
−0.3				0.22606
−0.1	0.1	0.3	0.8	0.13537
	0.3			0.12015
	0.4			0.11312
−0.1	0.2	0.0	0.8	0.14209
		0.1		0.13704
		0.2		0.13220
−0.1	0.2	0.3	0.9	0.13192
			1.0	0.13570
			1.1	0.13898

Table 9.3: Numerical data of local Sherwood number $\left(\frac{\mathrm{Re}}{2}\right)^{-1/2} Sh$ against S, N_b, N_t, Λ, α_1, E, Sc and m.

S	N_b	N_t	Λ	α_1	E	Sc	m	$\left(\frac{\mathrm{Re}}{2}\right)^{-1/2} Sh$
0.0	0.2	0.3	0.2	1.1	0.4	0.9	0.5	0.50855
−0.2								0.49944
−0.3								0.49269
−0.1	0.0	0.3	0.2	1.1	0.4	0.9	0.5	0.48714
	0.1							0.51569
	0.3							0.51926
−0.1	0.2	0.0	0.2	1.1	0.4	0.9	0.5	0.51259
		0.1						0.50891
		0.2						0.50765
−0.1	0.2	0.3	0.0	1.1	0.4	0.9	0.5	0.08581
			0.1					0.35329
			0.3					0.62579
−0.1	0.2	0.3	0.2	1.0	0.4	0.9	0.5	0.49861
				1.2				0.51829
				1.3				0.52784
0.2	0.2	0.3	0.2	1.1	0.1	0.9	0.5	0.55108
					0.2			0.53664
					0.3			0.52247
−0.1	0.2	0.3	0.2	1.1	0.4	0.8	0.5	0.50595
						1.0		0.51117
						1.1		0.51379
−0.1	0.2	0.3	0.2	1.1	0.4	0.9	0.1	0.43892
							0.2	0.45706
							0.3	0.47469

Table 9.4: Values for $f''(0)$ against δ and S.

δ	S	$f''(0)$		
		NDSolve	HAM [34]	Numerical solution [28]
0	-0.1	0.45011		0.53081
	-0.5	0.51813		0.61433
	-1.0	0.61179		0.71982
1.0	-0.1	-0.97795	-0.93712	-0.91892
	-0.5	-0.86371	-0.90621	-0.80071
	-1.0	-1.35688	-0.76731	-0.65204
2.0	-0.1	-3.17457	-2.97292	-3.11782
	-0.5	-3.01887		-2.96013
	-1.0	-2.82301		-2.76223

Table 9.5: Comparative values of $g'(0)$ for distinct values of δ and S.

δ	S	$-g'(0)$	
		NDSolve	Numerical solution [28]
0	-0.1	0.63586	0.57894
	-0.5	0.48479	0.42841
	-1.0	0.29261	0.34522
1.0	-0.1	1.4936	1.46565
	-0.5	1.40871	1.37973
	-1.0	1.21444	1.27163
2.0	-0.1	2.06844	2.05302
	-0.5	2.00626	1.99011
	-1.0	1.92767	1.91114

Chapter 10

Flow of hybrid nanofluid saturating porous medium of variable characteristics

This chapter provides numerical simulation for flow of $TiO_2-Al_2O_3$/water nanofluid filling porous medium. Combined effects of thermal stratification and nonlinear thermal radiation is studied. Velocity slip conditions are taken at the boundary. Rotating disk is used to generate disturbance in flow. Variable characteristics of porosity and permeability are characterized in porous space through Darcy-Forchheimer expression. NDSolve technique is employed for solution development of nonlinear equations. Graphical description is provided for the behavior of involved variables on flow fields. Role of emerging variables on physical quantities is discussed through numerical data. Our results reveal that heat transfer rate of TiO_2/water is higher in comparison to $TiO_2-Al_2O_3$/water nanofluid.

10.1 Model development

Three-dimensional (3D) steady flow of hybrid nanofluid induced by a rotating disk is taken. Velocity slip is accounted. Nonlinear thermal radiation and thermal stratification are accounted. Disk rotates subject to constant angular velocity ω. Here (u, v, w) are velocity components in

(r, ψ, z) directions. Resulting equations for 3D flow satisfy:

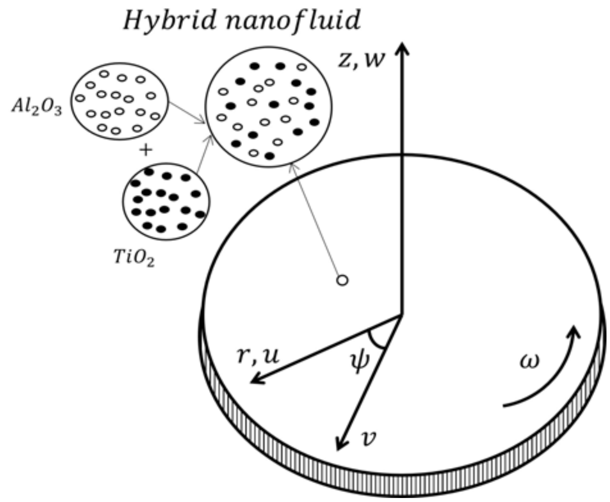

Fig. 10.1: Flow configuration [27].

$$\frac{\partial u}{\partial r} + \frac{u}{r} + \frac{\partial w}{\partial z} = 0, \tag{10.1}$$

$$u\frac{\partial u}{\partial r} - \frac{v^2}{r} + w\frac{\partial u}{\partial z} = \nu_{hnf}\left(\frac{\partial^2 u}{\partial z^2}\right) - \frac{\nu_{hnf}\varepsilon(z)}{K^*(z)}u - \frac{C_b\varepsilon^2(z)}{\sqrt{K^*(z)}}u\sqrt{u^2+v^2}, \tag{10.2}$$

$$u\frac{\partial v}{\partial r} + \frac{uv}{r} + w\frac{\partial v}{\partial z} = \nu_{hnf}\left(\frac{\partial^2 v}{\partial z^2}\right) - \frac{\nu_{hnf}\varepsilon(z)}{K^*(z)}v - \frac{C_b\varepsilon^2(z)}{\sqrt{K^*(z)}}v\sqrt{u^2+v^2}, \tag{10.3}$$

$$u\frac{\partial T}{\partial r} + w\frac{\partial T}{\partial z} = \alpha_{hnf}\left(\frac{\partial^2 T}{\partial z^2}\right) - \frac{1}{(\rho c_p)_{hnf}}\frac{\partial q_r}{\partial z}, \tag{10.4}$$

$$u = N_1\frac{\partial u}{\partial z}, \quad v = r\omega + N_1\frac{\partial u}{\partial z}, \quad w = 0, \quad T = T_w = T_0 + \tilde{A}r \quad \text{at} \quad z = 0, \tag{10.5}$$

$$u \to 0, \quad v \to 0, \quad T \to T_\infty = T_0 + \tilde{B}r \quad \text{as} \quad z \to \infty, \tag{10.6}$$

where

$$K^*(z) = K_\infty\left(1 + de^{-\frac{z}{\gamma}}\right), \tag{10.7}$$

$$\varepsilon(z) = \varepsilon_\infty\left(1 + d^* e^{-\frac{z}{\gamma}}\right), \tag{10.8}$$

$$q_r = -\frac{4\tilde{\sigma}}{3\epsilon}\frac{\partial T^4}{\partial z} = -\frac{16\tilde{\sigma}}{3\epsilon}T^3\frac{\partial T}{\partial z}, \tag{10.9}$$

The energy equation becomes

$$u\frac{\partial T}{\partial r}+w\frac{\partial T}{\partial z}=\alpha_{hnf}\left(\frac{\partial^2 T}{\partial r^2}+\frac{1}{r}\frac{\partial T}{\partial r}+\frac{\partial^2 T}{\partial z^2}\right)+\frac{1}{(\rho c_p)_{hnf}}\frac{16\tilde{\sigma}}{3\epsilon}\frac{\partial}{\partial z}\left(T^3\frac{\partial T}{\partial z}\right). \tag{10.10}$$

Theoretical model for hybrid nanofluid is [55] :

$$\left.\begin{array}{c}\mu_{hnf}=\frac{\mu_f}{(1-\xi_1-\xi_2)^{2.5}},\ \nu_{hnf}=\frac{\mu_{hnf}}{\rho_{hnf}},\ \rho_{hnf}=\rho_f(1-\xi_1-\xi_2)+\rho_1\xi_1+\rho_2\xi_2,\\ \alpha_{hnf}=\frac{k_{hnf}}{(\rho c_p)_{hnf}},\ (\rho c_p)_{hnf}=(\rho c_p)_f(1-\xi_1-\xi_2)+(\rho c_p)_1\xi_1+(\rho c_p)_1\xi_1,\\ \frac{k_{hnf}}{k_f}=\frac{\xi_1k_1+\xi_2k_2+2\xi k_f+2\xi(\xi_1k_1+\xi_2k_2)-2(\xi_1+\xi_2)^2k_f}{\xi_1k_1+\xi_2k_2+2\xi k_f-\xi(\xi_1k_1+\xi_2k_2)+(\xi_1+\xi_2)^2k_f}.\end{array}\right\} \tag{10.11}$$

In above expressions, ξ_1 is the solid volume fraction of TiO_2, ξ_2 the solid volume fraction of Al_2O_3, ρ_1 the density of TiO_2, ρ_2 the density of Al_2O_3, k_1 the thermal conductivity of TiO_2 and k_2 the thermal conductivity of Al_2O_3.

Table 10.1: Characteristics of water and nanoparticles [54].

Physical properties	Water	Nanoparticles	
		TiO_2	Al_2O_3
$\rho\left(kg/m^3\right)$	997.1	4230	4000
$k\,(W/mK)$	0.613	8.4	40
$c_p\,(J/kgK)$	4179	692	773

Considering

$$\begin{array}{c}u=r\omega\frac{\partial f(\eta,\zeta)}{\partial\zeta},\ v=r\omega g(\eta,\zeta),\ w=-\sqrt{\frac{\omega\nu_f}{2}}\left(f+\eta\frac{\partial f}{\partial\eta}\right),\\ \theta(\eta,\zeta)=\frac{T-T_\infty}{T_w-T_0},\ \zeta=\left(\frac{2\omega}{\nu_f}\right)^{1/2}z,\ \eta=\frac{r}{R}.\end{array} \tag{10.12}$$

with $T=(T_w-T_0)\,\theta+T_\infty$ the equation (10.1) is automatically verified and Eqs. (10.2)$-$(10.10) give

$$\begin{array}{c}\frac{1}{(1-\xi_1-\xi_2)^{2.5}\left(1-\xi_1-\xi_2+\frac{\rho_1}{\rho_f}\xi_1+\frac{\rho_2}{\rho_f}\xi_2\right)}\left(2\frac{\partial^3 f}{\partial\zeta^3}-\lambda\left(\frac{1+d^*e^{-\zeta}}{1+de^{-\zeta}}\right)\frac{\partial f}{\partial\zeta}\right)+2f\frac{\partial^2 f}{\partial\zeta^2}-\left(\frac{\partial f}{\partial\zeta}\right)^2+g^2-\\ F_r\eta\frac{\left(1+d^*e^{-\zeta}\right)^2}{\sqrt{1+de^{-\zeta}}}\left(\left(\frac{\partial f}{\partial\zeta}\right)^2+\frac{1}{2}g^2\right)=\eta\left(\frac{\partial f}{\partial\zeta}\frac{\partial^2 f}{\partial\zeta\partial\eta}-\frac{\partial f}{\partial\eta}\frac{\partial^2 f}{\partial\zeta^2}\right),\end{array} \tag{10.13}$$

$$\frac{1}{(1-\xi_1-\xi_2)^{2.5}\left(1-\xi_1-\xi_2+\frac{\rho_1}{\rho_f}\xi_1+\frac{\rho_2}{\rho_f}\xi_2\right)}\left(2\frac{\partial^2 g}{\partial\zeta^2}-\lambda\left(\frac{1+d^*e^{-\zeta}}{1+de^{-\zeta}}\right)g\right)+2f\frac{\partial g}{\partial\zeta}-2g\frac{\partial f}{\partial\zeta}- \\ F_r\eta\frac{\left(1+d^*e^{-\zeta}\right)^2}{\sqrt{1+de^{-\zeta}}}\left(g^2+\frac{1}{2}\left(\frac{\partial f}{\partial\zeta}\right)^2\right)=\eta\left(\frac{\partial f}{\partial\eta}\frac{\partial g}{\partial\zeta}-\frac{\partial f}{\partial\zeta}\frac{\partial g}{\partial\eta}\right), \tag{10.14}$$

$$\frac{2}{\left(1-\xi_1-\xi_2+\frac{(\rho c_p)_1}{(\rho c_p)_f}\xi_1+\frac{(\rho c_p)_2}{(\rho c_p)_f}\xi_2\right)}\frac{\partial}{\partial\zeta}\left(\left(\frac{k_{hnf}}{k_f}+\frac{4}{3}Rd\left[\eta\left(\theta+S_t\right)+\theta_w\right]^3\right)\frac{\partial\theta}{\partial\zeta}\right)+2\,\mathrm{Pr}\,f\frac{\partial\theta}{\partial\zeta}= \\ \eta\,\mathrm{Pr}\left(\frac{\partial f}{\partial\zeta}\frac{\partial\theta}{\partial\eta}-\frac{\partial f}{\partial\eta}\frac{\partial\theta}{\partial\zeta}\right), \tag{10.15}$$

$$2f(\eta,0)=-\eta\frac{\partial f(\eta,0)}{\partial\eta},\ \frac{\partial f(\eta,0)}{\partial\zeta}=\gamma_1\frac{\partial^2 f(\eta,0)}{\partial\zeta},\ g(\eta,0)=1+\gamma_1\frac{\partial g(\eta,0)}{\partial\zeta},\ \theta(\eta,0)=1-S_t, \tag{10.16}$$

$$\frac{\partial f(\eta,\infty)}{\partial\zeta}\to 0,\ g(\eta,\infty)\to 0,\ \theta(\eta,\infty)\to 0. \tag{10.17}$$

Flow variables are given as

$$\gamma_1=N_1\sqrt{\frac{2\omega}{\nu_f}},\ \lambda=\frac{\nu_f\varepsilon_\infty}{\omega K_\infty},\ F_r=\frac{C_b\varepsilon_\infty^2\bar{R}}{\sqrt{K_\infty}},\ Pe=\mathrm{Re}\,\mathrm{Pr},\ \frac{1}{\gamma}=\sqrt{\frac{\alpha_f}{\nu_f}}\frac{Pe^{1/2}}{\bar{R}}, \\ \theta_w=\frac{T_0}{\tilde{A}\bar{R}},\ S_t=\frac{\tilde{B}}{\tilde{A}},\ Rd=\frac{4\tilde{\sigma}\left(\tilde{A}\bar{R}\right)^3}{\epsilon k_f},\ \mathrm{Pr}=\frac{\nu_f}{\alpha_f}. \tag{10.18}$$

10.1.1 First order of truncation

In first order of truncation, the terms including $\frac{\partial(.)}{\partial\eta}$ are assumed to be very small and may be approximated by zero. We have

$$\frac{1}{(1-\xi)^{2.5}\left(1-\xi+\frac{\rho_{CNT}}{\rho_f}\xi\right)}\left(2f'''-\lambda\left(\frac{1+d^*e^{-\zeta}}{1+de^{-\zeta}}\right)f'\right)+2ff''-f'^2+g^2- \\ F_r\eta\frac{\left(1+d^*e^{-\zeta}\right)^2}{\sqrt{1+de^{-\zeta}}}\left(f'^2+\frac{1}{2}g^2\right)=0, \tag{10.19}$$

$$\frac{1}{(1-\xi)^{2.5}\left(1-\xi+\frac{\rho_{CNT}}{\rho_f}\xi\right)}\left(2g''-\lambda\left(\frac{1+d^*e^{-\zeta}}{1+de^{-\zeta}}\right)g\right)+2fg'-2gf'- \\ F_r\eta\frac{\left(1+d^*e^{-\zeta}\right)^2}{\sqrt{1+de^{-\zeta}}}\left(g^2+\frac{1}{2}f'^2\right)=0, \tag{10.20}$$

$$\frac{1}{1-\xi+\frac{(\rho c_p)_{CNT}}{(\rho c_p)_f}\xi}\left(\left(\frac{k_{hnf}}{k_f}+\frac{4}{3}Rd\left[\eta\left(\theta+S_t\right)+\theta_w\right]^3\right)\theta'\right)'+\mathrm{Pr}\,f\theta'=0, \tag{10.21}$$

$$f(\eta,0)=0,\ f'(\eta,0)=\gamma_1 f''(\eta,0),\ g(\eta,0)=1+\gamma_1 g'(\eta,0),\ \theta(\eta,0)=1-S_t, \tag{10.22}$$

$$f'(\eta,\infty)\to 0,\ g(\eta,\infty)\to 0,\ \theta(\eta,\infty)\to 0. \tag{10.23}$$

10.1.2 Second order of truncation

For non-similarity solutions of Eqs. (10.13) − (10.17) , one considers

$$f^* = \frac{\partial f}{\partial \eta},\ g^* = \frac{\partial g}{\partial \eta},\ \theta^* = \frac{\partial \theta}{\partial \eta} \text{ and } \frac{\partial f^*}{\partial \eta} = \frac{\partial g^*}{\partial \eta} = \frac{\partial \theta^*}{\partial \eta} = 0. \tag{10.24}$$

Taking partial derivatives of Eqs. (10.13) − (10.17) with respect to η, one arrives at

$$\begin{aligned}&\frac{1}{(1-\xi)^{2.5}\left(1-\xi+\frac{\rho_{CNT}}{\rho_f}\xi\right)}\left(2f^{*\prime\prime\prime} - \lambda\left(\frac{1+d^*e^{-\zeta}}{1+de^{-\zeta}}\right)f^{*\prime}\right) + 2f^*f'' + 2ff^{*\prime\prime} - 2ff^{*\prime} + 2gg^* - \\ &F_r\frac{\left(1+d^*e^{-\zeta}\right)^2}{\sqrt{1+de^{-\zeta}}}\left(f'^2 + \frac{1}{2}g^2\right) - F_r\eta\frac{\left(1+d^*e^{-\zeta}\right)^2}{\sqrt{1+de^{-\zeta}}}\left(2f'f^{*\prime} + gg^*\right) = f'f^{*\prime} - f^*f'' + \eta\left(f^{*\prime 2} - f^*f^{*\prime\prime}\right),\end{aligned} \tag{10.25}$$

$$\begin{aligned}&\frac{1}{(1-\xi)^{2.5}\left(1-\xi+\frac{\rho_{CNT}}{\rho_f}\xi\right)}\left(2g^{*\prime\prime} - \lambda\left(\frac{1+d^*e^{-\zeta}}{1+de^{-\zeta}}\right)g^*\right) + 2f^*g' + 2fg^{*\prime} - 2g^*f' - 2gf^{*\prime} - \\ &F_r\frac{\left(1+d^*e^{-\zeta}\right)^2}{\sqrt{1+de^{-\zeta}}}\left(g^2 + \frac{1}{2}f'^2\right) - F_r\eta\frac{\left(1+d^*e^{-\zeta}\right)^2}{\sqrt{1+de^{-\zeta}}}\left(2gg^* + f'f^{*\prime}\right) = f^*g' - f'g^* + \eta\left(f^*g^{*\prime} - g^*f^{*\prime}\right),\end{aligned} \tag{10.26}$$

$$\begin{aligned}&\frac{1}{1-\xi+\frac{(\rho c_p)_{CNT}}{(\rho c_p)_f}\xi}\left(\begin{array}{c}\left(\left(\frac{k_{hnf}}{k_f} + \frac{4}{3}Rd\left[\eta\left(\theta + S_t\right) + \theta_w\right]^3\right)\theta^{*\prime}\right)' + \\ 4Rd\left[\eta\left(\theta + S_t\right) + \theta_w\right]^2\left(\theta\theta' + S_t\theta' + \eta\theta'\theta^*\right)\end{array}\right) + 2\Pr f^*\theta' + \\ &2\Pr f\theta^{*\prime} = \Pr\left(f'\theta^* - f^*\theta'\right) + \eta\Pr\left(f^{*\prime}\theta^* - \theta^{*\prime}f^*\right),\end{aligned} \tag{10.27}$$

$$f^*(\eta,0) = 0,\ f^{*\prime}(\eta,0) = \gamma_1 f^{*\prime\prime}(\eta,0),\ g^*(\eta,0) = \gamma_1 g^{*\prime}(\eta,0),\ \theta^*(\eta,0) = 0, \tag{10.28}$$

$$f^{*\prime}(\eta,\infty) \to 0,\ g^*(\eta,\infty) \to 0,\ \theta^*(\eta,\infty) \to 0. \tag{10.29}$$

10.2 Quantities of interest

Components of skin friction and local Nusselt number yield

$$\left.\begin{aligned}\left(\tfrac{\mathrm{Re}}{2}\right)^{1/2}C_f &= \tfrac{1}{\eta}\tfrac{1}{(1-\xi_1-\xi_2)^{2.5}}f''(\eta,0),\\ \left(\tfrac{\mathrm{Re}}{2}\right)^{1/2}C_g &= \tfrac{1}{\eta}\tfrac{1}{(1-\xi_1-\xi_2)^{2.5}}g'(\eta,0),\\ \left(\tfrac{\mathrm{Re}}{2}\right)^{-1/2}Nu &= -\eta\left(\tfrac{k_{hnf}}{k_f} + \tfrac{4}{3}R_d\left(\eta + \theta_w\right)^3\right)\theta'(\eta,0),\end{aligned}\right\} \tag{10.30}$$

in which $\mathrm{Re} = \frac{\bar{R}^2\omega}{\nu_f}$ stands for local Reynolds number.

10.3 Analysis

This section intends to demonstrate the behavior of emerging flow variables on velocities and temperature fields. Results are achieved for both $TiO_2-Al_2O_3$/water hybrid nanofluid ($\xi_1 = 0.01$, $\xi_2 = 0.05$), Al_2O_3-water nanofluid ($\xi_1 = 0.0$, $\xi_2 = 0.06$) and TiO_2-water nanofluid ($\xi_1 = 0.06$, $\xi_2 = 0.0$). Fig. 10.2 interpreted the role of (γ_1) on velocity field $f'(\zeta)$. Here reduction in velocity field $f'(\zeta)$ is noticed through larger (γ_1) for hybrid nanofluid and nanomaterial. Role of (λ) on $f'(\zeta)$ is illustrated in Fig. 10.3. Here larger (λ) correspond to lower velocity field $f'(\zeta)$ for hybrid nanofluid and nanofluid. Consequences of (d) and (d^*) on velocity $f'(\zeta)$ is captured in Figs. 10.4 and 10.5. Here velocity $f'(\zeta)$ is an increasing function of (d) while reverse trend is observed for (d^*) for both hybrid nanofluid ($TiO_2-Al_2O_3$/water) and nanofluid (TiO_2-water and Al_2O_3-water). Here $f'(\zeta)$ against (F_r) is shown in Fig. 10.6. Here it is investigated that an enhancement in (F_r) produces resilience in fluid motion which corresponds to reduction in $f'(\zeta)$ for hybrid nanofluid ($TiO_2-Al_2O_3$/water) and nanofluid (TiO_2-water and Al_2O_3-water). Significant behavior of (γ_1) on $g(\zeta)$ is depicted in Fig. 10.7. Since (γ_1) is inversely related to kinematic viscosity. Thus higher values of (γ_1) encountered more resistance between fluid and disk which produce lower $g(\zeta)$ for both hybrid nanofluid and nanomaterial. Fig. 10.8 elaborated the impact of (λ) on $g(\zeta)$. Here $g(\zeta)$ is an increasing function of (λ) for both hybrid nanofluid and nanomaterial. Figs. 10.9 and 10.10 describe outcomes of (d) and (d^*) on $g(\zeta)$. It is noticed that $g(\zeta)$ possesses opposite trend for (d) and (d^*) for hybrid nanofluid and nanomaterial. Decreasing trend of $g(\zeta)$ is noted through (F_r) for both hybrid nanofluid and nanomaterial (see Fig. 10.11). Fig. 10.12 characterized consequences of (λ) on $\theta(\zeta)$. An increment in (λ) give rise to stronger $\theta(\zeta)$ and more associated layer thickness for hybrid nanofluid and nanofluid. Outcomes of (d) and (d^*) on $\theta(\zeta)$ is illustrated in Figs. 10.13 and 10.14. An enhancement in $\theta(\zeta)$ is analyzed through (d) while opposite behavior is seen through (d^*). Higher estimation of (F_r) yield an enhancement in $\theta(\zeta)$ for hybrid nanofluid ($TiO_2-Al_2O_3$/water) and nanofluid (TiO_2-water and Al_2O_3-water) (see Fig. 10.15). Fig. 10.16 is devoted to examine the contribution of (Rd) on temperature $\theta(\zeta)$. Clearly $\theta(\zeta)$ enhances for higher estimation of (Rd) for hybrid nanofluid and nanomaterial. It is due to the fact that more heat is transferred due to the transmission of waves. Role of (θ_w) on $\theta(\zeta)$ is pointed out in Fig. 10.17. Temperature $\theta(\zeta)$ decays through (θ_w) for hybrid nanofluid ($TiO_2-Al_2O_3$/water) and nanomaterial

(TiO_2-water and Al_2O_3-water). Variation of (S_t) on $\theta(\zeta)$ is sketched in Fig. 10.18. Physically thermal stratification is the formation of two discrete layers of fluid at different temperatures. Temperature difference between layers increases due to higher (S_t) which consequently reduces $\theta(\zeta)$ for hybrid nanofluid and nanofluid. Numerical data of drag force at the surface $\left(\frac{\mathrm{Re}}{2}\right)^{1/2} C_f$ and $-\left(\frac{\mathrm{Re}}{2}\right)^{1/2} C_g$ for distinct values of (γ_1), (λ), (d), (d^*) and (F_r) is characterized in Tables 10.2 and 10.3. Higher $\left(\frac{\mathrm{Re}}{2}\right)^{1/2} C_f$ is noted through (d) while opposite trend holds for $-\left(\frac{\mathrm{Re}}{2}\right)^{1/2} C_g$. Table 10.4 elaborated the local Nusselt number $\left(\frac{\mathrm{Re}}{2}\right)^{-1/2} Nu$ through (Rd), (θ_w) and (S_t). Local Nusselt number is reduced through larger (θ_w) and (S_t) while opposite trend is noticed for (Rd) in both hybrid nanofluid and nanomaterial. Table 10.5 is arranged to validate the current results with Miklavcic and Wang [27]. Results are in an excellent consensus.

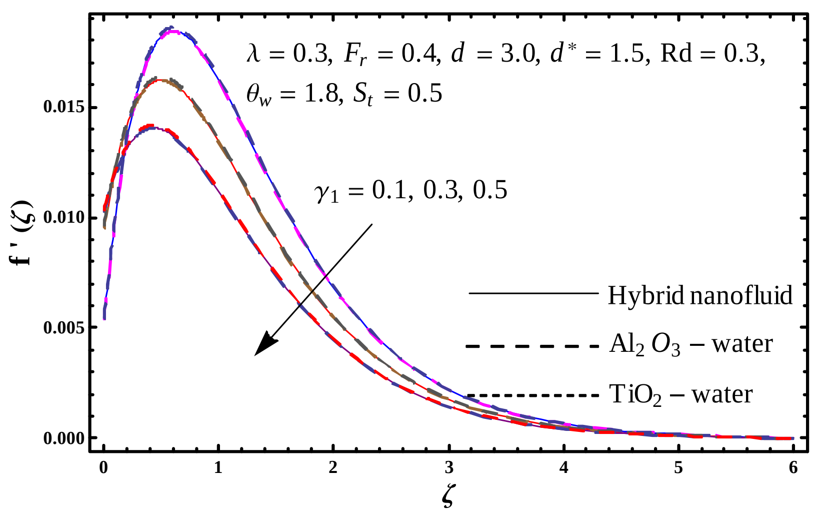

Fig. 10.2: Sketch of $f'(\zeta)$ against γ_1.

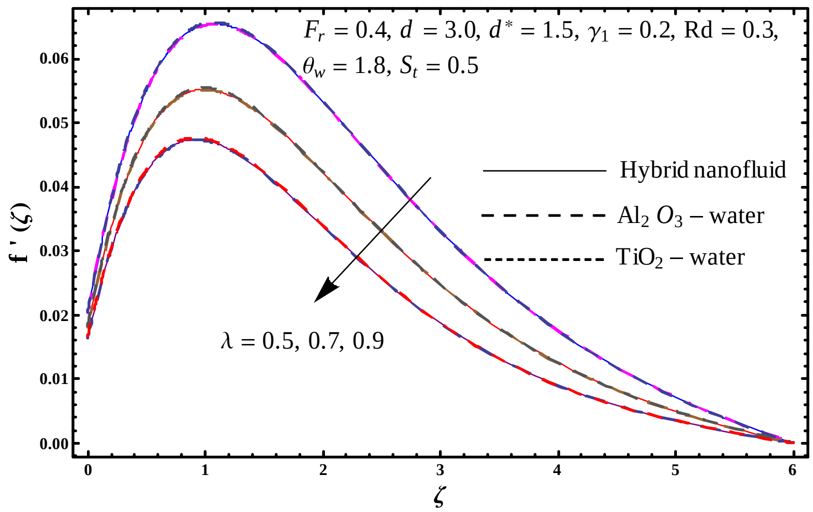

Fig. 10.3: Plot for $f'(\zeta)$ against λ.

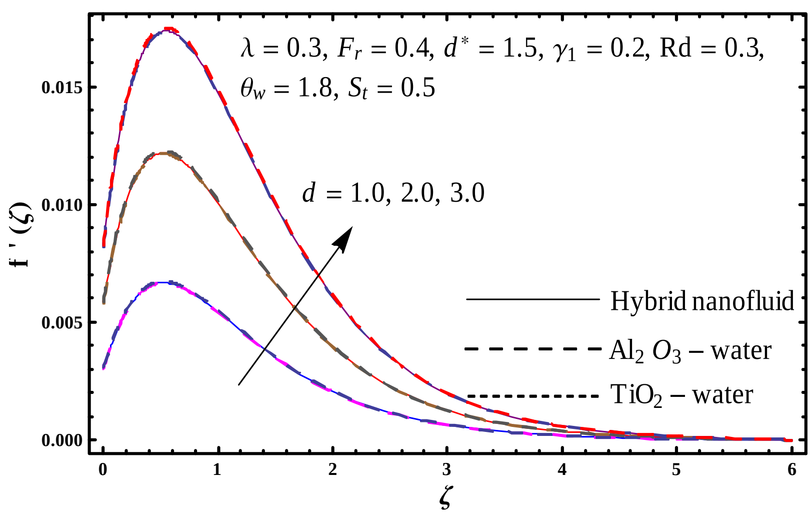

Fig. 10.4: Plot for $f'(\zeta)$ against d.

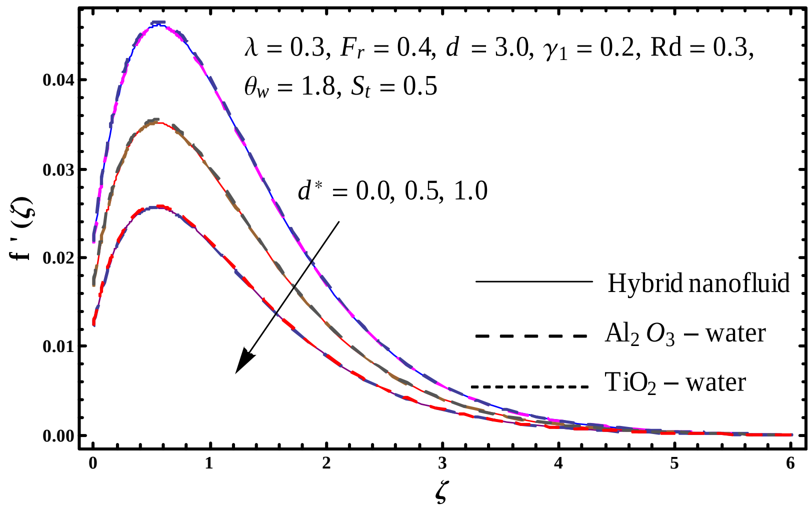

Fig. 10.5: Plot for $f'(\zeta)$ against d^*.

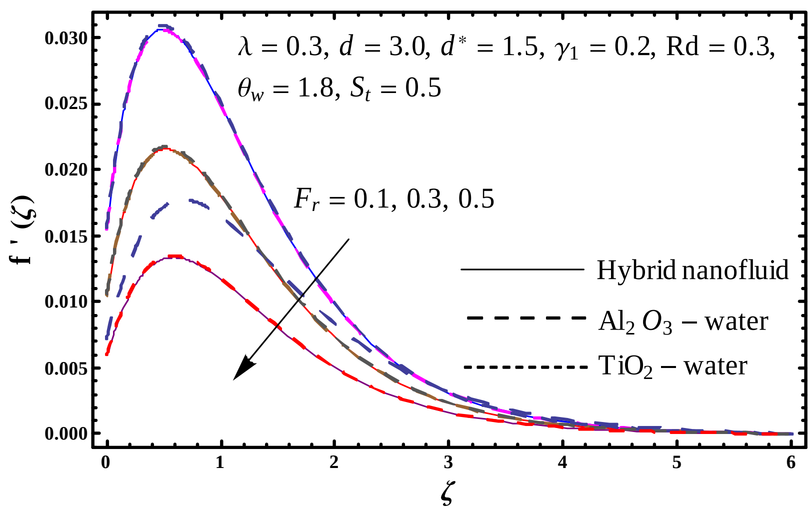

Fig. 10.6: Plot for $f'(\zeta)$ versus F_r.

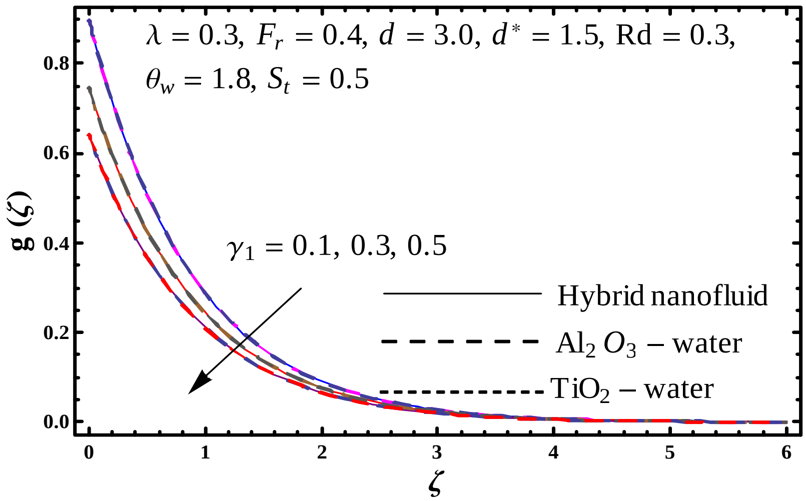

Fig. 10.7: Sketch of $g(\zeta)$ versus γ_1.

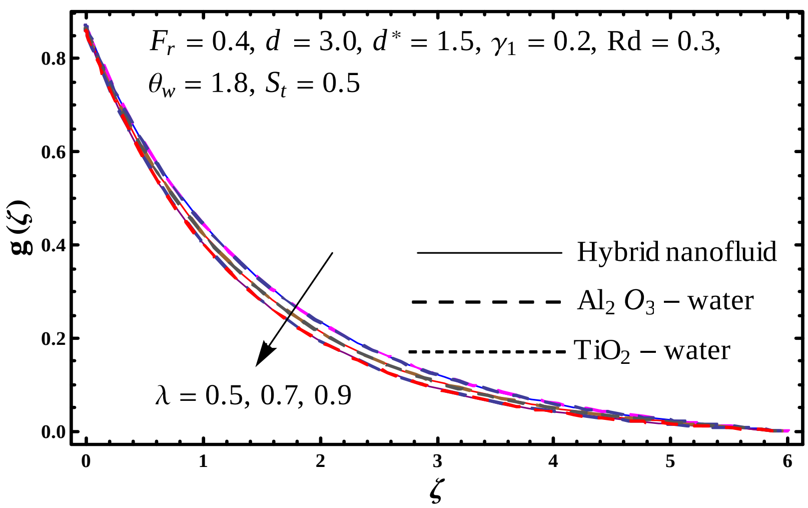

Fig. 10.8: Sketch of $g(\zeta)$ versus λ.

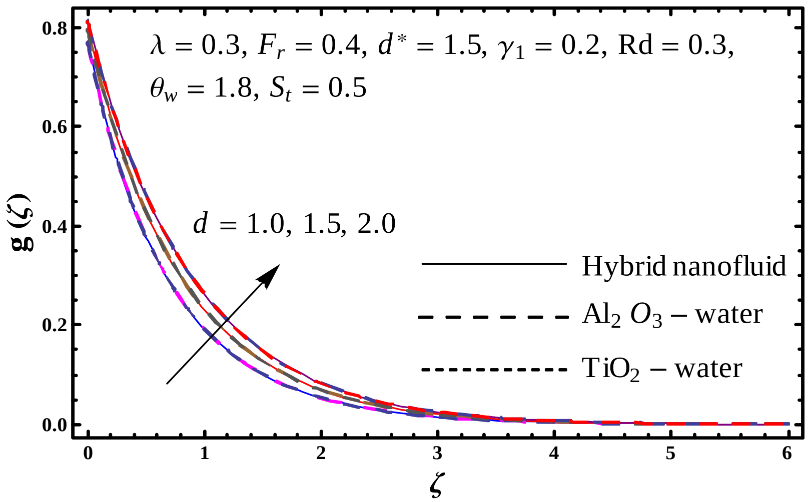

Fig. 10.9: Sketch of $g(\zeta)$ versus d.

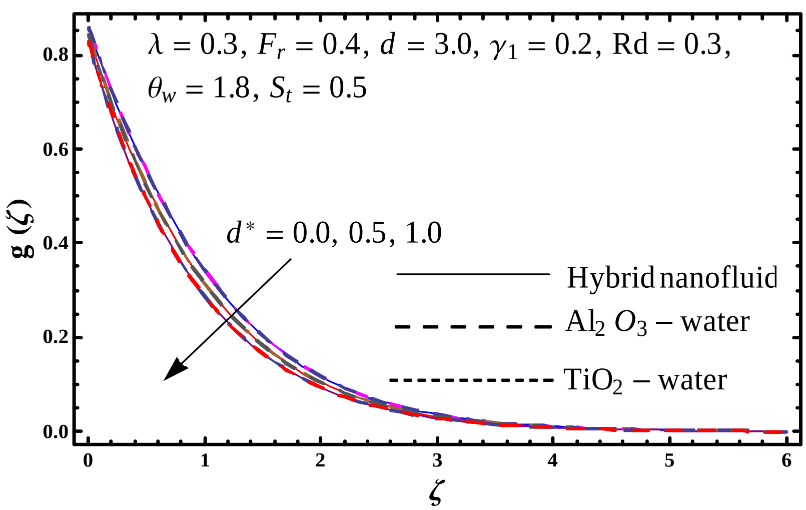

Fig. 10.10: Sketch of $g(\zeta)$ versus d^*.

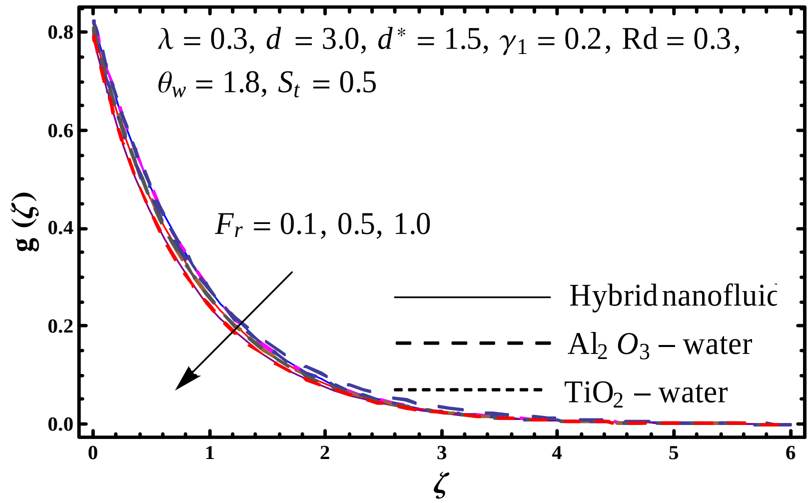

Fig. 10.11: Sketch of $g(\zeta)$ versus F_r.

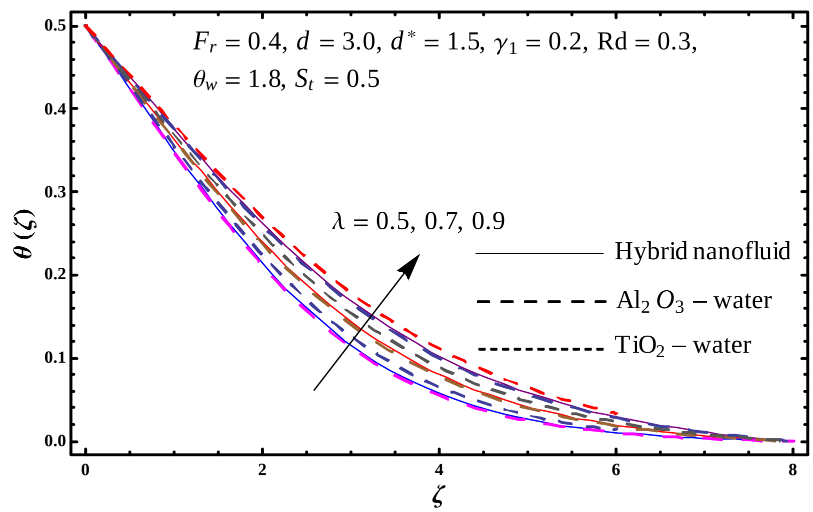

Fig. 10.12: Sketch of $\theta(\zeta)$ versus λ.

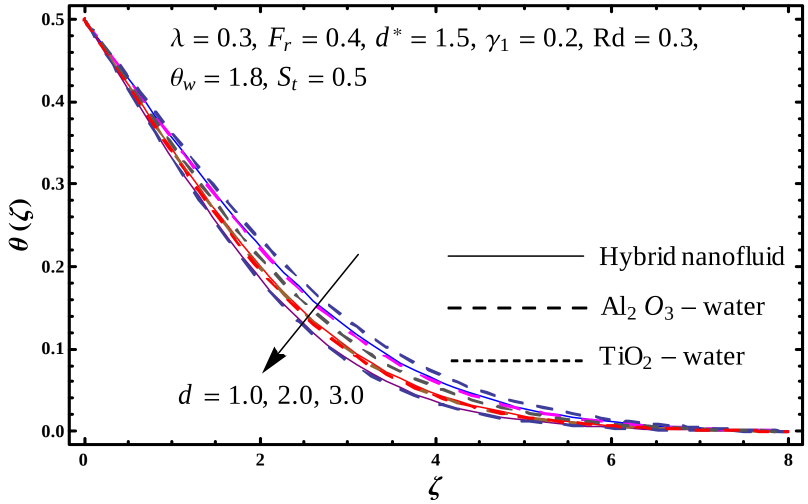

Fig. 10.13: Sketch of $\theta(\zeta)$ versus d.

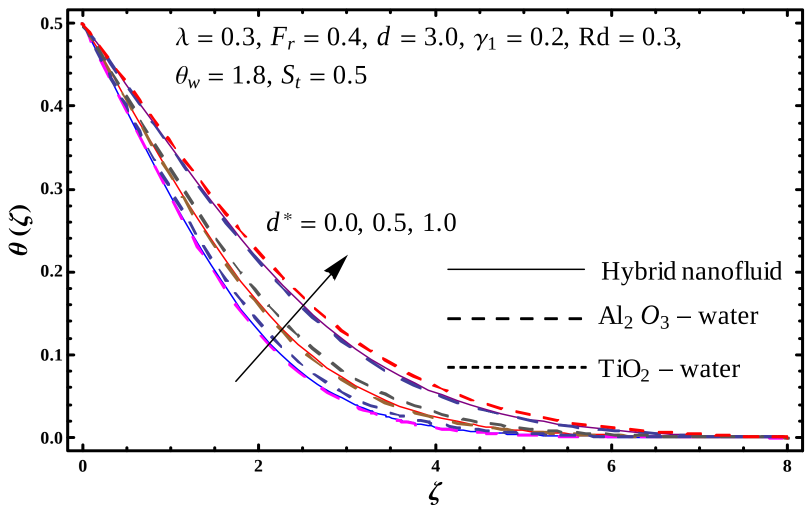

Fig. 10.14: Sketch of $\theta(\zeta)$ versus d^*.

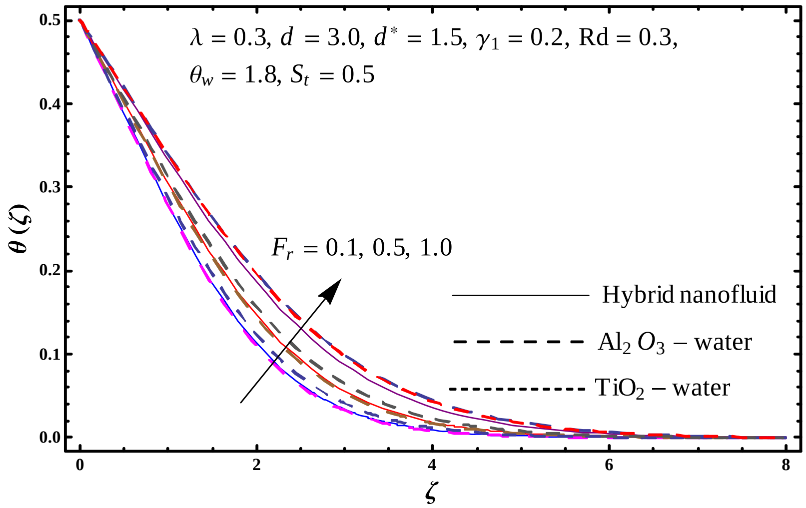

Fig. 10.15: Sketch of $\theta(\zeta)$ versus F_r.

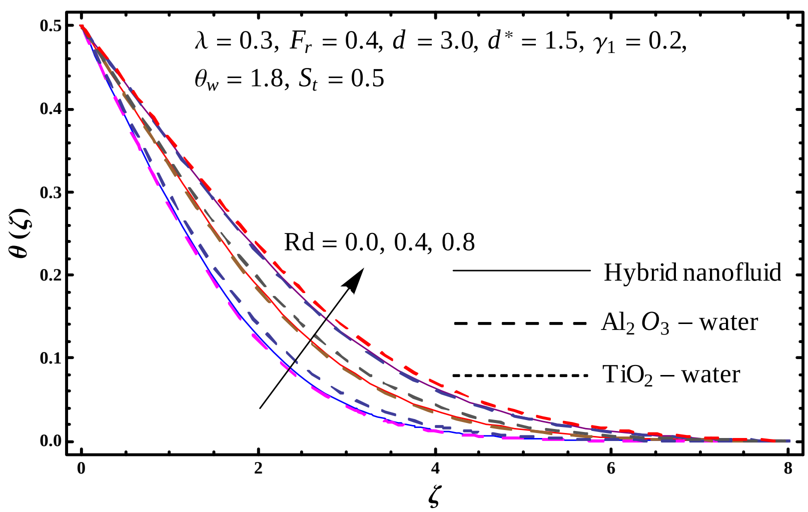

Fig. 10.16: Sketch for $\theta(\zeta)$ against Rd.

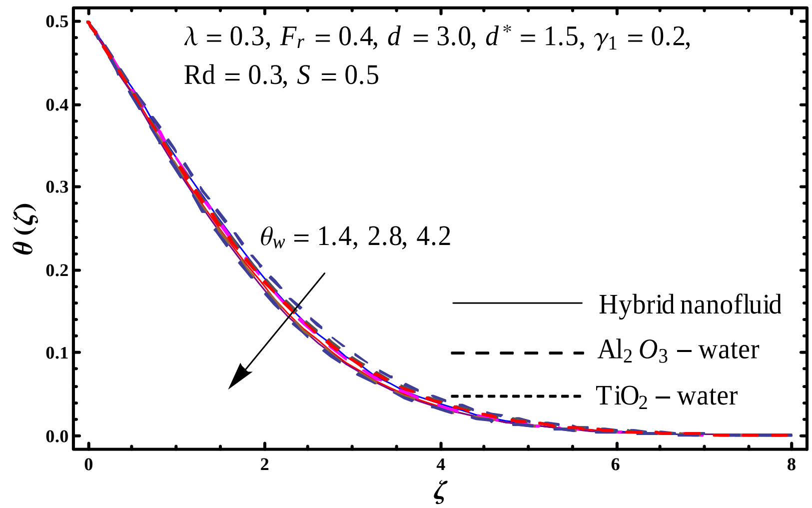

Fig. 10.17: Sketch of $\theta(\zeta)$ against θ_w.

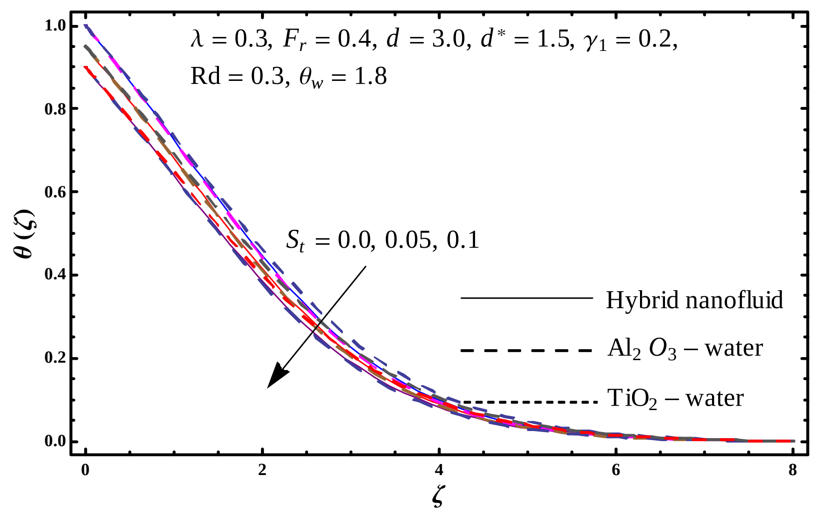

Fig. 10.18: Sketch of $\theta(\zeta)$ against S_t.

Table 10.2: Numerical data of skin friction coefficient $\left(\frac{\text{Re}}{2}\right)^{1/2} C_f$ against λ, d^*, γ_1, d, and F_r.

λ	d	d^*	F_r	γ_1	$\left(\frac{\text{Re}}{2}\right)^{1/2} C_f$		
					Hybrid nanofluid	Al_2O_3-water	TiO_2-water
0.1	3.0	1.5	0.4	0.2	0.00925	0.00922	0.00918
0.2					0.03551	0.03545	0.03583
0.4					0.05799	0.05790	0.05848
0.3	1.0	1.5	0.4	0.2	0.01785	0.01782	0.01801
	2.0				0.03399	0.03393	0.03428
	4.0				0.05986	0.05976	0.06036
0.3	3.0	0.0	0.4	0.2	0.12702	0.12679	0.12812
		0.5			0.09909	0.09892	0.09995
		1.0			0.07268	0.07256	0.07331
0.3	3.0	1.5	0.1	0.2	0.09073	0.09056	0.09155
			0.2		0.07586	0.07572	0.07653
			0.3		0.06157	0.06146	0.06211
0.3	3.0	1.5	0.4	0.0	0.08606	0.08590	0.08682
				0.1	0.06309	0.06297	0.06363
				0.3	0.03722	0.03716	0.03754

Table 10.3: Numerical data of skin friction coefficient $-\left(\frac{\mathrm{Re}}{2}\right)^{1/2} C_g$ against λ, d, F_r, d^* and γ_1.

λ	d	d^*	F_r	γ_1	$-\left(\frac{\mathrm{Re}}{2}\right)^{1/2} C_g$		
					Hybrid nanofluid	Al_2O_3-water	TiO_2-water
0.1	3.0	1.5	0.4	0.2	0.66901	0.66846	0.67175
0.2					0.68709	0.68656	0.68972
0.4					0.72321	0.72273	0.72558
0.3	1.0	1.5	0.4	0.2	1.34011	1.33993	1.34101
	2.0				1.18856	1.18836	1.18953
	4.0				1.02263	1.02242	1.02371
0.3	3.0	0.0	0.4	0.2	0.82854	0.82839	0.82933
		0.5			0.91843	0.91827	0.91925
		1.0			1.00631	1.00613	1.00721
0.3	3.0	1.5	0.1	0.2	1.02401	1.02391	1.02452
			0.2		1.04735	1.04721	1.04804
			0.3		1.06987	1.06969	1.07073
0.3	3.0	1.5	0.4	0.0	1.37408	1.37371	1.37593
				0.1	1.21575	1.21548	1.2171
				0.3	0.99152	0.99136	0.99231

Table 10.4: Numerical values of local Nusselt number $\left(\frac{\text{Re}}{2}\right)^{-1/2} Nu$ against Rd, θ_w and S_t.

Rd	θ_w	S_t	$\left(\frac{\text{Re}}{2}\right)^{-1/2} Nu$		
			Hybrid nanofluid	Al_2O_3-water	TiO_2-water
0.0	1.8	0.5	0.07952	0.07788	0.08846
0.1			0.10287	0.10092	0.11004
0.2			0.12600	0.12426	0.12945
0.3	1.8	0.5	0.14731	0.14597	0.15012
	2.4		0.13636	0.13461	0.13979
	3.0		0.12774	0.12574	0.13475
0.3	1.8	0.1	0.25027	0.24934	0.25786
		0.2	0.21937	0.21774	0.23537
		0.3	0.19872	0.19908	0.20607

Table 10.5: Skin friction coefficient $\left(\frac{\text{Re}}{2}\right)^{1/2} C_f$ against γ_1 when $\xi_1 = \xi_2 = F_r = \lambda = d = d^* = 0$.

γ_1	$(\frac{\text{Re}}{2})^{1/2}C_f$	
	Miklavcic and Wang [27]	Present
0.0	0.51023	0.35719
0.1	0.42145	0.31149
0.2	0.35258	0.27322
0.5	0.22384	0.19218
1.0	0.12792	0.12044
2.0	0.06101	0.06208
5.0	0.01858	0.01992
10.0	0.00681	0.00721
20.0	0.00236	0.00232

Chapter 11

Entropy generation analysis of Carreau fluid with entire new concepts of modified Darcy's law and variable characteristics

This chapter studied the characteristics of nonlinear partial slip in flow of Carreau fluid. Fluid saturates the porous medium. Modified Darcy's law is employed in modeling. Variable characteristics in modeling are accounted. Entropy generation rate is formulated. Heat transfer is analyzed with viscous dissipation. Relevant equations are presented by boundary layer theory. The resulting problems are nonlinear not in terms of equations but also through boundary conditions. Dimensionless equations are obtained through adequate transformations. Velocities, temperature and entropy generation rate are discussed. Numerical computations of skin friction coefficients and local Nusselt number are arranged. Physical interpretation of influential variables is arranged.

11.1 Model development

Here flow of Carreau fluid by a rotating disk is investigated. Partial slip condition in modeling is taken. Flow is modelled by modified Darcy's law. Variable characteristics of porous space are considered. Disk is at $z = 0$ (see Fig. 11.1). Viscous dissipation is taken. Here cylindrical coordinate frame $(r,\ \psi,\ z)$ is adopted. Resulting equations for the considered problem are:

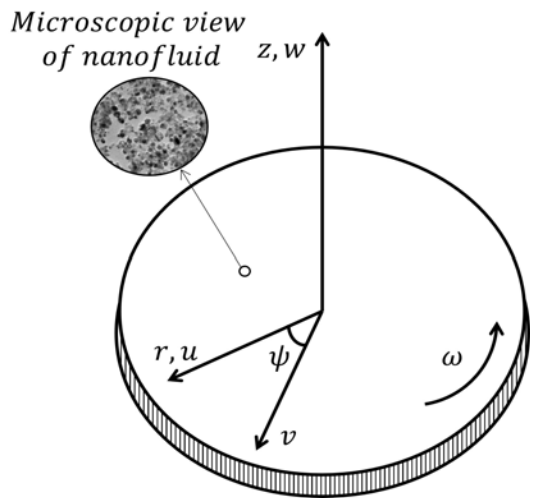

Fig. 11.1: Flow configuration.

$$\frac{\partial u}{\partial r} + \frac{v}{r} + \frac{\partial w}{\partial z} = 0, \tag{11.1}$$

$$\rho\left(u\frac{\partial u}{\partial r} - \frac{v^2}{r} + w\frac{\partial u}{\partial z}\right) = \frac{\partial \breve{S}_{rz}}{\partial z} - \frac{\varepsilon(z)}{K^*(z)}\left(\mu_0\left(1 + \frac{n-1}{2}(\Gamma\mathring{\gamma})^2\right)\right)u, \tag{11.2}$$

$$\rho\left(u\frac{\partial v}{\partial r} + \frac{uv}{r} + w\frac{\partial v}{\partial z}\right) = \frac{\partial \breve{S}_{\theta z}}{\partial z} - \frac{\varepsilon(z)}{K^*(z)}\left(\mu_0\left(1 + \frac{n-1}{2}(\Gamma\mathring{\gamma})^2\right)\right)v, \tag{11.3}$$

$$\begin{gathered}\rho c_p\left(u\frac{\partial T}{\partial r} + w\frac{\partial T}{\partial z}\right) = k\left(\frac{\partial^2 T}{\partial z^2}\right) + \mu_0\left(1 + \frac{n-1}{2}(\Gamma\mathring{\gamma})^2\right)\left(\left(\frac{\partial u}{\partial z}\right)^2 + \right.\\ \left.\left(\frac{\partial v}{\partial z}\right)^2\right) + \frac{\varepsilon(z)}{K^*(z)}\left(\mu_0\left(1 + \frac{n-1}{2}(\Gamma\mathring{\gamma})^2\right)\right)\left(u^2 + v^2\right),\end{gathered} \tag{11.4}$$

$$u - N_1\breve{S}_{rz} = 0, \quad v - N_1\breve{S}_{\theta z} = r\omega, \quad w = 0, \quad T = T_w \quad \text{at} \quad z = 0, \tag{11.5}$$

$$u \to 0, \quad v \to 0, \quad T \to T_\infty \quad \text{as} \quad z \to \infty, \tag{11.6}$$

where

$$\breve{S}_{rz}=\left(\frac{\partial w}{\partial r}+\frac{\partial u}{\partial z}\right)\left(\mu_0\left(1+\frac{n-1}{2}\left(\Gamma\mathring{\gamma}\right)^2\right)\right),\ \breve{S}_{\theta z}=\frac{\partial v}{\partial z}\left(\mu_0\left(1+\frac{n-1}{2}\left(\Gamma\mathring{\gamma}\right)^2\right)\right),\quad (11.7)$$

$$\mathring{\gamma}=\sqrt{2\left(\frac{\partial u}{\partial r}\right)^2+2\left(\frac{\partial w}{\partial z}\right)^2+\frac{2u^2}{r^2}},\quad (11.8)$$

$$K^*\left(z\right)=K_\infty\left(1+de^{-\frac{z}{\gamma}}\right),\quad (11.9)$$

$$\varepsilon\left(z\right)=\varepsilon_\infty\left(1+d^*e^{-\frac{z}{\gamma}}\right).\quad (11.10)$$

Considering

$$\begin{array}{c} u=r\omega\frac{\partial f(\eta,\zeta)}{\partial\zeta},\ v=r\omega g(\eta,\zeta),\ w=-\sqrt{\frac{\omega\nu_f}{2}}\left(f+\eta\frac{\partial f}{\partial\eta}\right), \\ \theta(\eta,\zeta)=\frac{T-T_\infty}{T_w-T_\infty},\ \zeta=\left(\frac{2\omega}{\nu_f}\right)^{1/2}z,\ \eta=\frac{r}{R}. \end{array}\quad (11.11)$$

We have

$$\begin{array}{c} 2\frac{\partial^3 f}{\partial\zeta^3}\left(1+\frac{n-1}{2}We^2\left(\begin{array}{c} 12\left(\frac{\partial f}{\partial\zeta}\right)^2+4\eta^2\left(\frac{\partial^2 f}{\partial\eta\partial\zeta}\right)+ \\ 10\frac{\partial f}{\partial\zeta}\frac{\partial^2 f}{\partial\eta\partial\zeta} \end{array}\right)\right)-\left(\frac{\partial f}{\partial\zeta}\right)^2+g^2+2f\frac{\partial^2 f}{\partial\zeta^2}- \\ \lambda\frac{1+d^*e^{-\zeta}}{1+de^{-\zeta}}\frac{\partial f}{\partial\zeta}\left(1+\frac{n-1}{2}We^2\left(\begin{array}{c} 12\left(\frac{\partial f}{\partial\zeta}\right)^2+4\eta^2\left(\frac{\partial^2 f}{\partial\eta\partial\zeta}\right)+ \\ 10\frac{\partial f}{\partial\zeta}\frac{\partial^2 f}{\partial\eta\partial\zeta} \end{array}\right)\right)+ \\ We^2\left(n-1\right)\frac{\partial^2 f}{\partial\zeta^2}\left(\begin{array}{c} 24\frac{\partial f}{\partial\zeta}\frac{\partial^2 f}{\partial\zeta^2}+8\eta^2\frac{\partial^3 f}{\partial\zeta^2\partial\eta}+ \\ 10\eta\frac{\partial^2 f}{\partial\zeta^2}\frac{\partial^2 f}{\partial\eta\partial\zeta}+10\frac{\partial f}{\partial\zeta}\frac{\partial^3 f}{\partial\zeta^2\partial\eta} \end{array}\right)=\eta\left(\frac{\partial f}{\partial\zeta}\frac{\partial^2 f}{\partial\zeta\partial\eta}-\frac{\partial f}{\partial\eta}\frac{\partial^2 f}{\partial\zeta^2}\right), \end{array}\quad (11.12)$$

$$\begin{array}{c} 2\frac{\partial^2 g}{\partial\zeta^2}\left(1+\frac{n-1}{2}We^2\left(\begin{array}{c} 12\left(\frac{\partial f}{\partial\zeta}\right)^2+4\eta^2\left(\frac{\partial^2 f}{\partial\eta\partial\zeta}\right)+ \\ 10\frac{\partial f}{\partial\zeta}\frac{\partial^2 f}{\partial\eta\partial\zeta} \end{array}\right)\right)-2g\frac{\partial f}{\partial\zeta}-2f\frac{\partial g}{\partial\zeta}- \\ \lambda\frac{1+d^*e^{-\zeta}}{1+de^{-\zeta}}g\left(1+\frac{n-1}{2}We^2\left(\begin{array}{c} 12\left(\frac{\partial f}{\partial\zeta}\right)^2+4\eta^2\left(\frac{\partial^2 f}{\partial\eta\partial\zeta}\right)+ \\ 10\frac{\partial f}{\partial\zeta}\frac{\partial^2 f}{\partial\eta\partial\zeta} \end{array}\right)\right)+ \\ We^2\left(n-1\right)\frac{\partial g}{\partial\zeta}\left(\begin{array}{c} 24\frac{\partial f}{\partial\zeta}\frac{\partial^2 f}{\partial\zeta^2}+8\eta^2\frac{\partial^3 f}{\partial\zeta^2\partial\eta}+ \\ 10\eta\frac{\partial^2 f}{\partial\zeta^2}\frac{\partial^2 f}{\partial\eta\partial\zeta}+10\frac{\partial f}{\partial\zeta}\frac{\partial^3 f}{\partial\zeta^2\partial\eta} \end{array}\right)=\eta\left(\frac{\partial f}{\partial\eta}\frac{\partial g}{\partial\zeta}-\frac{\partial f}{\partial\zeta}\frac{\partial g}{\partial\eta}\right), \end{array}\quad (11.13)$$

$$2\frac{\partial^2\theta}{\partial\zeta^2}+\lambda Br\eta^2\frac{1+d^*e^{-\zeta}}{1+de^{-\zeta}}\left(1+\frac{n-1}{2}We^2\left(\begin{array}{c}12\left(\frac{\partial f}{\partial\zeta}\right)^2+4\eta^2\left(\frac{\partial^2 f}{\partial\eta\partial\zeta}\right)+\\10\frac{\partial f}{\partial\zeta}\frac{\partial^2 f}{\partial\eta\partial\zeta}\end{array}\right)\right)\left(\left(\frac{\partial f}{\partial\zeta}\right)^2+g^2\right)+$$
$$2Br\eta^2\left(1+\frac{n-1}{2}We^2\left(\begin{array}{c}12\left(\frac{\partial f}{\partial\zeta}\right)^2+4\eta^2\left(\frac{\partial^2 f}{\partial\eta\partial\zeta}\right)+\\10\frac{\partial f}{\partial\zeta}\frac{\partial^2 f}{\partial\eta\partial\zeta}\end{array}\right)\right)\left(\left(\frac{\partial^2 f}{\partial\zeta^2}\right)^2+\left(\frac{\partial g}{\partial\zeta}\right)^2\right)+$$
$$2\,\mathrm{Pr}\,f\frac{\partial\theta}{\partial\zeta}=\eta\,\mathrm{Pr}\left(\frac{\partial f}{\partial\zeta}\frac{\partial\theta}{\partial\eta}-\frac{\partial f}{\partial\eta}\frac{\partial\theta}{\partial\zeta}\right), \tag{11.14}$$

$$\left.\begin{array}{c}2f(\eta,0)=-\eta\frac{\partial f(\eta,0)}{\partial\eta},\ \theta(\eta,0)=1,\\ \frac{\partial f(\eta,0)}{\partial\zeta}-\gamma_1\left(1+\frac{n-1}{2}We^2\left(\begin{array}{c}12\left(\frac{\partial f}{\partial\zeta}\right)^2+4\eta^2\left(\frac{\partial^2 f}{\partial\eta\partial\zeta}\right)+\\10\frac{\partial f}{\partial\zeta}\frac{\partial^2 f}{\partial\eta\partial\zeta}\end{array}\right)\right)\frac{\partial^2 f(\eta,0)}{\partial\zeta^2}=0,\\ g(\eta,0)-\gamma_1\left(1+\frac{n-1}{2}We^2\left(\begin{array}{c}12\left(\frac{\partial f}{\partial\zeta}\right)^2+4\eta^2\left(\frac{\partial^2 f}{\partial\eta\partial\zeta}\right)+\\10\frac{\partial f}{\partial\zeta}\frac{\partial^2 f}{\partial\eta\partial\zeta}\end{array}\right)\right)\frac{\partial g(\eta,0)}{\partial\zeta}=1,\end{array}\right\} \tag{11.15}$$

$$\frac{\partial f(\eta,\infty)}{\partial\zeta}\to 0,\ g(\eta,\infty)\to 0,\ \theta(\eta,\infty)\to 0, \tag{11.16}$$

Here Eq. (11.1) is identically justified. Involved flow parameters are given as:

$$\begin{array}{c}\lambda=\frac{\nu_f\varepsilon_\infty}{\omega K_\infty},\ We=\Gamma\omega,\ \mathrm{Re}=\frac{\bar{R}^2\omega}{\nu},\ Ec=\frac{\bar{R}^2\omega}{(T_w-T_\infty)(c_p)_f},\ Br=Ec\,\mathrm{Pr},\\ \gamma_1=N_1\mu_0\sqrt{\frac{2\omega}{\nu}},\ \mathrm{Pr}=\frac{\nu}{\alpha},\ Pe=\mathrm{Re}\,\mathrm{Pr},\ \frac{1}{\gamma}=\sqrt{\frac{\alpha}{\nu}}\frac{Pe^{1/2}}{\bar{R}}.\end{array} \tag{11.17}$$

11.1.1 First order of truncation

In first order of truncation, the terms including $\frac{\partial(.)}{\partial\eta}$ are assumed very small and may be approximated by zero. We thus express that

$$2f'''\left(1+\frac{n-1}{2}We^2\left(12f'^2\right)\right)-f'^2+g^2+2ff''-\lambda\frac{1+d^*e^{-\zeta}}{1+de^{-\zeta}}f'\left(1+\frac{n-1}{2}We^2\left(12f'^2\right)\right)+$$
$$We^2(n-1)f''\left(24f'f''\right)=0, \tag{11.18}$$

$$2g''\left(1+\frac{n-1}{2}We^2\left(12f'^2\right)\right)-2gf'-2fg'-\lambda\frac{1+d^*e^{-\zeta}}{1+de^{-\zeta}}g\left(1+\frac{n-1}{2}We^2\left(12f'^2\right)\right)+$$
$$We^2(n-1)g'\left(24f'f''\right)=0, \tag{11.19}$$

$$2\theta''+\lambda Br\eta^2\frac{1+d^*e^{-\zeta}}{1+de^{-\zeta}}\left(1+\frac{n-1}{2}We^2\left(12f'^2\right)\right)\left(f'^2+g^2\right)+2\,\mathrm{Pr}\,f\theta'+$$
$$2Br\eta^2\left(1+\frac{n-1}{2}We^2\left(12f'^2\right)\right)\left(f''^2+g'^2\right)=0, \tag{11.20}$$

$$f(\eta,0)=0,\ \theta(\eta,0)=1,\ f'(\eta,0)-\gamma_1\left(1+\tfrac{n-1}{2}We^2\left(12f'^2\right)\right)f''(\eta,0)=0,$$
$$g(\eta,0)-\gamma_1\left(1+\tfrac{n-1}{2}We^2\left(12f'^2\right)\right)g'(\eta,0)=1, \tag{11.21}$$

$$f'(\eta,\infty)\to 0,\ g(\eta,\infty)\to 0,\ \theta(\eta,\infty)\to 0. \tag{11.22}$$

11.1.2 Second order of truncation

For non-similarity solutions of Eqs. (11.12) – (11.16) , one considers

$$f^*=\frac{\partial f}{\partial \eta},\ g^*=\frac{\partial g}{\partial \eta},\ \theta^*=\frac{\partial \theta}{\partial \eta}\text{ and }\frac{\partial f^*}{\partial \eta}=\frac{\partial g^*}{\partial \eta}=\frac{\partial \theta^*}{\partial \eta}=0. \tag{11.23}$$

Differentiation of Eqs. (11.12) – (11.16) with respect to η yields

$$\begin{aligned}
&2f^{*'''}\left(1+\tfrac{n-1}{2}We^2\left(\begin{array}{c}12f'^2+4\eta^2f^{*'2}+\\10\eta f'f^{*'}\end{array}\right)\right)+2f'''\left(\tfrac{n-1}{2}\right)We^2\left(\begin{array}{c}24f'f^{*'}+8\eta f^{*'2}+\\10f'f^{*''}+10\eta f^{*'}f^{*''}\end{array}\right)+\\
&2(n-1)We^2f^{*''}\left(\begin{array}{c}12f'f^{*'}+4\eta f^{*'2}+\\5f'f^{*''}+5\eta f^{*'}f^{*''}\end{array}\right)+2(n-1)We^2f''\left(\begin{array}{c}12f^{*'}f''+12f'f^{*''}+\\8\eta f^{*''}+5f''f^{*'}+\\5\eta f^{*''}f^{*'}+5f^{*'}f^{*''}\end{array}\right)-\\
&\lambda\tfrac{1+d^*e^{-\zeta}}{1+de^{-\zeta}}f^{*'}\left(1+\tfrac{n-1}{2}We^2\left(\begin{array}{c}12f'^2+4\eta^2f^{*'2}+\\10\eta f'f^{*'}\end{array}\right)\right)-2f'f^{*'}+2gg^*+2f^*f''+2ff^{*''}-\\
&\lambda\tfrac{1+d^*e^{-\zeta}}{1+de^{-\zeta}}f'\tfrac{n-1}{2}We^2f'\left(\begin{array}{c}24f'f^{*'}+8\eta f^{*'2}+\\10f'f^{*''}+10\eta f^{*'}f^{*''}\end{array}\right)=f'f^{*'}-f^*f''+\eta\left(f^{*'2}-f^*f^{*''}\right),
\end{aligned} \tag{11.24}$$

$$\begin{aligned}
&2g^{*''}\left(1+\tfrac{n-1}{2}We^2\left(\begin{array}{c}12f'^2+4\eta^2f^{*'2}+\\10\eta f'f^{*'}\end{array}\right)\right)+2g''\left(\tfrac{n-1}{2}\right)We^2\left(\begin{array}{c}24f'f^{*'}+8\eta f^{*'2}+\\10f'f^{*''}+10\eta f^{*'}f^{*''}\end{array}\right)+\\
&2(n-1)We^2g^{*'}\left(\begin{array}{c}12f'f^{*'}+4\eta f^{*'2}+\\5f'f^{*''}+5\eta f^{*'}f^{*''}\end{array}\right)+2(n-1)We^2g'\left(\begin{array}{c}12f^{*'}f''+12f'f^{*''}+\\8\eta f^{*''}+5f''f^{*'}+\\5\eta f^{*''}f^{*'}+5f^{*'}f^{*''}\end{array}\right)-\\
&\lambda\tfrac{1+d^*e^{-\zeta}}{1+de^{-\zeta}}g^*\left(1+\tfrac{n-1}{2}We^2\left(\begin{array}{c}12f'^2+4\eta^2f^{*'2}+\\10\eta f'f^{*'}\end{array}\right)\right)+2f^*g'+2fg^{*'}-2f^{*'}g-2f'g^*-\\
&\lambda\tfrac{1+d^*e^{-\zeta}}{1+de^{-\zeta}}g\tfrac{n-1}{2}We^2f'\left(\begin{array}{c}24f'f^{*'}+8\eta f^{*'2}+\\10f'f^{*''}+10\eta f^{*'}f^{*''}\end{array}\right)=f^*g'-f'g^*+\eta\left(f^*g^{*'}-g^*f^{*'}\right),
\end{aligned} \tag{11.25}$$

$$
\begin{gathered}
2\theta^{*\prime\prime}+4Br\eta\left(1+\tfrac{n-1}{2}We^{2}\left(\begin{array}{c}12f^{\prime 2}+4\eta^{2}f^{*\prime 2}+\\10\eta f^{\prime}f^{*\prime}\end{array}\right)\right)\left(f^{\prime\prime 2}+g^{\prime 2}\right)+\\
Br\eta^{2}\left(n-1\right)We^{2}\left(\begin{array}{c}24f^{\prime}f^{*\prime}+8\eta f^{*\prime 2}+\\10f^{\prime}f^{*\prime\prime}+10\eta f^{*\prime}f^{*\prime\prime}\end{array}\right)\left(f^{\prime\prime 2}+g^{\prime 2}\right)+\\
2Br\eta^{2}\left(1+\tfrac{n-1}{2}We^{2}\left(\begin{array}{c}12f^{\prime 2}+4\eta^{2}f^{*\prime 2}+\\10\eta f^{\prime}f^{*\prime}\end{array}\right)\right)\left(2f^{\prime\prime}f^{*\prime\prime}+2g^{\prime}g^{*\prime}\right)+\\
2\lambda Br\eta\tfrac{1+d^{*}e^{-\zeta}}{1+de^{-\zeta}}\left(1+\tfrac{n-1}{2}We^{2}\left(\begin{array}{c}12f^{\prime 2}+4\eta^{2}f^{*\prime 2}+\\10\eta f^{\prime}f^{*\prime}\end{array}\right)\right)\left(f^{\prime 2}+g^{2}\right)+\\
\lambda Br\eta^{2}\tfrac{1+d^{*}e^{-\zeta}}{1+de^{-\zeta}}\left(n-1\right)We^{2}\left(\begin{array}{c}24f^{\prime}f^{*\prime}+8\eta f^{*\prime 2}+\\10f^{\prime}f^{*\prime\prime}+10\eta f^{*\prime}f^{*\prime\prime}\end{array}\right)\left(f^{\prime 2}+g^{2}\right)+\\
\lambda Br\eta^{2}\tfrac{1+d^{*}e^{-\zeta}}{1+de^{-\zeta}}\left(1+\tfrac{n-1}{2}We^{2}\left(\begin{array}{c}12f^{\prime 2}+4\eta^{2}f^{*\prime 2}+\\10\eta f^{\prime}f^{*\prime}\end{array}\right)\right)\left(2f^{\prime}f^{*\prime}+2gg^{*}\right)+\\
2\Pr f^{*}\theta^{\prime}+2\Pr f\theta^{*\prime}=\Pr\left(f^{\prime}\theta^{*}-f^{*}\theta^{\prime}\right)+\eta\Pr\left(f^{*\prime}\theta^{*}-\theta^{*\prime}f^{*}\right),
\end{gathered}
\tag{11.26}
$$

$$
\left.
\begin{gathered}
f^{*}\left(\eta,0\right)=0,\;\;\theta^{*}\left(\eta,0\right)=0,\\
f^{*\prime}\left(\eta,0\right)-\gamma_{1}\left(1+\tfrac{n-1}{2}We^{2}\left(\begin{array}{c}12f^{\prime 2}+4\eta^{2}f^{*\prime 2}+\\10\eta f^{\prime}f^{*\prime}\end{array}\right)\right)f^{*\prime\prime}\left(\eta,0\right)-\\
\gamma_{1}\tfrac{n-1}{2}We^{2}\left(\begin{array}{c}24f^{\prime}f^{*\prime}+8\eta f^{*\prime 2}+\\10f^{\prime}f^{*\prime\prime}+10\eta f^{*\prime}f^{*\prime\prime}\end{array}\right)f^{\prime\prime}\left(\eta,0\right)=0,\\
g^{*}\left(\eta,0\right)-\gamma_{1}\left(1+\tfrac{n-1}{2}We^{2}\left(\begin{array}{c}12f^{\prime 2}+4\eta^{2}f^{*\prime 2}+\\10\eta f^{\prime}f^{*\prime}\end{array}\right)\right)g^{*\prime}\left(\eta,0\right)-\\
\gamma_{1}\tfrac{n-1}{2}We^{2}\left(\begin{array}{c}24f^{\prime}f^{*\prime}+8\eta f^{*\prime 2}+\\10f^{\prime}f^{*\prime\prime}+10\eta f^{*\prime}f^{*\prime\prime}\end{array}\right)g^{\prime}\left(\eta,0\right)=0,
\end{gathered}
\right\}
\tag{11.27}
$$

$$
f^{*\prime}\left(\eta,\infty\right)\rightarrow 0,\;\; g^{*}\left(\eta,\infty\right)\rightarrow 0,\;\; \theta^{*}\left(\eta,\infty\right)\rightarrow 0. \tag{11.28}
$$

11.2 Entropy generation

Entropy generation equation for considered flow is

$$S_{gen}''' = \underbrace{\frac{k}{T_m^2}\left(\frac{\partial T}{\partial z}\right)^2}_{Thermal\ irreversibility} + \underbrace{\frac{\varepsilon(z)}{K^*(z)\,T_m}\left(\mu_0\left(1+\frac{n-1}{2}(\Gamma\mathring{\gamma})^2\right)\right)(u^2+v^2)}_{Porous\ dissipation\ irreversibility} + \underbrace{\frac{1}{T_m}\left(\mu_0\left(1+\frac{n-1}{2}(\Gamma\mathring{\gamma})^2\right)\right)\left(\left(\frac{\partial u}{\partial z}\right)^2+\left(\frac{\partial v}{\partial z}\right)^2\right)}_{Viscous\ dissipation\ irreversibility}, \tag{11.29}$$

Using transformations, Eq. (11.19) reduces to

$$\begin{aligned} N_g(\zeta) = {} & 2\alpha_1\theta'^2 + 2Br\eta^2\left(1+\tfrac{n-1}{2}We^2\left(12f'^2+4\eta^2f^{*\prime 2}+10\eta f'f^{*\prime}\right)\right)\left(f''^2+g'^2\right)+ \\ & Br\lambda\eta^2\tfrac{1+d^*e^{-\zeta}}{1+de^{-\zeta}}\left(1+\tfrac{n-1}{2}We^2\left(12f'^2+4\eta^2f^{*\prime 2}+10\eta f'f^{*\prime}\right)\right)\left(f'^2+g^2\right), \end{aligned} \tag{11.30}$$

where

$$\alpha_1 = \frac{T_w - T_\infty}{T_m},\ N_g = \frac{\nu}{k\omega}\frac{S_{gen}'''}{\alpha_1}. \tag{11.31}$$

11.3 Physical quantities

Coefficients of skin friction and local Nusselt number are

$$\left.\begin{aligned} \left(\tfrac{\mathrm{Re}}{2}\right)^{1/2}C_f &= \tfrac{1}{\eta}\left(1+\tfrac{n-1}{2}We^2\left(12f'^2(\eta,0)+4\eta^2f^{*\prime 2}(\eta,0)+10\eta f'f^{*\prime}(\eta,0)\right)\right)f^*(\eta,0), \\ \left(\tfrac{\mathrm{Re}}{2}\right)^{1/2}C_g &= \tfrac{1}{\eta}\left(1+\tfrac{n-1}{2}We^2\left(12f'^2(\eta,0)+4\eta^2f^{*\prime 2}(\eta,0)+10\eta f'f^{*\prime}(\eta,0)\right)\right)g'(\eta,0), \\ \left(\tfrac{\mathrm{Re}}{2}\right)^{-1/2}Nu &= -\eta\theta'(\eta,0). \end{aligned}\right\} \tag{11.32}$$

11.4 Solution methodology

Numerical approximations for solutions of nonlinear equations are obtained by NDSolve technique of mathematica. The solutions of nonlinear equations in terms of interpolating function are given as a table of values of unknown function for different independent variable. NDSolve finds a numerical value of the function for a specific value of independent variable by interpolation in this table.

11.5 Discussion

This section provides graphical outcomes of emerging variables against velocities $f'(\zeta)$, $g(\zeta)$, temperature $\theta(\zeta)$ and entropy generation rate $N_g(\zeta)$. Fig. 11.2 depicted the variation of $f'(\zeta)$ for (λ). Clearly (λ) reduces the velocity $f'(\zeta)$. Figs. 11.3 and 11.4 witnessed contrary behavior of $f'(\zeta)$ for (d) and (d^*). Fig. 11.5 illustrates the curves of $f'(\zeta)$ for (We). Higher (We) correspond to an increase in relaxation time of fluid. Such increase in relaxation time causes resistance between fluid particles and consequently velocity $f'(\zeta)$ decreases. Fig. 11.6 presents the outcomes of (γ_1) on velocity $f'(\zeta)$. Higher estimation of (γ_1) produces resistance between the fluid particles and rotating disk. Such resistance causes decay in velocity $f'(\zeta)$. Features of $g(\zeta)$ through (λ) is plotted in Fig. 11.7. Clearly higher (λ) strengthen the velocity $g(\zeta)$. Role of (d) on velocity $g(\zeta)$ is analyzed in Fig. 11.8. Higher estimation of (d) show an enhancement in $g(\zeta)$. Behavior of $g(\zeta)$ against (d^*) is portrayed in Fig. 11.9. Velocity $g(\zeta)$ is a decreasing function of (d^*). Impact of (We) on velocity $g(\zeta)$ are depicted in Figs. 11.10. Increasing trend of $g(\zeta)$ is observed through (We). Features of $g(\zeta)$ for (γ_1) is sketched in Fig. 11.11. Higher (γ_1) yields reduction in $g(\zeta)$. Characteristics of (λ) on $\theta(\zeta)$ is highlighted in Fig. 11.12. Higher (λ) weakens the temperature $\theta(\zeta)$ and thermal layer thickness. Since the presence of porous medium disturbed the boundary layer flow of liquid. Thus resistance is created in the fluid flow which decays the temperature. Significant behaviors of (d) and (d^*) on $\theta(\zeta)$ are declared in Figs. 11.13 and 11.14. Higher (d) and (d^*) yield adverse trend of $\theta(\zeta)$. Fig. 11.15 witnessed that $\theta(\zeta)$ is an increasing function of (We). Fig. 11.16 captured the effect of (Br) on $\theta(\zeta)$. Here higher (Br) strengthen the temperature $\theta(\zeta)$ and related layer thickness. Variation of (λ) on $N_g(\zeta)$ is declared in Fig. 11.17. An increment in (λ) depicts reduction of $N_g(\zeta)$. Higher estimation of (d) decay $N_g(\zeta)$ whereas reverse holds against (d^*) (see Figs. 11.18 and 11.19). Role of (We) on $N_g(\zeta)$ is pointed out in Fig. 11.20. Here $N_g(\zeta)$ is an increasing function of (We). Physically more heat loss is observed during motion of particles due to enhancement in relaxation time. $N_g(\zeta)$ against (Br) is portrayed in Fig. 11.21. Enhancement in $N_g(\zeta)$ is witnessed through (Br). Physically (Br) is the ratio of heat generated by fluid friction to heat transfer via molecular conduction. Higher (Br) lead to more heat generation which causes disorderedness in the system. Contribution of (α_1) on $N_g(\zeta)$ is captured in Fig. 11.22. It describes that $N_g(\zeta)$ enhances for (α_1). Characteristics of skin friction coefficients $\left(\frac{\text{Re}}{2}\right)^{1/2} C_f$ and $\left(\frac{\text{Re}}{2}\right)^{1/2} C_g$ against sundry variables are elaborated in Table 11.1. It is analyzed that $\left(\frac{\text{Re}}{2}\right)^{1/2} C_f$ and $\left(\frac{\text{Re}}{2}\right)^{1/2} C_g$ have opposite trend for (λ), (d), (d^*) and (We). Table 11.2 declared the contributions of (λ), (d), (d^*), (We) and (γ_1) on local Nusselt number $\left(\frac{\text{Re}}{2}\right)^{-1/2} Nu$. Clearly (d) strengthens local Nusselt number. Comparative values of local Nusselt number with existing studies [26, 69] is presented in Table 11.3. Acceptable agreement with these studies is noted [26, 69].

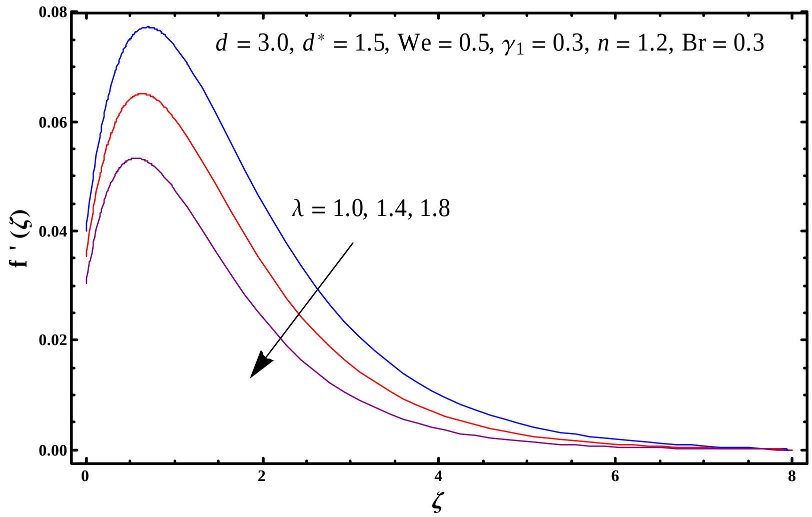

Fig. 11.2: Sketch of $f'(\zeta)$ versus λ.

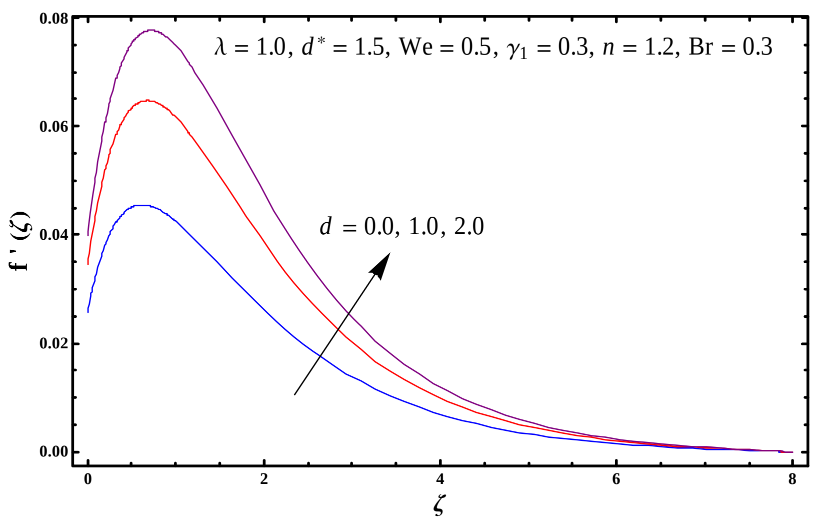

Fig. 11.3: Sketch of $f'(\zeta)$ versus d.

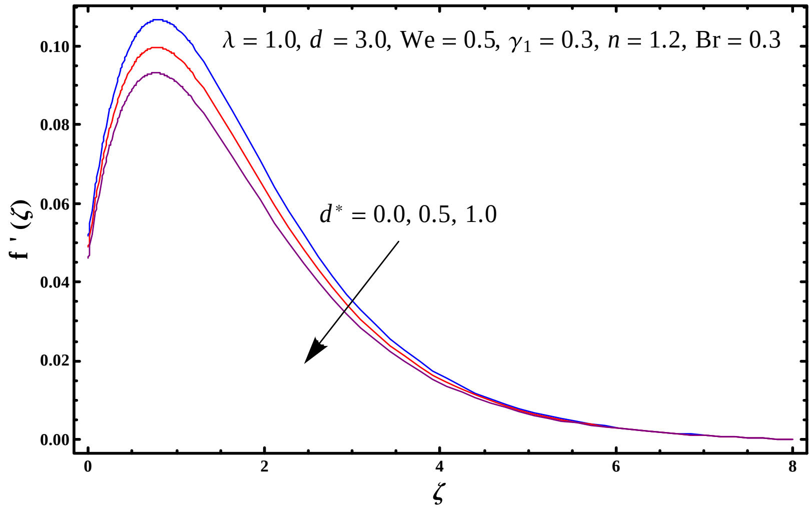

Fig. 11.4: Sketch of $f'(\zeta)$ versus d^{*}.

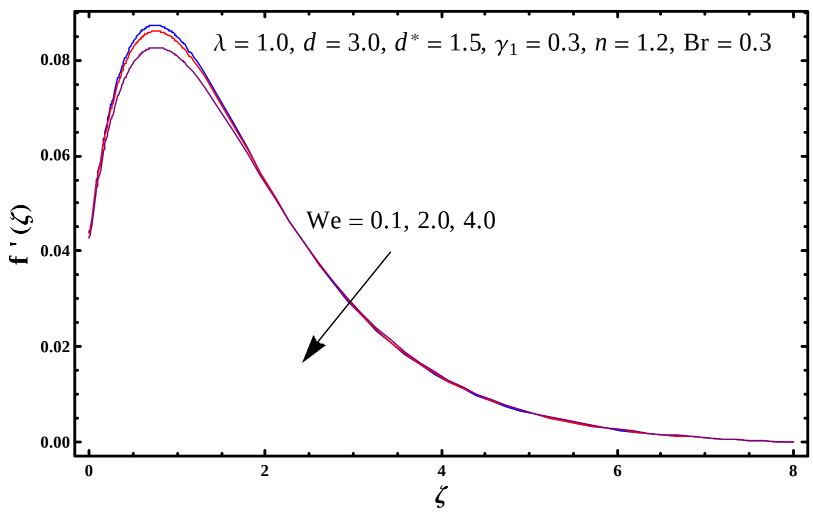

Fig. 11.5: Sketch of $f'(\zeta)$ versus We.

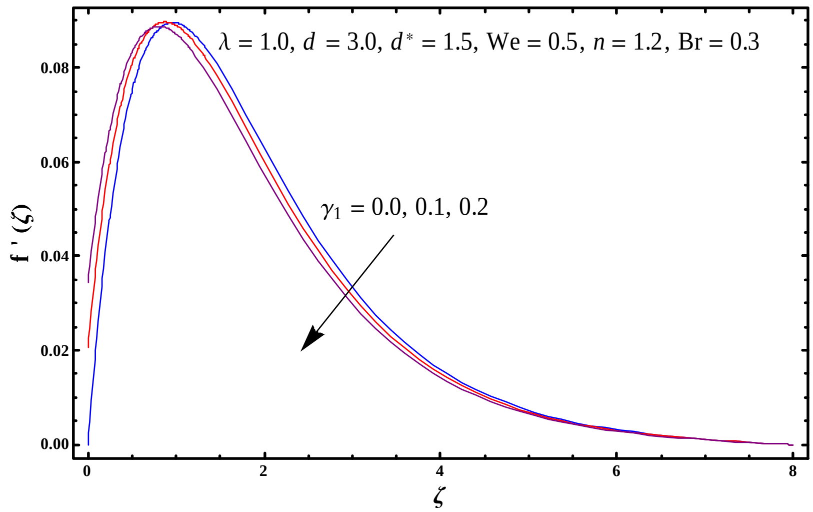

Fig. 11.6: Sketch of $f'(\zeta)$ versus γ_1.

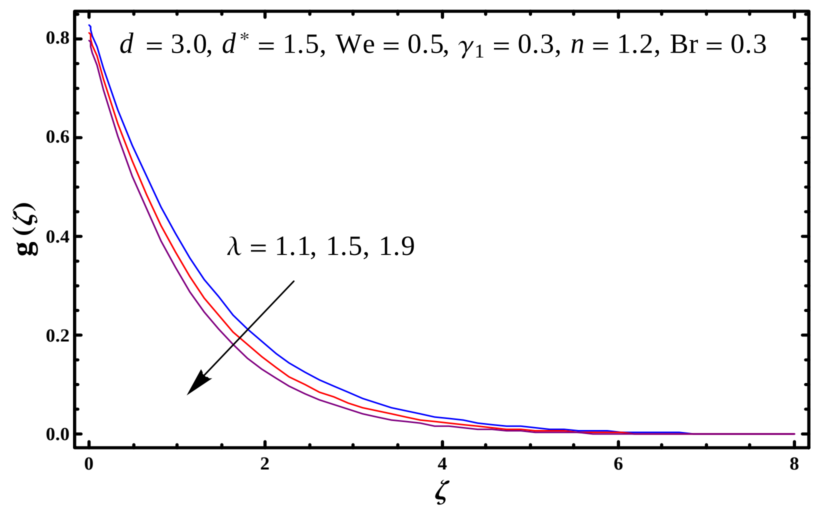

Fig. 11.7: Sketch of $g(\zeta)$ versus λ.

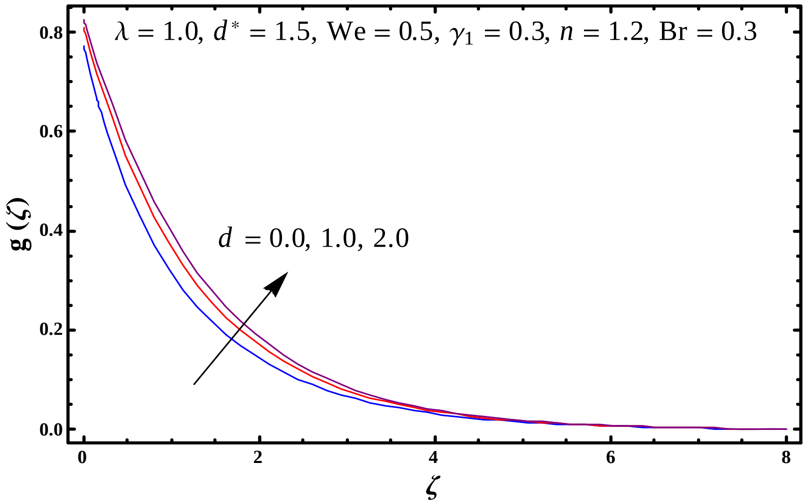

Fig. 11.8: Sketch of $g(\zeta)$ versus d.

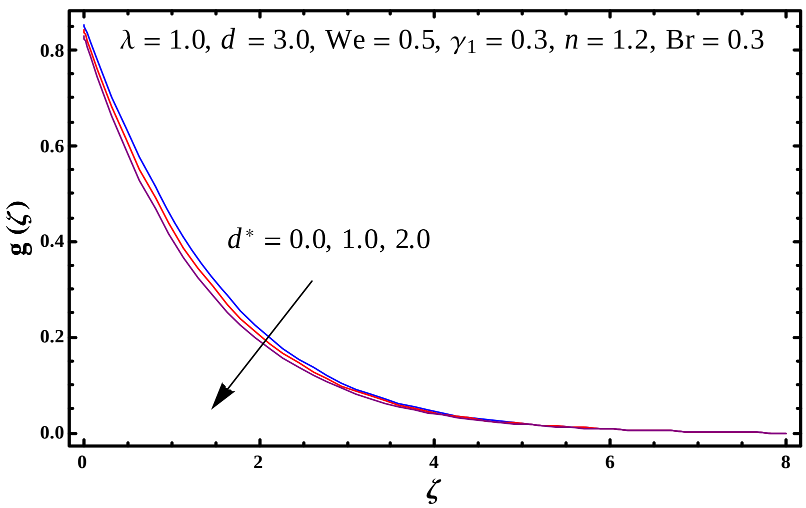

Fig. 11.9: Sketch of $g(\zeta)$ versus d^*.

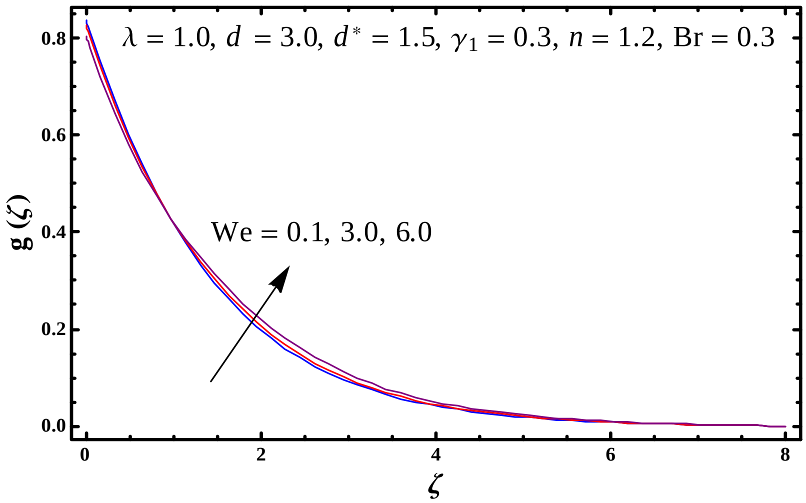

Fig. 11.10: Sketch of $g(\zeta)$ versus We.

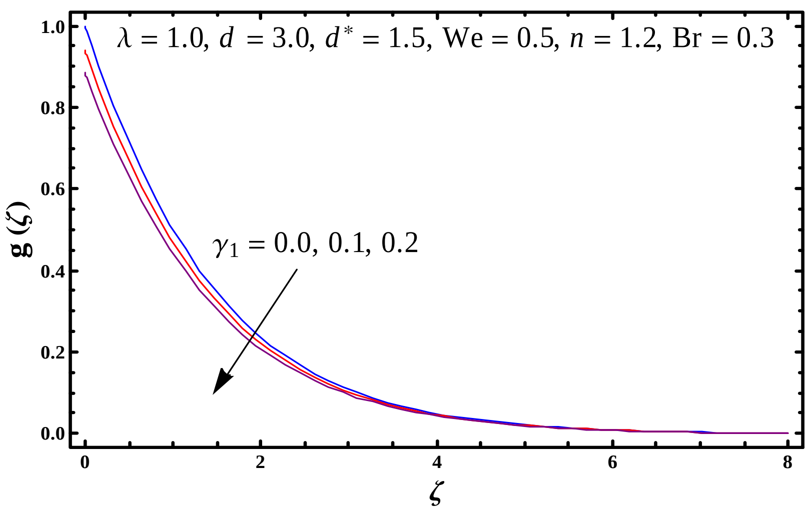

Fig. 11.11: Sketch of $g(\zeta)$ versus γ_1.

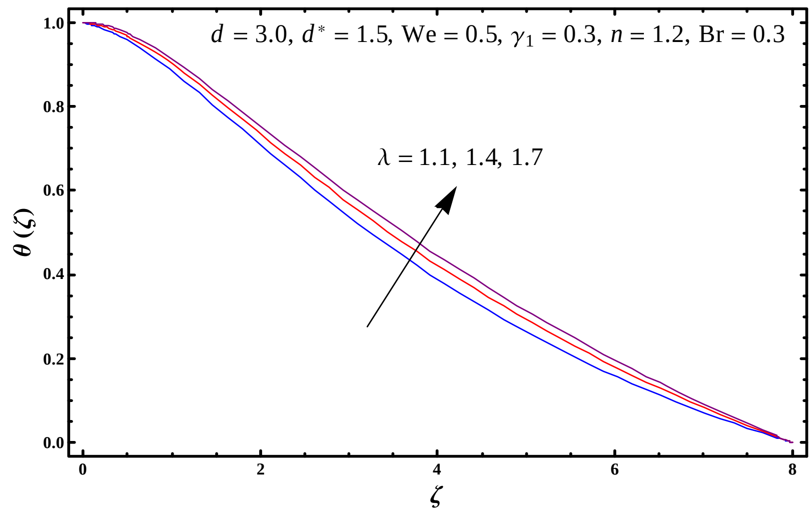

Fig. 11.12: Sketch of $\theta(\zeta)$ versus λ.

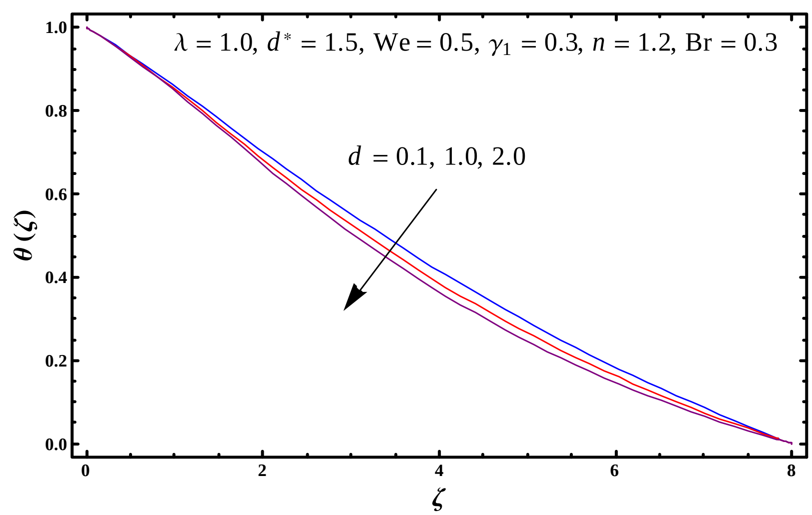

Fig. 11.13: Sketch of $\theta(\zeta)$ against d.

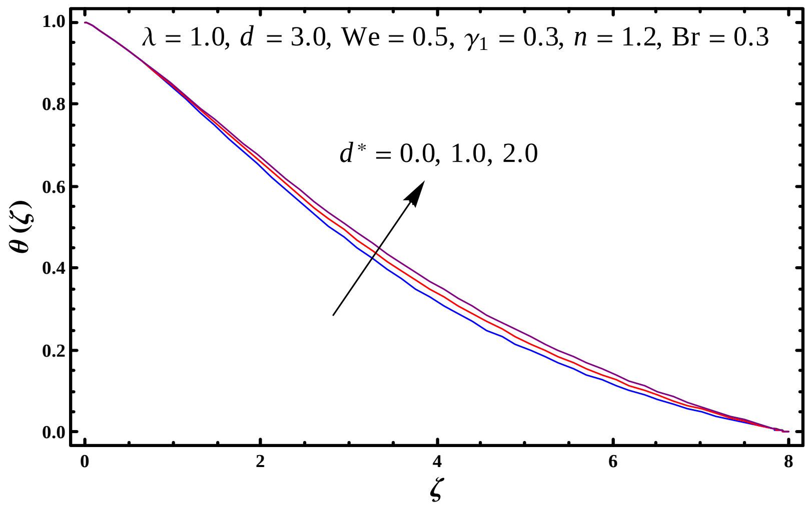

Fig. 11.14: Plot for $\theta(\zeta)$ versus d^*.

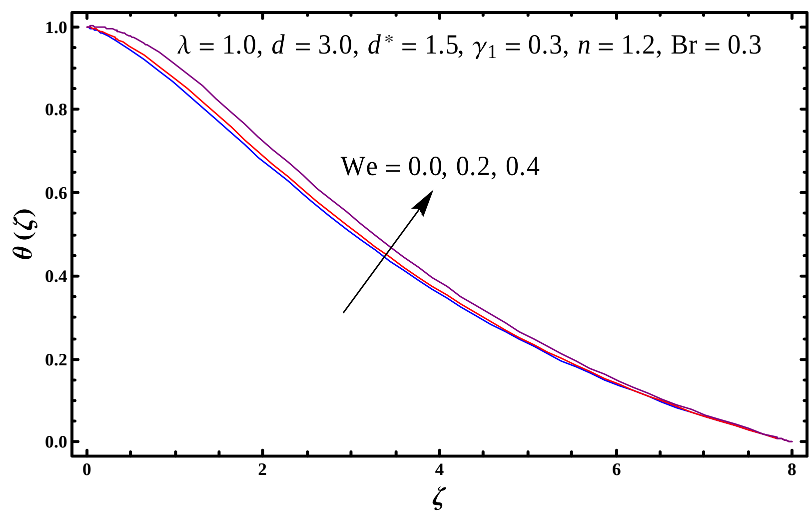

Fig. 11.15: Plot for $\theta(\zeta)$ versus We.

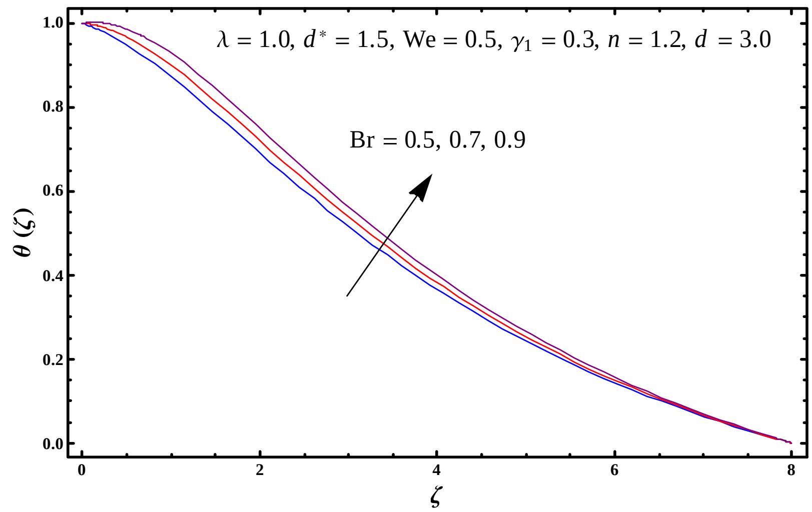

Fig. 11.16: Plot for $\theta(\zeta)$ against Br.

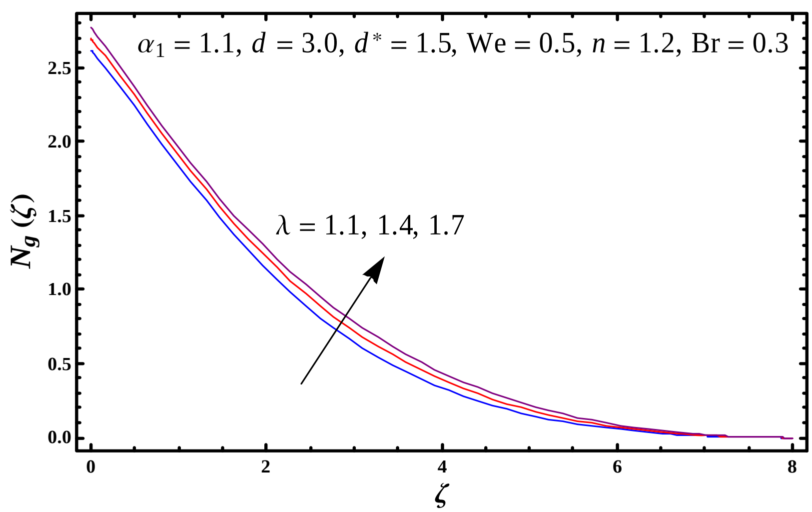

Fig. 11.17: Plot for $N_g(\zeta)$ against λ.

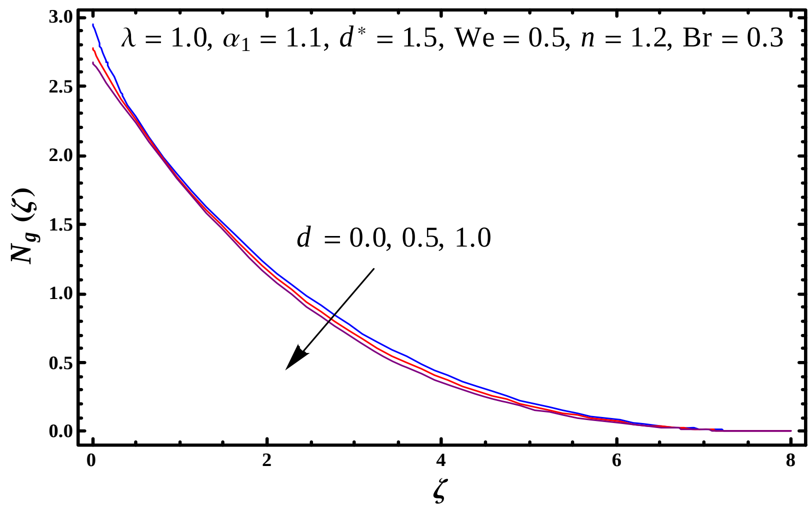

Fig. 11.18: Plot for $N_g(\zeta)$ against d.

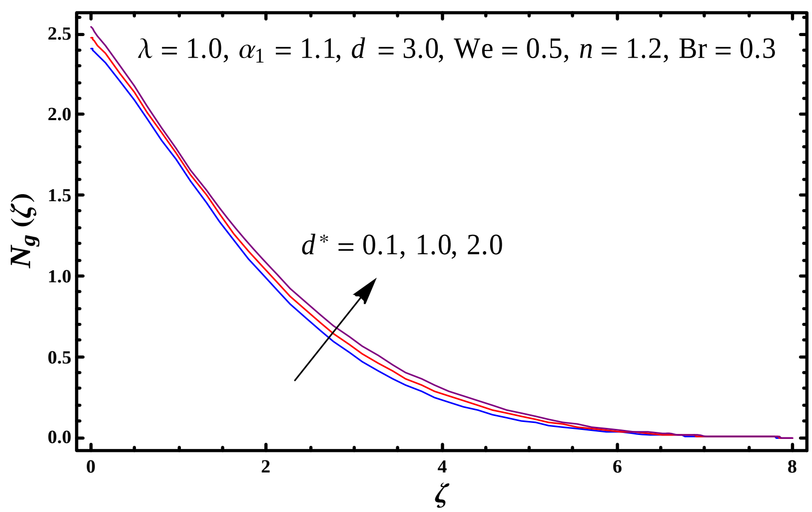

Fig. 11.19: Plot for $N_g(\zeta)$ against d^*.

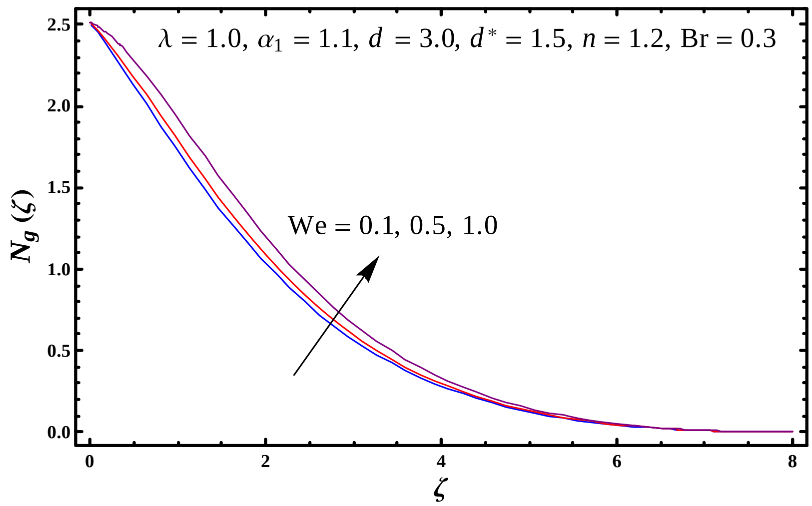

Fig. 11.20: Plot for $N_g(\zeta)$ against We.

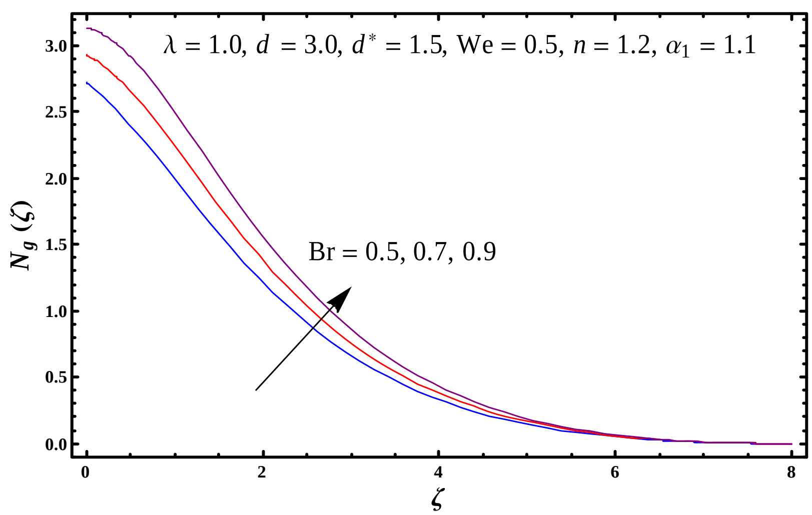

Fig. 11.21: Plot for $N_g(\zeta)$ against Br.

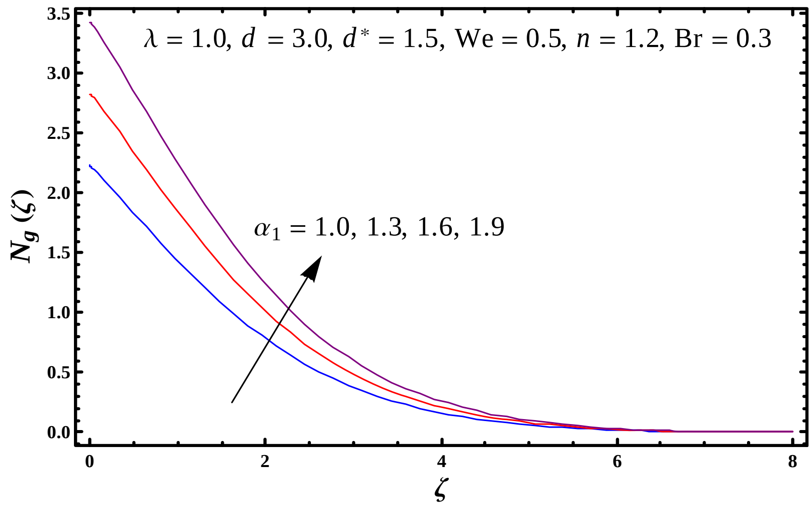

Fig. 11.22: Sketch of $N_g(\zeta)$ against α_1.

Table 11.1: Numerical computation of skin friction coefficients $\left(\frac{\text{Re}}{2}\right)^{1/2} C_f$ and $\left(\frac{\text{Re}}{2}\right)^{1/2} C_g$.

λ	d	d^*	We	γ_1	$\left(\frac{\text{Re}}{2}\right)^{1/2} C_f$	$-\left(\frac{\text{Re}}{2}\right)^{1/2} C_g$
1.1	3.0	1.5	0.5	0.3	0.13355	0.57487
1.2					0.12778	0.58856
1.3					0.12244	0.60193
1.0	0.0	1.5	0.5	0.3	0.08548	0.75491
	1.0				0.11489	0.63611
	2.0				0.13316	0.58075
1.0	3.0	0.0	0.5	0.3	0.17213	0.48760
		0.3			0.16646	0.49994
		0.6			0.16102	0.51213
1.0	3.0	1.5	0.0	0.3	0.14608	0.54725
			0.1		0.14608	0.54727
			0.2		0.14607	0.54734
1.0	3.0	1.5	0.5	0.0	0.24928	0.64272
				0.1	0.20611	0.61044
				0.2	0.17249	0.57835

Table 11.2: Values for local Nusselt number $\left(\frac{\text{Re}}{2}\right)^{-1/2} Nu$.

λ	d	d^*	We	Br	$-\left(\frac{\text{Re}}{2}\right)^{-1/2} Nu$
1.1	3.0	1.5	0.5	0.3	0.03904
1.2					0.02910
1.3					0.01996
1.0	0.0	1.5	0.5	0.3	0.02168
	1.0				0.03997
	2.0				0.05229
1.0	3.0	0.0	0.5	0.3	0.07936
		0.3			0.07551
		0.6			0.07180
1.0	3.0	1.5	0.0	0.3	0.04838
			0.1		0.04786
			0.2		0.04627
1.0	3.0	1.5	0.5	0.5	−0.03251
				0.6	−0.07948
				0.7	−0.12646

Table 11.3: Comparison for $-\theta'(0)$ through distinct Pr when $Ec = d^* = d = We = 0$.

Pr	Runge-Kutta method [26]	Shooting method [69]	NDSolve
0.71	0.3286	0.3054	0.3505
1.0	0.3963	0.3396	0.3575
10	1.1341	1.1540	0.5819
75	2.8672	2.3144	1.8519

Chapter 12

Conclusions

Theme here is to investigate nonlinear models through porous space. Flow is caused by an exponential stretching sheet, exponential curved stretching sheet and rotating disk. Both single-phase and two-phase models of nanofluid are utilized to interpret nanoliquid transport phenomena. Darcy-Brinkman, Darcy-Forchheimer and modified Darcy's law are utilized to characterize the flow in porous space. Flows in porous space with both constant and variable characteristics are elaborated. Entropy generation analyses of carbon nanotubes, hybrid nanofluid and Carreau nanofluid are provided. Slip and prescribed heat flux conditions are employed at the boundary. Inclined magnetic field, nonlinear radiation, heat generation/absorption, chemical reactions and activation energy impact are examined. Governing equations are constructed by employing boundary layer phenomenon. Reduction method is utilized for conversion of partial differential equations into ordinary differential equations. OHAM and NDSolve technique construct the solutions. Graphical analysis is performed for behavior of emerging variables on flow fields and entropy generation. Physical quantities of interest are also obtained and analyzed. Major outcomes of current thesis are:

- Augmentation in (λ) and (F_r) leads to decay of velocities.
- Decreasing trend of velocity is noted through (M) and (β).
- Improvement in velocities is noted through (ξ) and (Ω).
- Impacts of $\left(\hat{K}\right)$ and $\left(\hat{K}_s\right)$ on concentration are opposite.

- Behaviors of (Q^*) and (K) on temperature field are reverse.
- Velocities have opposite scenario for (d) and (d^*).
- Temperatures against (Br) and (Rd) have similar trend.
- Reduction in temperature is observed through (γ_2), (θ_w), (S_t) and (A).
- Concentration via (Λ) and (α_1) possesses similar trend.
- Features of (N_b) and (N_t) on temperature are quite similar.
- Augmentation in temperature is analyzed through (We).
- Entropy generation rate enhances for (Br), (Q^*), (L_1), (L_2) and (α_1).
- Skin friction coefficient enhances for (λ) and (F_r).
- Local Nusselt number reduces against (S_t), (Br) and (We).
- Augmentation in local Sherwood number is noted through (Λ), (α_1) and (m).
- Heat transfer rate for SWCNTs is much higher as compared to other nanoparticles.

Bibliography

[1] L. Prandtl, Uber Flussigkeitsbewegungen bei sehr kleiner Reibung, Verhandlungen des III. Internationalen Mathematiker Kongresses, Heidelberg, Germany, (1904) 484-491.

[2] H. Blasius, Grenzschichten in Flussigkeiten mit kleiner Reibung, Z. Angew. Math. Phys., 56 (1908) 1-37.

[3] B.C. Sakiadis, Boundary-layer behaviour on continuous solid surfaces: II. The boundary-layer on a continuous flat surface, AIChE J., 7 (1961) 221-225.

[4] L.J. Crane, Flow past a stretching plate, Z. Angew. Math. Phys., 21 (1970) 645-647.

[5] C.Y. Wang, The three dimensional flow due to a extending flat surface, Phys. Fluids, 27 (1984) 1915-1917.

[6] M.E. Ali, On thermal boundary layer on a power-law stretched surface with suction and injection, Int. J. Heat Fluid Flow, 16 (1995) 280-290.

[7] E. Magyari and B. Keller, Heat and mass transfer in the boundary layers on an exponentially stretching continuous surface , J. Phys. D, 32 (1999) 577-585.

[8] T. Javed, M. Sajid, Z. Abbas and N. Ali, Non-similar solution for rotating flow over an exponentially stretching surface, Int. J. Numer. Method Heat Fluid Flow, 21 (2011) 903-908.

[9] S. Nadeem and C.H. Lee, Boundary layer flow of nanofluid over an exponentially stretching surface, Nanoscale Res. Lett., 7 (2012) Article 94.

[10] S. Mukhopadhyay, Slip effects on MHD boundary layer flow over an exponentially stretching sheet with suction/blowing and thermal radiation, Ain Shams Eng. J., 4 (2013) 485-491.

[11] I.C. Liu, H.H. Wang and Y.F. Peng, Flow and heat transfer for three-dimensional flow over an exponentially stretching surface, Chem. Eng. Commun., 200 (2013) 253-268.

[12] H. Rosali, A. Ishak, R. Nazar and I. Pop, Rotating flow over an exponentially shrinking sheet with suction, J. Mol. Liq., 211 (2015) 965-969.

[13] M. Mustafa, A. Mushtaq, T. Hayat and A. Alsaedi, Radiation effects in three-dimensional flow over a bi-directional exponentially stretching sheet, J. Taiwan Inst. Chem. Eng., 47 (2015) 43-49.

[14] R. Jusoh, R. Nazar and I. Pop, Magnetohydrodynamic rotating flow and heat transfer of ferrofluid due to an exponentially permeable stretching/shrinking sheet, J. Magn. Magn. Mater., 465 (2018) 365-374.

[15] L.A. Lund, Z. Omar and I. Khan, Quadruple solutions of mixed convection flow of magnetohydrodynamic nanofluid over exponentially vertical shrinking and stretching surfaces: Stability analysis, Comput. Methods Programs Biomed., 182 (2019) Article 105044.

[16] S. Malik, M.B. Ashraf and A. Jahangir, Cattaneo–Christov heat flux model for three-dimensional flow of a viscoelastic fluid on an exponentially stretching surface, Math. Comput. Model. Dyn. Syst., 26 (2020) 344-356.

[17] M. Sajid, N. Ali, T. Javed and Z. Abbas, Stretching a curved surface in a viscous fluid, Chin. Phys. Lett., 27 (2010) Article 024703.

[18] N.C. Rosca and I. Pop, Unsteady boundary layer flow over a permeable curved stretching/shrinking surface, Eur. J. Mech. B. Fluids, 51 (2015) 61-67.

[19] Z. Abbas, M. Naveed and M. Sajid, Hydromagnetic slip flow of nanofluid over a curved stretching surface with heat generation and thermal radiation, J. Mol. Liq., 215 (2016) 756-762.

[20] N.F. Okechi, M. Jalil and S. Asghar, Flow of viscous fluid along an exponentially stretching curved surface, Results Phys., 7 (2017) 2851-2854.

[21] A. Alblawi, M.Y. Malik, S. Nadeem and N. Abbas, Buongiorno's nanofluid model over a curved exponentially stretching surface, Processes, 7 (2019) Article 665.

[22] K.A. Kumar, V. Sugunamma and N. Sandeep, Effect of thermal radiation on MHD Casson fluid flow over an exponentially stretching curved sheet, J. Therm. Anal. Calorim. 140 (2020) 2377-2385.

[23] A.K. Kempannagari, R.R. Buruju, S. Naramgari and S. Vangala, Effect of Joule heating on MHD non-Newtonian fluid flow past an exponentially stretching curved surface, Heat Transfer, 49 (2020) 3575-3592.

[24] T.V. Karman, Uber laminare and turbulente Reibung, Zeit. Angew. Math. Mech. 1 (1921) 233-252.

[25] W.G. Cochran, The flow due to a rotating disk, Proc. Camb. Philo. Soc. 30 (1934) 365-375.

[26] H.T. Lin and L.K. Lin, Heat transfer from a rotating cone or disk to fluids of any Prandtl number, Int. Commun. Heat Mass Transfer, 14 (1987) 323-332.

[27] M. Miklavcic, C.Y. Wang, The flow due to a rough rotating disk, Z. angew. Math. Phys. 55 (2004) 235-246.

[28] T. Fang and H. Tao, Unsteady viscous flow over a rotating stretchable disk with deceleration, Commun. Nonlinear Sci. Numer. Simul., 17 (2012) 5064-5072.

[29] M.M. Rashidi, N. Kavyani and S. Abelmanc, Investigation of entropy generation in MHD and slip flow over a rotating porous disk with variable properties, Int. J. Heat Mass Transfer, 70 (2014) 892-917.

[30] N.A. Latif, M.J. Uddin and A.I.M. Ismail, Stefan blowing effect on bioconvective flow of nanofluid over a solid rotating stretchable disk, Propuls. Power Res., 5 (2016) 267-278.

[31] D.H. Doh and M. Muthtamilselvan, Thermophoretic particle deposition on magnetohydrodynamic flow of micropolar fluid due to a rotating disk, Int. J. Mech. Sci., 130 (2017) 350-359.

[32] M. Turkyilmazoglu, Fluid flow and heat transfer over a rotating and vertically moving disk, Phys. Fluids, 30 (2018) Article 063605.

[33] S.M.R.S. Naqvi, T. Muhammad, H.M. Kim, T. Mahmood, A. Saeed and B.S. Khan, Numerical treatment for Darcy-Forchheimer flow of nanofluid due to a rotating disk with slip effects, Canadian J. Phys. 97 (2019) 856-863.

[34] M.A. Sadiq, Serious solutions for unsteady axisymmetric flow over a rotating stretchable disk with deceleration, Symmetry 12 (2020) Article 96.

[35] S.U.S. Choi, Enhancing thermal conductivity of fluid with nanoparticles developments and applications of non-Newtonian flow, ASME J. Fluid Eng., 66 (1995) 99-105.

[36] J. Buongiorno, Convective transport in nanofluids, ASME J. Heat Transfer, 128 (2006) 240-250.

[37] R.K. Tiwari and M.K. Das, Heat transfer augmentation in a two-sided lid-driven differentially heated square cavity utilizing nanofluid, Int. J. Heat Mass Transfer, 50 (2007) 2002-2018.

[38] J.A. Khan, M. Mustafa, T. Hayat, M.A.Farooq, A. Alsaedi and S.J. Liao, On model for three-dimensional flow of nanofluid: An application to solar energy, J. Mol. Liq., 194 (2014) 41-47.

[39] M. Sheikholeslami, D.D. Ganji and M.M. Rashidi, Magnetic field effect on unsteady nanofluid flow and heat transfer using Buongiorno model, J. Magn. Magn. Mater., 416 (2016) 164-173.

[40] I. Tlili, W.A. Khan and K. Ramadan, MHD flow of nanofluid flow across horizontal circular cylinder: Steady forced convection, J. Nanofluids, 8 (2019) 179-186.

[41] M. Khan, A. Ahmed and J. Ahmed, Transient flow of magnetized Maxwell nanofluid: Buongiorno model perspective of Cattaneo-Christov theory, Appl. Math. Mech., 41 (2020) 655-666.

[42] M. Irfan, Study of Brownian motion and thermophoretic diffusion on non-linear mixed convection flow of Carreau nanofluid subject to variable properties, Surf. Interfaces, 23 (2021) Article 100926.

[43] H. Brinkman, The viscosity of concentrated suspensions and solutions, J. Chem. Phys., 20 (1952) 571.

[44] R. Hamilton and O. Crosser, Thermal conductivity of heterogeneous two-component systems, Ind. Eng. Chem. Fundam., 125 (1962) 187-191.

[45] Q.Z. Xue, Model for thermal conductivity of carbon nanotube-based composites, Physica B, 368 (2005) 302-307.

[46] B.C. Pak and Y.I. Cho, Hydrodynamic and heat transfer study of dispersed fluids with submicron metallic oxide particles, Exp. Heat Transfer, 11 (1998) 151-170.

[47] J.A. Eastman, S.R. Phillpot, S.U.S. Choi and P. Keblinski, Thermal transport in nanofluids, Annu. Rev. Mater. Res., 34 (2004) 219-246.

[48] M. Turkyilmazoglu, Analytical solutions of single and multi-phase models for the condensation of nanofluid film flow and heat transfer, Eur. J. Mech. B/Fluid, 53 (2015) 272-277.

[49] T. Hayat, S. Nawaz and Ahmed Alsaedi, Entropy generation in peristalsis with different shapes of nanomaterial, J. Mol. Liq., 248 (2017) 447-458.

[50] R. Kumar, R. Kumar, M. Sheikholeslami and A.J. Chamkha, Irreversibility analysis of the three dimensional flow of carbon nanotubes due to nonlinear thermal radiation and quartic chemical reactions, J. Mol. Liq., 274 (2019) 379-392.

[51] M. Aleem, M.I. Asjad, A. Shaheen and I. Khan, MHD Influence on different water based nanofluids (TiO_2, Al_2O_3, CuO) in porous medium with chemical reaction and Newtonian heating, Chaos Solitons Fractals, 130 (2020) Article 109437.

[52] P.S. Reddy and P. Sreedevi, Effect of thermal radiation and volume fraction on carbon nanotubes based nanofluid flow inside a square chamber, Alex. Eng. J., 60 (2021) 1807-1817.

[53] L.S. Sundar, M.K. Singh and A.C.M. Sousa, Enhanced heat transfer and friction factor of MWCNT–Fe_3O_4/water hybrid nanofluids, Int. Commun. Heat Mass Transfer, 52 (2014) 73-83.

[54] M.K. Meybodi, S. Naseri, A. Shokrollahi and A. Daryasafar, Prediction of viscosity of water-based Al_2O_3, TiO_2, SiO_2, and CuO nanofluids using a reliable approach, Chemom. Intell. Lab. Syst., 149 (2015) 60-69

[55] M.A. Mansour, S. Siddiqa, R.S.R. Gorla and A.M. Rashad, Effects of heat source and sink on entropy generation and MHD natural convection of Al_2O_3-Cu/water hybrid nanofluid filled with square porous cavity, Therm. Sci. Eng. Prog., 6 (2018) 57-71.

[56] S. Shaiq, E.N. Maraj and Z. Iqbal, Remarkable role of $C_3H_8O_2$ on transportation of MoS_2-SiO_2 hybrid nanoparticles influenced by thermal deposition and internal heat generation, J. Phys. Chem. Solids, 126 (2019) 294-303.

[57] S. Manjunatha, B.A. Kuttan, S. Jayanthi, A. Chamkha and B.J. Gireesha, Heat transfer enhancement in the boundary layer flow of hybrid nanofluids due to variable viscosity and natural convection, Heliyon, 5 (2019) Article e01469.

[58] N.A.L. Aladdin, N. Bachok and I. Pop, Cu-Al_2O_3/water hybrid nanofluid flow over a permeable moving surface in presence of hydromagnetic and suction effects, Alex. Eng. J., 59 (2020) 657-666.

[59] N. Abbas, M.Y. Malik, M.S. Alqarni and S. Nadeem, Study of three dimensional stagnation point flow of hybrid nanofluid over an isotropic slip surface, Physica A, 554 (2020) Article 124020.

[60] F. Mabood, T.A. Yusuf and W.A. Khan, Cu–Al_2O_3–H_2O hybrid nanofluid flow with melting heat transfer, irreversibility analysis and nonlinear thermal radiation, J. Therm. Anal. Calorim., 143 (2021) 973-984.

[61] P.J. Carreau, Rheological equations from molecular network theories, Trans. Soc. Rheol., 16 (1972) Article 99127.

[62] P.J. Carreau, An analysis of the viscous behaviour of polymer solutions, Can. J. Chem. Eng., 57 (1979) 135-140.

[63] K. Vajravelu, S. Sreenadh and R. Saravana, Combined influence of velocity slip, temperature and concentration jump conditions on MHD peristaltic transport of a Carreau fluid in a non-uniform channel, Appl. Math. Comput., 2251 (2013) 656-676.

[64] M. Khan and M. Azam, Unsteady boundary layer flow of Carreau fluid over a permeable stretching surface, Results Phys., 6 (2016) 1168-1174.

[65] I.L. Animasaun and I. Pop, Numerical exploration of a non-Newtonian Carreau fluid flow driven by catalytic surface reactions on an upper horizontal surface of a paraboloid of revolution, buoyancy and stretching at the free stream, Alex. Eng. J., 56 (2017) 647-658.

[66] K.U. Rehman, A.S. Alshomrani and M.Y. Malik, Carreau fluid flow in a thermally stratified medium with heat generation/absorption effects, Case Stud. Therm. Eng., 12 (2018) 16-25.

[67] B. Mahanthesh, I.L. Animasaun, M. Rahimi-Gorji and I.M. Alarif, Quadratic convective transport of dusty Casson and dusty Carreau fluids past a stretched surface with nonlinear thermal radiation, convective condition and non-uniform heat source/sink, Physica A, 5351 (2019) Article 122471.

[68] U. Nazir, S. Saleem, M. Nawaz, M.A. Sadiq and A.A. Alderremy, Study of transport phenomenon in Carreau fluid using Cattaneo-Christov heat flux model with temperature dependent diffusion coefficients, Physica A, 554 (2020) Article 123921.

[69] M. Khan, T. Salahuddin, M.Y. Malik and F. Khan, Change in internal energy of Carreau fluid flow along with Ohmic heating: A Von Karman application, Physica A, 547 (2020) Article 123440

[70] M. Elayarani, M. Shanmugapriya and P.S. Kumar, Intensification of heat and mass transfer process in MHD Carreau nanofluid flow containing gyrotactic microorganisms, Chem. Eng. Process., 160 (2021) Article 108299.

[71] H. Darcy, Les Fontaines Publiques de la Ville de Dijon. Dalmont, Paris, (1856) 647-658.

[72] P. Forchheimer, Wasserbewegung durch boden, Zeitschrift Ver. D. Ing., 45 (1901) 1782-1788.

[73] M. Muskat, The flow of homogeneous fluids through porous media, Edwards, MI. (1946).

[74] S.A. Bakar, N.M. Arifin, R. Nazar, F.M. Ali and I. Pop, Forced convection boundary layer stagnation-point flow in Darcy-Forchheimer porous medium past a shrinking sheet, Frontiers Heat Mass Transfer, 7 (2016) Article 38.

[75] Z. Shah, A. Dawar, S. Islam, I. Khan and D.L.C. Ching, Darcy-Forchheimer flow of radiative carbon nanotubes with microstructure and inertial characteristics in the rotating frame, Case Stud. Therm. Eng., 12 (2018) 823-832.

[76] J.D. Audu, F. Fairag and K. Mustapha, Mixed finite element analysis for generalized Darcy-Forchheimer model in porous media, J. Comput. Appl. Math., 353 (2019) 191-203.

[77] N.U. Huda, A. Hamid and M. Khan, Impact of Cattaneo-Christov model on Darcy-Forchheimer flow of ethylene glycol base fluid over a moving needle, J. Mater. Res. Technol., 9 (2020) 4139-4146.

[78] H.C. Brinkman, A calculation of the viscous force exerted by a flowing fluid on a dense swarm of particles, Appl. Sci. Res., A1 (1947) 27-34.

[79] H.C. Brinkman, On the permeability of media consisting of closely packed porous particles, Appl. Sci. Res., A1 (1947) 81-86.

[80] D.A. Nield, Resolution of a paradox involving viscous dissipation and nonlinear drag in a porous medium, Transp. Porous Med., 41 (2000) 349-357.

[81] F.S. Ibrahim and I.A. Hassanien, Influence of variable permeability on combined convection along a nonisothermal wedge in a saturated porous medium, Transp. Porous Media, 39 (2000) 57-71.

[82] A.K. Al-Hadhrami, L. Elliott and D.B. Ingham, A new model for viscous dissipation in porous media across a range of permeability values, Trans Porous Med, 53 (2003) 117-122.

[83] M.S. Kausar, A. Hussanan, M. Mamat and B. Ahmad, Boundary layer flow through Darcy-Brinkman porous medium in the presence of slip effects and porous dissipation, Symmetry, 11 (2019) Article 659.

[84] D. Yadav, U.S. Mahabaleshwar, A. Wakif and R. Chand, Significance of the inconstant viscosity and internal heat generation on the occurrence of Darcy-Brinkman convective motion in a couple-stress fluid saturated porous medium: An analytical solution, International Commun. Heat Mass Transfer, 122 (2021) Article 105165.

[85] G.A. Amhalhel and P. Furmański, Problems of modeling flow and heat transfer in porous media, Biuletyn Instytutu Techniki Cieplnej Politechniki Warsza Wskiej, Nr 85, 1997

[86] J.C. Umavathi, O. Ojjela and K. Vajravelu, Numerical analysis of natural convective flow and heat transfer of nanofluids in a vertical rectangular duct using Darcy-Forchheimer-Brinkman model, Int. J. Thermal Sci., 111 (2017) 511-524.

[87] M.M. Bhatti, A. Zeeshan, R. Ellahi and G. C. Shit, Mathematical modeling of heat and mass transfer effects on MHD peristaltic propulsion of two-phase flow through a Darcy-Brinkman-Forchheimer porous medium, Adv. Powder Tech., 29 (2018) 1189-1197.

[88] U. Farooq, M.A. Ijaz, M.I. Khan, S.S.P.M. Isa and D.C. Lu, Modeling and non-similar analysis for Darcy-Forchheimer-Brinkman model of Casson fluid in a porous media, Int. Commun. Heat Mass Transfer, 119 (2020) Article 104955.

[89] W.C. Tan and T. Masuoka, Stokes' first problem for a second grade fluid in a porous half-space with heated boundary, Int. J. Nonlinear Mech., 40 (2005) 515-522.

[90] M. Khan, T. Hayat and S. Asghar, Exact solution for MHD flow of a generalized Oldroyd-B fluid with modified Darcy's law, Int. J. Eng. Sci., 44 (2006) 333-339.

[91] T. Hayat, S.B. Khan and M. Khan, Exact solution for rotating flows of a generalized Burgers' fluid in a porous space, Appl. Math. Model, 32 (2008) 749-760.

[92] N.A. Khan, S. Khan and A. Arab, Flow of micropolar fluid over an off centered rotating disk with modified Darcy's law, Prop. Power Res., 6 (2017) 285-295.

[93] A. Tanveer, T. Hayat, A. Alsaedi and B. Ahmad, Heat transfer analysis for peristalsis of MHD Carreau fluid in a curved channel through modified Darcy's law, J. Mech., 35 (2019) 527-535.

[94] S.U. Haq, Sehra, S.I.A. Shah, S.U. Jan and I. Khan, MHD flow of generalized second grade fluid with modified Darcy's law and exponential heating using fractional Caputo-Fabrizio derivatives, Alex. Eng. J., 6 (2021) 3845-3854.

[95] C.E. Schwartz and J.M. Smith, Flow distribution in packed beds, Indust. Eng. Chem., 45 (1953) 1209-1218.

[96] K. Vafai, Convective flow and heat transfer in variable porosity media, J. Fluid Mech., 147 (1984) 233-259.

[97] K. Vafai, R.L. Alkire and C.L. Tien, An experimental investigation of heat transfer in variable porosity media, J. Heat Transfer, 107 (1985) 642-947.

[98] B.C. Chandrasekhara and P.M.S. Namboudiri, Influence of variable permeability on combined free and forced convection about inclined surfaces in porous media, Int. J. Heat Mass Transfer, 28 (1985) 199-206.

[99] F.S. Ibrahim and I.A. Hassanien, Influence of variable permeability on combined convection along a nonisothermal wedge in a saturated porous medium, Transp. Porous Media, 39 (2000) 57-71.

[100] D.A.S. Rees and I. Pop, Vertical free convection in a porous medium with variable permeability effects, Int. J. Heat Mass Transfer, 43 (2000) 2565-2571.

[101] M.H. Hamdan and M.T. Kamel, Flow through variable permeability porous layers, Adv. Theor. Appl. Mech., 4 (2011) 135-145.

[102] R.S. Saif, T. Muhammad and H. Sadia, Significance of inclined magnetic field in Darcy-Forchheimer flow with variable porosity and thermal conductivity, Physica A, 551 (2020) Article 124067.

[103] A. Bejan, A study of entropy generation in fundamental convective heat transfer, ASME J. Heat Transfer, 101 (1979) 718-725.

[104] M. Shojaeian and A. Kosar, Convective heat transfer and entropy generation analysis on Newtonian and non-Newtonian fluid flows between parallel-plates under slip boundary conditions, Int. J. Heat Mass Transfer, 70 (2014) 664-673.

[105] M.M. Bhatti, T. Abbas, M.M. Rashidi and M.E.S Ali, Numerical simulation of entropy generation with thermal radiation on MHD Carreau nanofluid towards a shrinking sheet, Entropy, 18 (2016) Article 200.

[106] G.R. Kefayati and H. Tang, Double-diffusive natural convection and entropy generation of Carreau fluid in a heated enclosure with an inner circular cold cylinder, Int. J. Heat Mass Transfer, 120 (2018) 731-750.

[107] G. Huminic and A. Huminic, The heat transfer performances and entropy generation analysis of hybrid nanofluids in a flattened tube, Int. J. Heat Mass Transfer, 119 (2018) 813-827.

[108] M.I. Khan, A. Kumar, T. Hayat, M. Waqas and R. Singh, Entropy generation in flow of Carreau nanofluid, J. Mol. Liq., 278 (2019) 677-687.

[109] T.A. Yusuf, F. Mabood, W.A. Khan and J.A. Gbadeyan, Irreversibility analysis of Cu-TiO_2-H_2O hybrid-nanofluid impinging on a 3-D stretching sheet in a porous medium with nonlinear radiation: Darcy-Forchhiemer's model, Alex. Eng. J., 59 (2020) 5247-5261.

[110] R. Muhammad, M.I. Khan, M. Jameel and N.B. Khan, Fully developed Darcy-Forchheimer mixed convective flow over a curved surface with activation energy and entropy generation, Comput. Meth. Prog. Bio., 188 (2020) Article 105298.

[111] A. Sahoo and R. Nandkeolyar, Entropy generation in convective radiative flow of a Casson nanofluid in non-Darcy porous medium with Hall current and activation energy: The multiple regression model, Appl. Math. Comput., 402 (2021) Article 125923.

[112] P.S. Reddy and P. Sreedevi, Entropy generation and heat transfer analysis of magnetic hybrid nanofluid inside a square cavity with thermal radiation, Eur. Phys. J. Plus, 136 (2021) Article 39.

[113] T. Hayat, M. Qasim and S. Mesloub, MHD flow and heat transfer over permeable stretching sheet with slip conditions, Int. J. Numer. Methods Fluids, 66 (2011) 963-975.

[114] O.D. Makinde, W.A. Khan and Z.H. Khan, Buoyancy effects on MHD stagnation point flow and heat transfer of a nanofluid past a convectively heated stretching/shrinking sheet, Int. J. Heat Mass Transfer, 62 (2013) 526-533.

[115] N.A.H. Haroun, S. Mondal and P.Sibanda, Unsteady natural convective boundary-layer flow of MHD nanofluid over a stretching surfaces with chemical reaction using the spectral relaxation method: A revised model, Procedia Eng., 127 (2015) 18-24.

[116] S.K. Soid, A. Ishak A. and I. Pop, MHD flow and heat transfer over a radially stretching/shrinking disk, Chinese J. Phys., 56 (2018) 58-66.

[117] T. Muhammad, T. Hayat, S.A. Shehzad and A. Alsaedi, Viscous dissipation and Joule heating effects in MHD 3D flow with heat and mass fluxes, Results Phys., 8 (2018) 365-371.

[118] R. Sharif, M.A. Farooq and A. Mushtaq, Magnetohydrodynamic study of variable fluid properties and their impact on nanofluid over an exponentially stretching sheet, J. Nanofluids, 8 (2019) 1249-1259.

[119] S.Z. Alamri, A.A. Khan, M. Azeez and R. Ellahi, Effects of masstransfer on MHD second grade fluid towards stretching cylinder: A novelperspective of Cattaneo-Christov heat flux model, Phys. Lett. A, 383 (2019) 276-281.

[120] B.S. Goud, Heat generation/absorption influence on steady stretched permeable surface on MHD flow of a micropolar fluid through a porous medium in the presence of variable suction/injection, Int. J. Thermofluids, 7-8 (2020) Article 100044.

[121] M.V. Krishna, N.A. Ahamad and A.F. Aljohani, Thermal radiation, chemical reaction, Hall and ion slip effects on MHD oscillatory rotating flow of micro-polar liquid, Alex. Eng. J., 60 (2021) 3467-3484.

[122] R. Kalaivanan, P. Renuka, N.V. Ganesh, A.K.A. Hakeem, B. Ganga and S. Saranya, Effects of aligned magnetic field on slip flow of Casson fluid over a stretching sheet, Procedia Eng., 127 (2015) 531-538.

[123] F. Selimefendigil and A.J. Chamkha, MHD mixed convection in a lid-driven cavity having a corrugated bottom wall and filled with a non-Newtonian power-law fluid under the influence of an inclined magnetic field, J. Therm. Sci. Eng. Appl., 8 (2015) 021023-021031.

[124] F. Selimefendigil and H.F. Öztop, Natural convection in a flexible sided triangular cavity with internal heat generation under the effect of inclined magnetic field, J. Mag. Magn. Mater., 417 (2016) 327-337.

[125] M. Atashafrooz, M. Sheikholeslami, H. Sajjadi and A.A. Delouei, Interaction effects of an inclined magnetic field and nanofluid on forced convection heat transfer and flow irreversibility in a duct with an abrupt contraction, J. Magn. Magn. Mater., 478 (2019) 216-226.

[126] D.H. Doh, G.R. Cho, E. Ramya and M. Muthtamilselvan, Cattaneo-Christov heat flux model for inclined MHD micropolar fluid flow past a non-linearly stretchable rotating disk, Case Stud. Therm. Eng., 14 (2019) Article 100496.

[127] Q.M. Al-Mdallal, N. Indumathi, B. Ganga and A.K.A. Hakeem, Marangoni radiative effects of hybrid-nanofluids flow past a permeable surface with inclined magnetic field, Case Stud. Therm. Eng., 17 (2020) Article 100571.

[128] T. Srinivasulu and B.S. Goud, Effect of inclined magnetic field on flow, heat and mass transfer of Williamson nanofluid over a stretching sheet, Case Stud. Therm. Eng., 23 (2021) Article 100819.

[129] J. Mackolil and B. Mahanthesh, Inclined magnetic field and nanoparticle aggregation effects on thermal Marangoni convection in nanoliquid: A sensitivity analysis, Chin. J. Phys., 69 (2021) 24-37.

[130] A.R. Bestman, Natural convection boundary layer with suction and mass transfer in a porous medium, Int. J. Energy Res., 14 (1990) 389-396.

[131] K.L. Hsiao, To promote radiation electrical MHD activation energy thermal extrusion manufacturing system efficiency by using Carreau-Nanofluid with parameters control method, Energy, 130 (2017) 486-499.

[132] A. Majeed, F.M. Noori, A. Zeeshan, T. Mahmood, S.U. Rehman and I. Khan, Analysis of activation energy in magnetohydrodynamic flow with chemical reaction and second order momentum slip model, Case Stud. Therm. Eng., 12 (2018) 765-773.

[133] A. Hamid, Hashim and M. Khan, Impacts of binary chemical reaction with activation energy on unsteady flow of magneto-Williamson nanofluid, J. Mol. Liq., 262 (2018) 435-442.

[134] M. Dhlamini, P.K. Kameswaran, P. Sibanda, S. Motsa and H. Mondal, Activation energy and binary chemical reaction effects in mixed convective nanofuid flow with convective boundary conditions, J. Comput. Des. Eng., 6 (2019) 149-158.

[135] S. Rashid, T. Hayat, S. Qayyum, M. Ayub and A. Alsaedi, Three-dimensional rotating Darcy-Forchheimer flow with activation energy, Int. J. Numer. Method Heat Fluid Flow, 29 (2019) 935-948.

[136] Z. Shah, P. Kumam and W. Deebani, Radiative MHD Casson nanofluid flow with activation energy and chemical reaction over past nonlinearly stretching surface through entropy generation, Sci. Rep., 10 (2020) Article 4402.

[137] H. Waqas, S.U. Khan, I. Tlili, M. Awais and M.S. Shadloo, Significance of bioconvective and thermally dissipation flow of viscoelastic nanoparticles with activation energy features: Novel biofuels significance, Symmetry 12 (2020) Article 214.

[138] M.M. Bhatti and E.E. Michaelides, Study of Arrhenius activation energy on the thermo-bioconvection nanofluid flow over a Riga plate, J. Therm. Anal. Calorim., 143 (2021) 2029-2038.

[139] R. Kumar, A. Bhattacharyy, G.S. Seth and A.J. Chamkha, Transportation of magnetite nanofluid flow and heat transfer over a rotating porous disk with Arrhenius activation energy: Fourth order Noumerov's method, Chin. J. Phys., 69 (2021) 172-185.

[140] S.J. Liao, An optimal homotopy-analysis approach for strongly nonlinear differential equations, Commun. Nonlinear. Sci. Numer. Simul., 15 (2010) 2003-2016.

Turnitin Originality Report

Nonlinear Models with Darcy-Forchheimer Relation by Farwa Haider .

From CL QAU (DRSML)

turnitin

- Processed on 17-May-2022 08:38 PKT
- ID: 1838072074
- Word Count: 33489

PROFESSOR
Department of Mathematics
Quaid-i-Azam University
Islamabad

Similarity Index
6%
Similarity by Source

Internet Sources:
2%
Publications:
5%
Student Papers:
1%

Focal Person (Turnitin)
Quaid-i-Azam University
Islamabad

sources:

1 1% match (publications)
B. Kumar, G. S. Seth, M. K. Singh, A. J. Chamkha. "Carbon nanotubes (CNTs)-based flow between two spinning discs with porous medium, Cattaneoâ"Christov (non-Fourier) model and convective thermal condition", Journal of Thermal Analysis and Calorimetry, 2020

2 < 1% match (student papers from 03-Aug-2018)
Submitted to Higher Education Commission Pakistan on 2018-08-03

3 < 1% match (student papers from 14-May-2018)
Submitted to Higher Education Commission Pakistan on 2018-05-14

4 < 1% match (student papers from 21-Dec-2013)
Submitted to Higher Education Commission Pakistan on 2013-12-21

5 < 1% match (student papers from 24-Aug-2011)
Submitted to Higher Education Commission Pakistan on 2011-08-24

6 < 1% match (student papers from 16-Dec-2021)
Submitted to Higher Education Commission Pakistan on 2021-12-16

7 < 1% match (student papers from 03-May-2016)
Submitted to Higher Education Commission Pakistan on 2016-05-03

8 < 1% match (student papers from 06-Jun-2018)